Merocyanine Dyes as Organic Semiconductors for Vacuum-processed Solar Cell and Transistor Devices

Dissertation zur Erlangung des
naturwissenschaftlichen Doktorgrades
der Julius-Maximilians-Universität Würzburg

vorgelegt von
Alhama Arjona Esteban
aus Gijón (Spanien)

Würzburg 2015

Eingereicht bei der Fakultät für Chemie und Pharmazie am:
18.12.2015

Gutachter der schriftlichen Arbeit:
1. Gutachter: Prof. Dr. Frank Würthner
2. Gutachter: Prof. Dr. Klaus Meerholz

Prüfer des öffentlichen Promotionskolloquiums:
1. Prüfer: Prof. Dr. Frank Würthner
2. Prüfer: Prof. Dr. Klaus Meerholz
3. Prüfer: Prof. Dr. Matthias Lehmann

Datum des öffentlichen Promotionskolloquiums:
08.03.2016

Doktorurkunde ausgehändigt am:

_____

A mi madre

Caminante, son tus huellas
el camino y nada más;
caminante, no hay camino,
se hace camino al andar.
Al andar se hace camino,
y al volver la vista atrás
se ve la senda que nunca
se ha de volver a pisar.
Caminante, no hay camino,
sino estelas en la mar.

Antonio Machado [1875 - 1939]

List of Abbreviations

A	acceptor
Abs	absorption
Ac	acetyl
Ac_2O	acetic anhydride
AFM	Atomic Force Microscopy
AM1.5G	Air Mass
B3LYP	hybrid density functional
BHJ	bulk heterojunction
Bu	butyl
CT	charge transfer
CV	cyclic voltammetry
Cy	cyanine
d	day(s)
D	donor
DCM	dichloromethane
DFT	density functional theory
DMF	*N*,*N*′-dimethylformamide
DMSO	dimethylsulfoxide
DOS	density of states
DPFA	*N*,*N*-diphenylformamidine
DSC	differential scanning calorimetry
$E_{1/2}$	half-wave potential of a reversible redox process
EA	Electron affinity
EBL	Electron-blocking layer
EI	Electron ionization
EOA	electro-optic absorption
E_p	peak potential of an irreversible redox process
EQE	external quantum efficiency
Equiv	equivalent(s)
ESI	electrospray ionization
Et	ethyl
2-Ethex	2-ethylhexyl

Fc	ferrocene
FF	fill factor
FMO	frontier molecular orbital
FOPA	12,12,13,13,14,14,15,15,16,16,17,17,18,18,18H-pentadecafluoro-octadecyl phosphonic acid (FOPA)
FRET	Förster resonance energy transfer
FWHM	full width at half maximum
h	hour(s)
HCC	hole collecting contact
Hex	hexyl
HOMO	highest occupied molecular orbital
HRMS	high resolution mass spectrometry
HTL	Hole-transporting layer
*i*Pr	isopropyl
ICT	intramolecular charge transfer
IP	Ionization potential
IR	Infrared
ITO	indium tin oxide
J_{SC}	short circuit current density
LUMO	lowest unoccupied molecular orbital
M	molar
MALDI	matrix assisted laser desorption/ionization
MC	merocyanine
MCH	methylcyclohexane
Me	methyl
MeOH	methanol
min	minute(s)
Mp	melting point
MPP	maximal power point
MS	mass spectrometry
NIR	near infrared
NLO	nonlinear optic
NMR	nuclear magnetic resonance

OPV	organic photovoltaic
OTFT	organic thin-film transistor
OSC	organic solar cell
P3HT	poly(3-hexylthiophene)
Pc	phthalocyanine
$PC_{60}BM$	[6,6]-phenyl-C_{61}-butyric acid methyl ester
$PC_{70}BM$	[6,6]-phenyl-C_{71}-butyric acid methyl ester
PCE	power conversion efficiency
PEDOT:PSS	poly(3,4-ethylendioxythiophene) polystyrene sulfonate
PHJ	planar heterojunction
PMHJ	planar mixed heterojunction
ppm	parts per million
Pr	propyl
Ref.	reference
rpm	revolutions per minute
r.t.	room temperature
s	second
S_0	singlet ground state
S_1	first singlet excited state
SAM	self-assembled monolayer
SCE	standard calomel electrode
SVA	solvent-vapor annealing
TEM	transmission electron microscopy
THF	tetrahydrofuran
TPA	*n*-tetradecylphosphonic acid
UV-Vis	ultraviolet-visible
V_{OC}	open circuit voltage
Vol	volume
wt	weight
XRD	X-ray diffraction

Table of Contents

Chapter 1

Introduction and Aim of the Thesis

The energy economy of all countries, in particular the industrialized ones, still depends on fossil energy sources such as coal, oil, natural gas, and nuclear energy in the form of the uranium isotope ^{235}U. It is clear today that such energy sources will not last forever and this living model that consumes oxygen and produces carbon dioxide needs to be overcome. Therefore new technologies for the conversion of renewable energy sources such as wind or solar light into electricity have been developed in the last years.

The global energy consumption per year is about 13.2×10^9 t coal equiv./year, which makes a consumption of 2.19 kW/person and year. For comparison, the energy current from the Sun that continuously radiates toward the Earth is about 1.8×10^{14} t coal equiv./year.[1] This non-negligible energy source would cover our energetic needs if a sufficient efficiency for the conversion process of light into electricity can be achieved. In this regard, the improvement of solar cell efficiencies over time according to the National Renewable Energy Laboratory (NREL) can be found in Figure 1.

The research on solar cells started at the end of the seventies, where the first panels showed laboratory efficiencies up to 20 % using single junction cells with crystalline GaAs as semiconductor material. Today silicon-based solar panels represent nearly 90 % of the sales of photovoltaic products.[2] In particular, single-crystalline (c-Si) silicon panels dominate the industry at the moment, with laboratory efficiencies up to 28 % (single crystal devices, Figure 1). The main disadvantage of single-crystal wafer cells is the high production prices derived from the the high purity of the material required. Moreover, technologies based on thin-films of cadmium telluride (CdTe) or multijunction solar cells have been as well developed, but have not become the mainstream due to lower performance in the first case and too high production costs in the second case (Figure 1).[2]

Organic solar cells (OSC) based on polymers or small molecules have experienced a continuous improvement of performance since their first creation in the late eighties.

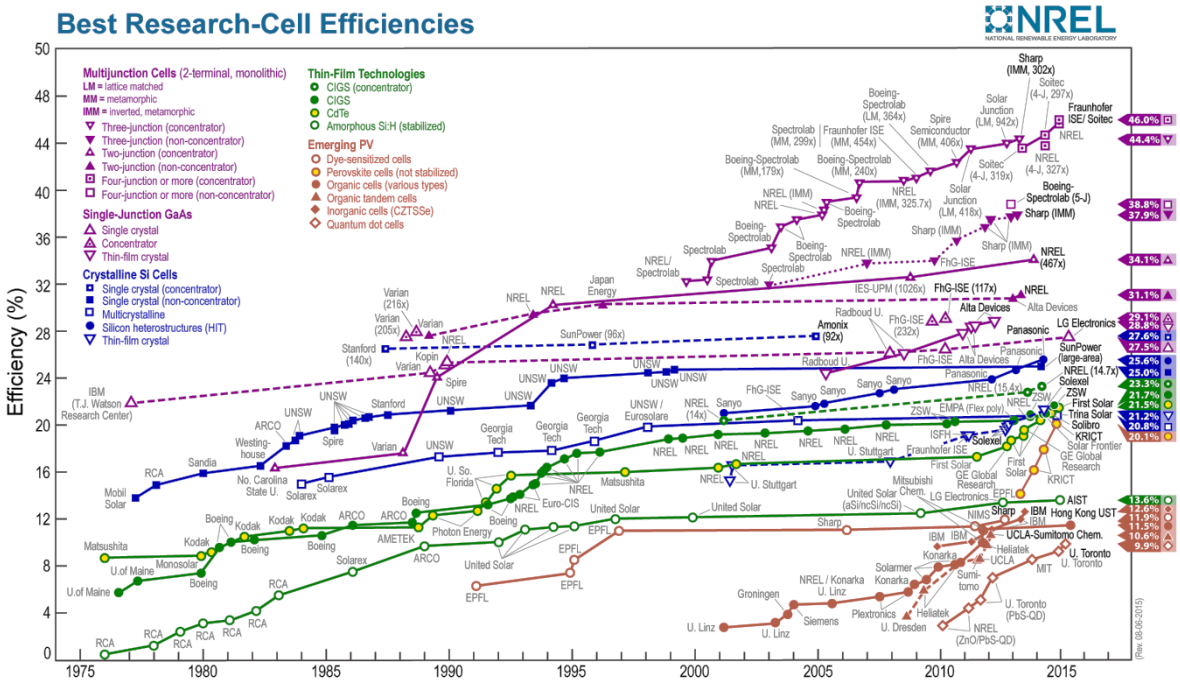

Figure 1. Conversion efficiencies of best research solar cells worldwide from 1976 through 2015 for various photovoltaic technologies, according to NREL.[2] Efficiencies determined by certified agencies/laboratories. This plot is courtesy of the National Renewable Energy Laboratory, Golden, CO.

Today, power-conversion efficiencies of more than 10 % have been reported for small-molecule solar cells.[3] This technology holds the promise of a substantial price reduction and faster return to investment in comparison with silicon-based counterparts. Organic compounds can be prepared rather inexpensively by following established design strategies, and their absorption and electrochemical properties can be tuned through suitable molecular design. Moreover, they can be processed in vacuum or from solution, thus allowing for simple and inexpensive roll-to-roll processes. Furthermore, when using flexible substrates, lightweight solar cells of various dynamic shapes can be obtained.

Previous work by the groups of Würthner and Meerholz focused on exploring the suitability of merocyanine dyes as donor (D) materials for organic solar cell applications.[4] These small molecular materials display high extinction coefficients and have the advantage of simple synthesis and purification procedures. Thus, the aim of this thesis was the synthesis and characterization of new functional merocyanine dyes for the application in organic photovoltaics in combination with the fullerene acceptor (A) C_{60}. The targeted compounds should display strong absorption in the visible and near infrared region as well as optimized energy levels which should provide enough driving force for the exciton dissociation at the donor/acceptor interface of the solar cells. Additionally, thermally stable

compounds are desired since vacuum-processing techniques offer a better control of the active layer morphology in comparison to solution-processing. Thus, several merocyanine dyes mostly based on indanedione derivatives combined with various electron-donating moieties have been envisaged. The study of the optical and electrochemical properties by UV-Vis spectroscopy and cyclic voltammetry enables a first screening of the dyes and their applicability as donor materials. Moreover, the semiconducting properties of the molecules should be investigated in vacuum-processed transistor devices. Single crystal analyses will be useful to establish a correlation between the packing in the solid state and the device performance. Finally, selected molecules are to be tested as donor materials for organic solar cells in combination with C_{60} in collaboration with the group of Prof. Dr. Meerholz.

In **Chapter 2** the basic physical concepts needed for understanding the processes involved in energy generation from light are described. Subsequently a literature overview on D-π-A based organic solar cells is presented. The focus is firstly put on merocyanine dyes while afterwards other D-π-A systems are as well discussed. Finally, a short introduction to the exciton theory developed by Kasha is provided.

Chapter 3 describes, analyzes and discusses the results obtained in this thesis. First, the synthesis of all new compounds is addressed in section 3.1. Section 3.2 focuses on a series of indanedione derivatives with optimized optical and electrochemical properties for the application in organic solar cells. Single crystal analyses reveal a new packing motif which results highly favorable for charge carrier transport and delivers the highest solar cell performance of the series. Section 3.3 presents the efficient lowering of the frontier molecular orbitals of a series of merocyanine dyes through introduction of halogen atoms in the conjugated scaffold. Section 3.4 and 3.5 describe polymethine dyes with a π-extended methine bridge. Finally, in section 3.5 the conformational change of a bifurcated molecule between a merocyanine-like and a cyanine-like structure with increasing solvent polarity is studied.

Chapters 4 and **5** summarize in English and German the contents of this thesis.

Chapter 6 describes the experimental procedures for the synthesis of new compounds, as well as the materials and methods used for their characterization.

Chapter 2

State of Knowledge

2.1 Organic Solar Cells

2.1.1 Device structure and processes involved in energy generation

The main difference between inorganic and organic solar cells (OSC) is that in inorganic solar cells the absorption of a photon immediately generates free charge carriers, whereas in organic materials the light absorption generates a coulombically bound electron-hole pair (exciton) which needs a high enough electrical field to overcome the exciton binding energy towards dissociation into free charge carriers. The solution to this problem was developed by Tang in 1986 with the first planar heterojunction (PHJ) solar cell,[5] composed of a bilayer of copper phthalocyanine and a π-extended perylene derivative sandwiched between two electrodes. The different energy levels at the donor/acceptor interface served as driving force for the electron-hole pair dissociation, thus providing an efficiency of almost 1 %.

Although the invention of the PHJ structure (Figure 2a) was a milestone in the development of organic solar cells, it still suffered from major deficiencies. Since the exciton dissociation only takes place at the donor/acceptor (D/A) interface and the exciton diffusion length of organic materials is below 10 - 20 nm,[6] the layer thickness has to remain very thin, implying that only a fraction of the solar light can be absorbed. Searching for rapid exciton diffusion to the D/A interface while maintaining a sufficient layer thickness, the groups of Heeger and Holmes independently developed the bulk heterojunction (BHJ) concept in 1995[7] (Figure 2b). In this cell architecture, the donor and acceptor compounds form an interpenetrating, phase-separated network with nanoscale morphology, which provides a maximal interface. The BHJ is nowadays the most common solar cell structure in organic solar cells, which has the advantage of being accessible by solution as well as vacuum-processing.

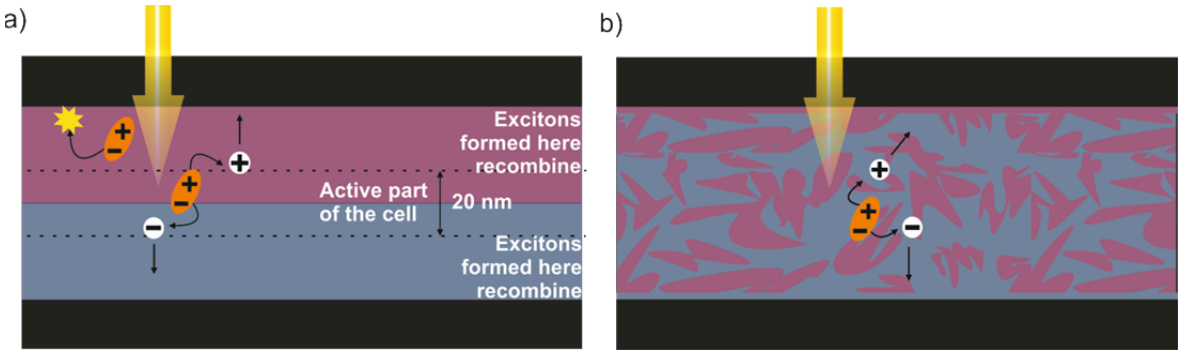

Figure 2. Schematic representation of a planar heterojunction (a) and a bulk heterojunction (b) solar cell. The pink and blue areas represent the donor and acceptor materials, respectively. The black areas represent the electrodes. Since exciton dissociation only takes place at the donor/acceptor interface, in the PHJ the excitons formed far from the interface recombine, whereas in the BHJ this is avoided by the much larger donor/acceptor interface.

The processes involved in energy production in organic solar cells are described in the following. Upon absorption of light, a molecule of donor or acceptor material is promoted to an excited state. Usually this process is described as the transition of an electron from the HOMO to the LUMO of the donor material and subsequent relaxation to the lowest excited state (Figure 3, steps 1 and 2) forming an electron-hole pair called exciton.[6] An exciton is an excited but neutral state with a limited lifetime, which consists of an electron and a hole paired on a single molecular unit by an energy E_{ex} (Frenkel exciton), which is smaller than the energy gap between the limits of the electrical gap (difference between LUMO and HOMO levels) (Figure 3, E_{ex}). Since excitons are neutral species, their motion cannot be influenced by an electric field. Thus, they diffuse randomly by hopping within the material (Förster or Dexter-type transfer, Figure 3, step 3).

Once the excitons reach the donor/acceptor interface, they can dissociate. The separation of the charges can be understood as a two-step process. First of all, supposing that the exciton was formed in the donor material, an electron is transferred to the LUMO of an acceptor molecule, but both are still coulombically bound (Figure 3, step 4). Secondly, the charge carriers are separated. Exciton binding energies ranging from 0 to 1.5 eV have been reported for organic semiconductors.[8] The energy of the final state can be described as $E_{final} = IP_D - EA_A$, (where IP is the ionization potential and EA the electron affinity), often taken as $E_{final} = (E_{LUMO})_{acceptor} - (E_{HOMO})_{donor}$ (Figure 3). E_{final} defines the upper limit for the achievable open-circuit voltage (V_{OC}) of the solar cell.

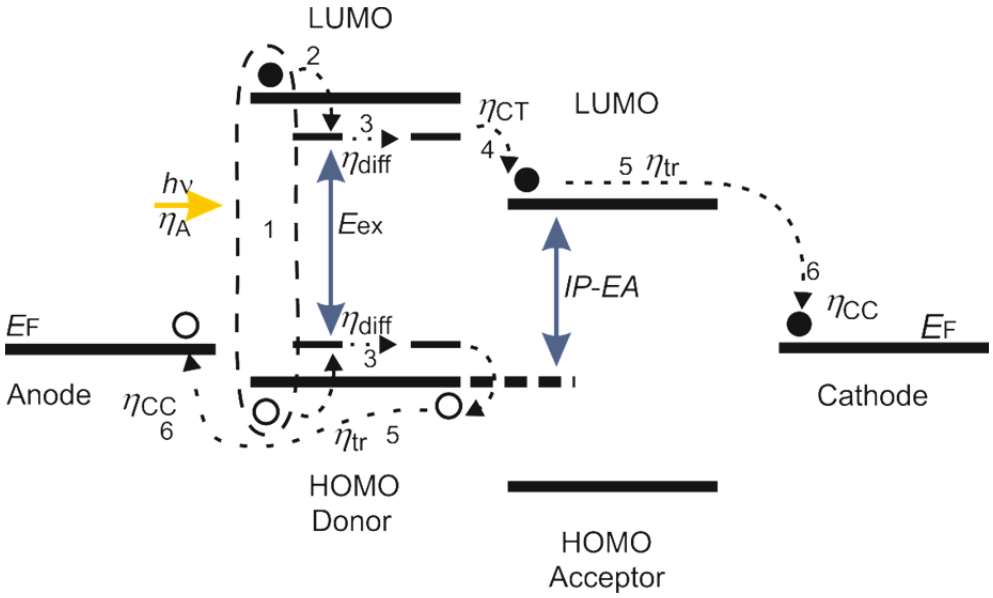

Figure 3. Diagram of molecular orbitals. The various steps involved on charge generation and collection of heterojunction organic solar cells are depicted: 1) Photon absorption by the donor material, 2) generation of excitons, 3) exciton diffusion to the donor/acceptor interface, 4) exciton dissociation at the interface, 5) charge transport towards the electrodes and 6) charge collection at the electrodes. Electrons are represented by filled circles, holes by hollow ones. Diagram inspired on description from A. Moliton and J-M. Nunzi and reused with permission of ref.[6a]

Finally, the charge carriers have to diffuse to the electrodes (Figure 3, step 5). The key parameter governing charge mobility is the overlap of frontier π-molecular orbitals between adjacent molecules, which characterizes the strength of the intermolecular couplings. In crystalline inorganic semiconductors, the mobility of charge carriers in conduction bands is about 10^2 - 10^3 $cm^2 V^{-1} s^{-1}$, whereas in organic compounds the weak electronic couplings and large electron-vibration couplings localize the charges in form of polarons (radical ions), which diffuse by hopping mechanism. Thus, the charge carrier mobility depends on the morphology of the material, and can vary over several orders of magnitude from amorphous materials (10^{-6} - 10^{-3} $cm^2 V^{-1} s^{-1}$)[9] to highly ordered materials (> 1 $cm^2 V^{-1} s^{-1}$).[9] The organic material-electrode interface is complex, and the charge collection mechanism (Figure 3, step 6) is still not completely understood. However, in order to have an efficient charge collection, the following conditions must be met: $(E_F)_{cathode} < (E_{LUMO})_{acceptor}$ and $(E_F)_{anode} > (E_{HOMO})_{donor}$, where E_F is the Fermi level of the corresponding electrode or interlayer. Surface modification by deposition of interlayers such as MoO_3 or LiF allows for modification of the Fermi levels and can improve the quality of the electrical contact.[10]

The main loss sources which have to be faced concern first of all the optical mismatch with the solar spectrum. For a given optical gap E_G, only the photons with energy $E_A > E_G$ will

be absorbed. In addition, for the absorbed photons there is a loss of energy by thermalization of "hot" carriers equal to $\Delta E = E_A - E_G$. Energy losses can as well occur during exciton dissociation and charge carrier generation, which is limited by bimolecular recombination. Furthermore, traps in the bulk will limit the charge transport to the electrodes. Finally, it has to be noticed that the solar cell efficiency is a device property and therefore depends on each of the parameters involved in energy production, as well as device structure and morphology.

2.1.2 Characterization of organic solar cells

In the dark the solar cell works as a diode. Under irradiation a photocurrent J_{ph} appears. The Shockley equation describes the current-voltage characteristics of this circuit:

$$J = \frac{1}{1 + R_S/R_P}\left[J_0 \left\{ \exp\left(\frac{V - JR_S A}{nkT/e} \right) - 1 \right\} - \left(J_{ph} - \frac{V}{R_P A} \right) \right] \qquad (1)$$

Where the R_S denotes the series resistance, R_P the shunt resistance, J_0 is the saturation current, e denotes the elementary charge, kT the thermal energy and A the area of the cell. From this equation we can derive the expressions describing the open-circuit voltage (V_{OC}) and the short-circuit current density (J_{SC}). For a very small R_S and very big R_P, the V_{OC} and J_{SC} can be approximated as follows:

$$V_{OC} \approx n\frac{kT}{e}\ln\left\{ 1 + \frac{J_{ph}}{J_0} \right\} \qquad (2)$$

$$J_{SC} \approx -J_{ph} \qquad (3)$$

The typical shape of the current-voltage curve under illumination for a solar cell is shown in Figure 4. In the fourth quadrant of the current-voltage curve the product of $J \cdot V$ is negative, so that power can be produced by the device. The optimized maximum power corresponds to the values J_{MPP} and V_{MPP} (Figure 4, blue area). The fill factor is then defined as the ratio of P_{max} to $V_{OC} \cdot J_{SC}$:

$$FF = \frac{J_{MPP} \cdot V_{MPP}}{J_{SC} \cdot V_{OC}} \qquad (4)$$

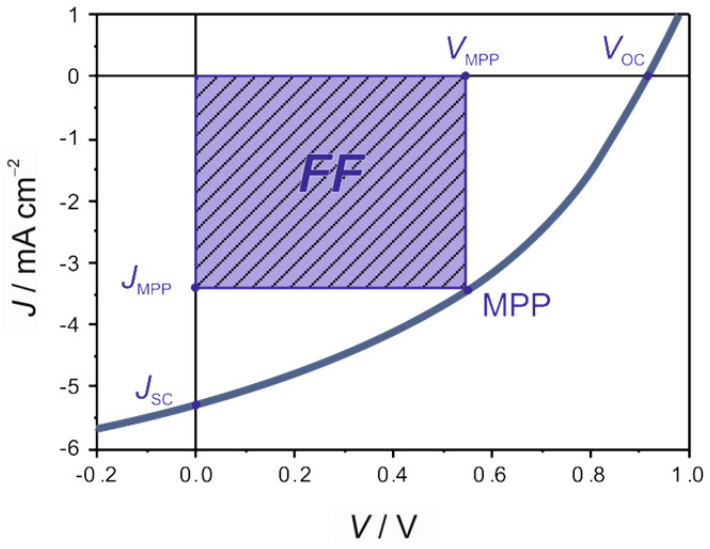

Figure 4. Current-voltage properties of a solar cell. The current-voltage behavior under illumination is shown. The blue area represents the maximum power of the cell, P_{max}, operated at the maximum power point (MPP).

The most important parameter used to compare the performance of solar cells is the external power-conversion efficiency (*PCE*), defined as the ratio of the maximum electric power (P_{max}) to the energetic flux:

$$PCE = \frac{P_{max}}{P_{in}} = \frac{FF \cdot J_{SC} \cdot V_{OC}}{P_{in}} \qquad (5)$$

This yield is the maximum value for the theoretical yield of a solar cell. In order to improve the *PCE*, each of the parameters in the numerator has to be optimized. In practice, the *PCE* is diminished by the series and shunt resistances in the cell, and by the reflection of the light facing the surface of the cell.

Another important evaluation tool for organic solar cells is the external quantum efficiency (*EQE*) spectrum, which represents the ratio between the number of generated electrons to the number of incident photons (incident photon-to-current efficiency, *IPCE*). Experimentally the wavelength-dependent *EQE* values are obtained from the ratio between the measured photocurrent and the intensity of the incoming monochromatic light.

The upper limits of J_{SC} can be obtained by integrating the *EQE* from the high photon energy side to the maximum wavelength (λ_{max}) of the material. Thus, the smaller the optical band gap, the larger the J_{SC}. However, reducing the optical band gap will increase

the energy loss by thermalization (this can be avoided in a tandem cell structure with different band gap materials, as described in section 2.2.1.3) and also decrease the V_{OC}.

On the other hand, it has been estimated that the maximum value of V_{OC} depends on the difference between the ionization potential (*IP*) of the donor material and the electron affinity (*EA*) of the acceptor material. This value can therefore be increased if the energy offset between the donor and acceptor molecular states is decreased. Ideally, this offset should be of about 0.3 - 0.5 eV. A larger offset will lead to energy losses, while a shorter one will compromise the exciton dissociation at the interface. Thus, in order to maximize the power conversion efficiency the energy band gap should be about 1.6 - 1.9 eV (775 - 650 nm).[6b] As a reference, the band gap of silicon is 1.1 eV.[6b] It should be however noticed that often the HOMO and LUMO levels, obtained from solution by means of cyclic voltammetry, are used instead of the corresponding *IP* and *EA* values for the evaluation of the upper limit of V_{OC}. In this regard, techniques such as UPS or XPS appear useful to determine the energy levels of the molecules in the solid state and avoid neglecting the solid state interactions and polarization effects at the donor/acceptor interface.[11]

2.2 Donor-Acceptor D-A Dyes as Donor Materials for OPV*

The field of organic solar cells was firstly inaugurated with small molecules,[5, 12] whose efficiencies were rapidly overcome by functional polymers,[13] resulting in great improvements in power-conversion efficiencies from about 1 % to over 8 % in the last decade. Although semiconducting polymers show good charge carrier mobilities, they usually present low absorption coefficients and challenging purification. On the contrary, small molecules have the advantages of easy synthesis and purification, monodispersity, and a well-defined structure. In some cases they allow for vacuum deposition techniques, which offer a better control over thin film morphologies than solution-processing techniques do. In this respect huge efforts have been made in the last years to improve performance of bulk heterojunction solar cells based either on polymers or small molecules. In the meanwhile efficiencies approaching 10 % have been reported.[3] Whilst these efficiencies demonstrate a great scientific advancement, they usually refer to very small solar cells of about 1 cm^2, which still do not meet the demands for successful commercialization.

With respect to the acceptor materials used so far in organic solar cells, fullerene derivatives such as $PC_{60}BM$, $PC_{70}BM$, C_{60} and C_{70} are the widest used acceptor materials for organic solar cells and therefore allow for comparison of the solar cell performance. Although other electron-poor organic semiconductor materials have been successfully applied to OPV recently,[14] they have not been taken into account in this overview.

Among the huge variety of molecules used as donor materials in the BHJ active layers, an increasing number of molecules with alternating donor (D) and acceptor (A) subunits have been reported during the last years.[15] The use of alternating electron-donating and electron-withdrawing functional groups allows for lowering the optical band-gap due to intramolecular charge transfer, therefore offering the possibility of tuning the optical absorption and the HOMO/LUMO levels of the molecules by careful design of their conjugated structure. Whilst the majority of research groups focused their efforts on either alternating $(D\text{-}\pi\text{-}A)_n$ polymers and D-A-D or A-D-A small molecules, the groups of

* The overview given in this chapter is accepted for publication in a book which collects the contribution of all groups engaged in the DFG-funded collaborative program SPP1355 "Elementary Processes of Organic Photovoltaics": A. Arjona-Esteban, M-Lenze, K. Meerholz, F. Würthner, *Adv. Polym. Sci*. **2016**.

Würthner and Meerholz decided in 2006 to focus their attention on dipolar D-π-A dyes. The unsymmetrical structure introduces a dipole moment in the molecule, which is considered to be detrimental for charge carrier transport in amorphous organic materials.[16] On the other hand, earlier work demonstrated that highly dipolar molecules preferentially assemble in centrosymmetric dimers leading to a vanishing of the dipolar character on the supramolecular level.[17] Furthermore, earlier studies demonstrated photorefractive effects in single component glassy materials of D-π-A dyes which is only possible if charge carriers are generated and exhibit a decent mobility.[18] Major advantages of D-π-A dyes are that the combination of available donor and acceptor moieties offers an almost infinite library of compounds with well adjustable molecular properties. The most common donor and acceptor groups are listed in Chart 1.

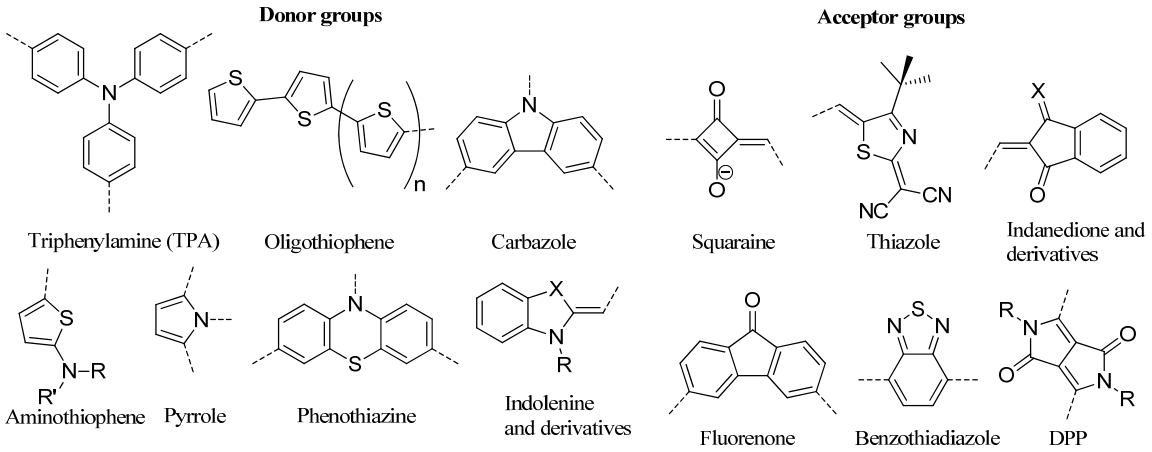

Chart 1. Examples of donor (left) and acceptor (right) moieties applied in dipolar dyes for BHJ solar cells.

2.2.1 Merocyanine dyes

Merocyanine dyes are the archetype class of push-pull molecules. The electronic properties of merocyanine dyes depend on the length of the polymethine chain and the strength of the donor and acceptor moieties, which determine the dipole moment and the absorption properties. In general their electronic structure can be described by two resonance forms, a neutral one and a zwitterionic one.[19]

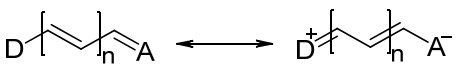

In the case of weakly electron-donating and electron-withdrawing end groups, the corresponding merocyanine dye is usually polyene-like, displaying alternating double C=C

and single C-C bonds within the methine bridge and small dipole moment in the ground state. Strengthening of the end groups increases the transfer of electron density from the donor unit to the acceptor group and leads to a leveling of the bond lengths and concomitantly a large ground state dipole moment. At the so-called *cyanine limit* the chromophore displays no bond length alternation at all.[19] For molecules at the *cyanine limit*, the geometric and electron density changes upon optical excitation are minimal, resulting in narrow and most intense absorption bands.[20] Further polarization of the polymethine chain by particularly strong donor and acceptor groups may lead to dyes whose ground state is even dominated by the zwitterionic structure. This is however only possible for short polymethine chains and heterocyclic donor and acceptor end groups that take advantage of aromatization in the zwitterionic structure.[21]

Figure 5. The optical properties of merocyanine dyes are easily modified by carefully adjusting the strength of the electron-rich and electron-poor end groups.

Interestingly, probably due to the outstanding absorption properties and lack of knowledge about charge transport mechanisms,[22] a few studies on merocyanine dyes can be found in the early literature of organic photovoltaics. Thus, in 1978 Morel *et al.* reported on a Schottky diode consisting of a layer of **1** sandwiched between aluminium and silver electrodes with a remarkable efficiency up to 0.70 %.[23] Few other groups reported as well studies on merocyanine-based solar cells with similar power-conversion efficiencies.[24] Furthermore, vacuum-processed OTFTs based on merocyanine dyes were reported by Kudo *et al.* in 1984.[25] The modest hole mobilities of ~ 10^{-5} cm^2 V^{-1} s^{-1} were rationalized by the formation of deep trap states near the SiO_2/dye interface. Besides these early publications on D-π-A chromophores, in the following years merocyanine dyes disappeared from organic electronics and photovoltaics but found application as spectral sensitizers in photography, as markers in biology and medicine and in the field of photorefractive materials and non-linear optics.[19, 26]

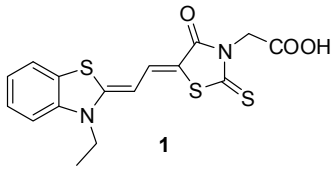

Chart 2. Chemical structure of dye **1**.

Unsymmetrical push-pull systems such as merocyanine dyes were thereafter presumably not applied in BHJ organic solar cells due to their high dipole moments. According to the Gaussian Disorder Model (GDM),[16] completely randomly arranged highly dipolar molecules are supposed to limit the transport of charge carriers in amorphous solid state materials due to a broadening of the density of states. However, the studies of merocyanines in several groups involved in research on non-linear optical materials including our group have demonstrated that the majority of these compounds arrange in the solid state as centrosymmetric dimers with small transversal or longitudinal displacement (Figure 6). This results in the annihilation of the dipole moment on the supramolecular level leading to an entirely new situation concerning charge transport.

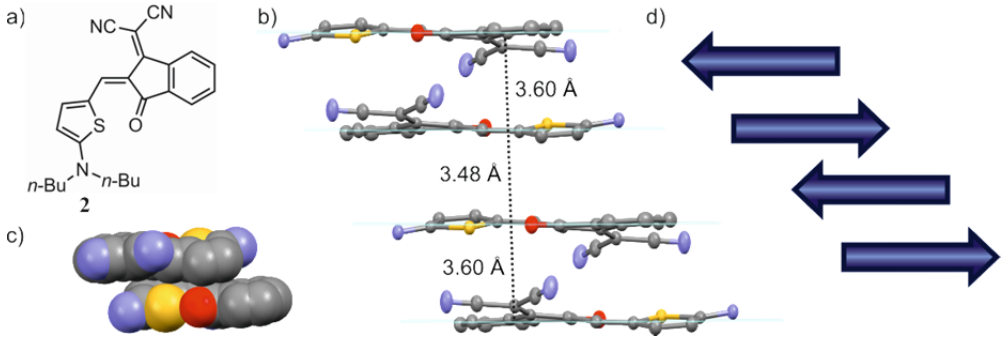

Figure 6. Example of antiparallel arrangement of a merocyanine dye (**2**) in the solid state. a) Molecular structure of dye **2** in the crystal. b) π-stack of dye **2** with antiparallel packing motif. c) Space filling view of the close dimer of dye **2** (alkyl chains and protons in (b) and (c) are omitted). d) Schematic representation of dye **2** stack showing the antiparallel orientation of the dipole moments (arrows). This Figure has been modified with permission of ref.[4a]

2.2.1.1 Solution-processed BHJ Solar Cells

Following previous work on A-D-A and D-A-D structures, the first application of D-π-A merocyanine dyes was reported by Kronenberg *et al*. in 2008 in solution-processed bulk heterojunction solar cells.[27] In this first study two series of chromophores bearing 2-aminothiophene or indolenine donor units combined with electron-withdrawing groups of different strength were blended with $PC_{60}BM$. While the increase of merocyanine content

enhanced photon absorption, a larger amount of $PC_{60}BM$ was favorable for the charge transport properties. For this series of chromophores a correlation between V_{OC} and HOMO level of the donor material could be found. The most efficient solar cells were built with thiazole-containing chromophore **3**, showing film absorption at the longest wavelength of 650 nm of the series. This enables a good overlap of the absorption spectrum with the solar irradiance and leads to the best J_{SC} of 6.3 mA cm^{-2} among the investigated D-π-A dyes. In combination with 70wt % $PC_{60}BM$ a *PCE* of 1.7 % was reached, which was among the best results in the field of solution-processed small molecules at the time. After this first promising results, the solar cells based on dye **3** were optimized by varying the top electrode. Ba/Ag provided the best results, mainly due to an increase in J_{SC}. The optimized cells displayed efficiency of 2.1 %, which could be further enhanced under reduced illumination conditions up to 2.7 %.[28]

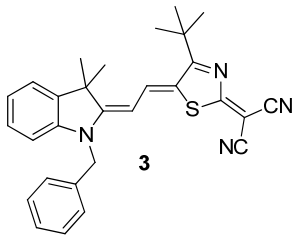

3

Chart 3. Chemical structure of dye **3**.

Further studies on solution-processed solar cells based on merocyanine dyes established some general rules that helped to define lead structures among the huge available library of possible D-π-A molecules. In order to obtain homogeneous films of sufficient thickness by spin-coating a solubility of at least 2 mg mL^{-1} in chlorobenzene is desired. From the energetic point of view, FMO levels of about −3.7 eV (LUMO) and −5.7 eV (HOMO) are preferred when using $PC_{60}BM$ as acceptor material in order to ensure an efficient electron transfer and minimize the energy losses. Thus, the optical band gap should be around 2.0 eV (560 - 690 nm). Finally, a high tinctorial strength (with μ^2_{ag} $M^{-1} \geq 0.20$ D^2 mol g^{-1}) will allow for high absorption (optical density about 0.4 - 0.5) while still having a relatively thin active layer of about 40 - 60 nm.

Several acceptor groups were investigated by Bürckstümmer *et al*. in combination with 2-aminothiophene donor unit, thus revealing the tunability of molecular properties by structural design. In Figure 7a the studied acceptor groups are ordered following their electron-withdrawing strength. From the UV-Vis absorption spectra, depicted in Figure 7b,

it becomes clear that increasing the acceptor strength decreases the LUMO level while maintaining an almost constant HOMO level. As a consequence, the molecular absorption shifted towards the NIR region. Solution-processed BHJ cells were built in combination with $PC_{60}BM$ using the device structure ITO/PEDOT:PSS (40 nm)/dye:$PC_{60}BM$/Al (120 nm) with an active layer thicknesses about 50 - 60 nm. A first comparison of the molecules showed that derivatives containing indandione-malononitrile displayed the highest V_{OC} and J_{SC}, reaching a *PCE* of 3.0 % for dye **6**. Moreover, solar cell fabrication was optimized by replacement of $PC_{60}BM$ by $PC_{70}BM$, which enhanced the cell absorption. Further replacement of PEDOT:PSS by MoO_3 and utilization of a Ba/Ag metal electrode provided the best efficiency for the cell based on dye **6**, which reached a *PCE* up to 4.5 % without any thermal post-treatment.[4a]

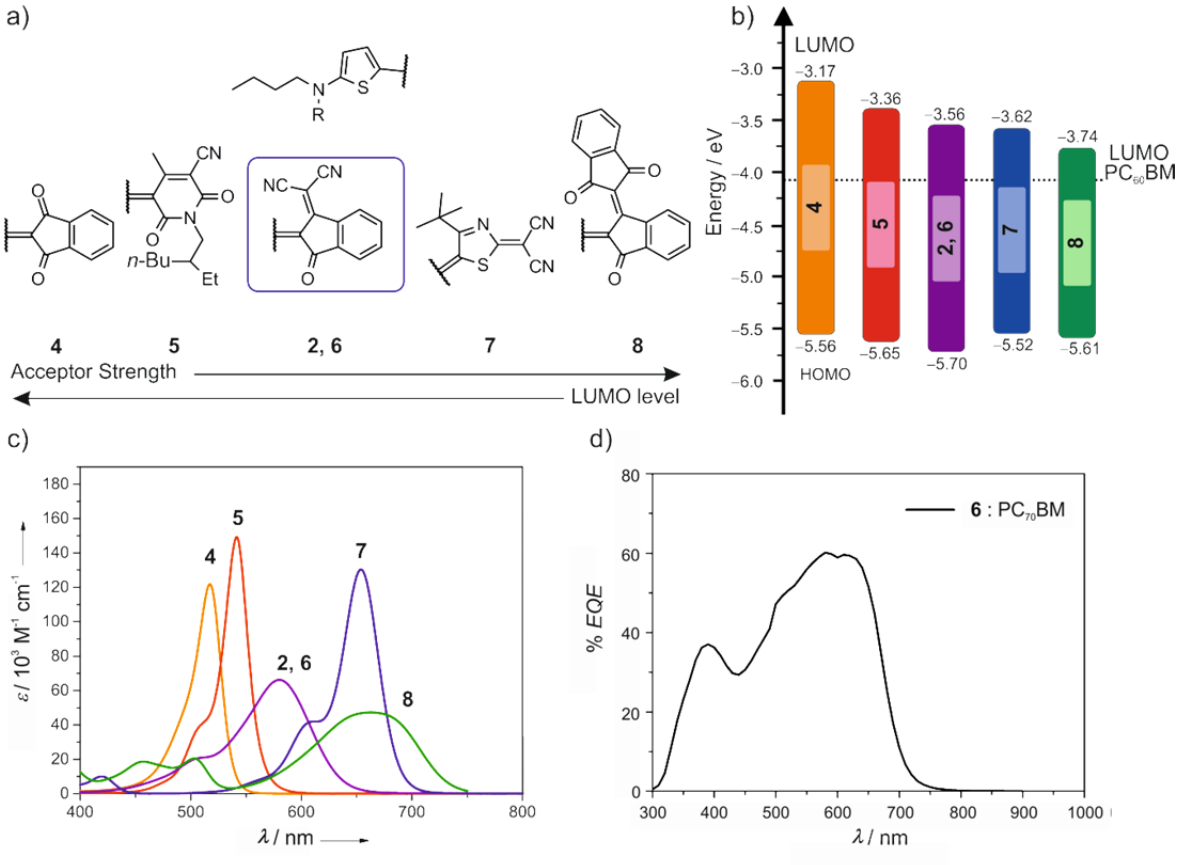

Figure 7. a) Molecular structures of the investigated dyes. R = *n*-Bu for all dyes except dye **6**, where R = Et. Dependence of the energy levels on the acceptor moiety. The best performing solar cells from solution could be obtained for dyes **2** and **6**.[4a] b) Schematic representation of FMO levels of molecules **2** and **4** - **8** with respect to the LUMO level of $PC_{60}BM$. c) UV-Vis spectra of dyes **2** and **4** - **8** in dichloromethane (10^{-5} M, 298 K). d) *EQE* of the optimized solution-processed BHJ device ITO/MoO_3/**6**:$PC_{70}BM$/Ba/Ag reaching a *PCE* of 4.5 %. This Figure has been modified with permission of ref.[4a]

Continuing with the indandione-malononitrile acceptor unit, variations were made on the indolenine donor by bridging the alkyl chain, which resulted in a more rigid structure with planar geometry. Both ethylene (**10**) and propylene (**11**) bridging groups were employed with the hope of improved solid state packing and solar cell morphology. The synthesized dyes displayed similar energy levels and absorption properties. Interestingly, dye **11** showed better performance for relatively high contents of dye vs. $PC_{60}BM$, thus displaying the highest J_{SC} of 8.24 mA cm^{-2} for this series. Together with a V_{OC} of 0.94 V, **11** gave the best solar cells with 2.59 % *PCE*.[29]

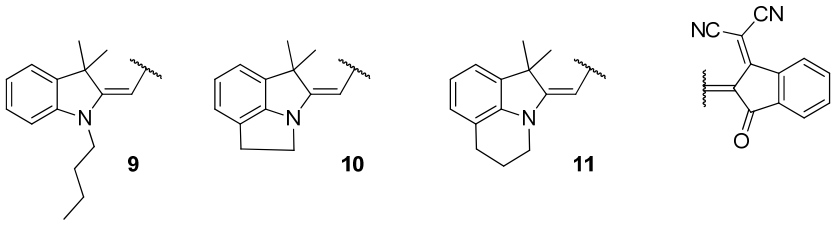

Chart 4. Chemical structures of dyes **9** - **11**.

Chromophores featuring NIR absorption have as well been developed and tested in solution-processed BHJ solar cells (Chart 5). The indolenine-containing dye **12** presents a π-extended system with absorption at 736 nm. The pyrrolidine acceptor group provides suitable FMO energy levels for application in solar cells using $PC_{60}BM$ as acceptor material. Despite the low bandgap of these dyes, V_{OC} up to 0.74 V could be measured and the *PCE* reached 1.0 %.[30] Furthermore, the π-extension of the methylene bridge of merocyanine dyes seems a simple way for obtaining NIR absorbing chromophores. Thiophene-based dyes **13** - **16** were synthesized and their performances in solution-processed solar cells were evaluated with respect to their shorter methylene bridge derivatives. Chromophores **13** - **16** displayed absorption maxima in the range of 656 - 764 nm. Despite the favorable absorption properties, these dyes showed lower J_{SC} than their shorter counterparts, which was attributed to a less advantageous packing in the solid state. Nevertheless, devices based on **16**, which featured the highest efficiency, could be optimized by replacing the PEDOT:PSS hole collecting layer by MoO_3 and using $PC_{70}BM$ as acceptor material to afford reasonably good V_{OC} (0.74 V), J_{SC} (6.65 mA cm^{-2}) and *FF* (47 %) values, thus reaching a *PCE* of 2.3 %.[31]

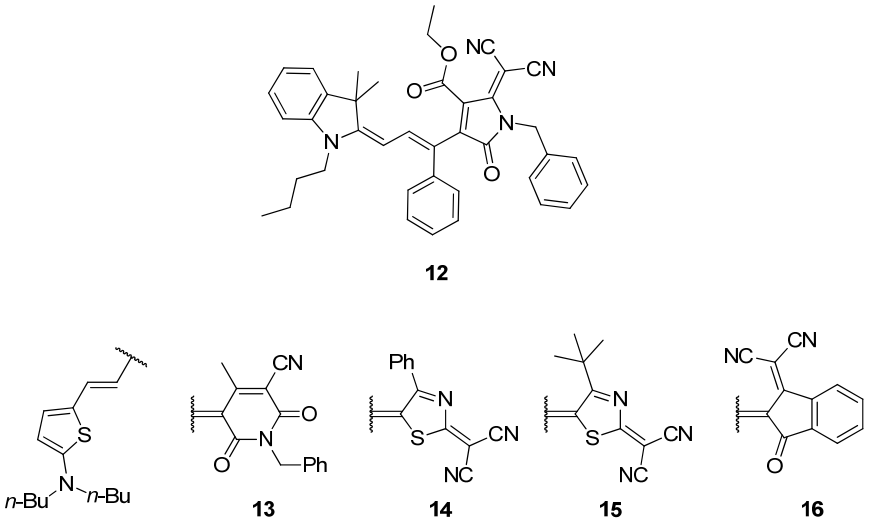

Chart 5. Chemical structures of dyes **12** - **16**.

For two reasons there is a particular interest in merocyanine based organic semiconductor research with regard to the impact of molecular packing on the functional properties such as absorption (λ_{max}, ε_{max}), hole carrier mobility (μ_h) and photovoltaic performance (*PCE*). One reason is given by the fact that dipolar disorder is known to slow down charge carrier transport in amorphous materials as given in BHJ blends. Accordingly, the question prevails if these D-π-A molecules indeed pack in a perfect and complete antiparallel arrangement or what distribution of mutual packing arrangement is given in BHJ materials composed of D-π-A dyes. The second reason is that the high transition dipole moments μ^2_{eg} of merocyanine dyes should give raise to pronounced excitonic coupling in closely π-stacked arrangements according to Kasha theory.[32] To address these issues Zitzler-Kunkel *et al*. have explored the effect of intramolecular folding-driven aggregation of bis-merocyanine dyes on the absorption properties and solar cell performance. Bis-merocyanine **17** underwent folding upon decreasing solvent polarity, thus forming a sandwich dimer of two stacked dyes with a hypsochromically displaced absorption maximum. Further addition of an unpolar solvent favored formation of supramolecular polymers which could be supported by UV-Vis spectroscopy through detection of an H-band at ~400 nm (Figure 8). The impact of supramolecular polymerization on solar cell performance was subsequently evaluated by processing the BHJ under aggregation-favoring conditions. As a consequence, a nearly two-fold increase in photocurrent generation was observed, due to the harvesting of high-energy photons in the 400 - 500 nm region.[33] Obviously the choice of the chromophore and sandwich-type packing motif which led to reduced absorption strength and a hypsochromic shift away from the highest

solar flux, were clearly not favorable towards high performance solar cells. However, this work illustrates nicely the impact of dye-dye contacts on relevant parameters for solar light harvesting, photocurrent generation and solar cell performance.

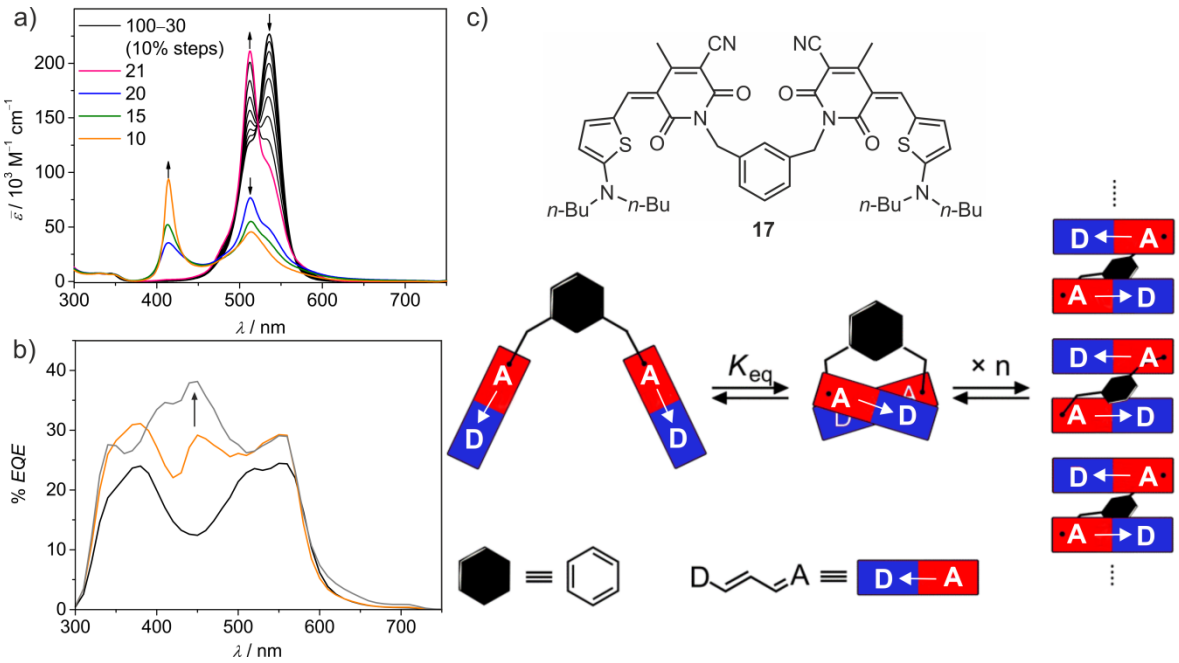

Figure 8. (a) Solvent dependent UV-Vis spectra of dye **17** in THF/MCH mixtures starting in pure THF (black). (b) *EQE* spectra of **17**:PCBM (30:70) blends depending on the casting solvent mixture $CHCl_3$ (black), $CHCl_3$/toluene (orange) and $CHCl_3$/*o*-xylene (grey). c) Chemical structure of dye **17** and schematic representation of the supramolecular aggregation pathway for dipolar merocyanine dyes composed of π-conjugated electron donor (D)–electron acceptor (A) subunits into cofacially stacked H-aggregates. This Figure has been modified with permission of ref.[33]

2.2.1.2 Vacuum-deposited BHJ Solar Cells

While solution-processing by spin-coating is a cheap and well established procedure widely used for polymer solar cells, small molecules enable the use of vacuum-deposition, which offers the advantages of a more controlled growth of high quality thin films from highly purified materials with reproducible layer thickness, while additionally allowing for complex multilayer architectures. Direct comparisons of both methods for the same molecules are not frequent. Therefore, in order to clearly evaluate the possibilities offered by vacuum-techniques in comparison with solution-processing, solar cells were built by Kronenberg *et al*. for a series of merocyanine dyes, which were chosen to display enough solubility as well as thermal stability. The fabricated devices had the common structure ITO/PEDOT:PSS/merocyanine:acceptor/BPhen/Ag.[34] As acceptor material $PC_{60}BM$ or C_{60} were used for solution and vacuum-processing, respectively. Most of the devices featured higher J_{SC} and *FF* for vacuum-deposited blends, thus showing higher overall

performance. Since hole mobility and absorption did not change between solution- and vacuum-processed devices, the better performance of the latter may be explained through much more efficient charge-carrier generation or reduced recombination of the charges, which is reflected in the higher *EQE* of vacuum-processed cells. Furthermore, for dye **11** (Chart 4) a much smaller scale phase separation of the active layer was found in vacuum-deposited devices, which would imply that a greater interface for exciton dissociation is present. The high *PCE* obtained for vacuum-processed devices based on **11** could be improved in a next step by replacement of PEDOT:PSS by MoO_3. Further optimization of the active layer thickness and composition enhanced J_{SC}, which was highest at 55 % C_{60} content. For the best device a *PCE* of 6.1 % could be measured.[4b]

2.2.1.3 Vacuum-deposited Tandem Devices and Ternary Blends

The main idea of a tandem solar cell is to combine different semiconductors with complementary absorption bands so that light harvesting is maximized. In Figure 9 a typical structure for tandem solar cells is shown. In order to avoid thermalization losses, the material with larger optical bandgap should be placed in the first subcell. As a consequence, only light of longer wavelength will reach the second subcell where the material with narrower bandgap is placed. Between both subcells a recombination layer should ensure that charge carriers meet at the same energy level, so that recombination can take place without energy losses. The generated photocurrent of a tandem solar cell is limited by the smallest photocurrent of the subcells, while the V_{OC} of the tandem cell is the sum of the V_{OC} values of the two subcells.

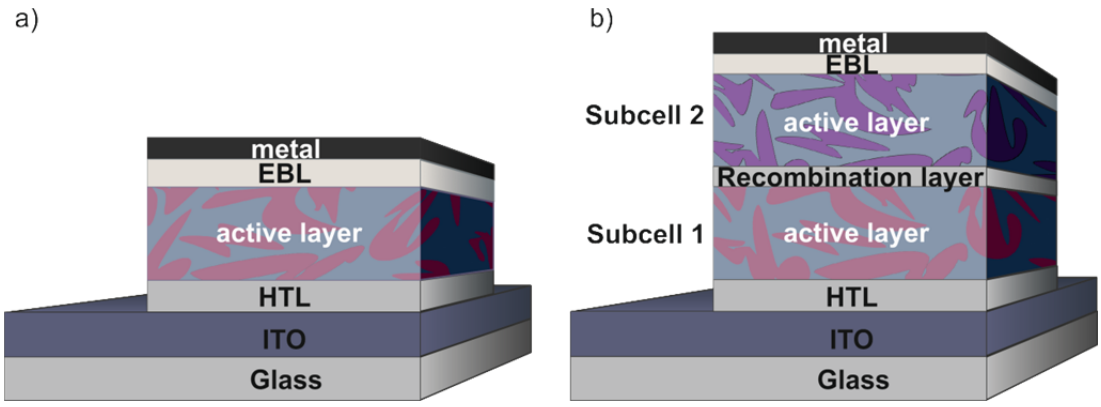

Figure 9. Schematic representation of a single BHJ solar cell (a) and a tandem solar cell structure composed of two subcells (b). In the first subcell the material with larger bandgap absorbs the high energy light. Subsequently the not absorbed long-wavelength light reaches the second subcell, where the narrow bandgap material is placed. Between both subcells a recombination contact ensures efficient recombination of the charge carriers. EBL = Electron blocking layer, HTL = Hole transporting layer.

Steinmann et al. published in 2013 a tandem solar cell bearing the well-established ZnPc chromophore **18** as long-wavelength absorber, combined with merocyanine **19**, which absorbs in the shorter 400 - 600 nm spectral region. Optimization of the single cells provided efficiencies of up to 2.6 and 3.1 % for **18** and **19**, respectively. Furthermore, the tandem solar cell was fabricated taking the parameters of the best single cells, and Al/MoO_3 as recombination contact. The V_{OC} of the tandem solar cell (1.60 V) almost equals the sum of the single cells V_{OC} (0.73 V and 0.93 V for **18** and **19**, respectively), showing a nearly loss-free contact between both subcells. Furthermore, the J_{SC} of 5.7 mA cm^{-2} measured for the tandem solar cell is in good agreement with the assumption that the single cell with lowest J_{SC} limits the overall short-circuit current density. In this case, the cell based on **18** is the limiting cell with a J_{SC} of 6.8 mA cm^{-2}. The *FF* of 50 % remains between the values of both subcells. Overall the tandem cell showed an improved performance of 4.5 %.[35] Tandem solar cells may as well be fabricated from two subcells bearing the same absorber material. This was performed with dye **9** in a BHJ/PHJ combined structure, where the active layer of each subcell was sandwiched between donor and acceptor-only layers.[36] The advantages of this cell structure have been discussed in literature.[37] Indeed, due to the extra donor and acceptor layers a direct contact of the active layer to the electrodes is avoided, thus improving the charge collection at the electrodes and featuring higher J_{SC}. A slight decrease in the *FF* was observed in comparison to pure BHJ devices. Overall a final *PCE* of 4.7 %, higher than the single cell performance (4.3 %), could be obtained thanks to a very high V_{OC} value of 2.1 V.

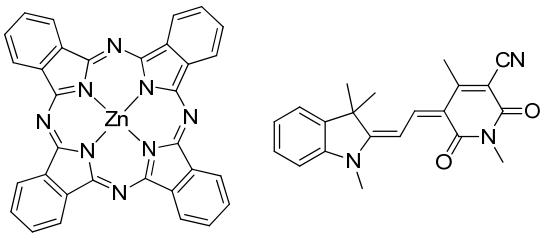

18 **19**

Chart 6. Chemical structures of dyes **18** and **19**.

An alternative to the tandem cell structure is the ternary concept, where the complementary absorbers are mixed together in the same layer. Dyes **20** and **21** were mixed in different ratios in combination with C_{60} as acceptor material in vacuum-deposited BHJ solar cells (Figure 10).[38] The dependence of V_{OC} on the dye ratio was found to be almost linear and increased while increasing the ratio of dye **20**, with the lowest HOMO level. This

observation, accompanied by the fact that the best performance was obtained for a 50 % mixture of the dyes suggested the presence of three different phases, a **20**-rich, a **21**-rich and a C_{60}-rich phase, thus providing parallel BHJ devices within the blend. The phase separation could be attributed to the very different values of the molecular dipole moments, which are 4.0 D and 13.0 D for **20** and **21**, respectively. Since the Coulomb attraction depends on the product of the molecular dipole moments, the formation of homoaggregates is preferred, at least for dye **21**, thus leading to separated phases in the bulk by means of a self-sorting process.[39]

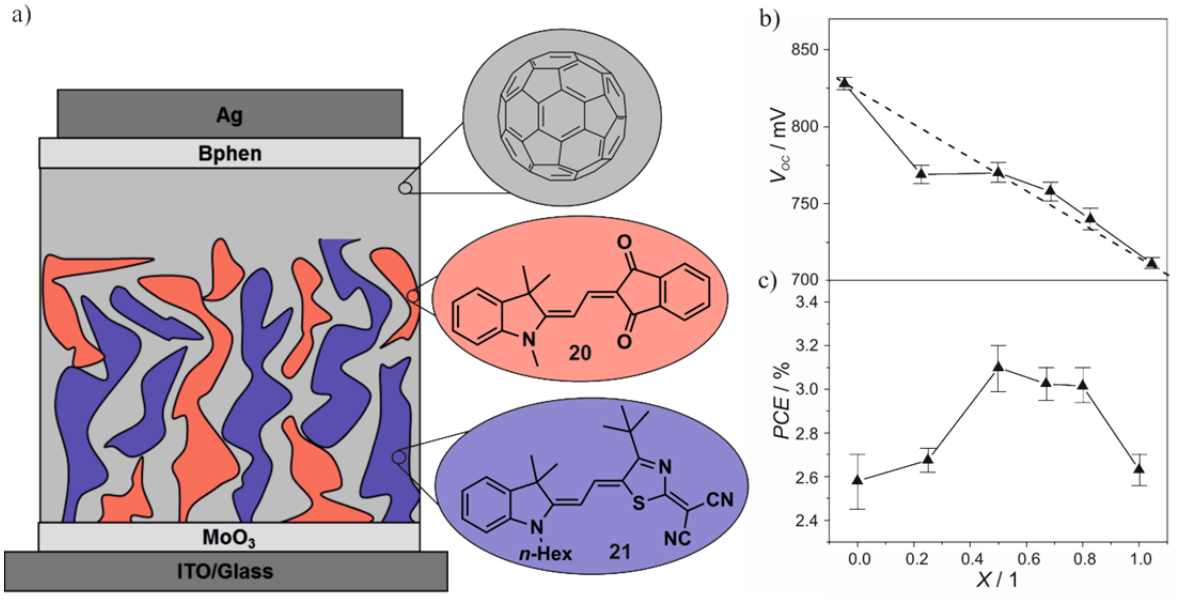

Figure 10. a) Schematic representation of the ternary blend containing phase separated domains of **20** and **21** as well as C_{60}. The molecular structures of **20** and **21** are depicted. Dependence of V_{OC} (b) and *PCE* (c) on dye **21** content in the ternary BHJ blend. *X* denotes the weight fraction of dye **21** with respect to dye **20**. The C_{60} content was 60 %wt. and the active-layer thickness 39 nm in all cases. The dashed line in (b) is a linear fit to the data. This Figure has been modified with permission of ref.[38]

2.2.1.3 Vacuum-deposited PHJ solar cells

Until now much effort has focused on the development of new semiconductor materials with improved absorption and conducting properties. Nevertheless, cell structure optimization is equally important. Studies about solar cell morphology have demonstrated that the dye orientation in the bulk plays an important role in solar cell efficiency. For example, the use of transition metal oxide buffer layers between the ITO electrode and the dye film modifies the crystallinity of the latter. Indeed, using V_2O_5-modified ITO substrates led to highly crystalline films of molecule **22**, which was not the case for other buffer layers such as WO_3 or MoO_3. Application of these buffer layers in PHJ solar cell

fabrication improved power conversion efficiencies due to an increase in V_{OC} from 0.69 V to 0.74 V while maintaining a very high *FF* of 68 %.[40]

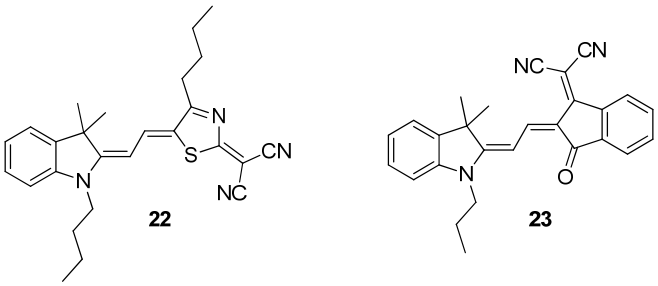

Chart 7. Chemical structures of dyes **22** and **23**.

Furthermore, deposition of the chromophores on a heated substrate or post-annealing of the latter above the glass transition temperature appears to be a suitable tool to change the orientation of the molecules, increase the crystallinity through centrosymmetric arrangement of the dye pairs and subsequently reduce the dipolar disorder. In the case of PHJ based on **23**, whose glass transition temperature is 77 °C, a two-fold increase of *FF* was observed after annealing the cell at 80 °C for 5 min.[41] This was attributed to a 45° tilting of the molecules upon annealing, while in as-cast films they tend to stand with their long axis perpendicular to the surface. Such arrangements have also been observed for highly crystalline merocyanine layers in OTFT studies, where the transition from amorphous to crystalline films improved the mobility by 4 - 5 orders of magnitude.[42]

2.2.2 Other D-π-A dyes

Several other groups have as well contributed to the development of organic solar cells based on D-π-A dyes. Triphenylamine (TPA) donor groups have been widely applied to linear and star-shaped systems in organic semiconductors. In particular, Roncali and coworkers investigated combinations with various acceptor groups leading to symmetrical D-A-D chromophores.[43] Unsymmetrical chromophores bearing triaryl groups have been studied as well by several groups in the last years. In 2008 a series of D-π-A compounds consisting of oligothiophene-based derivatives end-capped with triarylamine groups on one side and (di-, tri-) cyanovinyl electron-withdrawing units on the other side have been described.[44] The conjugation length of the central oligothiophene core was varied and its influence on solar cell performance was studied. For this purpose, PHJ solar cells were prepared by vacuum deposition of C_{60} on top of the donor material. It was found that increasing the conjugation length from two to four central thiophene units did as well

increase the absorption coefficient, while decreasing the optical bandgap. While the V_{OC} remained very similar for all molecules, devices based on **24c** displayed much higher *FF* of 48 %, thus reaching the maximal *PCE* of this series with 2.67 % after thermal annealing. These authors also investigated the suitability of dendritic oligothiophenes bearing hole-transporting carbazole as peripheral substituents and an electron-withdrawing dicyanovinyl core group in solution-processed BHJ solar cells. Dendrimer **25** presents a broad absorption and high ionization potential, which decreases the optical band gap to 1.74 eV. Compound **25** was combined with $PC_{70}BM$ as acceptor material and delivered devices with moderate *PCE* of 1.64 % and high V_{OC} of 0.93 V after annealing.[45]

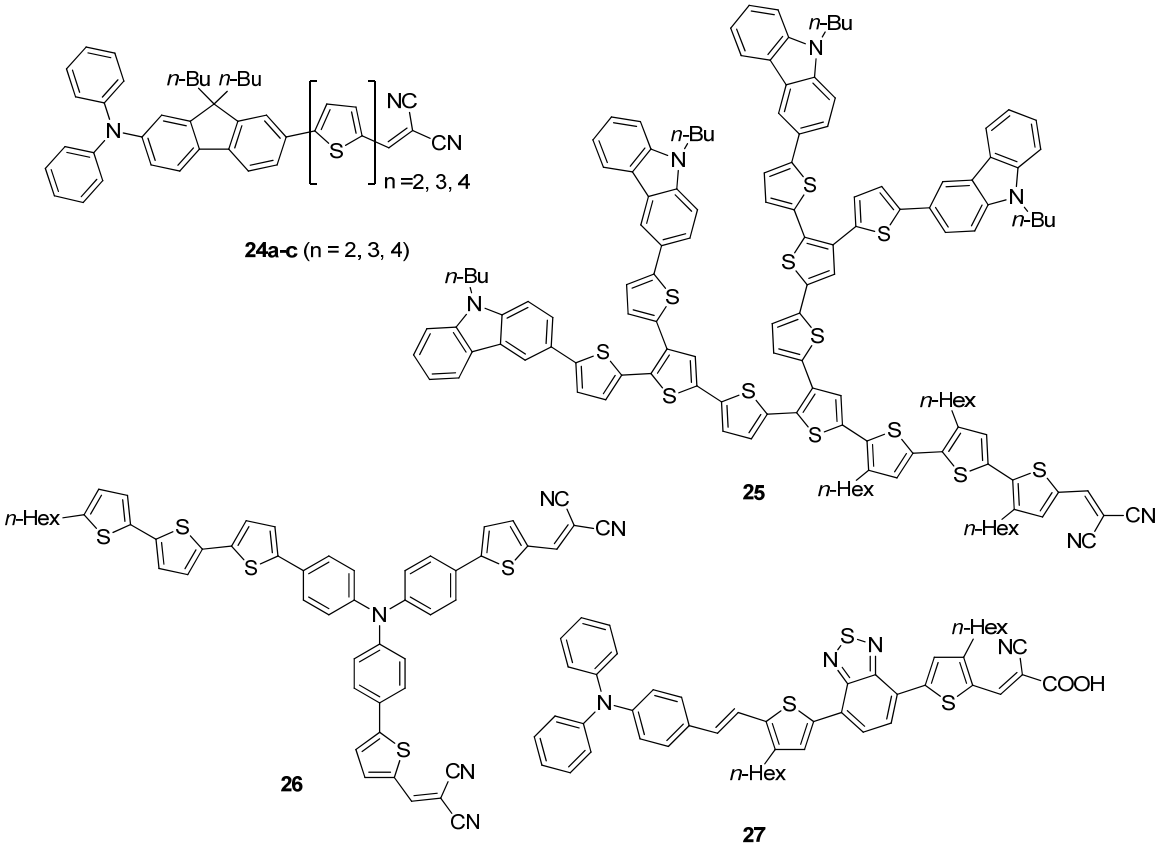

Chart 8. Chemical structures of dyes **24** - **27**.

After their early work on symmetric TPA dyes,[43] Roncali and coworkers published in 2011 a series of triphenylamine-based chromophores with different acceptor end-capped arms. Interestingly, the dye containing two dicyanovinyl groups showed an almost 100 nm red-shift and broader absorption compared to the one containing only one acceptor group, although the extinction coefficient was reduced from 104700 M^{-1} cm^{-1} to 57500 M^{-1} cm^{-1}. The best performance was obtained for compound **26** blended with $PC_{60}BM$, where a very high V_{OC} of 1.07 V and a *PCE* of 2.02 % were obtained.[46] Probably influenced by the

development of D-π-A dyes for dye-sensitized solar cells,[47] a large variety of push-pull molecules has been recently investigated in BHJ solar cells. An example is dye **27**, which was tested by Liu *et al*. in solution-processed solar cells and showed a still low but promising *PCE* of 1.23 % blended with $PC_{60}BM$. Interestingly, this *PCE* was identical in PHJ and BHJ devices.[48]

Later on, a series of D-π-A molecules bearing electron-rich bis-fluorenylaniline combined with different bridging units such as thiophene or indenothiophene[49] and end-capped with several acceptor moieties was reported by Lee *et al*. The dicyanovinyl-containing chromophore **28** demonstrated to have the greatest intramolecular charge transfer, which translated in a red-shifted absorption as well as the highest extinction coefficient ($\varepsilon = 40200\ M^{-1}\ cm^{-1}$) of this series. As a consequence, a much higher J_{SC} was found for **28** than for its homologues, reaching an efficiency of 3.66 % in solution-processed BHJ solar cells blended with $PC_{70}BM$ upon addition of 1-chloronaphthalene.[50] Continuing with the same donor moiety, a more rigid benzothiophene bridging unit was chosen (**29**), which slightly increased the light harvesting and improved *PCE* up to 4.01 % in the blend with $PC_{70}BM$ using a TiO_x functional layer as optical spacer.[51] Further studies about the effect of bridging units have demonstrated that the introduction of a naphthalene diimide moiety between the donor and acceptor subunits provides a red-shift of the absorption up to 630 nm and a two-fold improvement of the *PCE* (up to 3.0 %) with respect to the reference compound.[52]

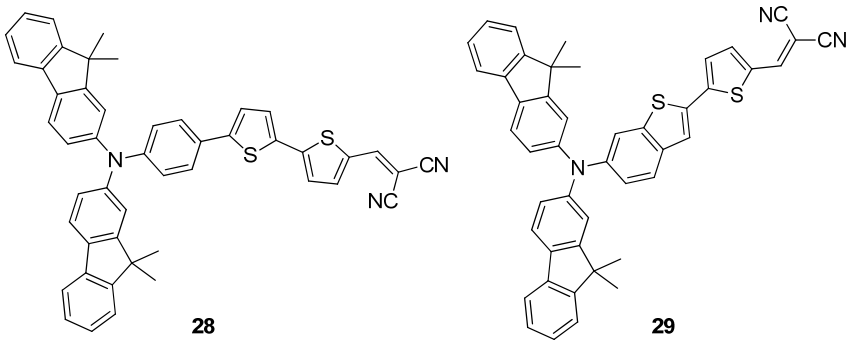

Chart 9. Chemical structures of dyes **28** and **29**.

The group of K.-T. Wong entered the field of BHJ solar cells in 2011 and reported the so far highest *PCE* values for D-π-A dye based organic solar cells. After working on A-D-A systems for bilayer and planar mixed heterojunction solar cells, they published a series of very similar structures based on a triarylamine electron donating group and acceptor

moieties such as benzothiadiazole[53] and pyrimidine,[37] or a simple dicyanovinylene group.[54] All compounds could be vacuum deposited and were tested in planar mixed heterojunction (PMHJ) solar cells using C_{70} as acceptor material. Among the reported compounds, the pyrimidine-containing dye **30**[37] obtained an impressive *PCE* of 6.4 %, showing a very high *EQE* of almost 80 % at 400 nm and over 50 % from 300 to 700 nm, together with the highest J_{SC} of 16.35 mA cm^{-2} among this series. Furthermore, *PCE*s up to 6.8 % have been reported for dye **31**.[55] Although the higher J_{SC} was observed for devices based on a homologue compound containing a thiophene bridging unit,[53] **31** allows for a better balance between J_{SC} and V_{OC}, leading to the best *FF* of this series, 54 %. Furthermore, the same compound demonstrated its suitability for application in simple BHJ solar cells. Thus, after layer thickness optimization *PCE*s of about 8 % were reported, which is among the best efficiencies reported up-to-date for vacuum-processed devices based on dipolar molecules.[56] Recently, compound **31** was combined with C_{70} in solution-processed BHJ. Although the *FF* was lower than for vacuum-deposited devices, V_{OC} and J_{SC} remained nearly the same, providing devices with *PCE* up to 5.9 % after solvent vapor annealing (SVA).[57]

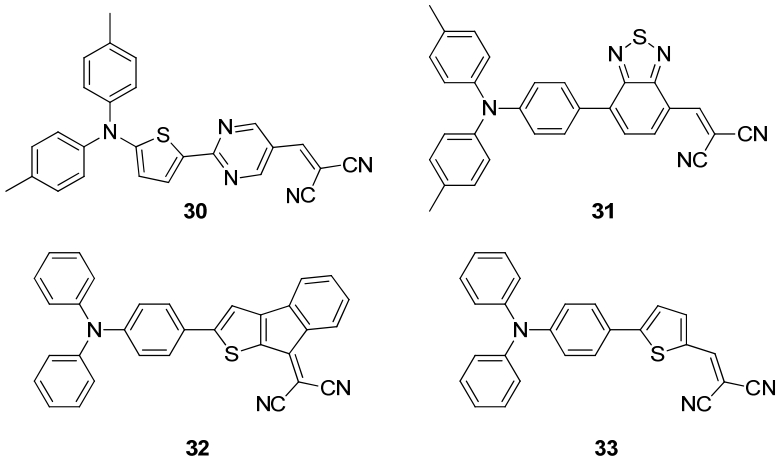

Chart 10. Chemical structures of dyes **30** - **33**.

Reducing molecular size to the basic donor and acceptor units is a trend which has gained increasing interest in the last years.[58] Playing with rigidity has shown that covalent cyclization of the acceptor unit represents an efficient way of modifying the intramolecular charge transfer, thus shifting the overall broader absorption bathochromically and improving *FF*. Efficiencies up to 2.97 % were obtained for compound **32** in thermally annealed planar heterojunction devices with C_{60} as acceptor material.[59] The non-bridged derivative **33** showed as well promising results and was therefore optimized for

vacuum-deposited PMHJ solar cells, where a 4,4'-bis[*N*-(1-naphtyl)-*N*-phenylamino]biphenyl (α-NPB) buffer layer was added in order to prevent the *J*-*V* S-shape. Finally, the active layer was tuned to show a composition gradient that favored exciton dissociation and charge transport, yielding an overall efficiency of 4 %.[60]

Furthermore, some chromophores originally developed for DSSC have been as well tested in OPV by Wang *et al*. Three indoline-based carboxy dyes were firstly employed as donor materials in solution-processed PHJ. For the best performing dye an esterification was performed in order to render the molecule thermally stable, thus enabling its application in vacuum-deposited BHJ. The optimized cell based on **34** showed *PCE*s up to 5.1 %.[61] Montcada *et al*. have as well recently published a series of dipolar molecules bearing an indoline donor unit and dicyanovinyl acceptor linked by different bridging groups such as thiophene, bithiophene, cyclopentadithiophene or benzothiadiazole moieties. BHJ solar cells were built by spin-coating of the molecules with $PC_{70}BM$ as acceptor material and solvent annealing was performed before deposition of the cathode. Devices based on dye **35** showed the slowest recombination dynamics, thus providing high V_{OC} of 0.91 V and the best performance among this series, with *PCE* of 3.36 %.[62]

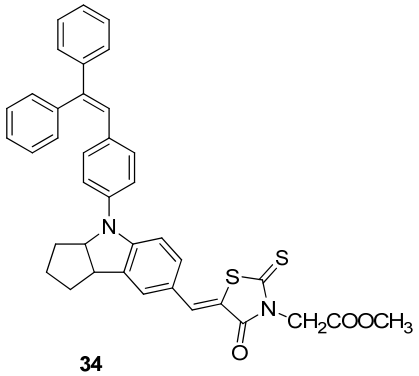

34

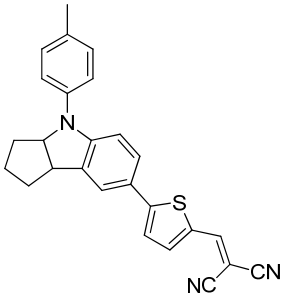

35

Chart 11. Chemical structures of dyes **34** and **35**.

Recently Cheng *et al*. compared the suitability of compound **36** as donor material with its symmetrical homologue. Although a better performance was shown by the corresponding A-D-A system due to the better light absorption and higher *FF*, dye **36** still had a *PCE* of 3.6 % in solution processed BHJ solar cells using $PC_{70}BM$ as acceptor material.[63] Interestingly, a study reported by Gao *et al*. about two dipolar molecules showed that increasing the dipolarity by addition of an extra acceptor unit to form a D-A-A' system improved crystallinity and hole mobility of the blend with $PC_{70}BM$ while decreasing the molecular band gap. Overall the D-A-A' system **37** featured more than the double

efficiency than the simple D-π-A system, which displayed a *PCE* of 5.9 %.[64] The success of the D-A-A' structures has been repeatedly emphasized by Wong and coworkers. Recently, six molecules bearing a coplanar dithienopyrrol donor moiety combined with several acceptor subunits have been studied in vacuum-deposited planar mixed heterojunctions. Chromophore **38** containing a pyrimidine-dicyanovinylene acceptor showed the best performance, with a *PCE* of 5.6 % and a high *FF* of 52 %.[65]

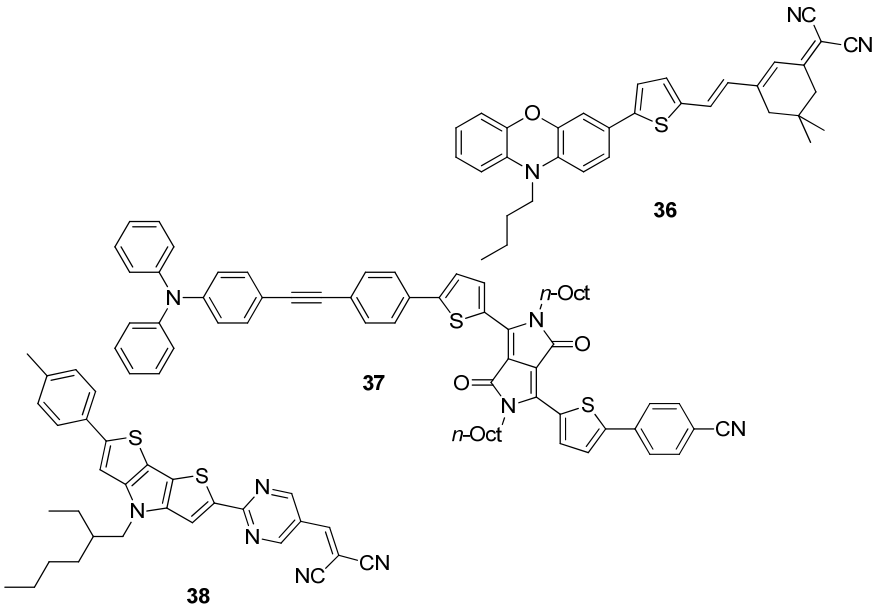

Chart 12. Chemical structures of dyes **36** - **38**.

Another interesting series of D-π-A dyes originates from the squaraine dye family. Squaraine dyes usually consist of two identical donor units attached to a central strong acceptor squaric acid unit, thus producing D-A-D architectures. Only few examples of unsymmetrical and accordingly dipolar squaraines have been reported until now, making the evaluation of their potential for OPV still difficult. Some examples of this kind of chromophores have been published by Yang *et al*. Two different squaraine dyes were synthesized and their performance in solution-processed solar cells with $PC_{70}BM$ was compared. Replacing the diisobutylamino group by a 9-carbazyl end-capper resulted in a much broader absorption band for dye **39a** and a HOMO level shifted to lower energies, thus improving the V_{OC} up to 1.12 eV and reaching a *PCE* of 2.34 %.[66] Following the same scheme, further end groups were tested while maintaining one donor part of the squaraine dye unchanged. Comparison of tetrahydroquinoline and indoline end-cappers revealed very similar absorption spectra and energy levels. All dyes studied showed performances about 3.4 - 3.8 % and similar cell parameters, which could be improved for

dye **39b** upon annealing to 4.3 %.[67] Recently, the diisobutylamino group has been replaced by a series of aminoaryl derivatives. As a consequence, the hole mobility of the corresponding devices decreased, while all other solar cell parameters increased giving much better performances than the original dye **39a**. The aryl groups attached to the squaraine contribute to the conjugated system, resulting in a broader absorption. Also the energy levels of aryl-containing dyes are shifted to lower energies. While all aryl-containing dyes showed improved SC performance, dye **39c** gave the better results with a *PCE* of 3.7 %.[68] Finally, some examples of squaraines where the donor units are directly attached to the central squaric acceptor group have been published recently by Chen *et al*. The use of pyrrole derivatives as donor units provide broad absorption bands and good hole mobilities. Therefore, three derivatives bearing pyrrole-based donor units combined with indoline derivatives were synthesized and tested in solution-processed BHJ. Derivative **40** featured good solubility as well as the lowest bandgap, yielding the best solar cells of this series with a very high J_{SC} of 12.03 mA cm^{-2} and *PCE* of 4.35 %.[69]

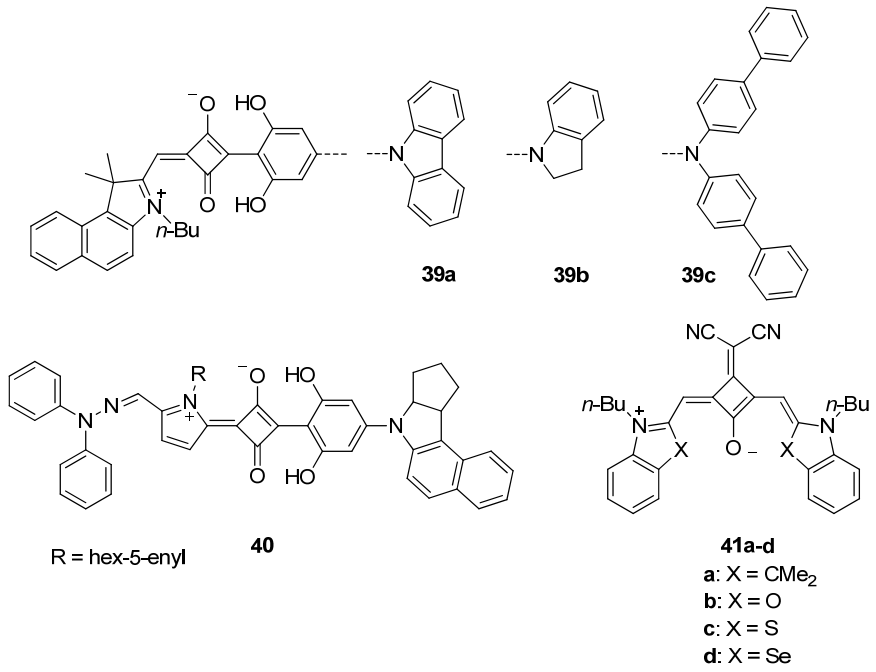

Chart 13. Chemical structures of dyes **39** - **41**.

Mayerhöffer *et al*. investigated squaraine chromophores as near infrared absorbing donor materials for solution-processed BHJ solar cells. The synthesized dyes featured identical donor moieties and a central squaric acid ring bearing a dicyanovinyl substituent, which generated a cisoid arrangement of the two donor units and concomitantly a dipole moment in the molecule. In comparison with symmetrical squaraine dyes, these dipolar ones

displayed red-shifted absorption bands at about 700 nm in solution, as well as low-lying FMO levels. Solar cells fabricated with **41c**:$PC_{60}BM$ (60:40) featured high J_{SC} of 12.6 mA cm^{-2} but a *PCE* of only 1.79 % after thermal annealing. The outstanding J_{SC} value was in part attributed to the high squaraine content in the solar cell, which increased the number or absorbed photons per volume unit. Furthermore, the tight packing of the molecules in the crystal revealed strong intermolecular interactions, which translate into a red-shift and broadening of the optical absorption in the solid state.[70] It is noteworthy that for the selenium derivative **41d** highly ordered thin films could be obtained that displayed charge carrier mobilities > 1 cm^2 V^{-1} s^{-1} in organic thin film transistors.[71]

In this section the fast development in the field of organic solar cells based on push-pull systems has been illustrated. Particularly, merocyanine dyes have demonstrated to be useful donor materials for photovoltaic applications. Thanks to their straight-forward synthesis, several electron-rich and electron-poor moieties can be combined to obtain a large library of compounds with tunable optical and electrochemical properties. The success of a given molecule in organic photovoltaics however is influenced by several factors, not only molecular properties. Therefore optimization of the cell structure and interface architecture are necessary to explore the full potential of these kind of chromophores.

2.3 Exciton Theory in Molecular Spectroscopy

Since the discovery of molecular aggregates by Jelley and Scheibe in the 1930s,[72] much effort has been invested in the investigation of their structures using several techniques such as cryo-TEM,[73] X-ray or electron diffraction. These are suitable methods to characterize the self-assembled structure of aggregates in the solid state,[74] which however might vary from the dynamic supramolecular arrangement in solution. In this regard, great achievements have been reported about the correlation of spectral changes and particular molecular arrangements.[75] A useful tool to study the behavior of interacting molecules in solution is the exciton theory developed by Kasha and McRae.[32, 76] This model is based on a point-dipole approximation and was inspired by the band splitting in molecular crystals earlier observed by Davydov.[77] In the exciton theory model the molecules are described as classic oscillators and it is assumed that they do not lose their identity upon aggregation. As a consequence, the interaction of the molecules can be described in terms of the perturbation theory, where the interacting molecules are described as the sum of their individual properties plus a perturbation term. Thus, upon formation of a dimer between two molecules A and B, the Hamiltonian operator for the dimer $\hat{H}_{dimer}$ equals the sum of the respective monomer Hamiltonians ($\hat{H}_A$ and $\hat{H}_B$) plus an intermolecular perturbation potential $\hat{V}_{AB}$. The perturbation potential $\hat{V}_{AB}$ is a coulombic potential approximated by the point-dipole interaction.

$$\hat{H}_{dimer} = \hat{H}_A + \hat{H}_B + \hat{V}_{AB} \qquad (6)$$

The solution of the corresponding Schrödinger equation (assuming two identical molecules) affords the energy offset between the ground (E_g) and excited state (E_e), for the dimer:

$$\Delta E_{dimer} = E_e - E_g = \Delta E_{mon} + \Delta E_{vdW} + \varepsilon \qquad (7)$$

Where ΔE_{mon} is the energy offset between ground and excited state of the monomer molecule, while ΔE_{vdW} refers to the difference in van der Waals intermolecular interaction (stabilization energy) of the molecules in the ground and in the excited state. While the ground state of the dimer is only slightly displaced by van der Waals interaction compared to the monomer ground state, the excited state of the dimer splits in two energy levels, as

deduced from equation (7). The splitted excited state levels have an energy offset of 2ε, where ε is the exciton splitting term which can be quantitatively defined as:

$$\varepsilon = \frac{\left|\vec{\mu}_{eg}\right|^2}{4\pi\varepsilon_0 r_{AB}^3}(\cos\alpha - 3\cos^2\theta) \qquad (8)$$

μ_{eg} is the transition dipole moment for the singlet-singlet transition in the monomer, ε_0 the dielectric constant of vacuum and r_{AB} the center to center distance between molecules A and B. α and θ describe the relative rotation and slipping of the monomers and their transition dipole moments, respectively. As stated in equation (8), the exciton splitting energy depends on the square of the monomer transition dipole moments. Consequently, dyes showing higher light absorption will as well feature greater energy splitting upon aggregation. The square of the transition dipole moment is the quantum mechanical analogue to the classical oscillator strength *f* for a given transition. In the following some examples of relative transition dipole moment orientations are illustrated.

Assuming that there is no rotation of the molecules with respect to each other ($\alpha = 0°$), we can distinguish between two limiting cases: parallel transition dipole moments in a card-pack arrangement ($\theta = 90°$), also known as *H*-aggregates, and parallel in-line transition dipoles ($\theta = 0°$), or *J*-aggregates (Figure 11). The probability of a transition from the ground state S_0 to the first excited state S_1 is determined by the oscillator strength, which is proportional to the sum of the transition dipole moments. For $\alpha = 0°$ only energy levels where the transition dipoles are in-phase (oscillator strength $2f$ in Figure 11) can be reached from the ground state S_0. In Figure 11 the allowed transitions are depicted by arrows.

For parallel transition dipoles in a card-pack arrangement ($\theta = 90°$, Figure 11, left), the out-of-phase arrangement of the transition dipoles corresponds to a lowering of energy, while the in-phase arrangement corresponds to a higher energy level. Thus, the transition to the upper energy levels translates in a hypsochromically shifted absorption band with respect to the monomer molecule.

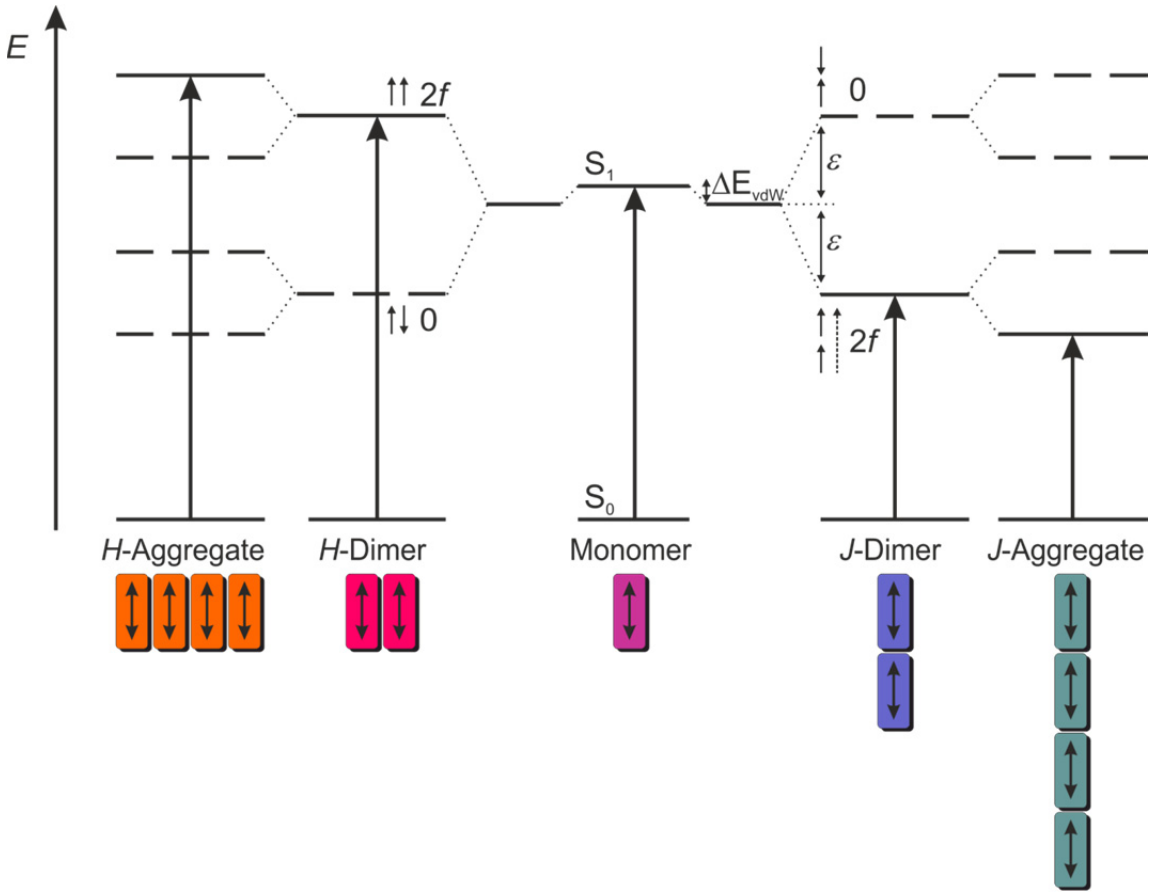

Figure 11. Schematic exciton band energy diagram for monomers, dimers and longer aggregates of molecules adopting a parallel (left, *H*-Aggregate) or in-line (right, *J*-Aggregate) arrangement of the transition dipole moments. The allowed optical transitions are signalized with arrows. Adapted from ref. [32]

On the other hand, for in-line transition dipoles ($\theta = 0°$, Figure 11, right) the in-phase arrangement of the transition dipoles leads to attraction and therefore to a lowering of energy, while the out-of-phase arrangement, due to repulsive forces, leads to a higher energy level. Thus, the allowed transition in this case is to the lower energy level, where the oscillator strength is $2f$. As a consequence, a bathochromic shift of absorption will be observed for *J*-aggregates. As indicated in Figure 11 for small aggregates, a number N of interacting molecules will lead to a splitting of the exciton energy into N levels. For the simple cases of *H*- and *J*-aggregates only one transition is allowed, thus implying a larger spectral shift while increasing N. This spectral shift is accompanied by a sharpening of absorption bands. Figure 11 illustrates only the limiting cases where θ is 0° or 90°. The simplified equation (9), valid for parallel transition dipoles ($\alpha = 0°$) describes the dependence of the exciton splitting term on the longitudinal slipping angle θ.

$$\varepsilon = \frac{\left|\vec{\mu}_{eg}\right|^2}{4\pi\varepsilon_0 r_{AB}^3}(1-3\cos^2\theta) \qquad (9)$$

Thus, the evolution of the energy levels and the corresponding allowed transitions with the molecular slipping angle is illustrated in Figure 12. From eq (9) it can be derived that for $\theta = 54.7°$ ($3\cos^2\theta = 1$) despite the interaction of the chromophores the exciton splitting energy is zero. For smaller angles ($0° \leq \theta < 54.7°$) a bathochromic shift of the aggregate absorption is expected (*J*-aggregates), while larger angles ($54.7° < \theta \leq 90°$) will lead to a hypsochromic shift (*H*-aggregates) of the aggregate absorption with respect to the monomer band.[32]

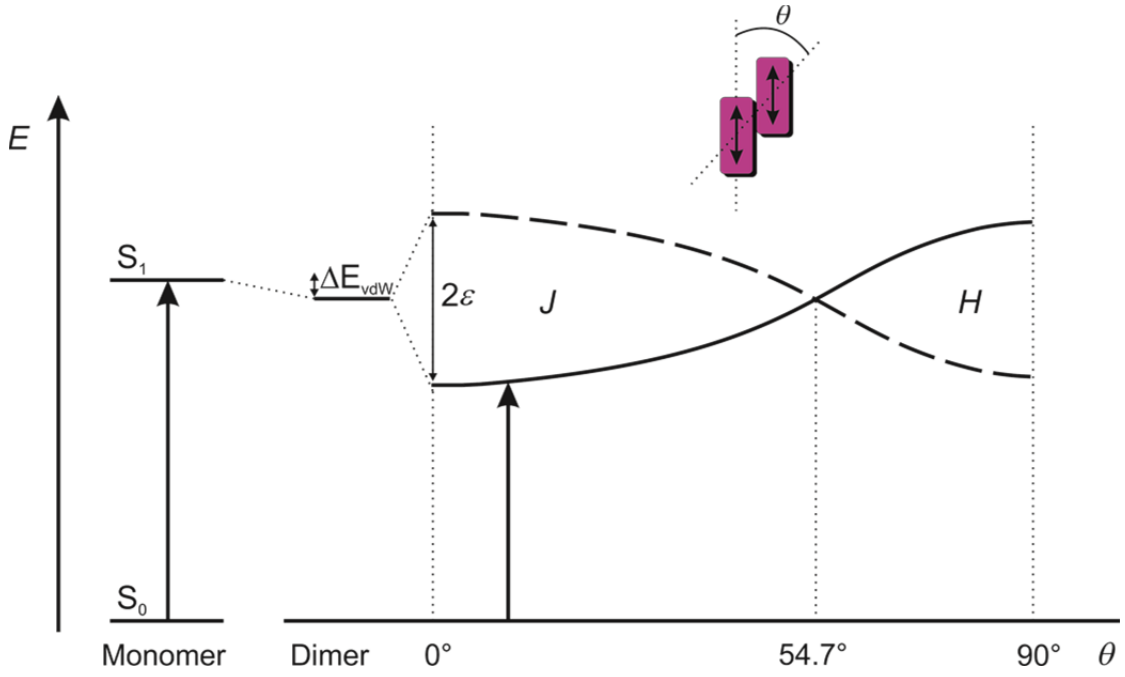

Figure 12. Schematic exciton band energy diagram for a molecular dimer with coplanar transition dipoles and longitudinal slipping of the transition dipoles at an angle θ with respect to the center-to-center line. The allowed transitions are signalized with arrows. For an angle of $\theta = 54.7°$ no splitting of the energy levels occurs. Adapted from ref. [32]

A geometrical variation of the *H*-dimer is illustrated in Figure 13, where the transition dipoles are rotated to an angle α with respect to each other. Since the transition dipoles are parallel ($\theta = 90°$), the simplified equation (10) can be used to describe the exciton splitting term as a function of the rotational displacement.

$$\varepsilon = \frac{\left|\vec{\mu}_{eg}\right|^2}{4\pi\varepsilon_0 r_{AB}^3}\cos\alpha \qquad (10)$$

Thus, for $\alpha = 0°$ we are in the case of an ideal *H*-aggregate, with allowed transitions only to the high energy excited state and consequently hypsochromically shifted absorption with respect to the monomer spectrum. Increasing the rotation angle progressively decreases the band splitting while the lower energy level becomes partially allowed due to the non-vanishing oscillator strength. As a consequence, for such aggregates both an intense hypsochromically shifted and a weak bathochromically shifted band can be observed. For a rotation angle of $\alpha = 90°$ no exciton splitting is provided.

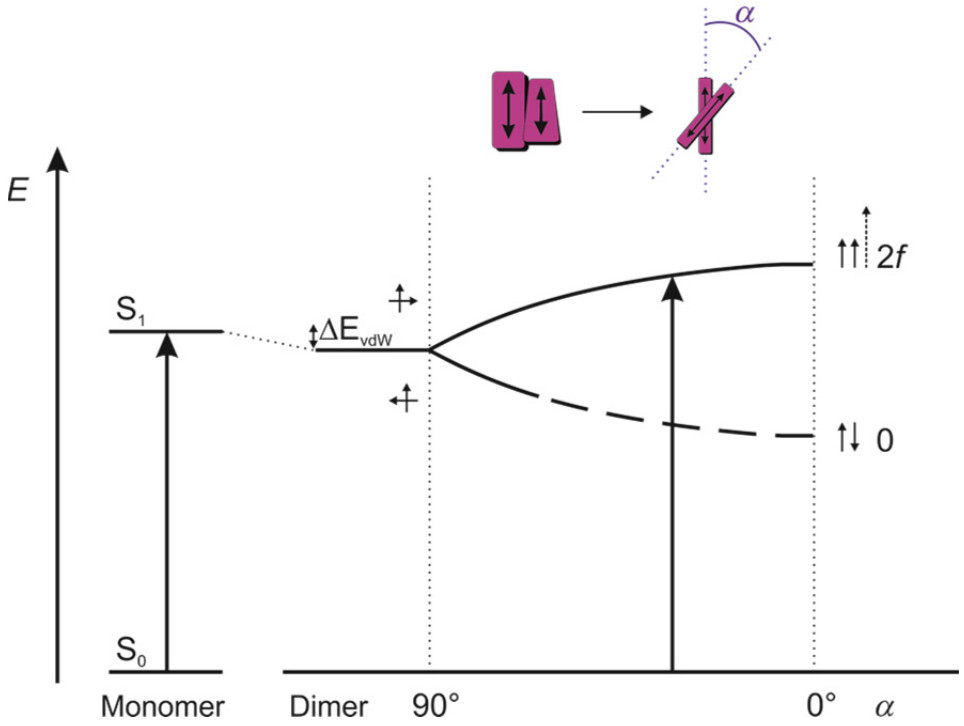

Figure 13. Schematic exciton band energy diagram for a molecular dimer with non-coplanar transition dipoles with an angle α between molecular planes. The allowed transitions are signalized with arrows. Note that for $\alpha = 0°$ an *H*-dimer is formed, while no interaction is provided for $\alpha = 90°$. Adapted from ref. [32]

In Figure 14 the energy diagram of a dimer with oblique transition dipoles, where both the slipping (θ) and rotational (α) angles are varied simultaneously, is illustrated. In this geometry the sum of the oscillator strengths for both in-phase and out-of-phase arrangement of the transition dipoles results in $f \neq 0$, thus allowing transitions to both excited energy levels (band splitting). The transition dipole moments to the exciton states for the corresponding in-phase and out-of-phase arrangements are described as a function of the slipping angle θ:

$$\vec{\mu}_{eg,in-phase} = (2\vec{\mu}_{eg}\cos\theta)^{1/2} \quad (11)$$

$$\vec{\mu}_{eg,out-of-phase} = (2\vec{\mu}_{eg}\sin\theta)^{1/2} \quad (12)$$

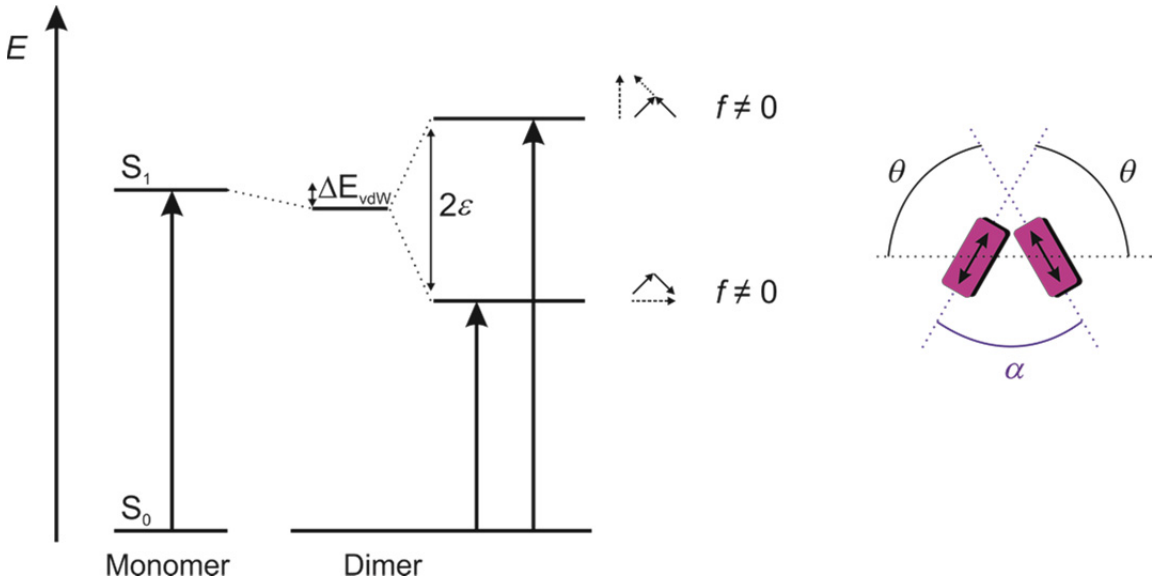

Figure 14. Schematic exciton band energy diagram for a molecular dimer with oblique transition dipoles. Transitions to both splitted energy levels are partially allowed. Adapted from ref. [32]

The interpretation of optical spectra of molecular aggregates or composite molecules with several interacting chromophores is a key step in the understanding of the relative orientation of the molecules. Thus, the exciton theory developed by Kasha is a useful and relatively simple model particularly suited for the study of dye molecules. Due to their strong absorption and high transition dipoles, interacting dye molecules display marked spectral changes with respect to the corresponding monomers. Furthermore, for molecules containing two conjugated chromophores the angle between those can be qualitatively estimated from the intensity ratio of the splitted absorption bands. Nevertheless, it has to be taken into account that these theories are based on point-dipole approximations and give therefore only approximate values of the molecular interaction.

Chapter 3

Results and Discussion

3.1 Synthesis

The merocyanine dyes described in this work are composed of electron-withdrawing (acceptor, A) and electron-donating (donor, D) groups linked by a conjugated polymethine chain. The synthesis of this kind of molecules usually follows a Knoevenagel condensation between an aldehyde and a C-H active acceptor compound in a water-withdrawing solvent such as acetic anhydride.

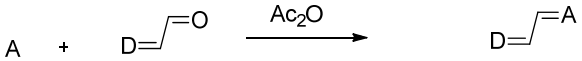

Scheme 1. General synthesis of merocyanine dyes under Knoevenagel condensation conditions.

The electron-donating and electron-withdrawing moieties used in this work are depicted in Chart 14. In the following sections the synthesis of these building blocks as well as the synthesis of the merocyanine chromophores is described.

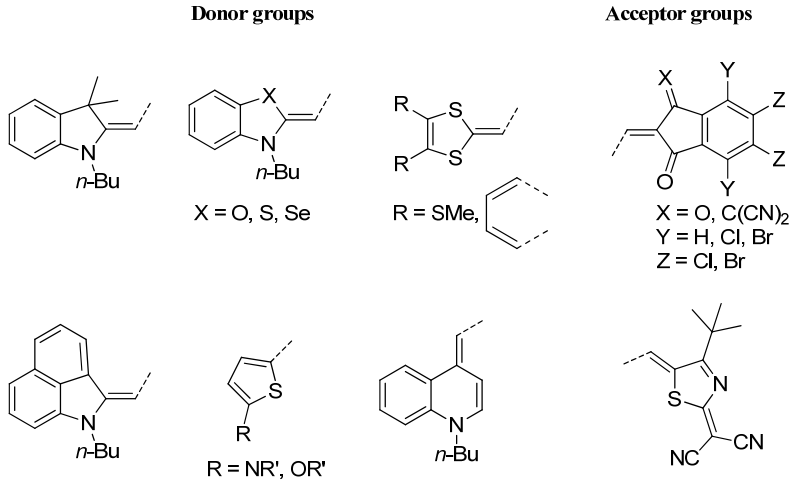

Chart 14. Chemical structure of donor and acceptor units used as building blocks for the synthesis of merocyanine dyes.

3.1.1 Synthesis of donor building blocks

The indolenine aldehyde derivative could be synthesized in three steps from the commercially available 2,3,3-trimethylindolenine (**42**). Following the literature known procedure, 2,3,3-trimethylindolenine (**42)** was alkylated with 1.1 equivalents of butyl iodide in acetonitrile.[78] The resulting salt **43** was isolated in good yields by precipitation with diethyl ether and was subsequently deprotonated with potassium hydroxide,[79] providing methylene base **44** after liquid-liquid extraction in almost quantitative yields. Finally a Vilsmeier formylation[80] was performed by slow addition of **44** to a cooled solution of $POCl_3$ in DMF, which formed an iminium salt. The latter was afterwards hydrolyzed to afford aldehyde **45** in 84 % yield.

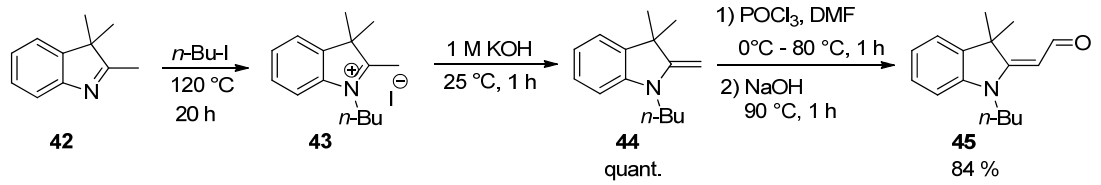

Scheme 2. Synthesis of (*E*)-2-(1-butyl-3,3-dimethylindolin-2-ylidene)acetaldehyde from 2,3,3-trimethylindolenine by Vilsmeier formylation reaction.

The rigid bridged indolenine homologue, compound **49**, was obtained in a multistep reaction involving a Fischer indole synthesis from 1-amino-3,4-dihydroquinoline **46**.[81] Compound **46** reacted with 3-methyl-butan-2-one in the presence of $NaNO_2$ and zinc in acetic acid to form the corresponding enamine, which underwent a [3,3'] sigmatropic rearrangement and cycle closure upon addition of ammoniac.

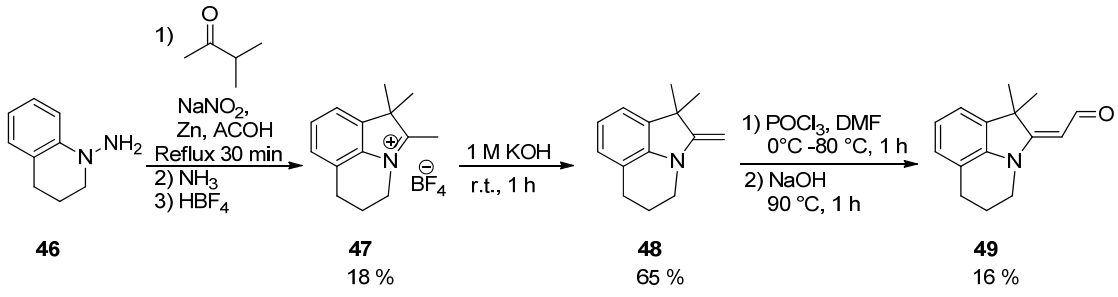

Scheme 3. Synthesis of the rigid bridged indolenine derivative **49**.

Further treatment with tetrafluoroboronic acid afforded salt **47** in 18 % yield. Furthermore, the obtained salt was deprotonated with potassium hydroxide and afterwards a Vilsmeier formylation[82] was performed to afford compound **49** in 16 % yield.

Moreover, commercially available benzoxazole **50**, benzothiazole **51** and benzoselenazole **52** were alkylated with 1.1 equivalents of alkyl iodide in acetonitrile solution.[78a, 83] Precipitation with diethyl ether afforded the corresponding salts **53** – **55** with moderate yields of 40 – 85 %.

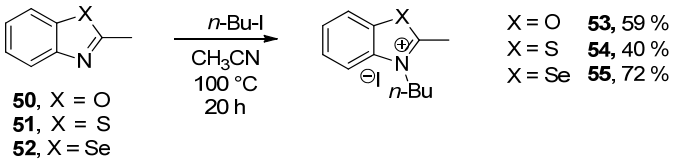

Scheme 4. Synthesis of compounds **53** – **55** from commercially available compounds.

The benzenedithiol-based building block could be synthesized following a literature known procedure from 1,2-benzenedithiol and 3,3-dichloropropenal (**57**).[84] 3,3-dichloropropenal was obtained by reaction of butyl vinyl-ether (**56**) with AIBN in CCl_4,[85] followed by acidic workup and slow distillation of the resulting residue. 1,2-Benzenedithiol (**58**) was then dissolved in THF and deprotonated with *n*-BuLi at low temperature. Subsequent addition of **57** afforded the crude compound **59** in ~50 % yield, which was used without further purification.

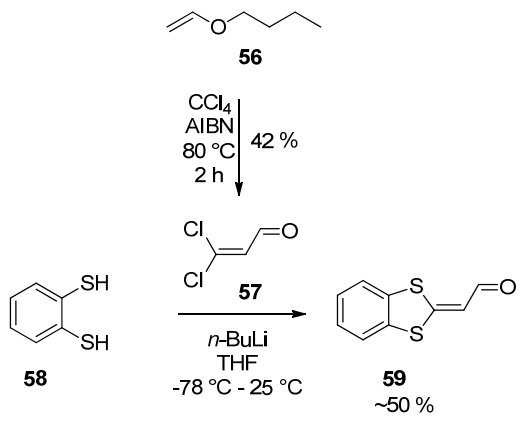

Scheme 5: Synthesis of the benzodithiol-based donor unit **59** from commercially available compounds.

Similarly 2-(4,5-bis(methylthio)-1,3-dithiol-2-ylidene)acetaldehyde **62** resulted from the reaction of the respective sodium salt **61** with 3,3-dichloropropenal (**57**). The sodium salt **61** was obtained in situ as described in literature by nucleophilic attack of sodium ethanolate to the commercial thione **60** and immediately further reacted.[86] The obtained product **62** was extracted from the reaction mixture and used without further purification.

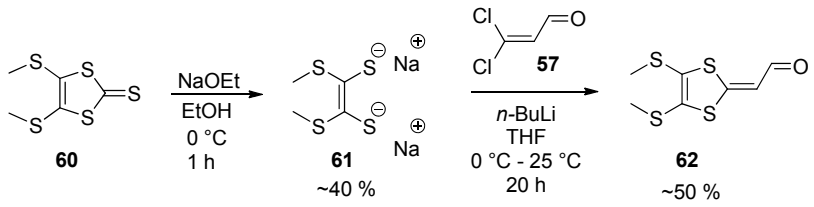

Scheme 6. Synthesis of **62** from commercially available thione **60**.

The synthesis of 5-dialkylaminothiophene-2-carbaldehyde derivatives from commercially available 5-bromothiophene-2-carboxaldehyde was performed in two similar pathways. Short alkyl chain derivatives such as methyl, ethyl and piperidine-containing molecules were obtained by reaction of 5-bromothiophene-2-carboxaldehyde **63** with the respective amines in aqueous solution, following a procedure developed by Prim *et al*.[87] Due to the low boiling point of these amines, the reactions were performed in pressure vessels.

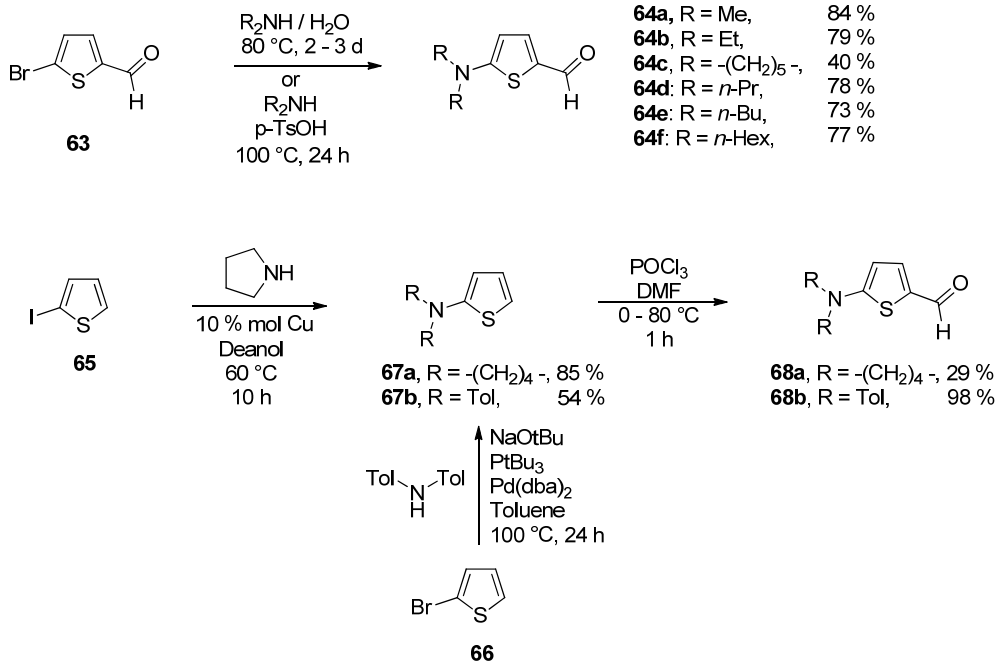

Scheme 7. Synthesis of 2-aminothiophene derivatives.

Amines bearing longer alkyl chains (higher boiling points) were successfully transformed to the corresponding products under no-solvent conditions using *p*-Toluensulfonic acid as catalyst using a modified procedure from Würthner *et al*.[88] The pyrrolidine derivative was however not formed in satisfactory yields using the pathways above described. 2-iodothiophene **65** was thus coupled with pyrrolidine under cupper catalysis to afford compound **67a** in 85 % yield.[89] Analogously, 2-bromothiophene **66** was coupled with ditolylamine to afford derivative **67b** in 54 % yield.[90] The obtained aminothiophenes

could subsequently undergo a Vilsmeier formylation[82] to aldehydes **68a,b** in 29 % and 98 % yields, respectively.

2-Methoxythiophene **69**, on the other hand, was deprotonated with *n*-BuLi in diethyl ether and subsequently reacted with DMF to afford 2-methoxythiophene-5-carboxaldehyde[91] **70** in almost quantitative yield. The crude product was used without further purification.

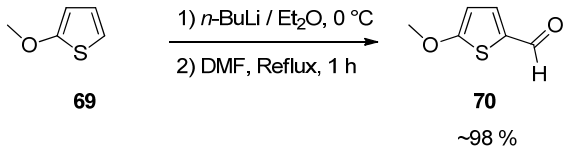

Scheme 8. Synthesis of methoxythiophene building block **70**.

Benz(c,d)indole-based dyes usually show highly red-shifted absorption around the near-infrared region. The synthesis of the corresponding building block starting from commercial naphtholactame **71** was performed following the procedure described by Deligeorgiev and Rozhinskii.[92] Alkylation of naphtholactame took place by nucleophilic substitution of the corresponding butyl halide in basic conditions. The alkylated compound **72** was afterwards successfully converted into a thiolactame by reaction with Lawson's reagent in almost quantitative yields. Furthermore, the nucleophilic substitution by isopropylidene malonate was possible thanks to the previous methylation of the thiolactame to provide a good leaving group.

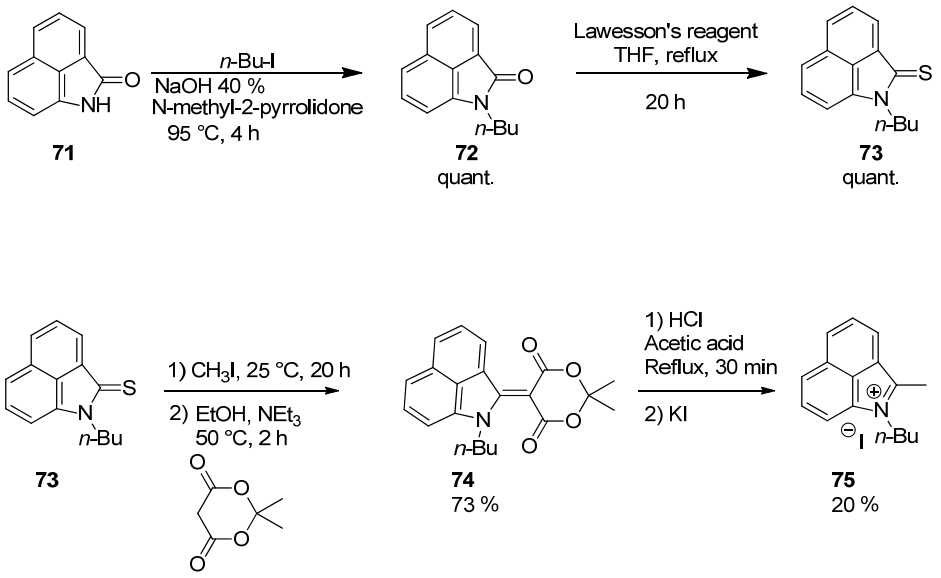

Scheme 9. Synthesis of naphtholactyl-based building block **75**.

Chromophore **74** was obtained after recrystallization in 73 % yield. Additionally, **74** underwent decarboxylation under acidic conditions and after addition of potassium iodide the corresponding iodide salt **75** could be isolated in 20 % yield.

Attempts to obtain the corresponding aldehyde **76** via Vilsmeier formylation were at first unsuccessful. Small quantities of dialdehydes were isolated and probably the cyanine resulting from two donor units reacting with each other was formed. Lately, a different approach was tested. The iodide salt was reacted with DMF in acetic anhydride to form the corresponding imine, which was afterwards hydrolyzed.[93] The aldehyde **76** was obtained in moderate yield of 64 % after recrystallization.

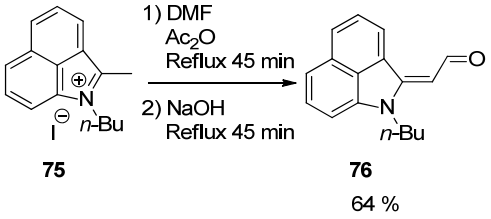

Scheme 10. Synthesis of aldehyde derivative **76**.

Quinoline derivative **78** was synthesized from the commercially available 4-methylquinoline by alkylation with butyl iodide in acetonitrile. Precipitation of the product with diethyl ether afforded compound **78** in quantitative yield.[94]

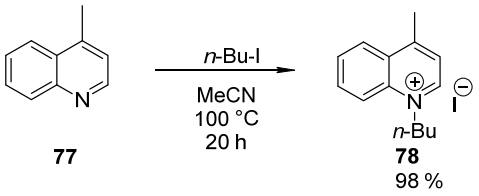

Scheme 11. Synthesis of quinoline derivative **78**.

3.1.2 Synthesis of acceptor building blocks

Commercial 1,3-indanedione **79** was used as received for the synthesis of the corresponding merocyanines. Furthermore, 1,3-indanedione could be converted to 2-(3-oxo-2,3-dihydro-1*H*-inden-1-ylidene)malononitrile **80** by nucleophilic attack of malononitrile in ethanol under basic conditions. Compound **80** was isolated after precipitation in 95 % yield.[95]

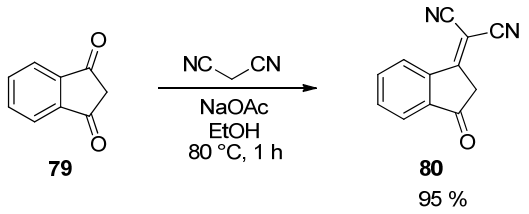

Scheme 12. Knoevenagel condensation of 1,3-indanedione with malononitrile in ethanol to provide compound **80**.

Tetrahalogenated indanediones were as well synthesized in order to lower the energy levels of the resulting chromophores. For this purpose, commercially available tetrahalogenated phthalic anhydrides **81a,b** were successfully reacted with *tert*-butyl acetoacetate and triethylamine in acetic anhydride[96] to afford after aqueous workup and recrystallization the corresponding tetrahalogenated indanediones **82a,b** in 85 % and 80 % yield, respectively.

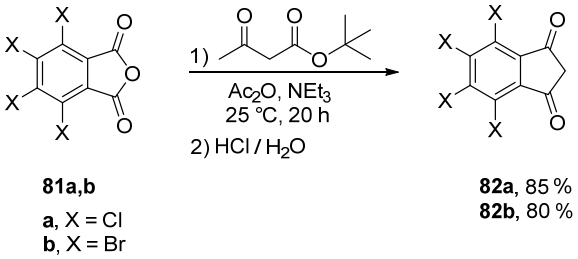

Scheme 13. Synthesis of tetrahalogenated 1,3-indanediones **82a,b**.

Analogously, 5,6-dichloroindene-1,3(2*H*)-dione **85** was obtained by conversion of the commercially available phthalic acid **83** to the corresponding anhydride **84**, followed by the reaction with *tert*-butyl acetoacetate and trimethylamine in acetic anhydride[96] to afford after aqueous workup and recrystallization compound **85** in 44 % yield.

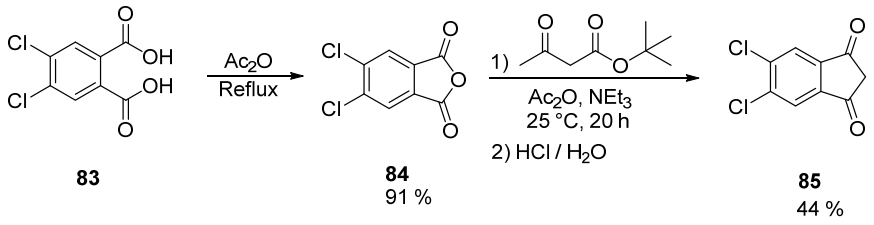

Scheme 14. Synthesis of dichlorinated 1,3-indanedione **85**.

The obtained halogenated 1,3-indanediones were subsequently reacted with malononitrile analogously to commercial 1,3-indanedione **79**. Unfortunately, for tetrahalogenated compounds **82a,b** no reaction took place, probably due to the bulkiness of the halogen

atoms in β-position to the ketone. On the contrary, dichlorinated compound **85** provided the desired product **86** in high yield of 80 %.

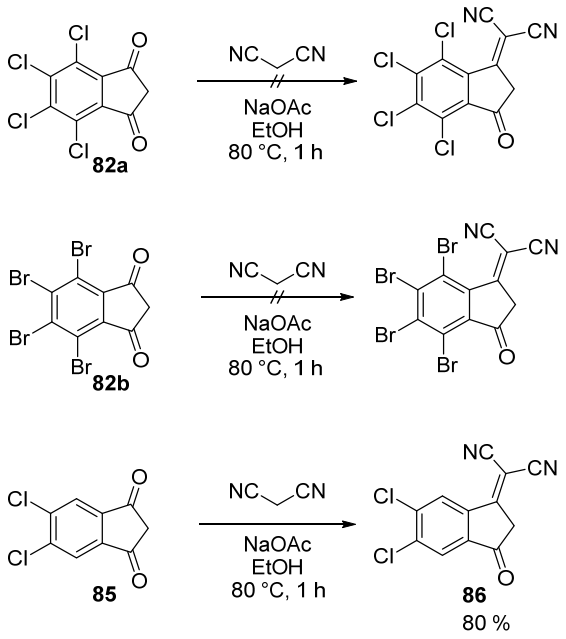

Scheme 15. Condensation of halogenated indanediones **82a,b** and **85** with malononitrile in ethanol.

Thiazole building blocks were obtained following the usual procedure[4a] from commercial α-chloroacetyl derivative **87** by nucleophilic substitution of the halogen atom by thiocyanate anion, followed by the condensation of malononitrile with the thiocyanate function in basic conditions and ulterior cyclisation. Compound **88** was thus obtained in a reasonable yield of 87 %.

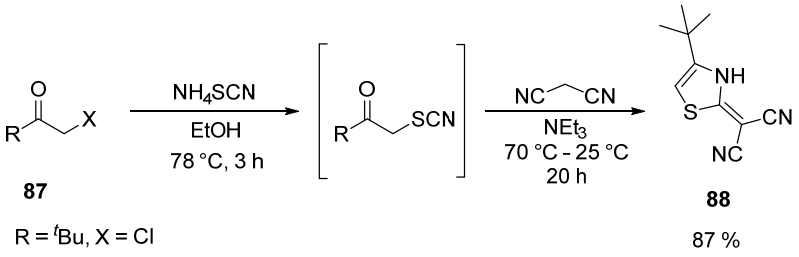

Scheme 16. General synthesis of thiazole acceptor unit **88**.

3.1.3 Synthesis of merocyanine dyes

3.1.3.1 Indanedione-acceptor derivatives

Several synthetic routes were followed for the synthesis of chromophores bearing an indanedione acceptor unit depending on the donor moiety. Those able to form an aldehyde derivative were condensed with the respective C-H active acceptor building block under Knoevenagel conditions. In this way the reaction of precursors **64a,b** and **70** with acceptor unit **80** afforded merocyanines **90a,b** and **91** in 57 - 84 % yields. Furthermore, commercially available thiophene-2-carboxaldehyde **89a** and 5-bromothiophene-2-caboxaldehyde **89b** provided the corresponding chromophores **92a,b** under the same reaction conditions in moderate yields of ca. 30 % (Scheme 17).

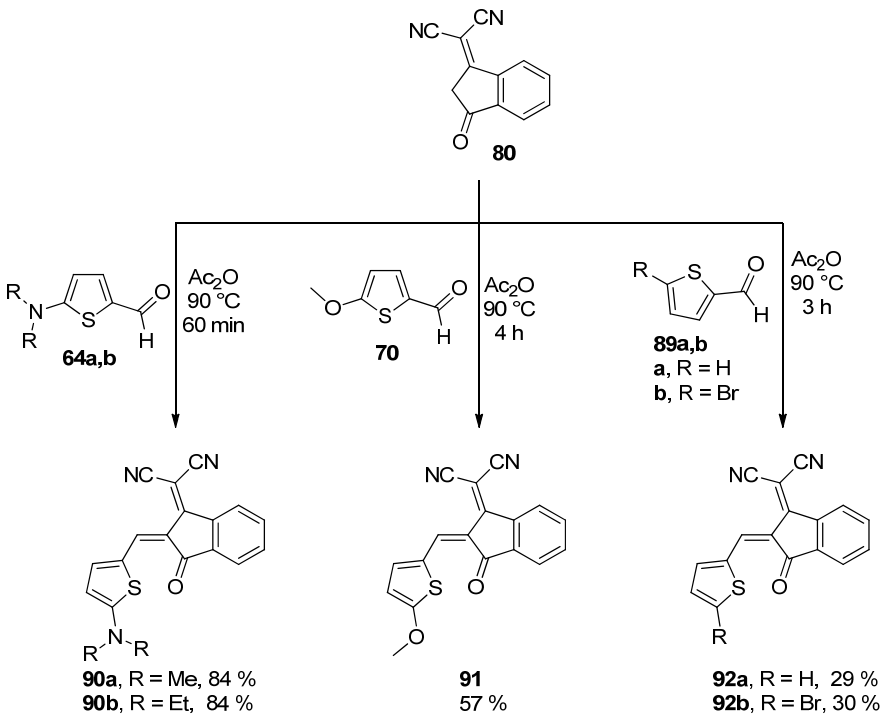

Scheme 17: Synthetic route to thiophene-based chromophores **90 - 92** via Knoevenagel condensation.

On the other hand, benzenedithiol substituted chromophores **93** and **94** were isolated in 30 - 75 % yields from reaction of precursor **59** with the respective acceptor moieties **79** and **80**.

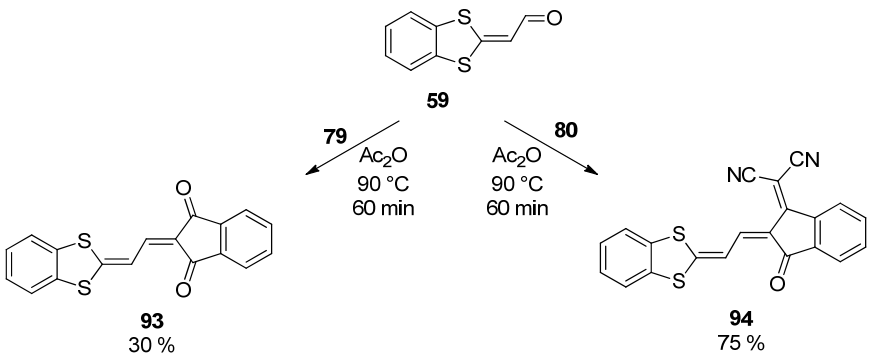

Scheme 18. Synthesis of benzenedithiol derivatives **93** and **94**.

Dyes **95 - 97** were synthesized according to Scheme 19. Benzoxazolium, benzothiazolium and benzoselenazolium iodide salts **53 - 55** were reacted with diphenylformamidine in acetic anhydride in order to obtain the corresponding formylation intermediates, to which the acceptor unit **80** and potassium acetate were added. Compounds **95 - 97** precipitated from the reaction mixture and were isolated by chromatography and recrystallization in 25 - 60 % yields.

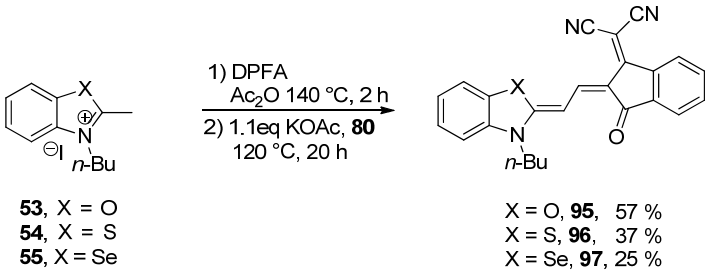

Scheme 19. Synthesis of compounds **95 - 97**.

On the other hand, naphthostyryl and quinoline donor building blocks **75** and **78** did not display any or sufficient product formation when reacted in the above described conditions. Alternatively, iodide salts **75** and **78** were deprotonated with potassium hydroxide and subsequently reacted in a three-component condensation reaction[93b] with triethylorthoformate and the acceptor component **80** to afford dyes **99** and **101** in 11 % and 39 % yields, respectively (Scheme 20).

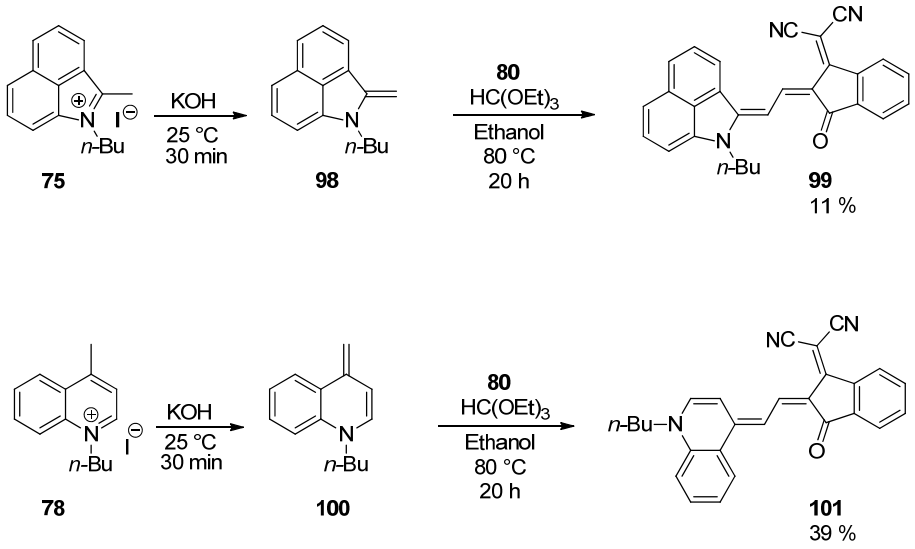

Scheme 20. Synthesis path for dyes **99** and **101**.

The main disadvantage of this method is the high probability of the side-reaction between two donor moieties giving rise to the corresponding cyanine dye (Chart 15). This side-product was indeed detected by mass spectra and turned hard to separate from the desired compound **99**. Therefore the aldehyde derivative **76** was preferred in reactions performed afterwards.

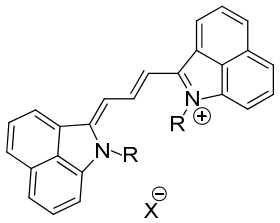

Chart 15. Product of condensation of two naphthostyryl donor units.

3.1.3.2 Halogenated derivatives

Chromophores bearing halogenated acceptor moieties could be easily obtained following the above described procedures. Indolenine-based molecules were condensed under Knoevenagel conditions to afford a variety of colorants bearing two or four chlorine atoms and four bromine atoms (Scheme 21). Dyes **102a-c** and **103a-c** were obtained in 28 - 58 % yields after purification by chromatography. It has to be noticed that the relatively low yields obtained for the condensation were due to impure acceptor materials (see explanation in the following).

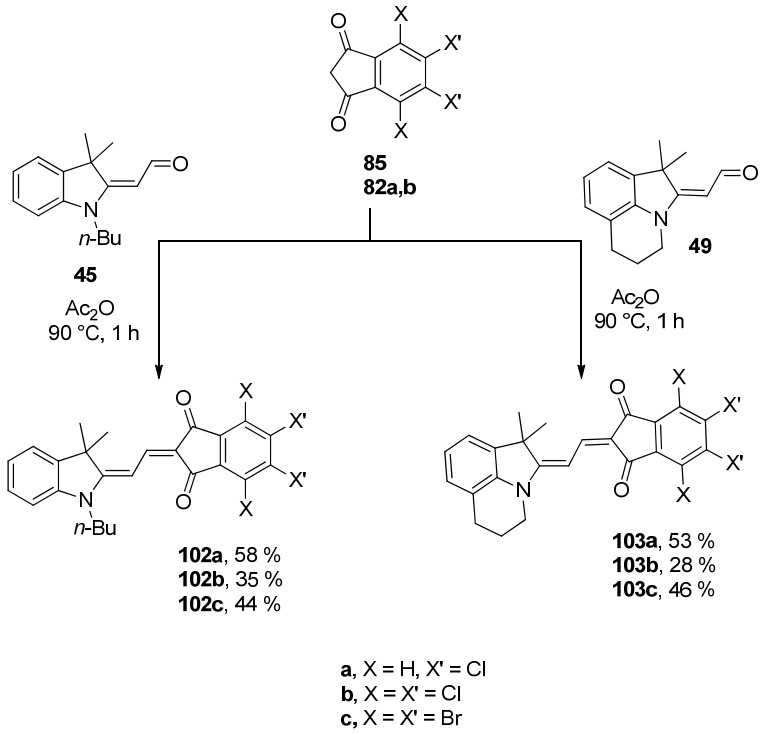

Scheme 21. Synthesis of new halogenated dyes **102a-c** and **103a-c** by Knoevenagel condensation between the respective C-H active acceptor units and aldehyde derivatives.

Analogously, benzoxazole- and benzothiazole-based colorants **104a-c** and **105a-c** were obtained in yields ranging from 17 % to 62 % by reaction of the respective salts with DPFA followed by addition of the acceptor component in acetic anhydride.

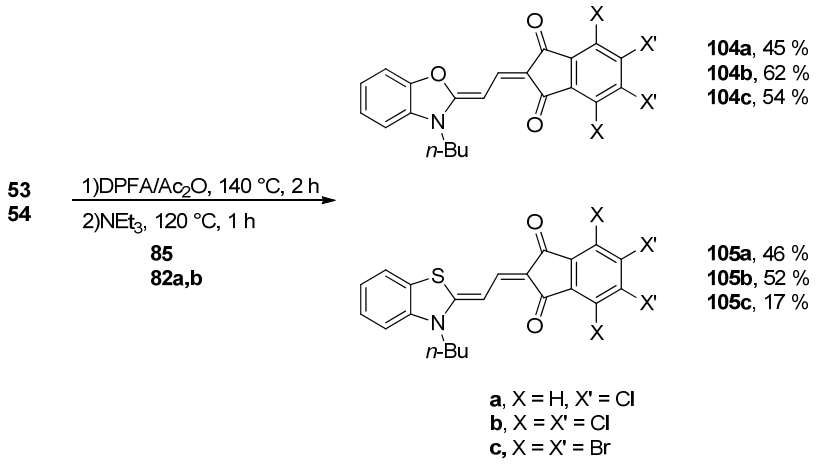

Scheme 22. Synthesis of halogenated dyes **104a-c** and **105a-c** by reaction of benzoxazolium and benzothiazolium salts **53** and **54** with DPFA and the respective C-H active acceptor units under basic conditions.

Furthermore, the dicyanovinyl-substituted acceptor **86** was as well condensed with the corresponding aldehydes to obtain dichlorinated dyes **106** and **107** in 24 % and 33 % yield,

respectively. The reaction of salts **53**, **54** and **55** with DPFA and subsequent addition of acceptor component **86** to afford dyes **108 – 110** could be improved by replacing potassium acetate by triethylamine; nevertheless the yields remained under 10 % in all cases (Scheme 23).

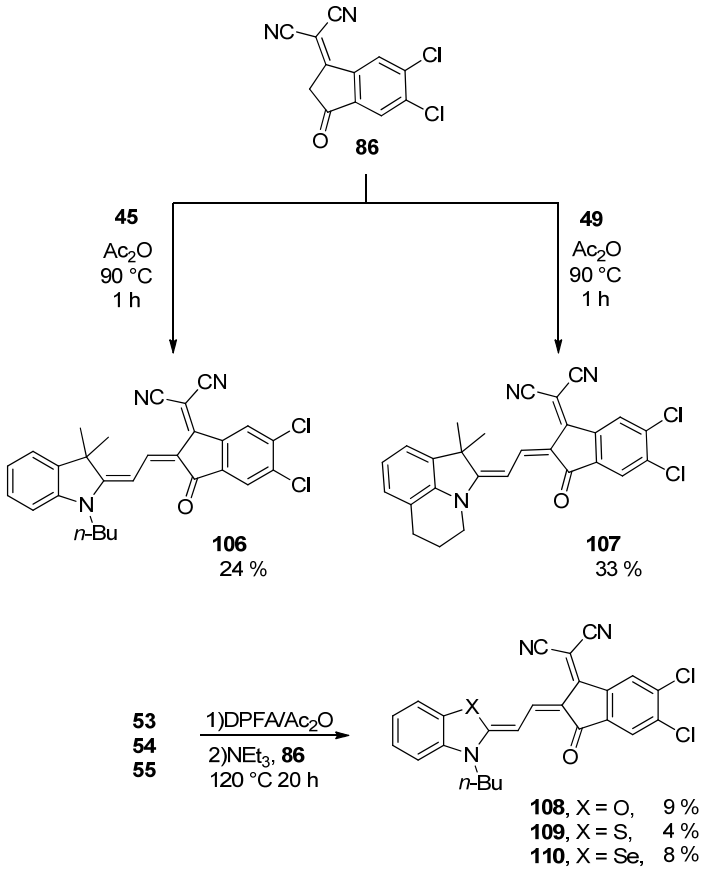

Scheme 23. Synthesis of dichlorinated dyes **106 - 110**.

During the synthesis of dyes **102a-c** and **103a-c** a blue side-product could be isolated. Since the quantity of side-product was not negligible, the corresponding characterization through NMR spectroscopy (^{1}H, ^{13}C, COSY, HSQC and HMBC), mass spectrometry and elemental analysis was performed in order to elucidate its structure. The ^{1}H-NMR analysis of the side-product indicated the presence of one methyl group as well as one olefinic proton more in comparison with chromophores **102 - 103**. Besides this, the side-product corresponding to the synthesis of **103b**, featured a mass spectrum pattern corresponding to four chlorine atoms and a mass of 533.030 a.u., while the elemental analysis confirmed the molecular formula $C_{27}H_{21}Cl_4NO_2$. The COSY analysis showed the following methylene-bridge coupling structure:

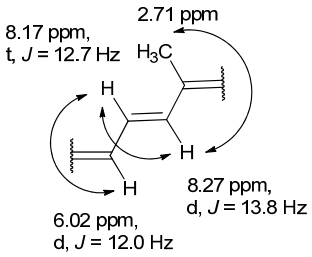

Finally, HSQC and HMBC NMR spectra allowed assigning the new methyl group to the side of the methylene chain closer to the acceptor unit. The proposed structure for the blue compound **103b-2** is shown together with the ^{1}H-NMR spectrum in Figure 15.

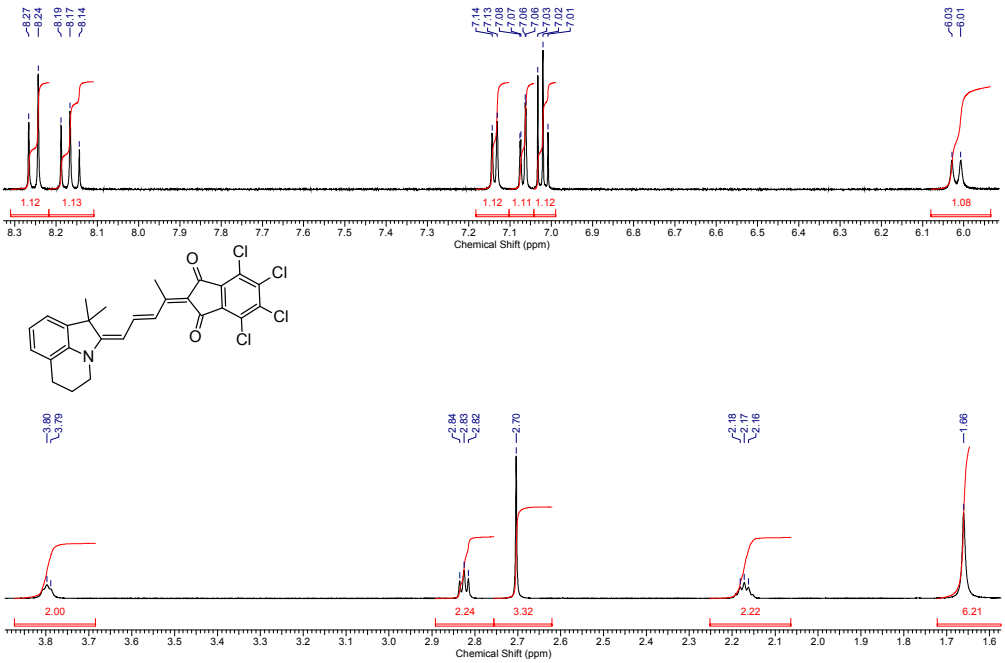

Figure 15. ^{1}H-NMR and proposed structure for blue compound **103b-2**.

The chemical structures of the isolated side-products are depicted in Chart 16.

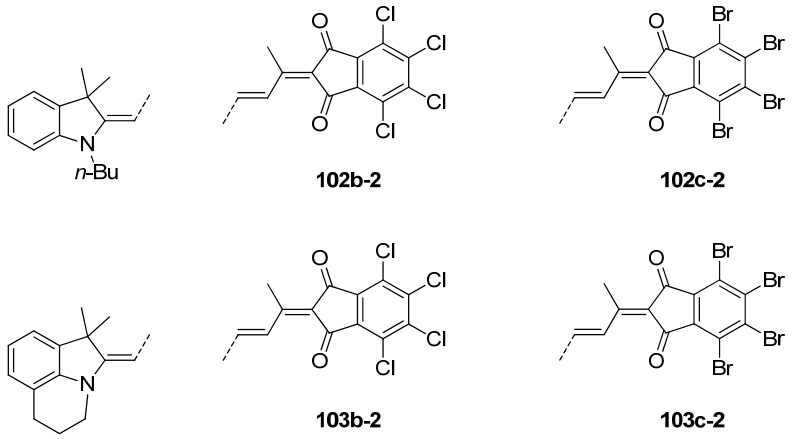

Chart 16. Chemical structure of π-extended side-products.

3.1.3.3 Synthetic path to π-extended molecules

The origin of the π-extended side-product has been attributed to an impurity, since different batches of halogenated indanedione acceptor gave different ratios of main and side-product. In order to identify such impurity, the halogenated indanedione acceptor materials were analyzed by mass spectrometry. While MALDI experiments did not provide useful information, EI measurements revealed an impurity which could be identified as the product of the condensation reaction between indanedione and acetone. This reaction may occur during recrystallization of the synthesized acceptor moieties.

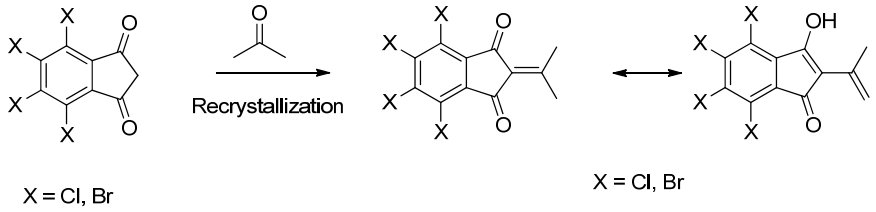

Scheme 24. Proposed mechanism for the formation of modified 1,3-indanedione acceptor moiety.

In order to prove this reaction pathway the condensation of commercial 1,3-indanedione (**79**) and halogenated indanedione (**82a**, **85**) with acetone was performed following a literature-known procedure:[97]

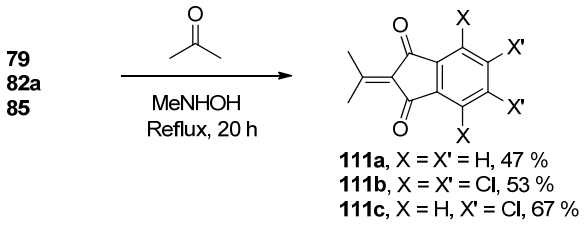

Scheme 25. Condensation of 1,3-indanedione derivatives with acetone.

Finally, the modified acceptor moieties could be reacted with the corresponding aldehydes to obtain exclusively the π-extended merocyanines. Chlorinated acceptor moieties featured higher reactivity and therefore afforded higher yield.

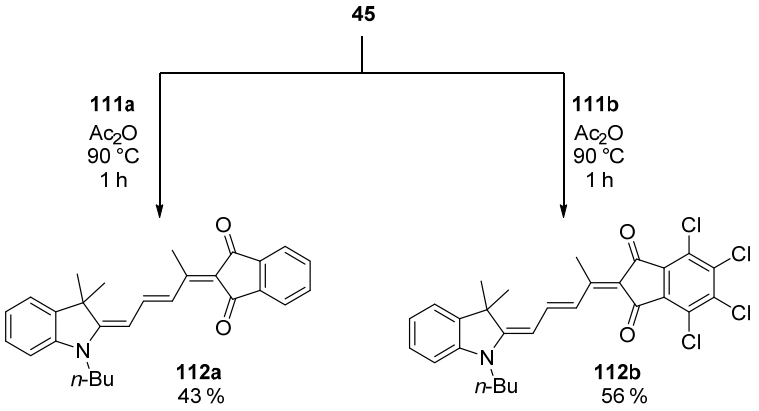

Scheme 26. Synthesis of π-extended dyes **112a,b**.

Although the condensation reaction between acetone and 1,3-indanedione was reported in 2012,[97-98] no application for this reaction had been accomplished so far. Therefore it seemed a logical step to vary the ketone to introduce solubilizing alkyl chains in the polymethine bridge. Thus, 1,3-indanedione was condensed with 2-hexanone to afford the corresponding butyl-substituted π-extended derivative **113** in 25 % yield, which has not been reported until now.

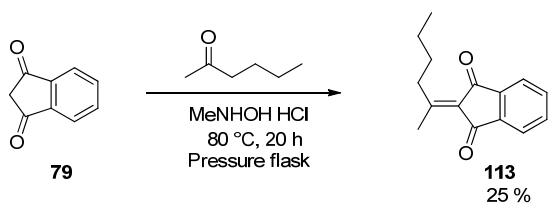

Scheme 27. Condensation of 1,3-indanedione with 2-hexanone to provide the butyl-functionalized acceptor **113**.

The condensation of the modified acceptor unit **113** with the corresponding aldehyde or imine derivatives under mild conditions afforded molecules **114 - 117**. This synthetic path

is very effective for aldehyde derivatives. Indeed, the yield of a homologue of dye **116** reported in ref. [99] which has been synthesized using the benzyl derivative of base **75** is only of 11 %, while taking the aldehyde derivative **76** affords a decent yield of 55 %. The reaction performed best at room temperature. This may be a disadvantage when using imine derivatives as in the case of **54**, because higher reaction temperatures are needed, which may lead to decomposition of the acceptor moiety. As a consequence dye **117** was obtained in a low yield of 13 %. The obtained chromophores exhibited very high solubility even in unpolar solvents such as *n*-hexane.

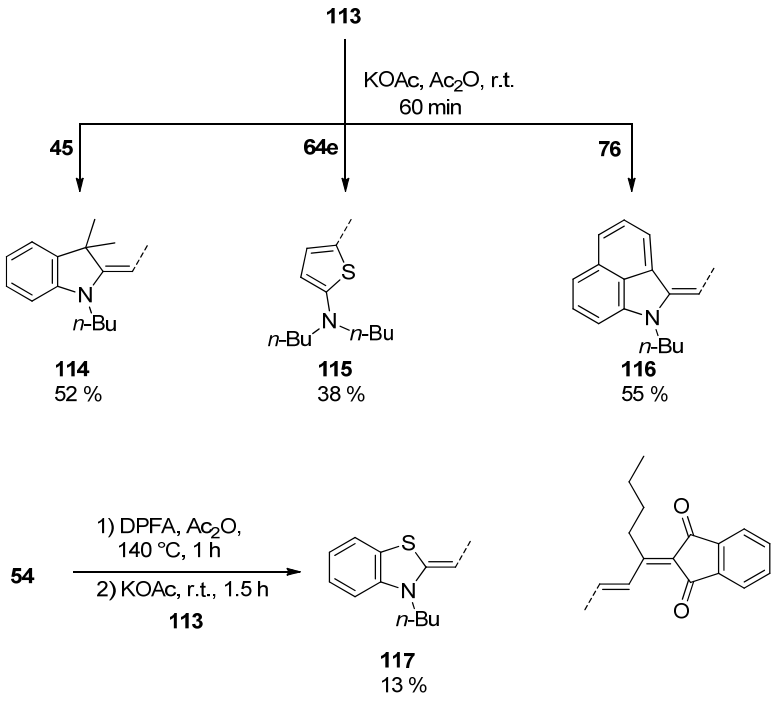

Scheme 28. Synthesis of π-extended merocyanine dyes **114 - 117**.

Furthermore, taking advance of the new extended acceptor unit **111c**, a double condensation could be performed by reaction of one acceptor moiety with two donor units to give a bifurcated AD_2 scaffold. Since the condensation of the second donor unit is not sterically favored, the presence of a base and high temperatures were necessary to obtain the desired product. For this reaction the dichlorinated acceptor **111c** was chosen due to the higher reactivity demonstrated in earlier reactions and the easier interpretation of the ^{1}H-NMR spectra of the product.

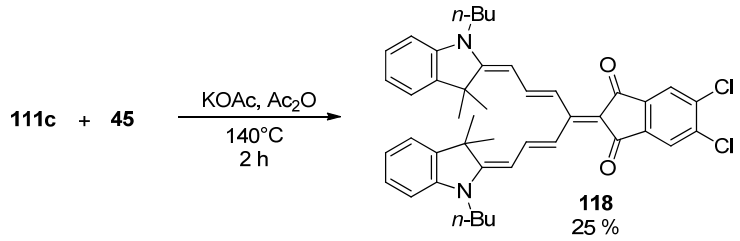

Scheme 29. Synthesis of bifurcated AD_2 scaffold **118**.

The respective reference D-A dye was synthesized as well using a literature-known procedure for the condensation of **45** with the corresponding extended acceptor unit **119**.[100]

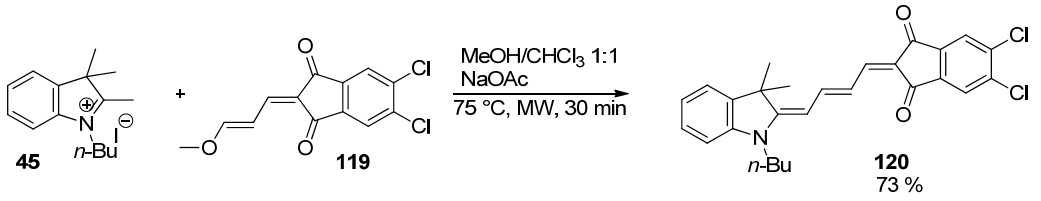

Scheme 30. Synthesis of reference D-A compound **120**.

3.1.3.4 Thiazole-based dyes

Thiazole acceptor component **88** reacted quickly with aminothiophene aldehyde derivatives under Knoevenagel condensation conditions to provide dyes **121a-h** in moderate to good yields. In this way a variety of molecules with different alkyl chains could be obtained and easily purified by recrystallization or chromatography, depending on solubility. The corresponding synthesis is shown in Scheme 31.

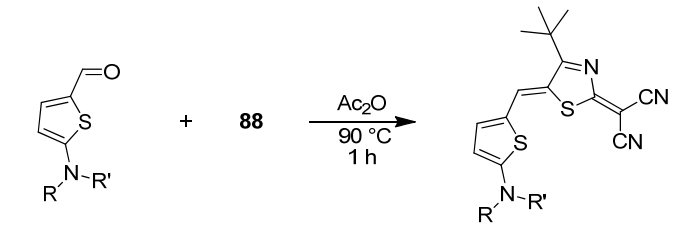

Scheme 31. Synthesis of dyes **121a-h** by Knoevenagel condensation.

Less reactive aldehydes needed longer reaction times in order to complete the Knoevenagel condensation. Compounds **123** and **124** were isolated after one hour in 38 % and 11 %

yield, respectively. The low yield obtained for **124** is probably due to the instability of the aldehyde in the reaction conditions, since longer reaction times did not provide better yields. Dyes **125** and **126**, on the other hand, could be obtained in moderate yields of 30 % after 20 h of reaction (Scheme 32).

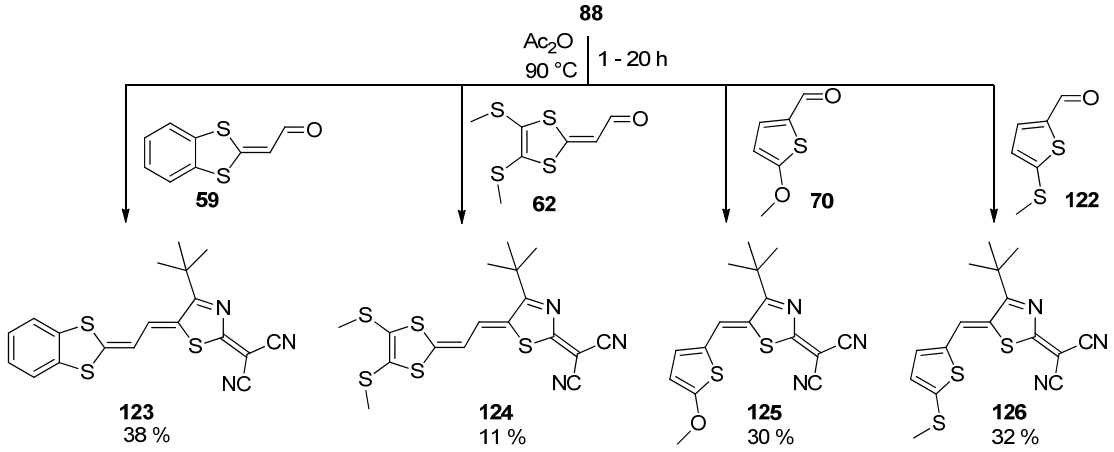

Scheme 32: Synthesis of compounds **123** - **126** by Knoevenagel condensation.

Furthermore, benzothiazolium and benzoselenazolium salts **54** and **55** were reacted with DPFA in acetic anhydride to undergo enamine formation. Unfortunately, the further reaction of the enamine with the acceptor unit **88** did not provide more than 1 - 3 % of desired compound when using potassium acetate as base. Triethylamine improved the yield to 18 % for **127** and 6 % for **128** (Scheme 33).

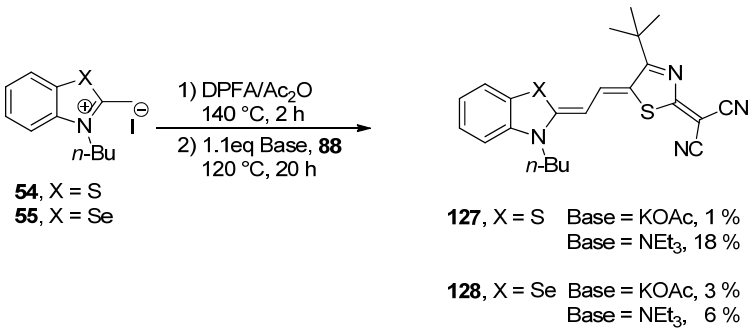

Scheme 33: Synthesis of dyes **127** and **128**.

3.2 Solid State Packing of Indanedione-based Merocyanine Dyes and Application in Transistor and Solar Cell Devices*

Among the various kinds of molecules used so far as donor counterparts of the ubiquitously utilized fullerene acceptors in the BHJ active layers, an increasing number of molecules with alternating electron donor (D) and acceptor (A) subunits have been reported during the last years.[15] These materials have the advantage of low band-gap and high tinctorial strength, having their absorption properties tunable by careful design of the corresponding donor and acceptor units. The common approach is based on D-A-D and A-D-A scaffolds for small molecules or $(D\text{-}A)_n$ structures for polymers to avoid a broadening of the density of states by dipolar disorder. This is considered detrimental for charge transport according to the Gaussian Disorder Model (GDM)[16], as already discussed in the introduction of this thesis. As a consequence, dipolar molecules (D-A dyes, push-pull dyes) such as merocyanine dyes have been omitted in the whole field of organic electronics during the last three decades including organic photovoltaics. However, dipolar disorder only arises for randomly distributed dipolar molecules. The fact that merocyanine dyes tend to pack tightly in antiparallel dimers with no overall dipole moment, accordingly opens the door to applications in organic photovoltaics.[101] This concept was already introduced in 2008 by the groups of Würthner and Meerholz with the first solution-processed merocyanine-based BHJ solar cell showing a respectable *PCE* of 1.7 %.[27] Later on improved materials for both solution- (**6**, 4.5 %)[4a] as well as vacuum-processed devices (**11**, 5.8 %)[4b] were reported. The groups of Blanchard, Roncali and Wong, among others[44, 46, 59-60, 102] have investigated other types of D-A dyes and pushed solar cell devices based on dipolar D-A molecules even further, reaching *PCE*s of up to 6.8 %.[55]

* A part of this chapter has been published in: A. Arjona-Esteban, J. Krumrain, A. Liess, M. Stolte, L. Huang, D. Schmidt, V. Stepanenko, M. Gsänger, D. Hertel, K. Meerholz, F. Würthner, *J. Am. Chem. Soc*. **2015**, *137*, 13524. Reproduced in parts with permission of the American Chemical Society (2015). Transistor devices were fabricated by Andreas Liess, Astrid Kudzus or Dr. Lizhen Huang. Solar cell devices were built by Julian Krumrain (University of Köln). Single crystal and thin-film X-Ray analyses were performed by Dr. M. Gsänger and Dr. David Schmidt. AFM measurements were carried out by Dr. Vladimir Stepanenko and electro-optical absorption measurements by Dr. M. Stolte.

Still, despite the continuously increasing performance of organic solar cells, it is difficult to predict the success of a given absorber molecule because the power-conversion efficiency depends on many parameters beyond those given by the individual molecule. In this chapter a series of structurally related D-A dyes, i.e. a series of nine merocyanine dyes (Chart 17) bearing the same 2-(3-oxo-2,3-dihydro-1*H*-inden-1-ylidene)malononitrile or 1,3-indanedione acceptor moiety is investigated. The synthesized dyes exhibit similar optical absorption properties, yet showing very different performances in organic solar cells (OSC) and organic thin film transistor (OTFT) devices. With the help of UV-Vis spectroscopy, atomic force microscopy (AFM) and X-ray diffraction (XRD) measurements of thin films and single crystal analyses, the varying performance is attributed to different packing arrangements of the dyes in the solid state. Consequently, the supramolecular packing of merocyanines is correlated with both OTFT and OSC performance.

3.2.1 Optical and electrochemical properties & crystal packing analysis

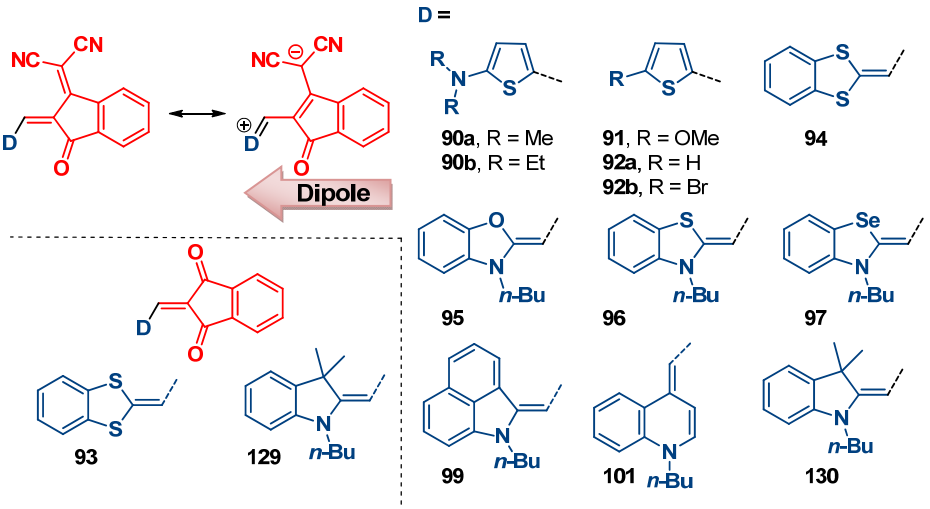

Chart 17. Chemical and resonance structure of merocyanine dyes investigated in this work bearing acceptor units 2-(3-oxo-2,3-dihydro-1*H*-inden-1-ylidene)malononitrile and 1,3-indanedione.

The synthesis of dyes depicted in Chart 17 has been described in section 3.1. As a general procedure, the chromophores were obtained by Knoevenagel condensation between an aldehyde or imine derivative and the C-H active acceptor unit in acetic anhydride in moderate to good yields. Reference dyes **129** and **130** have been described previously.[29, 103]

3.2.1.1 Molecular properties

The optical properties of dyes described in Chart 17 were investigated by means of UV-Vis and electro-optical absorption (EOA) spectroscopy. In addition, cyclic voltammetry (CV) was performed to estimate the frontier molecular orbital (FMO) energy levels. The optical absorption spectra are depicted in Figure 16. The corresponding data is listed in Table 1.

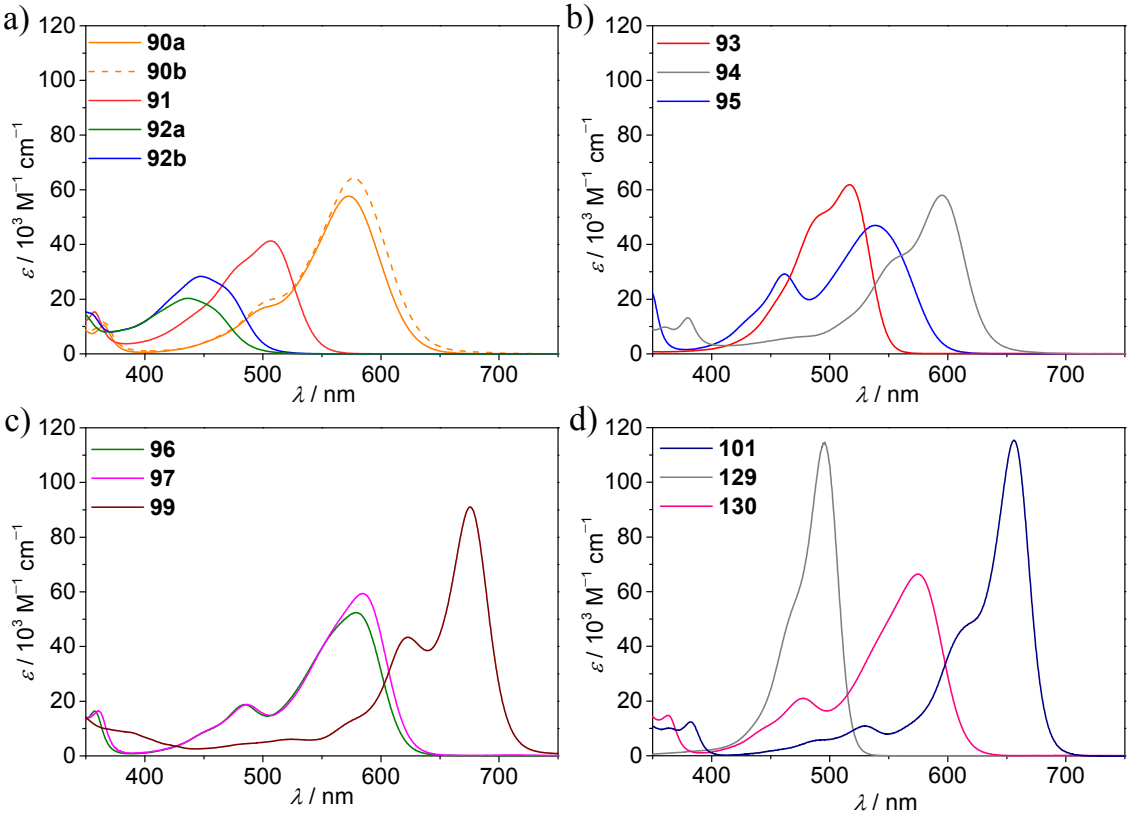

Figure 16. UV-Vis spectra of dyes **90a,b**, **91, 92a**,**b** (a), **93 - 95** (b), **96, 97**, **99** (c) and **101**, **129**, **130** (d), $c \approx 10^{-5}$ M in dichloromethane at 298 K.

The optical properties are similar for most of dyes containing 2-(3-oxo-2,3-dihydro-1*H*-inden-1-ylidene)malononitrile as acceptor moiety, featuring absorption maxima around 580 nm and extinction coefficients (ε_{max}) varying from $46 \cdot 10^3$ M^{-1} cm^{-1} to $113 \cdot 10^3$ M^{-1} cm^{-1}. The tinctorial strength $\mu^2_{eg} M^{-1}$ remains strong in all cases, ranging from 0.20 to 0.26 D^2 mol g^{-1}. X-ray photoelectron spectroscopy (XPS) studies on merocyanines bearing azaheterocyclic donor units containing oxygen, sulfur and selenium have analyzed the conjugation and partial charge distribution over the nitrogen atom and the corresponding heteroatom within the donor unit.[104] The heteroatom positive charge contribution and conjugation was found to decrease in the order O>S>Se. These studies concluded that the positive charge (zwitterionic resonance structure) in the donor moiety of

merocyanine dyes mainly lies on the nitrogen atom, except for the benzoxazole heterocycle where the contribution of the O^+ form is not anymore negligible. This conjugation effect can be observed in the absorption spectrum of dye **95**, which is slightly blue shifted in comparison with the other dyes of this series, in particular dyes **96** and **97**. A similar behavior has been reported for other benzoxazole-containing compounds.[105] Dyes **99** and **101** showed red-shifted absorption due in the first case to the higher effective conjugation length featured by benzo[*c,d*]indole donor moiety in comparison with other nitrogen-containing heterocycles and the second case to the longer conjugation path provided by the quinolone donor unit.[92a, 93a] On the other hand, dyes **93** and **129** show absorption at shorter wavelengths due to the lack of the dicyanovinyl acceptor group, i.e. shorter conjugation path provided by the 1,3-indanedione acceptor unit.

Furthermore, in the series **90-92** the effect of the donor strength in the absorption properties is clearly shown. The absorption is progressively blue-shifted as the donor strength decreases, and the extinction coefficient ε_{max} is diminished as well due to the weaker intramolecular charge transfer. Indeed, EOA studies of these dyes revealed a decrease in the dipole moment to the point that dye **92b**, with absorption maximum at 437 nm, shows an almost inexistent dipole moment of 1.6 D. Due to the weak absorption in the visible region of dyes **92a,b** these molecules were not further investigated for application in solar cell devices.

Regarding the electrochemical properties, only (1-alkyl-3,3-dimethylindolin-2-ylidene)-containing dye **130** features both reversible oxidation and reduction waves. The difference between the electrochemical gap determined from the redox potentials and the optical gap determined from the UV-Vis absorption maxima was in all cases below 0.2 eV, thus implying that the $S_0 \rightarrow S_1$ transition observed in the UV-Vis spectra corresponds to an electronic excitation from the HOMO to the LUMO level. Indeed, this difference would vanish for these merocyanine dyes if the onset of the absorption bands were used instead, which are about 30-50 nm bathochromically shifted with respect to the absorption maxima. The corresponding FMO levels (Figure 17) were calculated taking an Fc/Fc^+ value of −5.15 eV vs. vacuum[106] and the optical gap. Compounds **90a,b**, **93**, **95-97**, **99**, have HOMO levels in the range of 5.69 - 5.86 eV. Thus, when comparing their solar cell performance, similar open-circuit voltage (V_{OC}) values are expected. Dyes **91** and **94**, in

the contrary, display very low-lying HOMO levels, while dye **101**, with absorption in the NIR, should suffer from low V_{OC} values due to the high HOMO level of 5.54 eV.

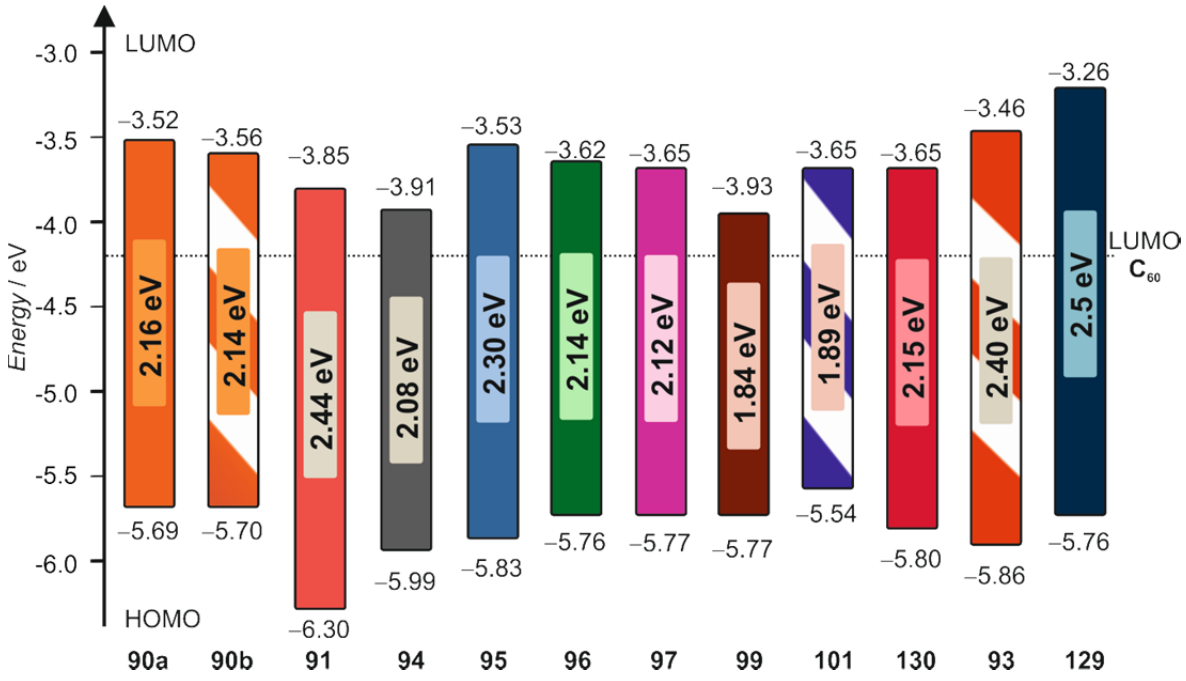

Figure 17. Schematic representation of HOMO and LUMO levels of the studied dyes and their relative positions to the LUMO level of the most commonly used fullerene acceptor material C_{60}, calculated from CV measurements taking a Fc/Fc^+ value of −5.15 eV vs. vacuum and the optical gap from the UV-Vis absorption maxima, respectively.

Most of the dyes feature LUMO levels about 3.52 - 3.65 eV. Therefore the 0.3 eV driving force required to overcome the exciton binding energy is provided and an efficient charge separation at the donor/acceptor heterojunction is expected.[107] Exceptions are dyes **91**, **94** and **99**, which show very low LUMO levels and driving force below 0.3 eV. As a consequence, charge transfer will occur with reduced probability and the influence of polarization effects in the solid state and local packing arrangements may become influential on the charge separation thermodynamics and kinetics of these dyes. On the other hand, a larger band-gap translated in a higher LUMO level is observed for dyes **93** and **129** due to the shorter conjugation path of 1,3-indanedione. Accordingly, the charge separation process is expected to be efficient, whilst higher voltage losses will arise from the large energy offset between donor and acceptor material LUMO levels.

Table 1. Optical, dipolar and electrochemical properties of the investigated compounds, extracted from UV-Vis[a], EOA[b] and CV[c] measurements.

Dye	λ_{max} [a] / nm	ε_{max} [a] / M^{-1} cm^{-1}	μ^2_{eg} [a] / D^2	$\mu^2_{eg}M^{-1}$ [a] / D^2 $mol\ g^{-1}$	μ_g [b] / D	$\Delta\mu$ [b] / D	c^2 [b] / 1	$E_{1/2,ox}$ [c] / V	$E_{1/2,red}$ [c] / V
90a	572	58700	84	0.25	8.6	4.0	0.40	0.54	-1.49*
90b	577	64200	94	0.26	9.1	4.4	0.39	0.55	−1.53*
91	506	41100	63	0.20	3.1	9.3	0.24	1.14	-1.30*
92a	437	20100	35	0.12	1.6[d]	5.8[d]			
92b	447	27500	48	0.13	2.0[d]	3.7[d]			
93	516	62200	82	0.25	-	-	-	0.70*	-1.51*
94	595	61900	82	0.22	3.9	8.9	0.26	0.84*	−1.18*
95	539	46100	86	0.22	8.7	3.8	0.40	0.68*	−1.61
96	579	52400	82	0.20	8.2	3.0	0.43	0.61*	−1.58*
97	584	60200	89	0.20	7.7	3.2	0.42	0.63*	−1.57*
99	675	91200	97	0.23	4.8	7.7	0.42	0.61*	−1.18
101	656	113300	103	0.25	-	-	-	0.38*	-1.48
129	496	114600	94	0.25	3.8	3.8	0.40	0.61*	−1.94
130	576	66400	98	0.23	6.2	4.2	0.40	0.65	-1.52

[a] UV-Vis: CH_2Cl_2, $c \approx 10^{-5}$ M, 298 K; [b] EOA in 1,4-dioxane, $c \approx 10^{-6}$ M, 298 K, with Onsager cavity field correction to give "gas phase" dipole moments.[108] [c] CV in CH_2Cl_2, $c \approx 10^{-4}$ M, using Fc/Fc^+ as internal reference and $N^tBu_4PF_6$ as electrolyte. * Peak potential of irreversible redox process. [d] Perpendicularly polarized.

3.2.1.2 Single crystal analysis

Bond Length Alternation (BLA). Depending on the strength of their donor and acceptor substituents, merocyanine dyes can exist as a resonance structure of two formal states: the polyene-like form and the zwitterionic one (Figure 18). A hint about the contribution of each of these structures is provided by the BLA of the (tri-)methine bridge. For a neutral polyene-like structure, bonds **B1** and **B3** are expected to be shorter than **B2** and vice versa for the zwitterionic form.[21b]

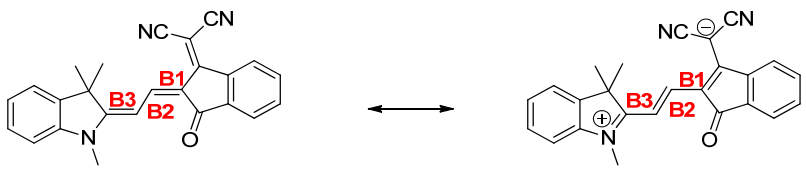

Figure 18. Resonance structures of merocyanine dyes: polyene-like (left) and zwitterionic (right) and the corresponding polymethine chain bonds **B1** - **B3**.

Crystal structures could be obtained and analyzed for the majority of the dyes described in this study. The corresponding bond lengths are shown in Figure 19. The experimentally obtained BLA is defined as BLA = R(C-C) − R(C=C), where R(C-C) and R(C=C) correspond to the bond lengths of **B2** as well as **B1** and **B3**, respectively. As a general trend **B2** was found to be slightly shorter than **B1** and **B3**, thus indicating a higher contribution of the zwitterionic form in the solid state. Since the bond length difference remained below 0.03 Å for all dyes, it appears that all dyes exhibit an electronic structure close to the cyanine limit, which is known to provide the highest absorption strength and the fewest changes of bond length and molecular structure upon photoexcitation.[109]

EOA experiments reveal that the situation in solution is slightly different. Thus, in the absence of the polarizing environment of the solid state, all molecules exhibit a ground state that is more polyene-like and an excited state that is more zwitterionic, as indicated by the increase of the dipole moment upon excitation (positive dipole difference $\Delta\mu$) and a c^2 value of less than 0.5 (Table 1). Two dyes (**91**, **94**) are clearly polyene-like, with small c^2 values of around 0.25, whereas the other dyes already show a stronger transfer of charge from the donor to the acceptor subunit in the ground state ($c^2 \geq 0.4$). The investigated dyes display dipole moments in the range 4 - 9 D.

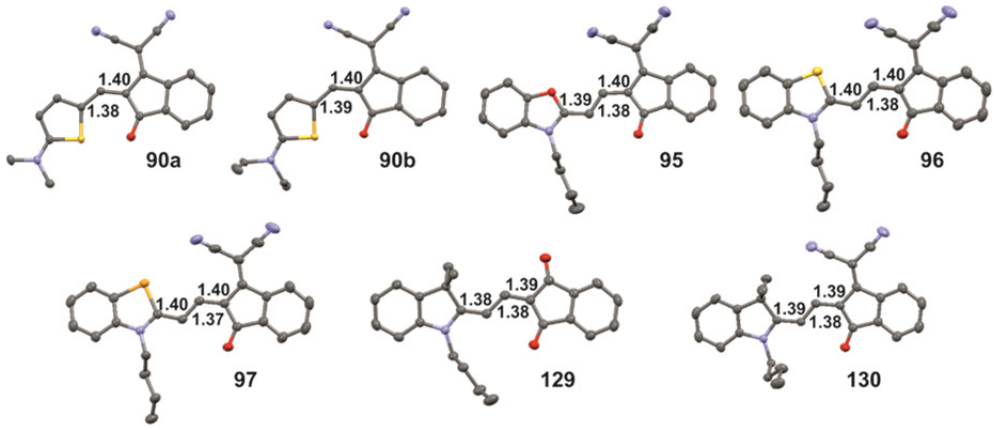

Figure 19. Molecular structure of dyes **90a,b**, **95 - 97**, **129** and **130** and the corresponding methine bridge bond lengths measured in the crystal.

Crystal packing analysis. In Figure 20, Figure 21 and Figure 22 the packing arrangements of the molecules are shown. The studied dyes display an almost planar π-scaffold where the donor and acceptor units are slightly twisted out of the plane, with torsion angles varying from 3° for dye **95** up to 15° for dye **129**. Consequently, the π-π-distances were calculated from parallel planes of the acceptor moieties. With regard to the relative

arrangement between molecules, the dyes can be divided into three groups varying in the dimensionality of the respective dye arrangement as will be discussed below:

(I) centrosymmetric dimer units with no π-contact to the neighboring molecules,

(II) 1-dimensional stack of slipped antiparallel dimer units featuring π-overlapping with the neighboring molecules,

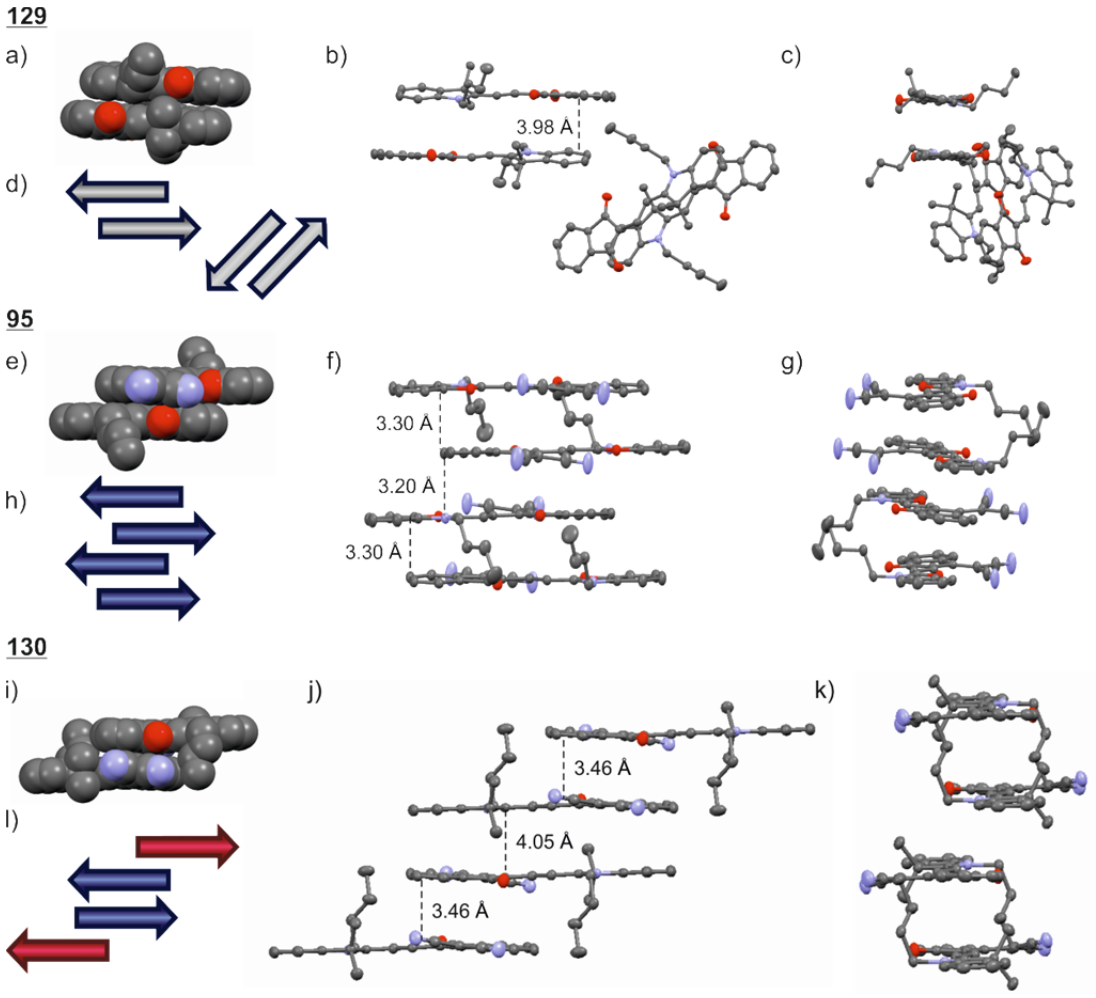

Figure 20. Packing motifs for merocyanine dyes based on single crystal X-ray analyses. a-d) Group (I), centrosymmetric dimer units with no π-contact to the neighboring molecules: a) Space-filling view of close dimer of **129**. b) Side- and c) front-view of neighboring dimers of **129** with antiparallel packing motif. d) Schematic representation of **129** showing the antiparallel orientation of the dipole moments (arrows) of the merocyanine dyes and their arrangement to the next neighboring dimer. e-l) Group (II), 1-dimensional stack of slipped antiparallel dimer units featuring π-overlapping with the neighboring molecules: e) Space-filling view of close dimer of **95**. f) Side- and g) front-view of **95** π-stack with antiparallel packing motif. h) Schematic representation of **95** π-stack showing the antiparallel orientation of the dipole moments (arrows) of the dyes and the different spacing to the upper and lower neighboring dyes. i) Space-filling view of close dimer of **130**. j) Side- and k) front-view of **130** π-stack with antiparallel packing motif. l) Schematic representation of **130** π-stack showing the antiparallel orientation of the dipole moments (arrows) of the dyes and the different spacing to the upper and lower neighboring dyes. In all figures protons are omitted for clarity. Acceptor-to-acceptor plane distances are given.

(III) 1-dimensional staircase arrangement of parallel highly slipped molecules with equidistant spacing.

Group (I), represented here by dye **129**[42a] (Figure 20, top), is characterized by dimer units of antiparallel molecules with no overall dipole moment. The distance between adjacent dyes within the dimer is 3.98 Å. The neighboring dimer unit is rotationally displaced, thus any contact between the π-surfaces is hindered.

Group (II) dyes, represented by dyes **95** (Figure 20, middle) and **130** (Figure 20, bottom), arrange in centrosymmetric dimers, where each molecule is slightly slipped to the next one and presents a close and a distant neighbor, similarly to the packing of previously reported merocyanines with 2-aminothiophene electron donor units.[4a] For dye **95** the π-π-distance between close neighbors is extremely short (3.20 Å), resulting in a much larger longitudinal slip than between the distant neighbors. Interestingly, while the packing arrangement of dye **130** shows a π-stack with alternating orientations of the dicyanovinyl groups, for dye **95** these are found to group in pairs, thus creating a lateral dipole moment which is annulated by the neighboring pair of molecules. Dye **130** shows larger distances between close neighbors than dye **95**. This group of dyes is thus characterized by a one-dimensional π-stack of dimers which should provide good contact area between π-surfaces and enable charge percolation pathways at least in one dimension in the solid state.

Finally, group (III) dyes, represented by compounds **96**, **97** (Figure 21) and **90a,b** (Figure 22) were found to pack in a completely new arrangement for dipolar compounds. The dyes show equidistance to the upper and lower neighbor, being the dipole moments parallel to each other in a staircase-like conformation. Near the first stair, a second one is found with oppositely directed dipole moment. This arrangement follows a herringbone pattern. The π-π-distance varies from 3.41 Å (**90b**), 3.43 (**90a**), 3.50 Å (**96**) to 3.52 Å (**97**). The effect of the alkyl chains on the longitudinal displacement of neighboring stairs is more pronounced for dyes **96** and **97**, bearing butyl chains. The ethyl substituted dye **90b** shows an almost equidistant distribution of the stairs. Interestingly, dye **90a** was found to pack as well in a staircase-like arrangement with equal distances to the upper and lower neighbors. However, in the case of **90a** no herringbone pattern is provided, but rather a sheet-like ordering of the molecules all over the crystal. A closer insight into the relative arrangement of the molecules reveals dimer-like units between adjacent stairs and two different dimer-forming directions.

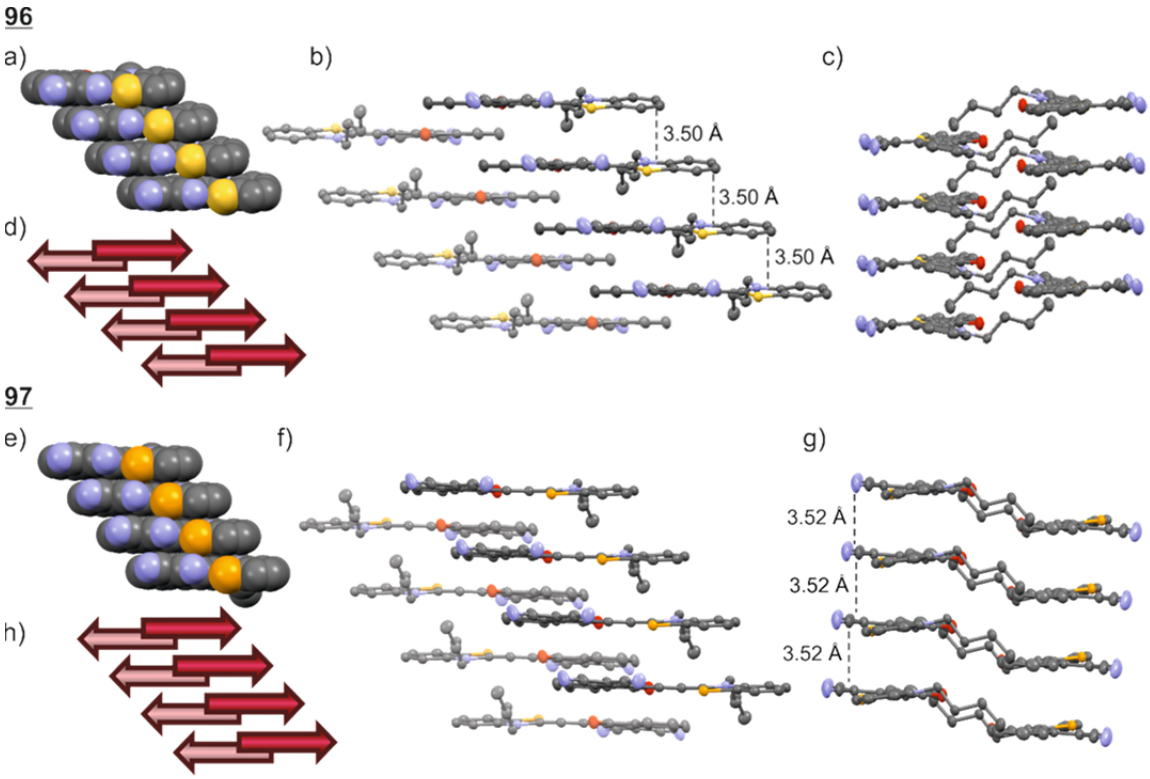

Figure 21. Packing motifs for merocyanine dyes of group (III) based on single crystal X-ray analyses. a) Space-filling view of staircase-like packing of dye **96**. b) Side- and c) front-view of neighboring staircase packing motif of dye **96**. d) Schematic representation of dye **96** π-stack showing the parallel orientation of the dipole moments (arrows), and the equal distances to the upper and lower neighbors. e) Space-filling view of staircase-like packing of dye **97**. f) Side- and g) front-view of neighboring stairs of dye **97**. h) Schematic representation of dye **97** π-stack showing the parallel orientation of the dipole moments (arrows), and the equal distances to the upper and lower neighbors. In all figures protons are omitted for clarity. Acceptor-to-acceptor plane distances are given.

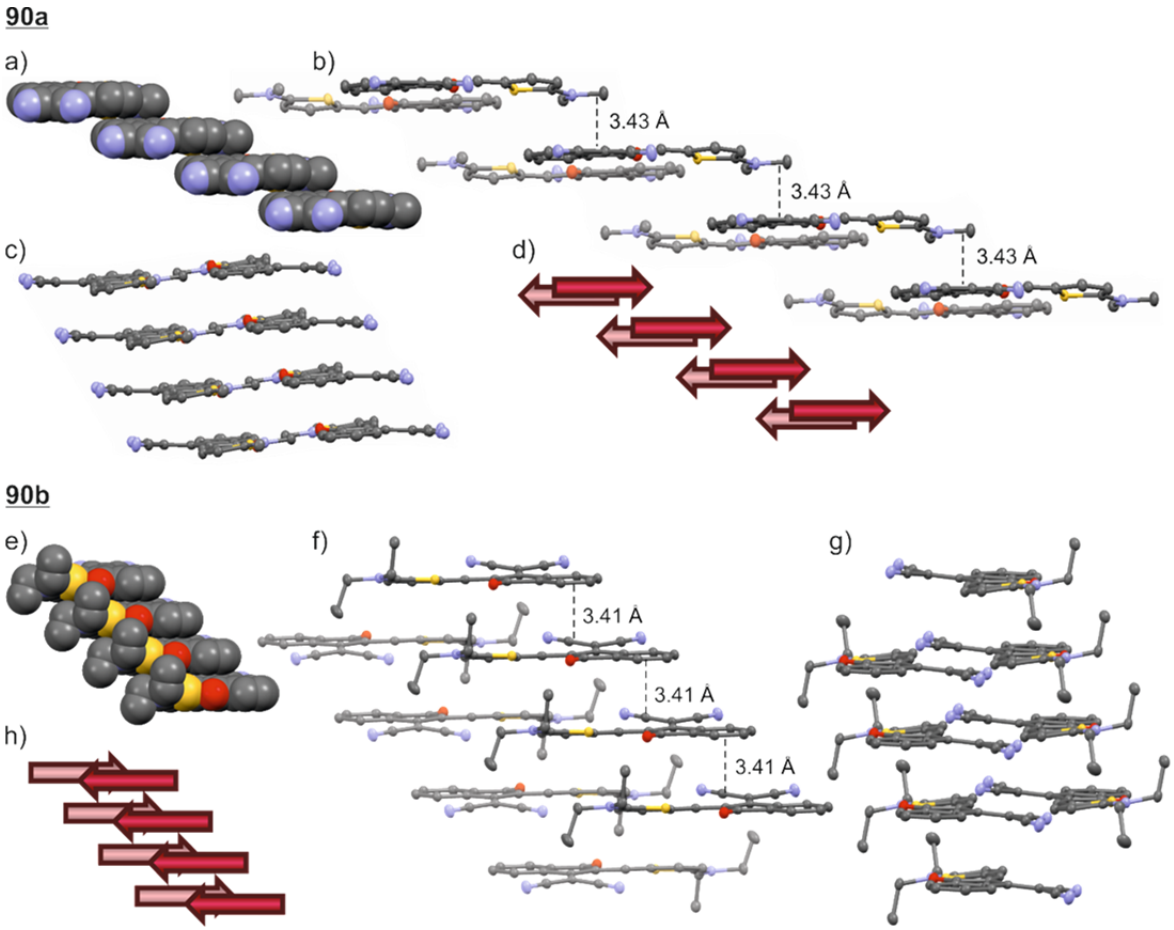

Figure 22. Packing motifs for merocyanine dyes of group (III) based on single crystal X-ray analyses. a) Space-filling view of staircase-like packing of dye **90a**. b) Side- and c) front-view of neighboring stairs of dye **90a**. d) Schematic representation of dye **90a** π-stack showing the parallel orientation of the dipole moments (arrows), and the equal distances to the upper and lower neighbors. e) Space-filling view of staircase-like packing of dye **90b**. f) Side- and g) front-view of neighboring stairs of dye **90b**. h) Schematic representation of dye **90b** π-stack showing the parallel orientation of the dipole moments (arrows), and the equal distances to the upper and lower neighbors. In all figures protons are omitted for clarity. Acceptor-to-acceptor plane distances are given.

3.2.2 Organic Thin-Film Transistor (OTFT) devices

In order to estimate the charge carrier mobilities of the synthesized molecules, organic thin-film transistor devices were fabricated. For this purpose, the molecules were vacuum evaporated to form thin films with a nominal thickness of 30 nm on top of Si/SiO_2 substrates as well as $Si/SiO_2/AlO_x$/*n*-tetradecylphosphonic acid (TPA) or $Si/SiO_2/AlO_x$/12,12,13,13,14,14,15,15,16,16,17,17,18,18,18-pentadecafluorooctadecyl phosphonic acid (FOPA) substrates. During the sublimation of some dyes, the substrates were heated to elevated temperatures to induce a more crystalline film growth. Subsequently, thin-film transistors in a bottom-gate top-contact configuration were

fabricated. The transfer characteristics of the devices were measured under ambient conditions for a drain-source voltage of $V_{DS} = -50$ V. Determination of the charge carrier mobility μ_p as well as the threshold voltage V_{th} was carried out using equation (13) which is valid for the saturation regime:

$$\mu_p = (2\, I_{DS}\, L / [W\, C_i\, (V_{GS} - V_{th})^2]) \qquad (13)$$

Here, I_{DS} describes the drain-source current and C_i the capacitance of the dielectric, while L and W represent the length and width of the transistor channel. For every merocyanine, the electrical parameters were averaged over at least five OTFTs and showed a variation of less than 10 %. The resulting hole mobilities, on-off ratios as well as threshold voltages of the OTFTs of the studied molecules on the Si/SiO_2 and TPA or FOPA modified $Si/SiO_2/AlO_x$ substrates can be found in Table 2. For each molecule only the data of the substrate with best performance is listed.

As a general trend, transistor devices built on Si/SiO_2 substrates from dyes **90b**, **91, 94** and **99** showed no field effect behavior while all other dyes (except dye **101**, which decomposed during sublimation) gave OTFTs with similar low charge carrier mobilities in the range of $\mu_p \approx 10^{-5}$ - 10^{-6} $cm^2\ V^{-1}\ s^{-1}$. According to an earlier study for another series of merocyanine dyes, the low mobility values can be attributed to formation of amorphous thin films, while the fact that some devices did not work on Si/SiO_2 substrates can be explained by the formation of small discontinuous droplet-like regions.[42a] Hence, no percolation pathways are provided for charge carrier transport. On the other hand, devices deposited on TPA modified $Si/SiO_2/AlO_x$ substrates showed much variation of mobility ranges. Devices of dyes **90b**, **99**, **129** and **130** did not show any field effect, while dyes **93, 94** and **95** gave OTFTs with low mobilities in the range of 10^{-4} - 10^{-6} $cm^2\ V^{-1}\ s^{-1}$. Interestingly, dye **91** showed n-type behavior with mobilities about 10^{-3} $cm^2\ V^{-1}\ s^{-1}$. Devices of dyes **96** and **97,** in the contrary, were significantly better than on Si/SiO_2 substrates with values up to 0.08 $cm^2\ V^{-1}\ s^{-1}$ for dye **97**. Likewise, the current on/off ratios were rather low for dyes **94** and **95** with values on the order of 10^2 and rose up to 10^5 for dyes **96** and **97**.

Table 2. Electrical properties of OTFT devices prepared by vacuum deposition and measured in air.

Dye	T_S[a] / °C	μ[b] / $cm^2 V^{-1} s^{-1}$	I_{on}/I_{off}[b] / a.u.	V_{th}[b] / V	SAM
90a	60	$(1.6 \pm 0.1)\cdot10^{-4}$	$1.\cdot10^{3}$	−6	None
90b		No FE			TPA
91	50	$(1.8 \pm 0.8)\cdot10^{-3}$	$2\cdot10^{4}$	+14	TPA
93	20[c]	$(2.5 \pm 0.3)\cdot10^{-4}$	$1\cdot10^{4}$	−8	TPA
94	80	$(3.3 \pm 0.9)\cdot10^{-6}$	$3\cdot10^{2}$	+3	TPA
95	80	$(6.7 \pm 0.5)\cdot10^{-6}$	$6\cdot10^{2}$	+8	TPA
96	80	$(3.2 \pm 0.5)\cdot10^{-2}$	$1\cdot10^{5}$	−5	TPA
97	80	$(7.7 \pm 0.8)\cdot10^{-2}$	$1\cdot10^{5}$	−2	TPA
99	65	$(5.7 \pm 2.5)\cdot10^{-6}$	$3\cdot10^{2}$	−8	FOPA
101		decomposed			
129	20[c]	$(3.2 \pm 0.8)\cdot10^{-6}$	$3\cdot10^{2}$	−8	None
130	20[c]	$(6.5 \pm 0.3)\cdot10^{-5}$	$4\cdot10^{3}$	−6	None

[a] Substrate temperature. [b] Average value of three-to-five randomly picked devices. [c] At elevated temperatures dewetting of the thin films was observed.

When comparing the threshold voltages, it can be seen that the devices based on dyes **91**, **94**, and **95** show positive threshold voltages of +8 V, +3 V and +14 V, respectively, which indicates that the OTFTs are already in the on-state due to trap states, although there is no applied bias voltage. In contrast, devices with higher mobility values (dyes **96** and **97**) feature negative threshold voltages of −5 V and −2 V, respectively, as expected for devices which are in the off-state when no bias voltage is applied. Finally, dye **99**, which did not show any field effect on Si/SiO_2 and TPA modified $Si/SiO_2/AlO_x$ substrates did show poor mobility of $\sim10^{-6}$ cm^2 V^{-1} s^{-1} when processed on FOPA modified $Si/SiO_2/AlO_x$ substrates.

In Figure 23 the AFM measurements of most of the devices fabricated on TPA modified $Si/SiO_2/AlO_x$ substrates are depicted. The fact that devices of dyes **90b**, **99**, **129** and **130** did not show any field effect can be attributed to a dewetting of the substrates. The AFM results of the thin films of dyes **94** and **95** are counterintuitive to the low mobility values of the respective devices since well-defined structures can be seen. Here, one would expect

high mobility values due to crystalline thin films. However, as the nominal thickness of the films is only 30 nm, the films appear to be very rough with height maxima of 300 nm (dye **94**) or even 500 nm (dye **95**).

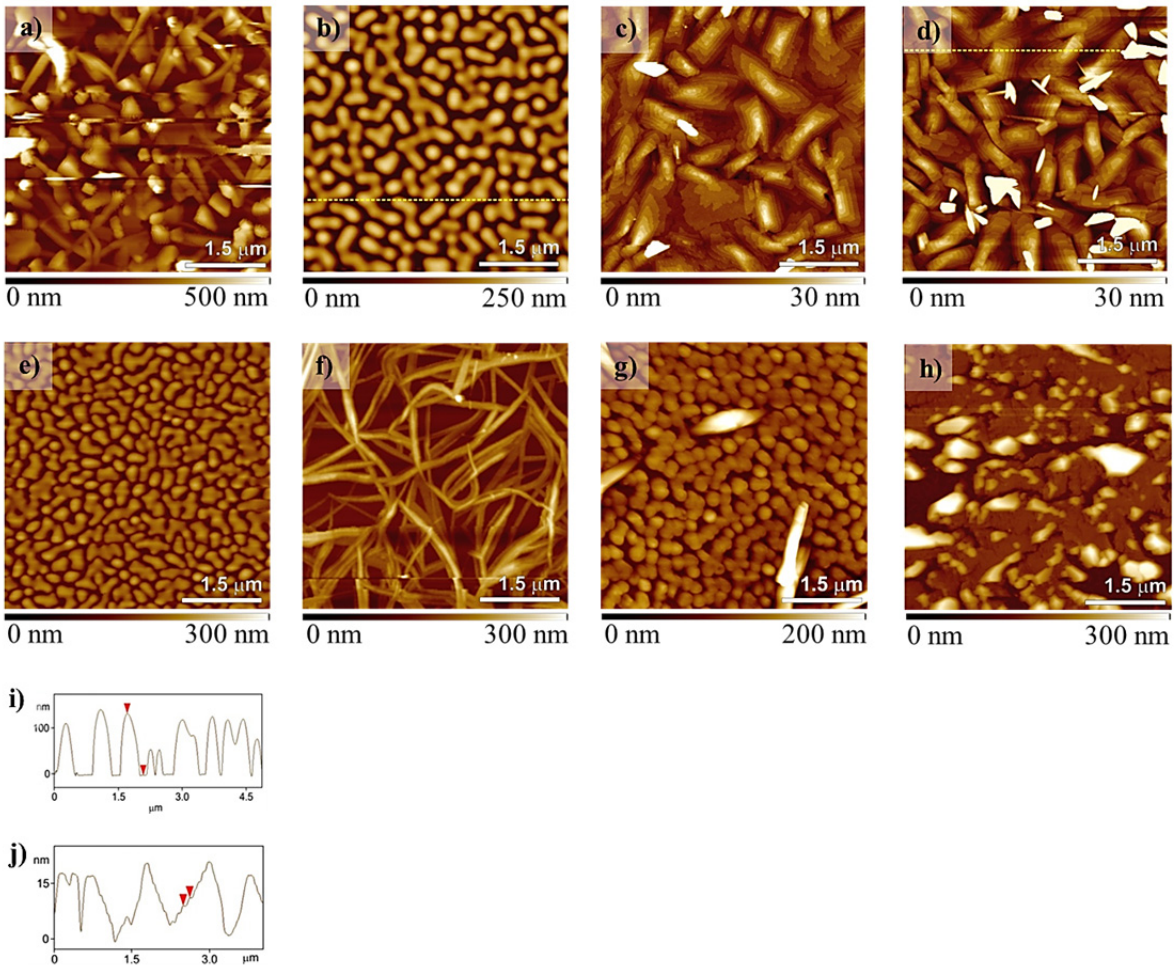

Figure 23. AFM images of thin films of dyes **95** (a), **130** (b), **96** (c), **97** (d), **90b** (e), **94** (f), **99** (g) and **129** (h) on TPA modified $Si/SiO_2/AlO_x$ substrates. The cross sections of the AFM image of **130** (i) and **97** (j) at the position of the dotted yellow line in images (b) and (d) are given as well, indicating the dewetting of the surface for **130** and crystalline, terrace-like growth for **97**, respectively.

The best mobilities were obtained for devices of dyes **96** and **97** with values of $\mu_p = 0.03\ cm^2\ V^{-1}\ s^{-1}$ and $\mu_p = 0.08\ cm^2\ V^{-1}\ s^{-1}$, respectively. The corresponding AFM results show highly crystalline films for both dyes with terrace-like growth. The respective step heights are 2.4 nm for dye **96** and 2.2 nm for dye **97** with grain sizes of about 1 - 2 µm.

Furthermore, XRD experiments were performed for films based on **95** and **97** to estimate their crystallinity. For dye **95** only two diffraction peaks with very low intensity are shown

in the diffraction pattern (Figure 24a). The two peaks of dye **95** films could be attributed to signals of the powder diffraction pattern which was simulated from our single crystal data using the program Mercury.[110] Therefore the AFM and XRD results lead us to the conclusion that the low mobility can be attributed to rough amorphous domains which are not favorable for charge transport.

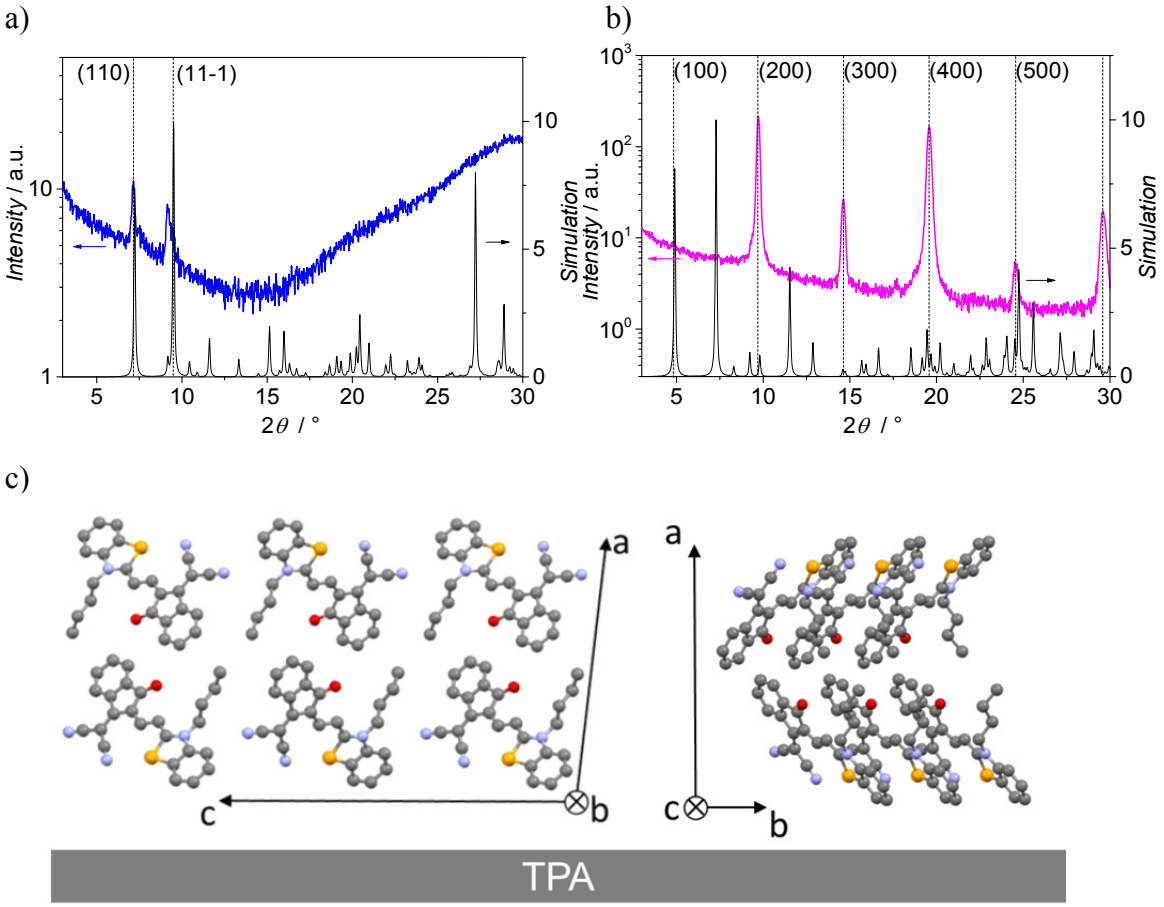

Figure 24. a) X-ray diffractogram (upper blue line) of thin film of **95** on the TPA modified $Si/SiO_2/AlO_x$ substrate and simulated powder spectrum (lower black line) from the crystal structure. b) X-ray diffractogram (upper pink line) of thin film of **97** on the TPA modified $Si/SiO_2/AlO_x$ substrate and simulated powder spectrum (lower black line) from the crystal structure. c) relative orientation of molecules of dye **97** on the TPA modified $Si/SiO_2/AlO_x$ substrate.

On the other hand, the high crystallinity of the films formed by dye **97** has been confirmed with XRD measurements which show many diffraction peaks with high intensity and a sharp line width (Figure 24b). The diffraction peaks correspond to the *h*00 orientation of the simulated powder diffraction pattern. The orientation of the molecules on the TPA modified $Si/SiO_2/AlO_x$ substrate is illustrated in Figure 24. The molecules adopt an edge-on packing with the π-π-stacking direction parallel to the substrate surface.

These studies show that the variation of the heteroatom in the donor part of dyes **95 - 97** and **130** has a pronounced impact on the formation of crystalline films and subsequently on the charge carrier mobility in OTFTs. While for the $C(Me)_2$ group in dye **130** a dewetting of the substrate occurred, its replacement by an oxygen atom in dye **95** lead to the formation of closed films. Unfortunately, these featured only low crystallinity and were therefore not suitable for providing high charge carrier mobilities. Finally, if the $C(Me)_2$ group was replaced by a sulfur or selenium atom (dyes **96** and **97**), smooth crystalline films were formed and high charge carrier mobilities up to $\mu_p = 0.08\ cm^2\ V^{-1}\ s^{-1}$ could be achieved for dye **97**.

3.2.3 Bulk Heterojunction solar cells

The synthesized dyes were tested as donor materials in bulk heterojunction (BHJ) solar cells using C_{60} as acceptor material. Due to the low solubility of the chromophores and in analogy to the OTFT measurements, vacuum-deposition was chosen for solar cell fabrication. This method allows for a better control of the layer thickness and morphology in comparison to solution-processing. The fabricated BHJ solar cells displayed the general architecture ITO/MoO_3 (15 nm)/dye : C_{60} (50 nm, ratio 1:1)/Bphen (6 nm)/Ag (120 nm). Dye **93** showed very low absorption in the solid state; for this reason it was not included in this study. Dye **101**, which decomposed during sublimation, was also not included in this study. The current-voltage (*J-V*) response of the fabricated cells were measured under nitrogen atmosphere and simulated AM 1.5 G irradiation. The corresponding data were averaged over at least ten solar cells, showing a standard deviation below 10 % (Table 3). The open-circuit voltage V_{OC}, which varied in the range of 0.6 - 1.0 V, correlated well with the HOMO energies of the dyes determined by CV measurements (Table 1), in agreement with several recent publications.[111] Since most of the studied dyes have similar absorption profiles and HOMO/LUMO gaps, it is reasonable to expect similar short-circuit currents (J_{SC}). Indeed, for dyes **90a,b** as well as **95 - 97** and **130** J_{SC} values of about 9 mA cm^{-2} were obtained. Dyes **91**, **94**, **99** and **129**, however, showed much lower J_{SC} values. In the case of dyes **91**, **94** and **99** the low J_{SC} might be rationalized by the fact that their low-lying LUMO might hinder efficient charge generation with C_{60} as acceptor material due to the lack of driving force. Only for an offset of at least 0.3 eV,[111b, 112] which is the case for dyes **90a,b**, **95 - 97** and **130** the exciton binding energy can be overcome and the probability of charge separation saturates. On the other hand, the low short-circuit current

of dye **129** devices may be influenced by its less favorable packing arrangement (Figure 20). Indeed, the low order of the zero-dimensional packing adopted by **129** can lead to a high geminate recombination rate and therefore to a strong voltage dependent photocurrent. Furthermore, the larger band-gap of dyes **91** and **129** limits the absorbed photons to higher energies (see Figure 16).

Table 3. Optical parameters for the vacuum deposited blends, as well as main solar cell parameters.

Dye	V_{OC}[a] / V	J_{SC}[a] / mA cm^{-2}	FF[a] / 1	PCE[a] / %
90a	0.86 ± 0.01	10.9 ± 0.5	0.50 ± 0.01	4.7 ± 0.1
90b	0.83 ± 0.01	8.8 ± 0.2	0.46 ± 0.01	3.4 ± 0.1
91	0.85 ± 0.01	0.4 ± 0.1	0.31 ± 0.01	0.1 ± 0.1
94	0.98 ± 0.01	3.4 ± 0.1	0.31 ± 0.01	1.0 ± 0.1
95	0.90 ± 0.01	9.2 ± 0.2	0.45 ± 0.01	3.7 ± 0.1
96	0.90 ± 0.01	8.2 ± 0.5	0.52 ± 0.01	3.7 ± 0.2
97	0.93 ± 0.01	10.0 ± 0.6	0.56 ± 0.03	5.2 ± 0.2
99	0.60 ± 0.01	3.8 ± 0.2	0.35 ± 0.01	0.80 ± 0.1
129	0.87 ± 0.01	3.7 ± 0.2	0.30 ± 0.01	1.0 ± 0.1
130	0.90 ± 0.01	9.0 ± 0.1	0.42 ± 0.01	3.4 ± 0.1

[a] Average values of ten BHJ solar cells.

Moreover, the fill factor (*FF*) ranged from 0.30 to 0.56. The lowest values were obtained for dyes **91**, **94**, **99** and **129** possibly due to amorphous films. Dyes **90a,b**, **95** and **130** showed *FF* in the range 0.42 - 0.50, while **96** and **97** displayed the highest *FF* of 0.52 and 0.56, respectively. Since OTFTs are based on neat films and OSCs in bulk heterojunctions we can assume that the morphologies in both device structures are significantly different. Nevertheless, the correlation between high mobility in OTFT devices fabricated with **96** and **97** and the remarkably good fill factors achieved for these dyes compared to other merocyanine dye BHJ cells are striking and indicative for related dye arrangements in both types of devices, leading to favorable charge transport properties within the donor phase. This implies a more balanced transport of electrons and holes in the solar cells thus leading to higher *FF*s.

Summarizing, on the one hand dyes **91**, **94, 99** and **129** gave BHJ solar cells with poor efficiency. This is mainly attributed to unsuitable energy levels, which either did not provide the necessary driving force for exciton dissociation (dyes **91, 94** and **99**) or suffered from high energy losses while limiting absorption to higher photon energies (dyes **91** and **129**). On the other hand, dyes **90a,b**, **95 - 97** and **130**, which displayed ideally placed energy levels, showed satisfactory performances. In particular selenium-containing dye **97** provided the best combination of absorption properties and supramolecular ordering, thus affording the best power-conversion efficiency *(PCE*) of this series, 5.2 %.

Taking advantage of our OTFT results on molecular structure, packing and mobility, a cell optimization could be performed for the OSC based on dye **97** by introducing neat contact layers of the corresponding donor and acceptor materials above and below the active layer (mixed heterojunction, MHJ). Finally, a postproduction thermal treatment was performed. The fabricated cell displays the following architecture: ITO/MoO_3 (15 nm)/**97** (3 nm)/**97**:C_{60} (50 nm, ratio 1:1)/C_{60} (5 nm)/Bphen (6 nm)/Ag (120 nm). For comparison a planar heterojunction solar cell (PHJ) with the structure ITO/MoO_3 (15 nm)/**97** (10 nm)/C_{60} (30 nm)/Bphen (6 nm)/Ag (120 nm) was fabricated. The *J-V* characteristics of MHJ, PHJ as well as the reference BHJ devices are listed in Table 4.

Table 4. Solar cell characteristics of the standard BHJ solar cell compared with PHJ and MHJ solar cells based on dye **97**, measured under simulated AM 1.5 G irradiation.

Device	Processing	V_{OC}[a] / V	J_{SC}[a] / mA cm^{-2}	FF[a] / 1	PCE[a] / %
BHJ	as grown	0.92	9.8	0.58	5.2
PHJ	as grown	0.98	4.9	0.49	2.2
	post annealing (2 min @ 130 °C)	0.30	4.7	0.49	0.7
MHJ	as grown	0.92	12.0	0.51	5.6
	post annealing (2 min @ 130 °C)	0.93	11.7	0.57	6.2

[a] Values obtained for a solar cell of each type. “As grown” cells were deposited by sublimation on a substrate held at room temperature. The solar cell parameters were measured once before and after annealing at 130 °C for 2 min.

The reference BHJ solar cell, described above, displayed a *PCE* of 5.2 %. The PHJ solar cell on the other hand showed a *PCE* of 2.2 %. The introduction of donor and acceptor neat layers on both sides of the BHJ active layer, led to an improvement of performance to 5.6 % due to an enhancement of J_{SC}.

The neat and thermally annealed film of dye **97** in optimized MHJ solar cells has two functions: First, contact of the electron acceptor C_{60} with the hole collecting MoO_3 layer is avoided, which reduces surface recombination. Second, the transport of charge carriers to the hole collection contact is accelerated. As a result, the MHJ solar cell shows an enhancement in *PCE* in comparison to the reference BHJ solar cell, by only introducing 3 nm of selenium-containing dye **97.** The "as grown" MHJ showed an increased J_{SC} but a lower *FF* in comparison to the reference BHJ solar cell. In our previous studies on BHJ solar cells post-production thermal annealing had no influence on cell performance.[113] However, the investigation of OTFTs with dye **97** described above and previous studies of annealing on the performance of PHJ devices[41] suggested applying post-production annealing to the MHJ device in order to recover the *FF*. Similar improvement in solar cell performance of other small molecule donor materials as a consequence of thermally favored solid state packing has been reported.[114] After an annealing procedure of 2 min at 130 °C on a hot plate, the MHJ displayed still a very high J_{SC}, plus an improved *FF* which equals the reference BHJ cell, thus leading to an overall improvement of performance to 6.2 %.

The impact of thermal annealing in the optimized MHJ solar cell based on **97** has been analyzed in detail. For this purpose, grazing incidence X-ray diffraction as well as ellipsometric and AFM measurements were performed. In Figure 25 the grazing incidence X-ray pattern of a neat dye **97** thin film (solid lines) as well as dye **97**:C_{60} blend (dotted lines) deposited on glass substrates before and after annealing are shown. "As-grown" films of both neat dye **97** and dye **97**:C_{60} blend do not show any pronounced features, while annealing at 130 °C for 2 min led to arising of peaks for the neat dye **97** film. Comparing the peaks with the powder pattern simulated from the single crystal data allows to assign them to the (*h*00)-orientation. The slight shift of the measured peak positions compared with the simulated data from the single crystal structure is a consequence of the different temperatures applied for single crystal and thin film measurements as well as a possible tilting of the unit cell with respect to the substrate. Thus, our findings indicate a high degree of order in the neat film.

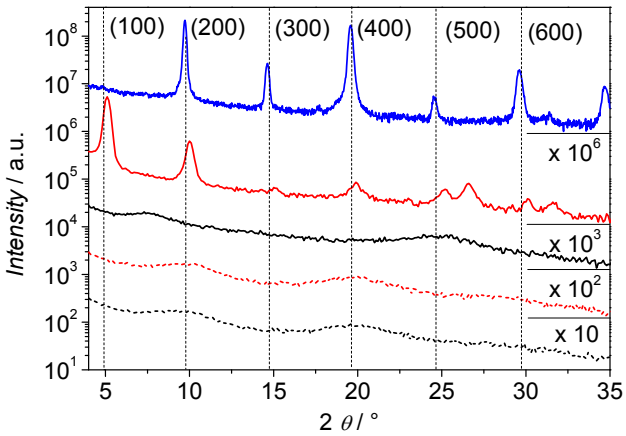

Figure 25. X-ray pattern of a neat thin film of dye **97** (solid lines) and its mixture with C_{60} (dotted lines) on glass substrates before (black) and after thermal annealing (red) at 130 °C for 2 min. For comparison, the X-ray diffractogram of dye **97** deposited on heated $Si/SiO_2/AlO_x$/TPA substrate (blue line) is shown, as well as the reflections corresponding to the (*h*00) orientation.

This is as well supported by AFM measurements (Figure 26). Indeed, thin films of neat **97** clearly gave rise to very crystalline domains of 1 – 2 µm upon annealing, while the blend with C_{60} remained rather amorphous.

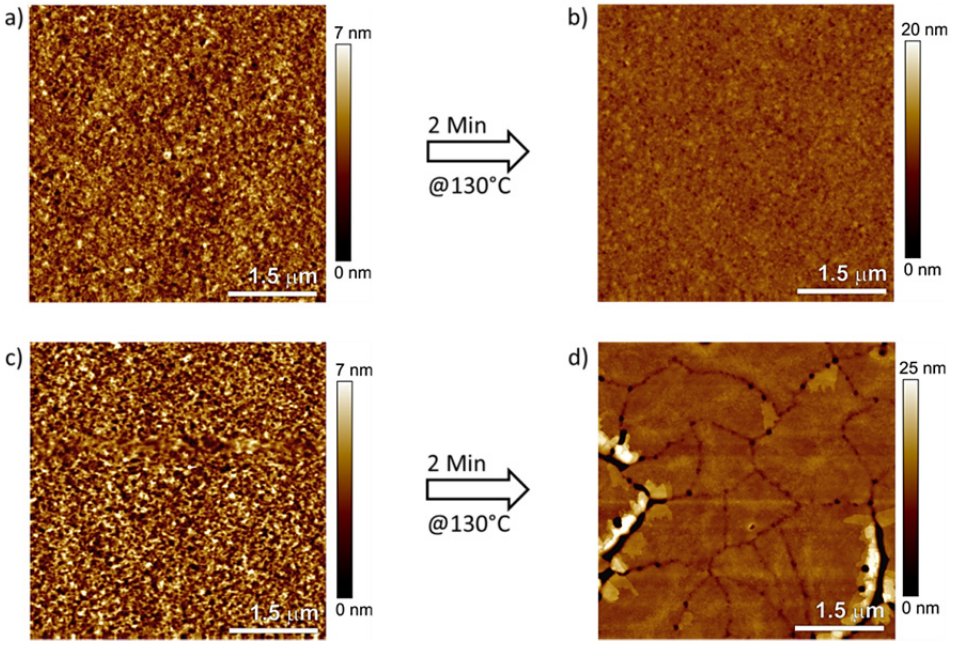

Figure 26. AFM images of thin films of dye **97**:C_{60} blend on ITO substrate before and after annealing at 130 ºC for 2 min (a,b) and AFM images of **97** films on ITO substrate before and after annealing at 130 ºC for 2 min (c,d).

Moreover, the UV-Vis absorption spectrum of the BHJ solar cell based on dye **97** was compared to the spectra of thin films on quartz and reflective $Si/Al/AlO_x$/TPA substrates, as well as with the molecular absorption in solution. For this purpose, thin films were

deposited on transparent quartz in order to obtain amorphous films (high deposition rate and substrate at room temperature) whereas thin films on Si/Al/AlO_x/TPA substrates were fabricated like the films used for OTFT in order to obtain higher crystallinity (low deposition rate and elevated substrate temperature). In Figure 27 the thin film and dichloromethane solution UV-Vis spectra are compared for compounds **95 - 97** and **130**. In the solar cell spectrum, depicted in red, the characteristic absorption of C_{60} at ~350 nm can be observed. Moreover, all solid state spectra feature broader absorption than the corresponding solution spectra. Interestingly, dye **97** shows spectra centered at about 650 nm with remarkably small changes between the neat thin films and the solar cell spectrum.

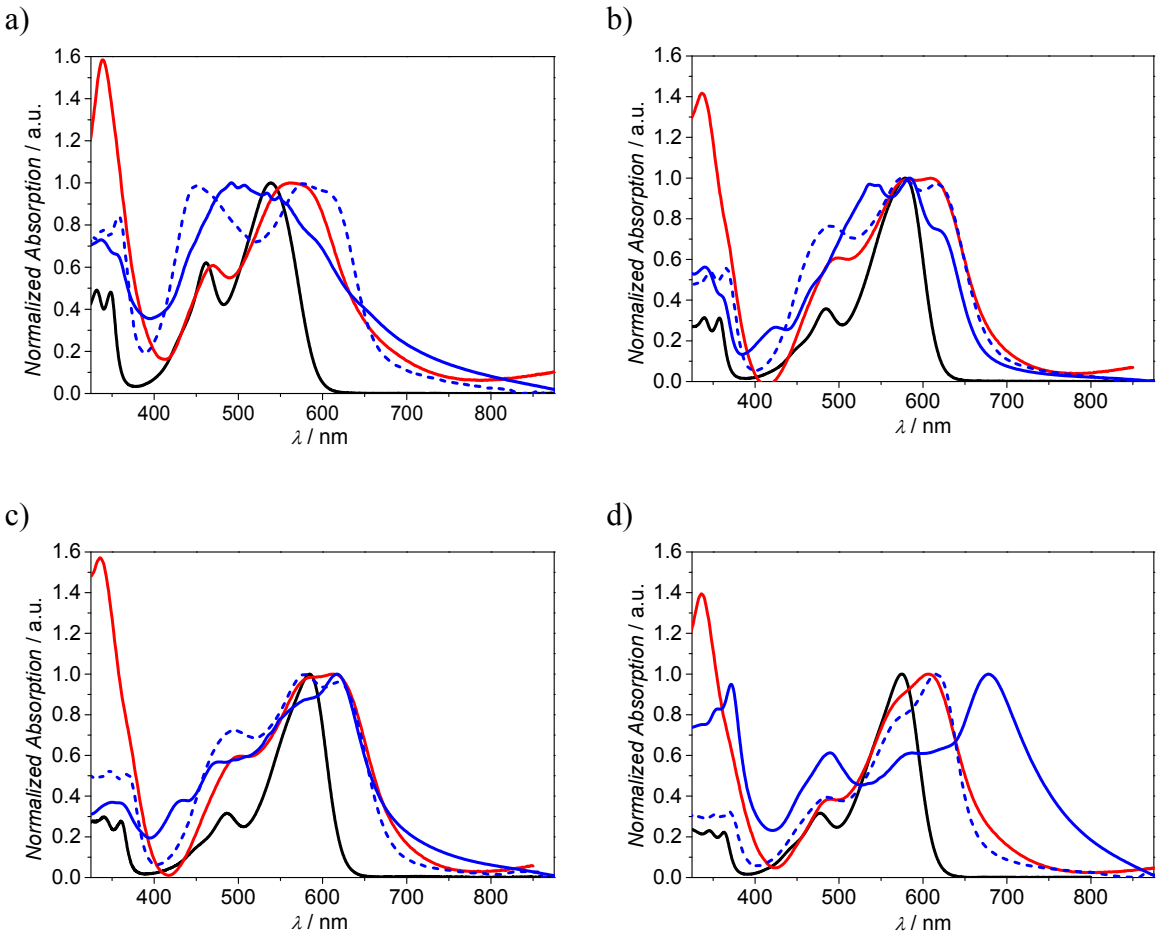

Figure 27. Comparison of UV-Vis spectra in dichloromethane solution ($c \approx 10^{-5}$ M, black line), vacuum-deposited thin film on heated reflective Si/SiO_2/AlO_x/TPA substrate (solid blue line), vacuum-deposited thin film on non-heated quartz (dashed blue line) and the corresponding solar cell (50 % C_{60}, red line) for dyes **95** (a), **96** (b), **97** (c) and **130** (d), respectively.

3.2.4 Discussion

In this section the influence of various parameters ranging from molecular properties to the packing in the solid state on BHJ solar cell efficiency are analyzed. With respect to the molecular properties of the studied dyes we find similar absorption in the 450 – 650 nm region for compounds **90a,b** and **94 - 97**, resulting in similar J_{SC} values. Compounds **99** and **101** show absorption maxima about 650 nm, while compounds **91**, **93** and **129** display blue-shifted absorption at around 500 nm. Moreover, the energy levels of dyes **90a,b**, **95 - 97** and **130** are ideally located with respect to the LUMO level of C_{60}. Accordingly, little variation on V_{OC} values was found for these materials. In the case of dyes **91, 94** and **99** the low-lying LUMO levels may have prevented efficient exciton dissociation into charge carriers, thus reducing the final photocurrent and consequently the solar cell performance. On the other hand, dye **129**, with the largest optical gap, features very high LUMO level, which implies high energy losses by thermalization upon exciton dissociation. Accordingly, based on these results and those from our earlier studies[4a, 27] we can conclude that for the class of merocyanine dyes whose lowest energy transition is attributable to a HOMO-LUMO transition, simple design rules can be applied to tailor the molecular properties for BHJ solar cells. These include an approximately 0.3 eV higher LUMO level of the dye compared to the one of C_{60} and an intense absorption band in the visible range which requires a substitution of the polymethine chain by strong heterocyclic electron donor and acceptor units.

3.2.4.1 Solid state packing analysis & DFT calculations

Molecular properties alone are however not sufficient to achieve high performance OSC and OTFT materials. Not only *FF* and J_{SC} but also V_{OC} is strongly influenced by the morphology, i.e. solid state packing on a supramolecular level.[114a] Merocyanine dyes tend to arrange in an antiparallel fashion due to dominant dipole-dipole interaction.[4a] The dimers formed in this manner are found to show different long range order varying from a higher ordered π-stacked network (group III) to isolated dimers which lack further π-contacts to their neighboring molecules (group I). The reason for adopting one packing or the other has been previously discussed in terms of steric hindrance:[42a] Small substituents allow the molecules to perfectly pack in overlapping dimers with no overall dipole moment. Thus, for the next molecule no electrostatic driving force is provided to direct subsequent antiparallel π-stacking and isolated dimers are therefore more likely to be

formed. This is the case of dye **129** (group I). On the other hand, sterically hindered molecules tend to form more slipped dimers where the acceptor or donor moieties overlap, thus forming a dimer unit which is still slightly polarized and therefore favoring the interaction with the next molecule, which will more likely stack on top of the existing dimer. This is the case of dyes **95** and **130** (group II). Finally, dyes **90a,b**, **96**, and **97** arrange in a so far unprecedented staircase-like pattern of translationally displaced dyes were the dipole moments are not balanced within the π-stack (group III). Accordingly, the parallel slipped π-stack of closest neighbors builds up a macrodipole that is only balanced by the neighbor staircase stacks that are oriented in the opposite direction. The fact that four dyes, all with good performance in BHJ solar cells, arrange similarly in such an unusual packing motif is indeed striking.

DFT calculations were performed in order to visualize the electrostatic surface potential of the isolated monomers of **95** and **97**, as well as the different packing arrangements found in the crystal structure (Figure 28). For this purpose, the geometry of the molecules was taken from the single crystal structure and a single point energy optimization (B3-LYP 6-31G(d), Gaussian)[115] was performed.

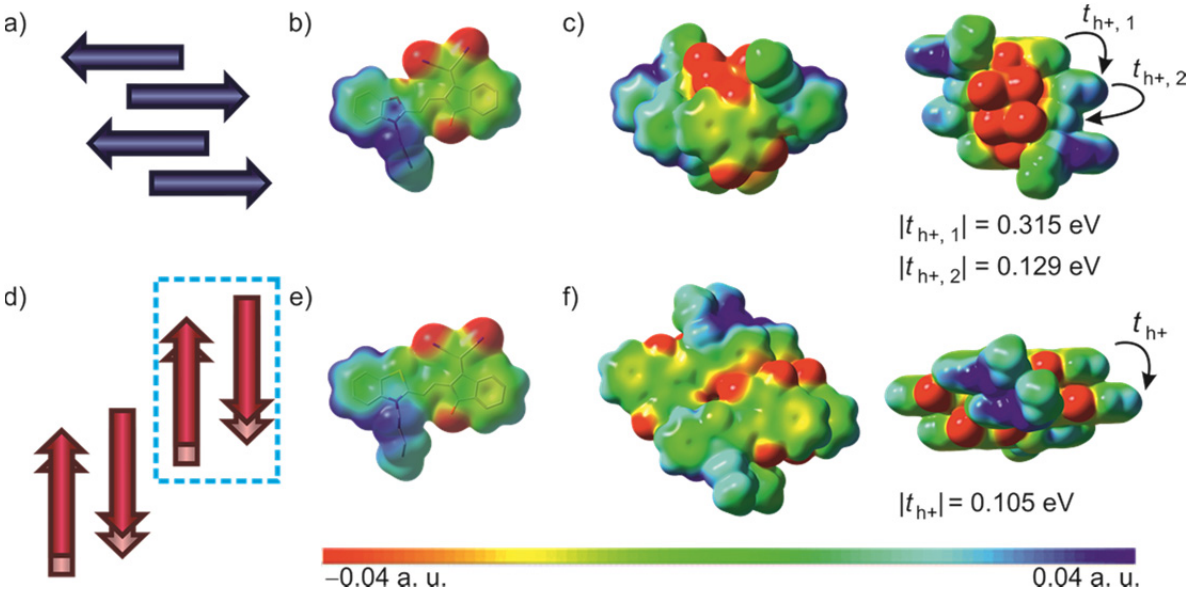

Figure 28. Schematic representation of π-stack of dye **95** (a) and staircase-like arrangement of dye **97** (d) in the crystal indicating the orientation of the dipole moments (arrows). The corresponding electrostatic surface potential of the monomer as well as the stack (left: front view, right: side view) calculated from the crystal geometry taking an isovalue of 0.01 is depicted for dyes **95** (b, c) and **97** e, f). For **97** the stair-stair arrangement contained in the blue rectangle (d) was taken for the calculations. The values of the calculated charge transfer integrals are depicted as well (c, f).

For dye **95** (Figure 28a-c) the stacking of the molecules creates a polarized ensemble with higher electron density in the center, where the acceptor groups are placed on top of each other, while lower electron density is found in the sides. On the other hand, compound **97** (Figure 28d-f) presents two relative stair-stair arrangements (Figure 28d). The smallest longitudinal displacement between stairs is given for the arrangement where the alkyl chains are oriented to the outer side (blue rectangle in Figure 28d). In this arrangement each donor unit is facing an acceptor unit, which results in a less polarized system than the isolated monomer. This antiparallel arrangement of the stairs ensures thus the overall neutrality of the crystal (stair-dimer).

Since selenium is known to have a strong Lewis acidic character and its interactions with halogen and nitrile groups have been previously reported,[71, 116] it seems reasonable to explain the adopted packing structure by CN-Se electrostatic interactions.[71] The electrostatic potential surface in Figure 28f shows indeed a reddish area at the selenium position near the nitrile group, thus suggesting that there is some electronic density lying on the Se atom. This is supported by the small intermolecular N-Se distance (3.60 Å) found in the crystal.

The charge transfer integrals for the close and distant neighbors of **95** as well as for the staircase arranged dye **97** have been calculated and are depicted in Figure 28c,f. The calculations show very balanced charge transport for dye **97** within the staircase stack. Moreover, dye **95** displayed even higher transfer integral values for the close dimer ($t_{h+,1}$) and similar values for the far dimer ($t_{h+,2}$). This is however not reflected by field-effect transistor measurements. Close inspection of AFM image of **95** in Figure 23a offers a clue to this apparent discrepancy. The irregular growth of the films gives rise to a large number of grain boundaries with amorphous regions connecting them. Thus, the charge carrier mobility of films based on dye **95** is rather limited by these defects. Indeed, transistor devices which are composed of a neat layer of organic material are extremely sensitive to molecular ordering.[117] This is in agreement with theoretical calculations of charge transfer integrals in oligoacenes and rubrene, which are prototypical examples of OTFT materials and crystalize in a herringbone arrangement.[118] The slight displacement of co-facial rubrene dimers increases the charge transfer integrals leading to a higher mobility. It is thus quite evident to relate the high mobility of 0.03 $cm^2 V^{-1} s^{-1}$ and 0.08 $cm^2 V^{-1} s^{-1}$ of dyes **96** and **97**, respectively, to the particular arrangement in the crystal.

3.2.4.2 Effect of solid state packing on solar cell performance

In BHJ solar cell devices crystallinity and orientation of the dyes influence all performance parameters such as V_{OC}, J_{SC} and *FF*. However, mixing donor and acceptor materials in the blend reduces the overall ordering of the active layer as well as the domain size. It is therefore not straight forward to predict the effect of ordering on V_{OC}.[119] A good estimate of V_{OC} for the active layer in the BHJ is the difference between the HOMO level of the donor material and the LUMO level of the acceptor material. It is therefore not surprising that solar cells based on dyes **90a,b**, **95 - 97** and **130** show similar V_{OC}. Based on this simple estimate V_{OC} of dyes **97** and **99** are expected to be similar, however they differ by 0.3 V pointing to the importance of supramolecular order and morphology.[120] Dyes **90a**, **95**, **96** and **97** display, in the blend with C_{60}, the highest absorption in films of equal thickness within this series. The differences with respect to absorption in solution might be due to polarization as well as to exciton coupling effects in the solid state. The high absorption of dyes **90a**, **95** and **97**, together with the favorable calculated charge transfer integrals correlate well with the J_{SC} values found for the corresponding solar cells, the highest of this series. Dye **90a**, which shows the highest J_{SC} of the series, suffers however from lower V_{OC} than **95** and **97**, remaining thus the second best solar cell behind dye **97** despite its high absorption. Since *FF* is influenced by charge generation and recombination, it benefits most from a proper supramolecular order and crystallinity as well as from a high mobility, which have demonstrated to be superior for dye **97**.

Since the AFM images (Figure 23) and X-ray analyses (Figure 24) of thin films on TPA modified $Si/SiO_2/AlO_x$ substrates clearly showed crystalline terrace-like growth of the dyes, we can assume that the corresponding absorption spectrum has the signature of highly ordered molecules with a packing arrangement that is similar to the one in the single crystal (although with smaller domain size and more disorder). The thin film spectra showed in all cases a characteristic red-shifted band with respect to the solution spectrum. Such a bathochromic shift in the absorption peak can be attributed to *J*-type coupling between the closely π-stacked dyes, in accordance to the packing arrangement in the single crystal, i.e. staircase stack slip of $\theta < 50°$.[76b] Whilst recent research indicates that high exciton mobilities may also be possible for other arrangements of π-stacked dyes, e.g. even some *H*-aggregates,[121] *J*-aggregation is still considered to enable the largest exciton mobilities and the least undesired non-radiative deactivation channels.[122]

For this reason it is worth to emphasize the similarity of all thin film spectra shown for dye **97** in Figure 27d because they indicate the presence of similar local contacts between slipped stacked merocyanine **97** chromophores in neat films and in BHJ devices. This was notably not the case for most of the other dyes of the given series (Figure 27a-c) which suggests that these dyes exhibit a less unequivocal preference for a particular arrangement. Accordingly domains composed of different dye arrangements may co-exist and their ratio may depend on the deposition parameters, interactions with the used substrate and the presence of fullerene C_{60}.

In summary, in this chapter a series of structurally related D-A merocyanine dyes bearing an indanedione or malononitrile-indanedione acceptor moiety linked to different donor units has been presented. On the molecular level most chromophores display similar absorption properties in the 450 - 650 nm range and favorable FMO levels which would provide enough driving force for the exciton dissociation at the donor/acceptor interface of BHJ solar cells. Moreover, on the supramolecular level the reported chromophores were found to arrange in three different packing motifs: isolated antiparallel dimers (group I), one-dimensional π-stacks of antiparallel dimeric units (group II) and staircase-like slipped parallel π-stacks (group III). The latter packing arrangement was found to provide the best hole mobilities in thin film transistor devices, where dye **97** reached up to $\mu_p = 0.08\ cm^2\ V^{-1}\ s^{-1}$.

With respect to BHJ solar cell devices, a number of dyes displayed power-conversion efficiencies higher than 3.0 %. The best devices were fabricated with the selenium containing dye **97**, which reached a *PCE* of 5.2 %. The superiority of dye **97** devices has been attributed to the slipped π-stacking packing motif (group III), the *J*-type coupling with very high absorption displayed in the blend with C_{60}, together with the higher polarizability of selenium and the high charge carrier mobility found in OTFT devices. Moreover, an optimization of the solar cells based on selenium containing merocyanine dye **97** and C_{60} was performed by addition of of neat donor and acceptor films above and below the active layer as well as post-processing annealing, which lead to a *PCE* of 6.2 %.

3.3 Tuning the Energy Levels of Merocyanine Dyes

Merocyanine dyes have demonstrated to be useful donor counterparts to fullerene acceptor materials in organic solar cells.[4] This push-pull chromophores are characterized by very high extinction coefficients and tunable absorption properties through careful design of their electron-donating and electron-withdrawing moieties. Thanks to their small size and thermal stability these molecules usually allow for vacuum-processing techniques, thus appearing interesting as short-wavelength absorbing materials for highly developed tandem devices in combination with long-wavelength absorbing dyes such as ZnPc.[35]

In the search for dyes absorbing in the ~500 nm range for tandem applications several chromophores with outstanding absorption properties have been identified. However, the energy levels of merocyanine dyes absorbing in this region are usually much higher than the LUMO levels of the fullerene derivatives used as acceptor materials. Ideally, an offset of at least 0.3 eV should be provided between the LUMO levels of the donor and acceptor materials in order to have an efficient charge transfer between those at the donor/acceptor interface of solar cells.[6b] Thus, larger offsets will lead to energy losses upon exciton dissociation. In order to reduce these energy losses, the LUMO levels of short-wavelength absorbing merocyanine dyes should be lowered. Common methods for lowering the FMO levels without disturbing the absorption properties are the introduction of electron-withdrawing groups in the molecular structure such as fluorine,[123] chlorine or nitrile.[124] Studies comparing the effect of chlorine vs. fluorine substitution in organic semiconductors have determined that the LUMO level is more efficiently lowered via chlorine substitution in spite of the higher electronegativity of fluorine.[48, 125] This has been attributed to the fact that chlorine possesses unoccupied 3d orbitals, which would easily accommodate delocalized π-electrons, which is not possible for fluorine. This appears to be an advantage since chlorinated precursors are usually commercially available, which is not the case for the fluorinated ones. Within the LOTsE project a series of merocyanine dyes have been synthesized where the electron-withdrawing indanedione unit has been functionalized with chlorine and bromine atoms. The actual lowering of the energy levels has subsequently been compared with the non-halogenated reference molecules.

3.3.1 Molecular properties

The investigated chromophores, depicted in Chart 18, were obtained by Knoevenagel condensation as described in section 3.1.

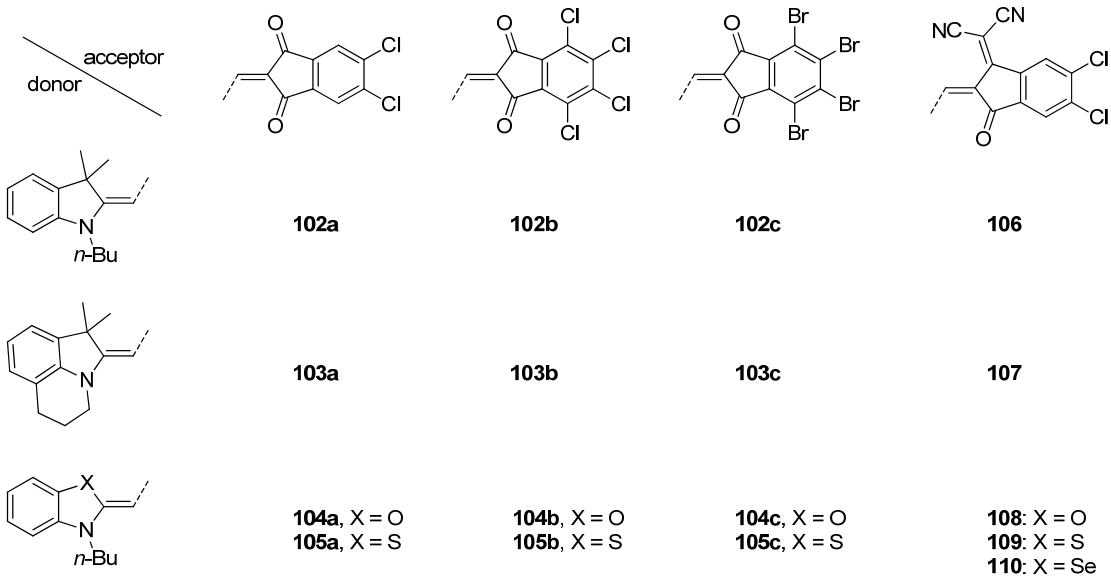

Chart 18. Chemical structure of halogenated indanedione dyes **102-110**.

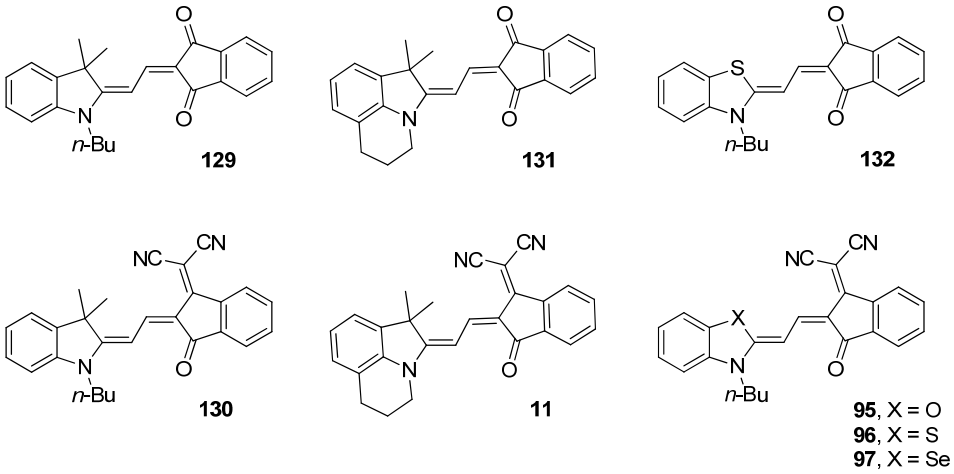

Chart 19. Chemical structure of non-halogenated reference molecules.

The optical properties of the molecules were investigated by means of UV-Vis spectroscopy. Furthermore, the FMO levels were estimated with the help of cyclic voltammetry (CV) measurements. The obtained data were compared with the non-halogenated reference substances depicted in Chart 19. The corresponding spectra and optical data are shown in Figure 29 and Table 5, respectively.

The absorption maxima of 1,3-indanedione derivatives **102 - 105** vary in the range of 482 - 526 nm for all molecules. In comparison with the reference substances, dichlorinated dyes displayed bathochromic shifts about 10 – 12 nm, while tetrachlorinated dyes showed an overall bathochromic shift of 13 – 16 nm. Thus, the introduction of the first two chlorine atoms had the highest impact on the absorption properties. Moreover, replacement of chlorine by bromine (tetrabrominated dyes) further shifted the absorption maxima 3 nm to the red. All dyes showed high extinction coefficients around ~$120 \cdot 10^3$ M^{-1} cm^{-1}. Interestingly, the highest extinction coefficients correspond in all cases to the dichlorinated dyes, probably due to an increment of the transition dipole moment in the direction of the long molecular axis. As expected, the tinctorial strength $\mu^2_{ag} M^{-1}$ decreases as the number of chlorine atoms increases, due to the high mass of the halogens. An exception is found for benzothiazole-containing dyes, where the increase in extinction coefficient for chlorinated dyes is much higher.

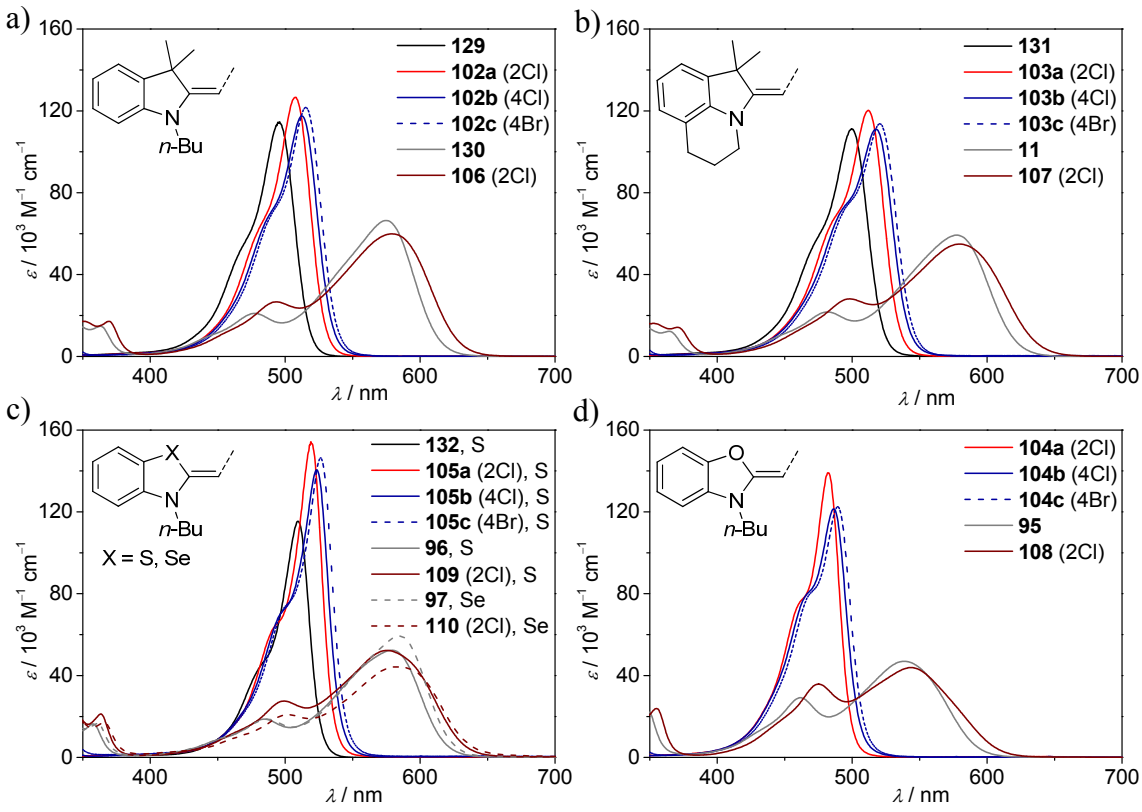

Figure 29. UV-Vis spectra of a) indolenine-containing dyes **129**, **102a** (2Cl), **102b** (4Cl), **102c** (4Br), **130** and **106** (2Cl); b) bridged indolenine-containing dyes **131**, **103a** (2Cl), **103b** (4Cl), **103c** (4Br), **11** and **107** (2Cl); c) benzothiazole-containing dyes **132**, **105a** (2Cl), **105b** (4Cl), **105c** (4Br), **96**, **109** (2Cl) and benzoselenazole-containing dyes **97**, **110** (2Cl); d) benzoxazole-containing dyes **104a** (2Cl), **104b** (4Cl), **104c** (4Br), **95** and **108** (2Cl) ($c \approx 2$ x 10^{-5} M in CH_2Cl_2, 298 K).

On the other hand, dyes containing 2-(3-oxo-2,3-dihydro-1*H*-inden-1-ylidene)malononitrile derivatives **106 - 110** featured absorption maxima around 543 - 581 nm. The absorption bands of these molecules, compared with the reference dyes, are broader and slightly red-shifted (~3 nm). The extinction coefficients remain in the range of 44 - 59·10^3 M^{-1} cm^{-1}, slightly lower than the reference compounds. Interestingly, the selenium-containing compound **110** showed the largest difference with respect to the reference molecule, with a much lower extinction coefficient (45200 vs 60200 M^{-1} cm^{-1}) and a slightly blue-shifted absorption maximum.

Regarding the electrochemical properties of 1,3-indanedione derivatives, the cyclic voltammetry studies reveal irreversible oxidation waves for all compounds. The reference indolenine-containing compounds (**129**, **131**) displayed reversible reduction waves, which were partially maintained for dichlorinated dyes (**102a** and **103a**) and became irreversible for tetrahalogenated dyes. It should be noted that for **102b** reversibility is observed at higher scan rates (500 mV s^{-1}). In the case of benzothiazole-containing dyes reversibility is already lost for the dichlorinated dyes. Interestingly, the bromo-substituted compounds show very intense and broad reduction waves, which suggest that more than one electron is involved. This could be due to decomposition of the molecule to form Br^- anion during the reduction process. With respect to 2-(3-oxo-2,3-dihydro-1*H*-inden-1-ylidene)malononitrile derivatives **106 - 110**, dyes containing indolenine donor moieties featured reversible oxidation and reduction waves independently of the presence of chlorine atoms in their structure. Similarly, benzothiazole and benzoxazole-containing dyes showed in all cases irreversible oxidation waves and reversible reduction waves.

As a general trend, both oxidation and reduction waves are progressively displaced to higher potentials upon increasing the number of halogen atoms in the molecules. However, the effect of halogenation is more pronounced in the reduction than in the oxidation potentials. Concretely, the introduction of two chlorine atoms leads to ca. 0.07 V shifts of oxidation potentials, and a ca. 0.12 V shift of reduction potentials with respect to the non-halogenated dyes. Introduction of four chlorine atoms leads to shifts around 0.11 - 0.15 V for oxidation and around 0.12 - 0.18 V for reduction potentials respect to the non-halogenated dyes. Similarly, 2-(3-oxo-2,3-dihydro-1*H*-inden-1-ylidene)malononitrile derivatives featured a shift of oxidation and reduction potentials to higher voltages. The

oxidation potentials are shifted about 0.06 - 0.09 V and reduction potentials about 0.11 - 0.16 V with respect to the non-halogenated analogues.

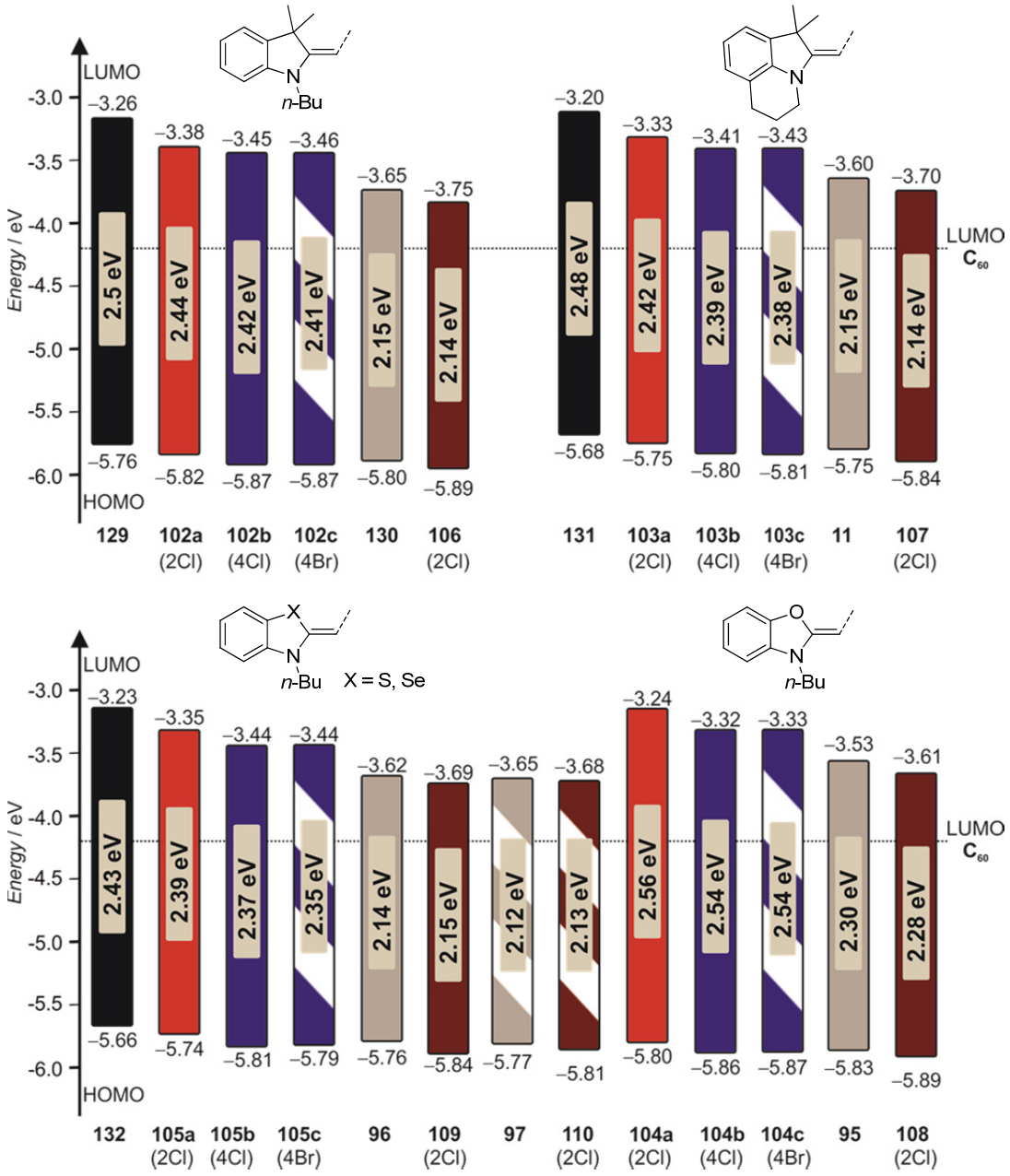

Figure 30. Schematic representation of the HOMO and LUMO levels of the dyes **102 – 110** and their non halogenated reference dyes distributed according to their donor unit and compared to the LUMO level of the most frequently used fullerene acceptor material C_{60}.

The comparison between the electrochemical gap, determined from the redox potentials, and the optical gap, determined from the UV-Vis absorption maxima gave a variation of at most 0.12 eV for the ensemble of the dyes. If only the chlorinated dyes are taken into account to avoid the large irreversible reduction waves characteristic for the decomposition

of brominated compounds, the variation is reduced to at most 0.07 eV. This implies that the $S_0 \rightarrow S_1$ transition observed in the UV-Vis spectra corresponds well to an electronic excitation from the HOMO to the LUMO level, thus allowing for the estimation of the FMO levels from CV using a Fc/Fc^+ value of −5.15 eV[106] vs. vacuum and the optical gap. The estimated FMO levels are shown in Figure 30, together with the LUMO level of the most commonly used fullerene acceptor material C_{60}. Furthermore, in Figure 31 the variation of the FMO levels with the halogen substitution on the acceptor unit is illustrated for each donor moiety. As indicated by the red lines (data roughly fitted for the bridged indolenine donor derivatives) the LUMO levels showed a more pronounced decrease upon increasing the number of electron withdrawing functions than the HOMO levels.

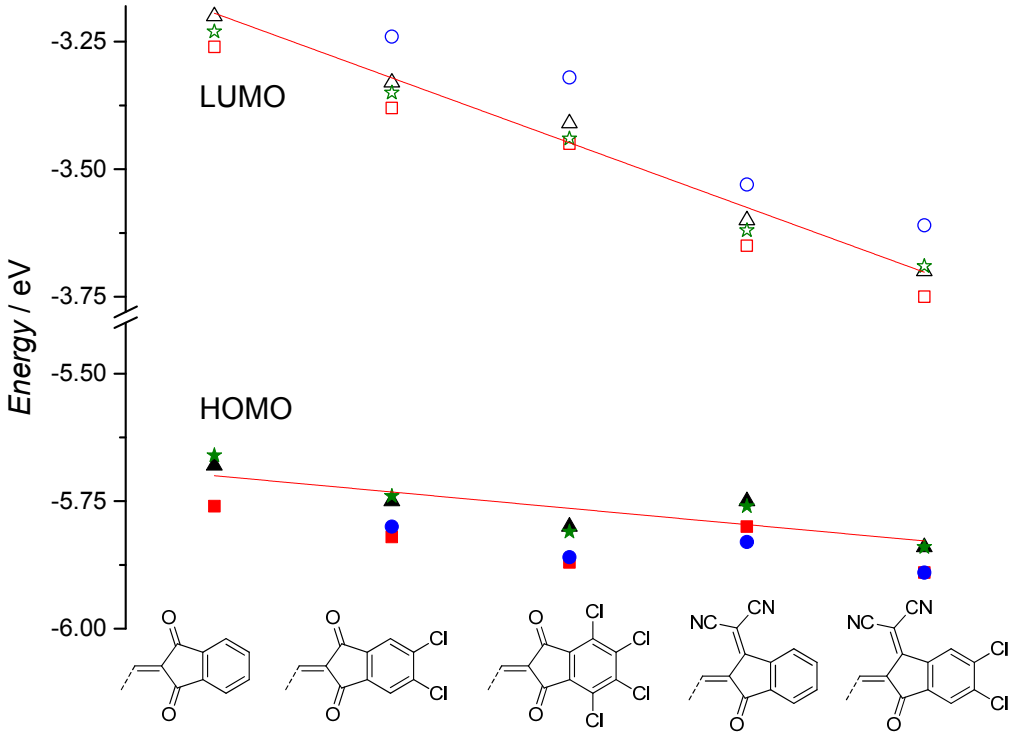

Figure 31. Dependence of the LUMO (open symbols) and HOMO (filled symbols) levels on the acceptor unit substitution for the following donor moieties: indolenine (red squares), bridged indolenine (black triangles), benzothiazole (green stars) and benzoxazole (blue circles).

Table 5: Optical and electrochemical properties of compounds **102 – 110** and their non halogenated reference dyes, extracted from the UV-Vis and CV measurements.

Dye	λ_{max}[a] (nm)	ε_{max}[a] (M^{-1} cm^{-1})	μ^2_{ag} (D^2)	$\mu^2_{ag} M^{-1}$ (D^2 mol g^{-1})	E_{ox}[b] (V)	E_{red}[b] (V)
129	496	114600	95	0.26	0.61*	−1.91
102a (2Cl)	508	125800	105	0.24	0.67*	−1.79
102b (4Cl)	512	117500	105	0.21	0.72*	−1.73
102c (4Br)	515	121700	108	0.16	0.72*	−1.78*
131	500	110700	95	0.27	0.53*	−1.93
103a (2Cl)	512	112300	107	0.25	0.60*	−1.81
103b (4Cl)	517	111700	108	0.22	0.65*	−1.81*
103c (4Br)	520	111800	110	0.16	0.66*	−1.84*
132	509	115400	77	0.21	0.51*	−1.88
105a (2Cl)	519	154200	108	0.25	0.59*	−1.79*
105b (4Cl)	523	141100	108	0.22	0.66*	−1.73*
105c (4Br)	526	144800	114	0.17	0.64*	−1.75*
104a (2Cl)	482	139400	104	0.25	0.66*	−1.92*
104b (4Cl)	486	120150	106	0.22	0.72*	−1.82*
104c (4Br)	489	123200	107	0.16	0.72*	−1.79*
130	575	66400	99	0.24	0.65	−1.52
106 (2Cl)	578	59700	104	0.21	0.74	−1.41
11	577	60300	98	0.24	0.60	−1.55
107 (2Cl)	579	54600	103	0.22	0.69	−1.43
96	578	52400	82	0.20	0.61*	−1.58
109 (2Cl)	575	53100	99	0.21	0.69*	−1.42
97	584	60200	89	0.20	0.63*	−1.57*
110 (2Cl)	581	45200	85	0.16	0.66*	−1.48*
95	539	46100	86	0.22	0.68*	−1.61
108 (2Cl)	543	44450	96	0.21	0.74*	−1.48

[a] UV-Vis: CH_2Cl_2, $c \approx 10^{-5}$ M, 298 K; [b] CV in CH_2Cl_2, $c \approx 10^{-4}$ M, using Fc/Fc^+ as internal reference and $N^tBu_4PF_6$ as electrolyte. * Peak potential of irreversible redox process.

3.3.2 OTFT devices*

In order to estimate the effect of halogen substitution in charge carrier mobility, thin-film transistors were fabricated with representative dyes. The transistors were fabricated by vacuum evaporation in a bottom-gate-top-contact configuration using different self-assembled monolayers (SAM) as substrate. The substrate temperature was varied in order to favor crystallinity of the deposited films. All dyes showed poor mobilities in the range $\mu_p \approx 10^{-5}$ - 10^{-6} cm^2 V^{-1} s^{-1} for devices built on Si/SiO_2 substrates. This can be possibly attributed to the formation of amorphous thin-films or dewetting of the substrates. Furthermore, most of the dyes showed the highest charge carrier mobilities when processed on top of FOPA modified Si/SiO_2/AlO_x substrates. The data of the devices fabricated on FOPA modified Si/SiO_2/AlO_x substrates are listed in Table 6. Representative transfer curves of devices based on **105a** and **109** are depicted in Figure 32.

Table 6. Electrical properties of OTFT devices prepared on FOPA modified Si/SiO_2/AlO_x substrates by vacuum deposition and measured in air.

Dye	T_S[a] / °C	μ[b] / cm^2 V^{-1} s^{-1}	I_{on}/I_{off}[b] / a.u.	V_{th}[b] / V
102a	50	No FE		
103a	50	No FE		
104a	60	$(9.3 \pm 0.9)\cdot10^{-3}$	$1\cdot10^5$	-5
105a	60	$(1.8 \pm 0.2)\cdot10^{-2}$	$2\cdot10^6$	-8
105b	70	$(1.6 \pm 0.2)\cdot10^{-6}$	$2\cdot10^3$	−11
105c	70	$(1.8 \pm 0.3)\cdot10^{-6}$	$4\cdot10^3$	4
109	80	$(4.4 \pm 0.9)\cdot10^{-2}$	$2\cdot10^7$	-8
110	80	$(1.5 \pm 0.2)\cdot10^{-2}$	$2\cdot10^5$	-13

[a] Substrate temperature. [b] Average value of five randomly picked devices.

The above described devices can be analyzed in two groups. On one hand, the influence of the halogen substitution for a given molecular structure can be compared. In this regard, dichlorinated dyes containing sulfur and selenium heteroatoms featured charge carrier mobilities about 10^{-2} cm^2 V^{-1} s^{-1} on FOPA modified Si/SiO_2/AlO_x substrates. Indeed, dye

* The transistor devices reported in this chapter were fabricated by Stephan Harrer or Astrid Kudzus.

109 showed the highest mobility of this series with $\mu_p = 0.04$ cm^2 V^{-1} s^{-1}. Furthermore, derivatives based on **132** showed the highest mobility for the dichlorinated compound **105a**, with $\mu_p = 0.02$ cm^2 V^{-1} s^{-1}. Increasing the number of halogen atoms however was found to be detrimental for the charge carrier mobility, which dropped to ca. 10^{-6} cm^2 V^{-1} s^{-1} for dyes **105b** and **105c**. This might be attributed to the bulkiness of four halogen atoms, which would hinder an appropriate packing of the molecules. A direct comparison with the reference molecules is not straight forward since the charge carrier mobility depends on the different SAMs used. Thus, when processed on FOPA modified $Si/SiO_2/AlO_x$ substrates dichlorinated dyes demonstrated to be superior to the reference non halogenated compounds. However, when processed on TPA modified $Si/SiO_2/AlO_x$ substrates the halogenated compounds showed much lower mobility or no field-effect at all.

On the other hand, the evolution of charge carrier mobility for a given halogen number through donor group variation reveals that sulfur containing dye **105a** again features the highest mobility, while oxygen containing **104a** suffers from a mobility decrease of one order of magnitude and indolenine derivatives **102a** and **103a** display no field effect at all. This trend is common to all SAMs used.

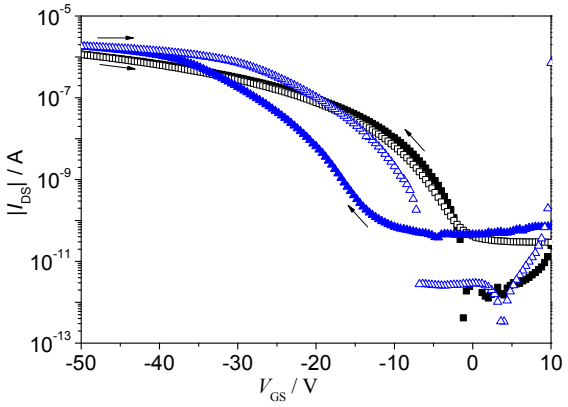

Figure 32. Transfer curves of the OTFTs of dyes **105a** (black) and **109** (blue), on FOPA modified $Si/SiO_2/AlO_x$ substrates with forward (full symbol) and backward (open symbol) measurement cycle.

In summary, new chlorinated and brominated chromophores have been synthesized. The aim the project was the synthesis of thermally stable merocyanine dyes bearing high absorption in the the ~500 nm range as well as lower energy levels in order to avoid energy losses upon exciton dissociation in organic solar cells. The synthesized dyes show high extinction coefficients and a favorable absorption range for application in tandem solar

cells, which is currently pursued in other laboratories. The introduction of halogen atoms has demonstrated to be a useful tool to modify the energy levels of the molecules without much altering their absorption properties. As already described in other studies,[48, 125] halogenation did more effectively decrease the LUMO level than the HOMO level. This provides a better match to fullerene LUMO energy levels. Interestingly, the effect of chlorine atoms was found to be more pronounced for indanedione derivatives than for malononitrile-indanedione derivatives. The resulting decrease of the HOMO levels would imply an increase of V_{OC}, while the lower LUMO levels would reduce the energy losses upon charge transfer to the acceptor material. Indeed, the energy offset of the merocyanines with respect to C_{60} is reduced from ~1 eV to ~0.85 eV for dichlorinated, or ~0.75 eV for tetrachlorinated dyes for 1,3-indanedione derivatives. Malononitrile-indanedione derivatives show even smaller offsets of ~0.5 eV after chlorination, which makes them promising structures for the fabrication of organic solar cells. Moreover, from these series the dichlorinated dyes resulted in higher charge carrier mobilities in the range $\mu_p \approx 10^{-2}$ cm^2 V^{-1} s^{-1}; tetrahalogenated dyes displayed low mobilities probably due to unfavorable packing in the solid state owed to the bulkiness of four halogen atoms. The relatively high mobilities of dichlorinated dyes will be as well advantageous for application in solar cells, where the transport of the charge carriers to the respective electrodes will be favored, thus increasing the fill factor of the devices.

3.4 Characterization of π-extended D-A Merocyanine Dyes

This short chapter is dedicated to the characterization of two kinds of π-extended merocyanine dyes. After the serendipitous discovery of a series of blue side-products during reactions aiming at compounds **102b,c** and **103b,c**, efforts were put on the elucidation of the structures of these blue side-products, as described in section 3.1. The formation of the side-products was subsequently attributed to the presence of a modified acceptor building block resulting from the condensation of a 1,3-indanedione derivative with acetone during recrystallization. Because this reaction pathway to π-extended merocyanine dyes had not been reported before, test reactions were performed to confirm the reaction mechanism.

In literature the extension of the polymethine chain of merocyanine dyes is commonly done by Wittig reaction on aldehyde derivatives.[126] Other methods involving acceptor unit extension have as well been published recently. In 2011 Kulinich *et al*. described the synthesis of several dyes bearing different polymethine chain lengths. Some derivatives were prepared by extension of 1,3-indanedione by reaction with DMF.[99] Two years later Hahn *et al*. reported on a large library of merocyanine dyes where the acceptor unit had been functionalized by reaction with 1,1,3,3-tetramethoxypropane.[100] Both methods have demonstrated to be effective for synthesizing π-extended polymethine dyes, however the low solubility of the molecules remains an issue. In this regard, the reaction of C-H active compounds with ketones provides a new synthetic pathway for introducing solubilizing chains in the polymethine chain. This concept was tested using 2-hexanone to afford the respective alkylated and highly soluble merocyanine dyes. Further variation of the ketone would provide a library of chromophores with different solubilizing alkyl chains.

3.4.1 Halogenated blue side-products 102b-2, 102c-2, 103b-2 and 103c-2

The isolated side-products from reactions aiming at compounds **102b,c** and **103b,c** are depicted in Chart 20. The structure of the dyes was elucidated with the help of NMR spectroscopy (^{1}H, ^{13}C, COSY, HSQC and HMBC), mass spectrometry and elemental analysis. The compounds were further characterized by UV-Vis spectroscopy and cyclic voltammetry (for **103b-2**). The corresponding spectra as well as data extracted thereof are shown in Figure 33 and listed in Table 7, respectively.

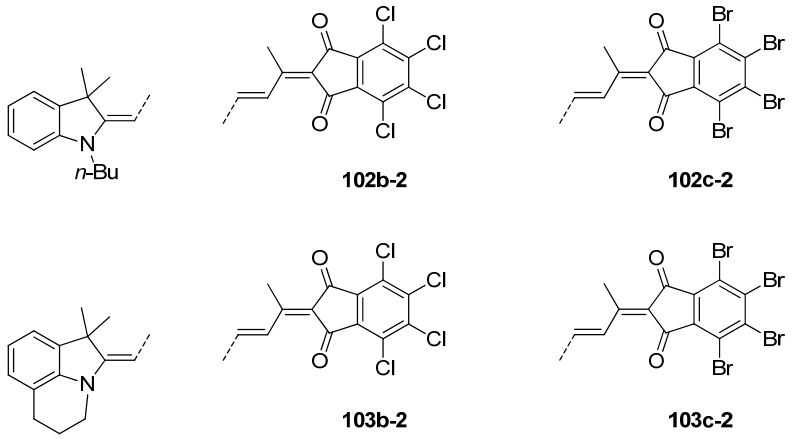

Chart 20. Chemical structure of π-extended side-products isolated from reactions **102b,c** and **103b,c**.

The chromophores display sharp absorption bands centered at ca. 610 – 620 nm and feature very high extinction coefficients reaching up to $200 \cdot 10^3$ M^{-1} cm^{-1}. In comparison to the shorter homologues described in section 3.3, the π-extended chromophores display a 100 nm bathochromic shift of the absorption maxima, as expected for a by one methine unit longer merocyanine dye.

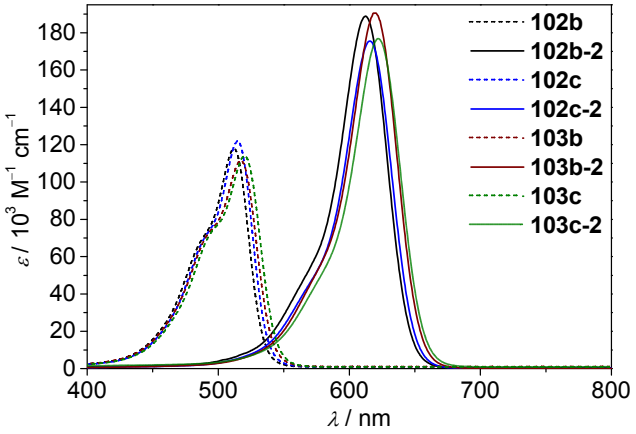

Figure 33. UV-Vis spectra of blue dyes **102b-2**, **102c-2**, **103b-2**, **103c-2** compared to the shorter homologues **102b**, **102c**, **103b** and **103c** ($c \approx 2$ x 10^{-5} M in CH_2Cl_2).

Cyclic voltammetry was measured for compound **103b-2**, showing, similarly to **103b**, one irreversible oxidation wave and one reversible reduction wave. The band gap is reduced with respect to the shorter homologues described in section 3.3 and the LUMO and HOMO levels are situated at approximately -3.43 eV and -5.43 eV, respectively.

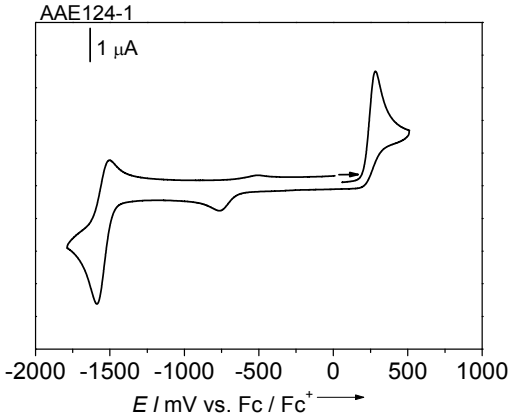

Figure 34. Cyclic voltammetry of compound **103b-2** (2 x 10^{-4} M in CH_2Cl_2).

Table 7. Optical and electrochemical properties of compounds **102b-2**, **102c-2**, **103b-2** and **103c-2**, extracted from the UV-Vis spectra.

Dye	λ_{max} [a] (nm)	ε_{max} [a] (M^{-1} cm^{-1})	μ^2_{ag} (D^2)	μ^2_{ag} M^{-1} (D^2 mol g^{-1})	E_{ox} [b] (V)	E_{red} [b] (V)
102b-2	612	187900	159	0.29		
102c-2	616	175700	147	0.20		
103b-2	619	191400	160	0.30	0.28*	−1.54
103c-2	623	178600	148	0.21		

[a] UV-Vis: CH_2Cl_2, $c \approx 10^{-5}$ M, 298 K; [b] CV in CH_2Cl_2, $c \approx 10^{-4}$ M, using Fc/Fc^+ as internal reference and $N^tBu_4PF_6$ as electrolyte. * Peak potential of irreversible redox process.

3.4.2 π-extended merocyanine dyes bearing solubilizing chains

An advantage of the π-extension of the acceptor unit through condensation with ketones is that there is a great variety of ketones which can be used. Thus, replacing acetone by 2-hexanone led to the formation of an acceptor unit with a butyl chain. The subsequent Knoevenagel condensation of the modified acceptor unit with the corresponding aldehyde or imine led to the formation of dyes **114 - 117** under mild conditions. These compounds showed high solubility even in unpolar solvents such as *n*-hexane. The chemical structure of compounds **114 - 117** are depicted in Chart 21.

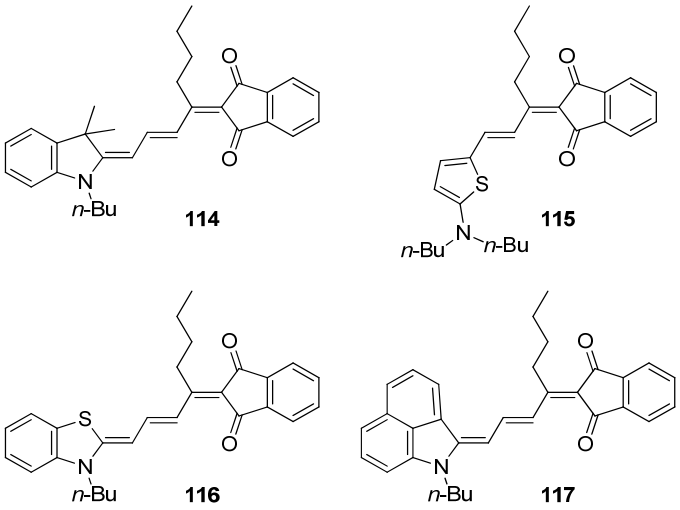

Chart 21. Chemical structure of π-extended dyes synthesized by Knoevenagel condensation.

Characterization of the new chromophores by UV-Vis spectroscopy revealed sharp absorption bands in the range 550 – 650 nm except for dye **117**, which showed much broader absorption up to 750 nm. As expected, a red-shift of about 100 nm with respect to the shorter derivatives is observed. Moreover, EOA measurements in 1,4-dioxane solution were performed for dye **114**, revealing that the π-extended system features a slightly smaller dipole moment than its shorter homologue **129** (3.7 D vs. 3.8 D), as well as a more polyene-like structure ($c^2 = 0.29$, vs. $c^2 = 0.40$ for **129**). The corresponding UV-Vis spectra are depicted in Figure 35 and the optical data are listed in Table 8.

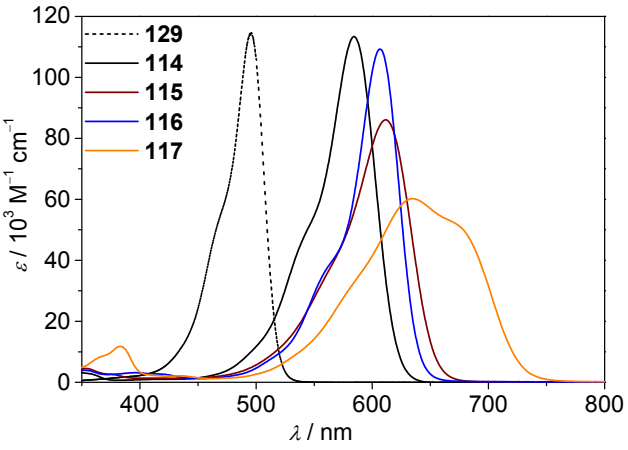

Figure 35. UV-Vis spectra of **114** - **117** and reference dye **129** ($c \approx 2 \times 10^{-5}$ M in CH_2Cl_2).

Table 8. Optical properties of compounds **114** - **117** extracted from the UV-Vis spectra.

	λ_{max} [a] / nm	ε_{max} [a] / M^{-1} cm^{-1}	μ^2_{ag} [a] / D^2	$\mu^2_{ag}M^{-1}$ [a] / D^2 mol g^{-1}
114	584	115900	118	0.26
115	611	85300	102	0.23
116	606	109250	100	0.24
117	635	61200	109	0.23

[a] UV-Vis: CH_2Cl_2, $c \approx 10^{-5}$ M, 298 K.

In summary, in this chapter a series of π-extended merocyanine dyes have been presented. On the one hand, the halogenated dyes which were isolated as side-products from the reactions leading to compounds presented in section 3.3 have been described. On the other hand, the synthesized dyes bearing solubilizing butyl chains were characterized. Most of the chromophores, with exception of dye **117**, displayed absorption bands in the 550 - 650 nm range. Interestingly, halogenated compounds featured sharper and higher absorption than non-halogenated ones. Indeed, non-halogenated dyes displayed extinction coefficients up to ~$120 \cdot 10^3$ M^{-1} cm^{-1}, which is in the range of literature-known π-extended polymethine dyes,[100] whereas halogenated compounds displayed even sharper absorption bands with extinction coefficients reaching up to ~$200 \cdot 10^3$ M^{-1} cm^{-1}. The higher extinction coefficients may be the consequence of larger transition dipole moments due to the electron withdrawing effect of the halogen atoms. For the shorter homologues (section 3.3) such a great difference in the absorption strength was however not observed.

The merocyanine dyes presented in this chapter are interesting materials for application as light-absorbers in organic solar cells. The absorption in the near-infrared region together with the high extinction coefficients displayed by these polymethine dyes seem very promising for the obtention of transparent devices with moderate *PCE*s. The thermal stability of the chromophores is unknown, however the possibility of variation of the alkyl chains makes them suitable for solution-processing, which is a very cheap and straight-forward technique. In this regard, a study of the effect of different alkyl chains in thin film formation and morphology as well as solar cell performance is promising.

3.5 Conformational Switching of π-conjugated Junctions from Merocyanine to Cyanine States by Solvent Polarity*

Because of the exciting perspectives arising for sensing, actuation or other functional properties there is currently a great interest in molecular scaffolds whose properties are strongly governed by conformational changes.[127] Among π-conjugated scaffolds temperature-dependent topology changes between Hückel and Möbius conformations have received particular attention[128] as well as the planarization of V-shaped antiaromatic cyclooctatetraenes (COT) in the reduced or photoexcited state.[129] The latter effect has recently been exploited by Yamaguchi and co-workers to shift the emission wavelength bathochromically by about 100 nm with concomitant color change from blue to green by embedding a COT unit between two anthraceneimides.[130] Accordingly, whilst the special resonance stabilizations of cyclic π-scaffolds attracted lots of attention, another special resonance state given for conjugated chains, i.e. the ideal polymethine state[131] (also called cyanine limit[21b, 109]), received little attention with regard to conformational switching phenomena. This chapter describes the synthesis of an unusual bifurcated π-scaffold which exhibits an unprecedented solvent polarity dependent conformational switching, leading to a shift of the absorption maximum by more than 160 nm.

As described in section 3.1, the conformationally amphoteric dye **118** (Scheme 34) could be synthesized in 28 % yield by double Knoevenagel condensation of one equivalent of the π-extended 5,6-dichloro-2-(propan-2-ylidene)-1*H*-indene-1,3(2*H*)-dione acceptor (A) moiety, which possesses two reactive sites, and two equivalents of 1-butyl-3,3-dimethyl-2-methyleneindolenine carbaldehyde donor (D) derivative. Since the second aldehyde condensation reaction to afford the bifurcated π-system is not sterically favored, high temperatures and the presence of a base were necessary to obtain the desired product in reasonable yield. For comparison, reference merocyanine dye **120** was as well synthesized by condensation of the respective indolenine salt with the π-extended (*E*)-5,6-dichloro-2-(3-methoxyallylidene)-1*H*-indene-1,3(2*H*)-dione. Both dyes were fully characterized by NMR spectroscopy, high resolution mass spectrometry and elemental analysis. The second reference cyanine dye **133** was purchased from commercial sources.

* This chapter has been accepted for publication: A. Arjona-Esteban, M. Stolte, F. Würthner, *Angew. Chem. Int. Ed.* Reference dye **120** was synthesized by Christian Simon.

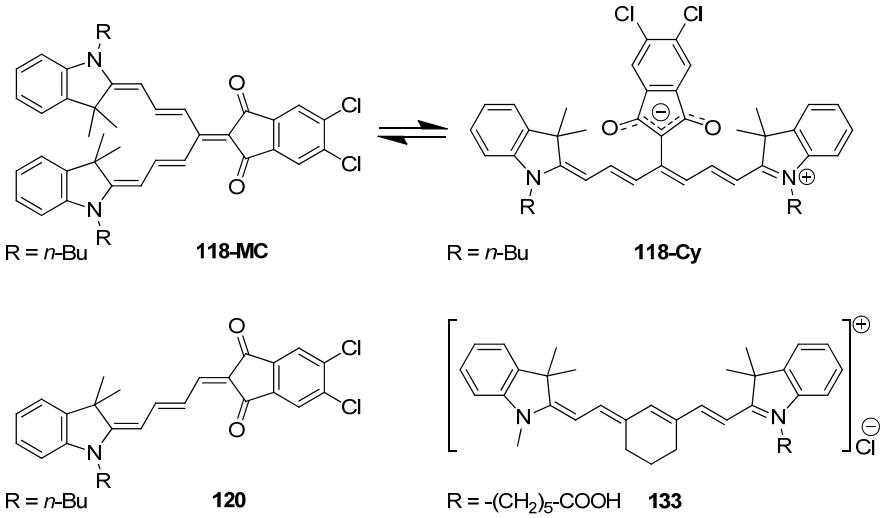

Scheme 34. Conformational equilibrium for dye **118** between merocyanine- and cyanine-type structures as well as chemical structures of reference merocyanine dye **120** and cyanine dye **133**.

3.5.1 UV-Vis & Fluorescence spectroscopy

Figure 36a,b shows the UV-Vis absorption spectra of reference dyes **120** and **133** as well as the bifurcated dye **118** for selected solvents of varying polarity. In unpolar solvents such as methylcyclohexane (MCH) dye **118** features the clear signature of a push-pull chromophore (conformation **118-MC** in Scheme 34) with an intense absorption band at 576 nm and vibronic progressions similar to merocyanine **120**. On the other hand, in polar protic solvents such as methanol the main absorption band of dye **118** is even more intense and located at 748 nm. This strongly red-shifted band of high intensity is typical for cyanine dyes with the same polymethine chain length as suggested by structure **118-Cy**,[132] as demonstrated in Figure 36a by comparison with reference cyanine **133.** In solvents of intermediate polarity such as dichloromethane or trichloromethane a broad and unstructured band is observed that is still centered at 585 nm (**118-MC**) but exhibits a shoulder above 700 nm.

It is well known that solvent polarity has a profound impact on the absorption wavelengths of dipolar merocyanine dyes which is explained by a different stabilization of ground and excited state molecules of different dipolarity by polar solvents (solvatochromism).[20, 133] In the case of positive solvatochromism, as observed here, indeed red-shifts of up to 130 nm have been observed for D-A dyes when going from *n*-hexane to DMF/water mixtures.[133b] However, in our case the even larger red-shift of 160 nm cannot be attributed to such a kind of solvatochromism because otherwise a continuous displacement of the

absorption band with increasing solvent polarity should be observed instead of the bimodal distribution of absorption intensity at ca. 585 nm and ca. 750 nm which is most striking in ethanol where both bands coexist in almost equal intensity. Thus, different molecular species have to be considered to explain the observed bands at 585 and 748 nm.

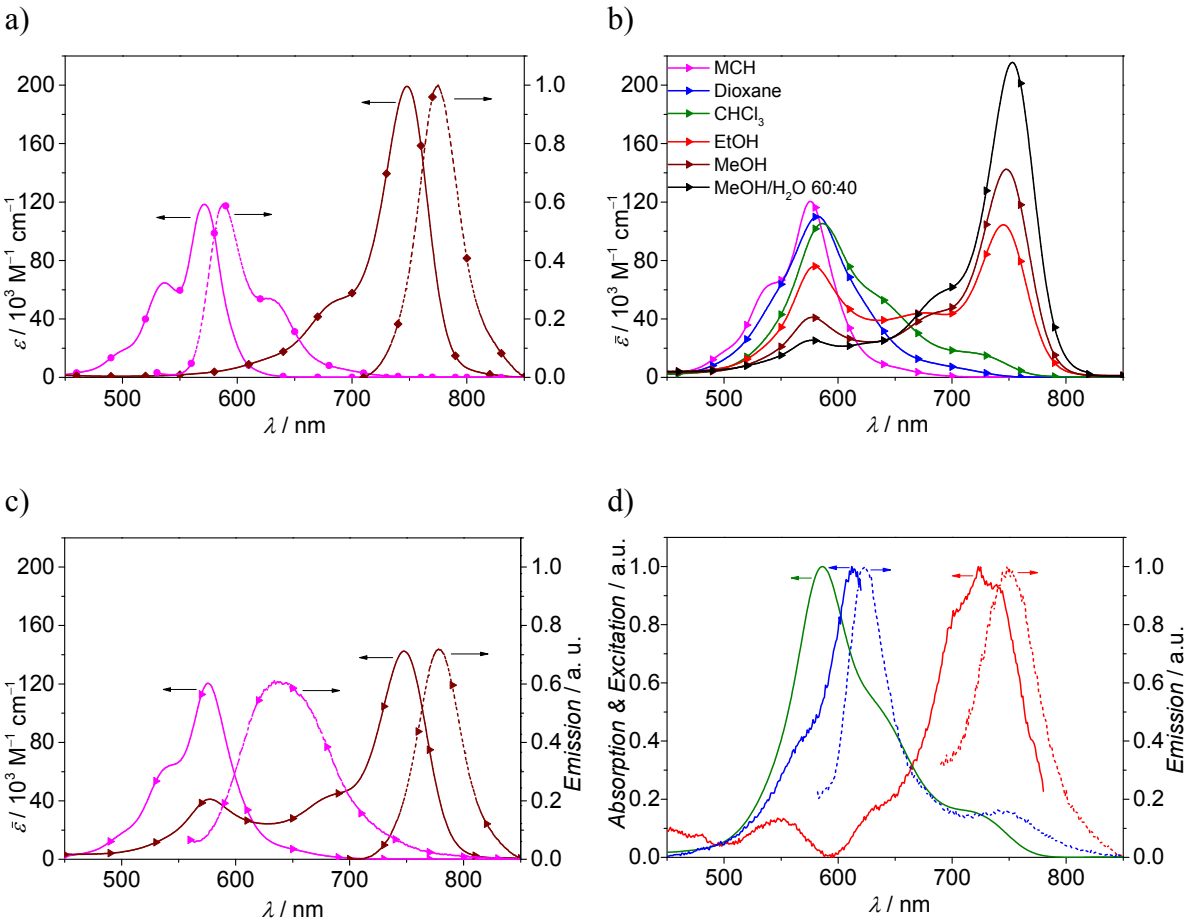

Figure 36. a) UV-Vis (solid lines) and fluorescence (dashed lines) spectra of reference dyes **120** (pink circles, $c \approx 10^{-6}$ M, 298 K) and **133** (brown diamonds, $c \approx 10^{-6}$ M, 298 K) as well as b) of dye **118** (triangles, $c \approx 10^{-5}$ M, 298 K) in solvents of increasing polarity (methylcyclohexane: pink; 1,4-dioxane: blue; trichloromethane: green; ethanol: red; methanol: brown; methanol/water 60:40, black); c) Absorption (solid lines) and normalized emission (dashed lines) of dye **118** in MCH (pink) and MeOH (brown) solutions. d) Normalized absorption (green), excitation (solid lines, blue for $\lambda_{em} = 630$ nm and red for $\lambda_{em} = 790$ nm) and emission (dashed lines, blue for $\lambda_{exc} = 550$ nm and red for $\lambda_{exc} = 680$ nm) spectra of dye **118** in trichloromethane solution ($c \approx 10^{-6}$ M, 298 K) The blue curves correspond to the merocyanine conformation **118-MC** and the red curves to the cyanine conformation **118-Cy**.

The nature of the two bands has been studied further by fluorescence spectroscopy. In Figure 36c the normalized absorption and emission spectra of dye **118** in MCH and methanol solutions are depicted. Again the fluorescence spectra are very similar to those of reference dyes **120** and **133** in the same solvents, depicted in Figure 36a. Moreover, the absorption, excitation and emission spectra of dye **118** in trichloromethane solutions are depicted in Figure 36d. Interestingly, for an excitation wavelength of 550 nm the recorded

emission is centered at 624 nm with a small shoulder at 750 nm. The main emission at 624 nm is accordingly very similar to the emission of reference merocyanine dye **120**. The corresponding excitation spectrum for an emission wavelength of 630 nm featured a maximum at 612 nm and a shape typical for merocyanine dyes. In contrast, when exciting at 680 nm the small shoulder observed in the previous experiment evolved as the main emission band, with a maximum at 750 nm. This band correlates well with the emission in methanol attributed to the cyanine conformation. Likewise, the corresponding excitation spectrum for the emission maximum of 790 nm revealed a band centered at 725 nm. The fact that two different excitation spectra were found for the two emission bands supports the hypothesis of two independently absorbing species, i.e. co-existence of conformational isomers **118-MC** and **118-Cy**. Due to the similarity of the spectra with the corresponding reference dyes, we can assume that the short-wavelength absorption belongs to the merocyanine-type conformational isomer **118-MC** while the long-wavelength transition corresponds to the cyanine-type conformational isomer **118-Cy** (Scheme 34).

3.5.2 Single crystal analysis & Theoretical calculations

We were able to confirm the merocyanine conformation **118-MC** by single crystal analysis of crystals grown from dichloromethane solutions where **118-MC** is the dominating species (Figure 37). Due to the steric hindrance between the polymethine chain and the carbonyl groups of the acceptor unit, the V-shaped dye **118-MC** is not expected to be planar. Indeed, a flat D-A scaffold with a donor-acceptor twist of 10° is found for the polymethine chain between one of the donor units and the acceptor heterocycle, whilst the polymethine chain connected to the second donor subunit is twisted out of planarity by an angle of almost 60° with respect to the acceptor unit. The symmetry-broken situation for the two polymethine chains from the π-junction to the respective donor units is as well reflected in the bond lengths of the polymethine chain. Thus, the bond length alternation (BLA) is significantly smaller for the polymethine chain of the planar DA-system than for the out-of-plane twisted polymethine chain to the second donor unit (Figure 37a). It is accordingly reasonable to conclude that the π-electronic system is delocalized within one D-π-A merocyanine scaffold and that the second donor unit of the second polymethine chain is disconnected, leading to a more polyene-like BLA behavior of this chain. Moreover, the flat D-A scaffold directs the formation of centrosymmetric dimer units which stack on top of each other, similarly to previously reported D-A merocyanine

dyes.[4a] For dye **118-MC** the spacing within the close neighbors of a dimer unit is quite small (3.28 Å), which is translated in a larger longitudinal displacement in comparison to distant neighbors (Figure 37b,c).

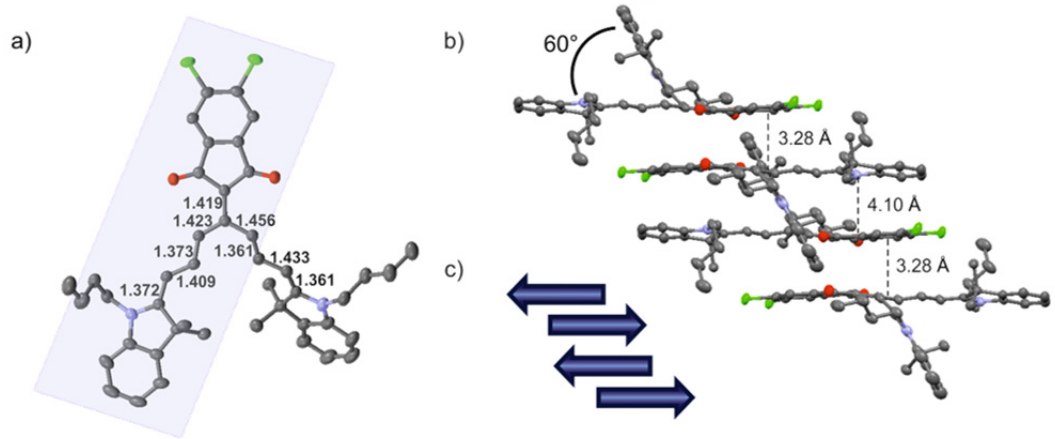

Figure 37. a) Top-view of the molecular structure of dye **118** in the crystal with the corresponding bond lengths of the polymethine chains. The planar D-A scaffold is highlighted in the blue rectangle. b) Side-view of π-stack of dye **118** in the crystal, where the angle between both donor units is noted. c) Schematic representation of **118** π-stack showing the antiparallel orientation of the dipole moments (arrows), and the unequal distances to the upper and lower neighbors.

Theoretical calculations were performed for a better understanding of the electronic properties of dye **118**. On the one hand, a single point energy optimization was performed using the geometry of the molecule in the crystal structure, in order to calculate the frontier molecular orbitals for this conformational isomer. For this purpose, the Gaussian 09[115a] software was used, with the functional B3-LYP[115b-d] and the basis set 6-31G(d). On the other hand, a geometry optimization of the merocyanine conformation **118-MC**, the cyanine conformation **118-Cy**, as well as the reference molecule **120** was performed using the same level of theory. In Figure 38 the crystal geometry (a) as well as the optimized geometries of both conformations of dye **118** (b,c) are depicted, together with the optimized geometry of reference dye **120** (d).

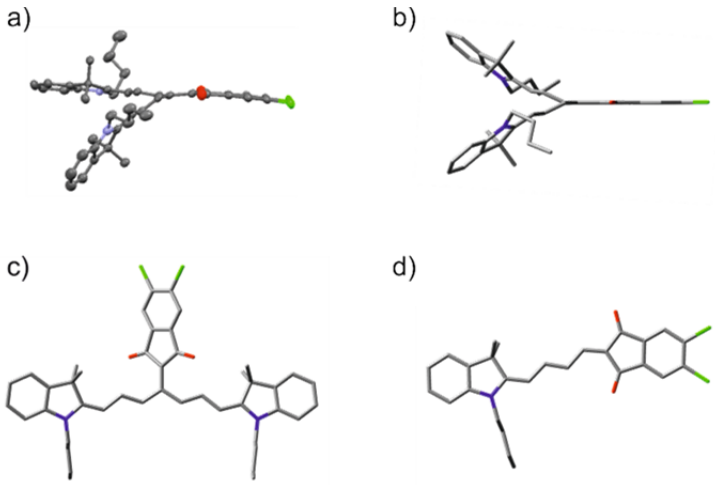

Figure 38. a) Dye **118** in the crystal structure geometry. Optimized geometry of the **118-MC** (b) conformation, the **118-Cy** conformation (c), as well as reference merocyanine dye **120** (d). DFT calculations were performed using Gaussian 09 and B3-LYP/6-31G(d) level of theory.

In Figure 39 the FMO levels of dye **118** in both the **118-MC** conformation (crystal geometry) and the optimized geometry for the **118-Cy** conformation are depicted together with the FMO levels of reference merocyanine dye **120**. Interestingly, while the LUMO of dye **118-MC** in the crystal geometry is distributed all over the molecule, this is not the case for the HOMO and HOMO−1 orbitals. The HOMO−1 orbital is localized along the D-A planar scaffold, in analogy to the HOMO of reference merocyanine dye **120**. Thus, we can assume that the main merocyanine-like absorption band displayed by dye **118-MC** in unpolar solvents corresponds to a transition from the HOMO−1 to the LUMO orbitals. This transition is of high intensity since both HOMO−1 and LUMO orbitals overlap well within the planar D-A system, leading to a large oscillator strength. In contrast, the HOMO orbital of dye **118-MC** in the crystal geometry is localized on the distorted donor subunit and features almost no overlap with the LUMO orbital. Thus, the low intensity absorption from 650 to 700 nm is attributable to the HOMO-LUMO transition. For the by two methine units longer cyanine conformation **118-Cy**, the calculated FMOs are equally distributed along the cyanine π-scaffold, indicative of a fully conjugated polymethine chain which is responsible for the intense long-wavelength absorption at 748 nm.

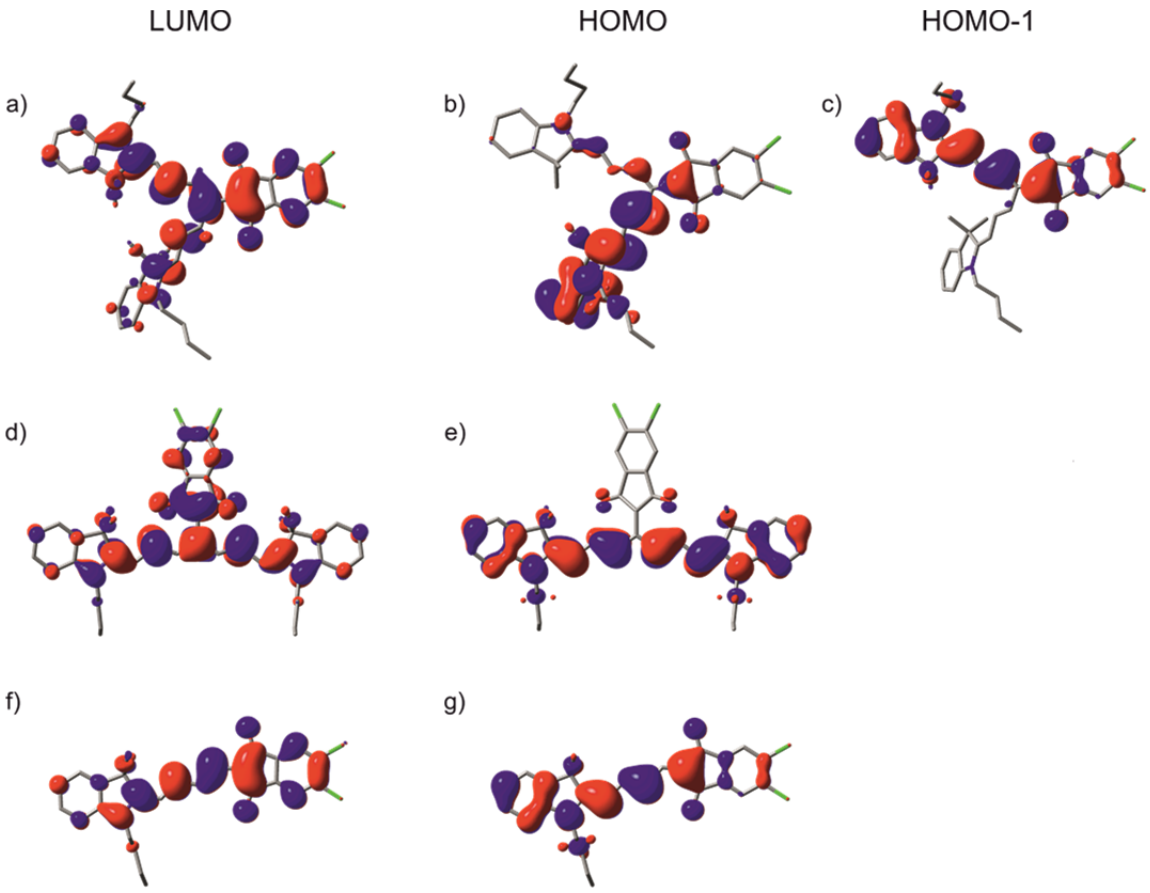

Figure 39. a-c) Dye **118-MC** in the crystal geometry showing the electron density distribution of the LUMO (a), HOMO (b) and HOMO−1 (c) orbitals. d-e) Optimized geometry of the **118-Cy** conformation showing the electron density distribution of the LUMO (d) and HOMO (e) orbitals. f-g) Optimized geometry of reference merocyanine **120** showing the electron density distribution of the LUMO (f) and HOMO (g) orbitals. DFT calculations were performed using Gaussian 09[115a] and B3-LYP/6-31G(d)[115b, 115c] level of theory.

3.5.3 Solvent polarity driven conformational switching

The possibility of conformational switching between the merocyanine form **118-MC** and the cyanine form **118-Cy** by the solvent polarity is illustrated in Figure 40. Here, solutions with different CH_2Cl_2/MeOH and MeOH/H_2O ratios have been prepared and their absorption spectra were recorded. For the MeOH/H_2O 60:40 mixture the cyanine band shifts slightly from 748 nm to 753 nm, reaching an absorption of $200 \cdot 10^3$ M^{-1} cm^{-1}, which is in the range of reference cyanine **133**. As shown in the inset of Figure 40, upon increasing the methanol content the short-wavelength absorption band decreases, while the long-wavelength absorption rapidly rises. Since a quasi-isosbestic point (~660 nm) can be observed for the transition between the merocyanine-like **118-MC** and the cyanine-like **118-Cy** conformations, a two-state equilibrium for the process is confirmed.

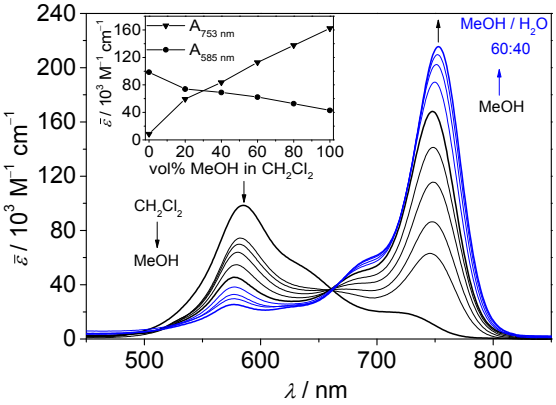

Figure 40. Solvent-dependent UV-Vis absorption spectra of dye **118** ($c \approx 4 \cdot 10^{-6}$ M, 298 K) in CH_2Cl_2/MeOH mixtures starting in pure CH_2Cl_2 changing to pure MeOH by increasing the MeOH content (black lines, 20 vol % steps) as well as MeOH/H_2O mixtures up to 40 % H_2O (blue lines, 10 vol % steps). Inset: Plot of the absorption maxima at 585 nm and 753 nm against the content of MeOH in CH_2Cl_2.

In order to determine the thermodynamic data of the conformational equilibrium the absorption maximum at 753 nm was chosen since this band is the most sharp and defined, and features no overlap with the **118-MC** absorbance. For this analysis two assumptions have been made. First, for methanol/water mixtures with 40 % water dye **118** is supposed to be exclusively in the cyanine conformation **118-Cy** which is reasonable because of the similarity of the extinction coefficient value with the one of the reference cyanine **133**. Second, the spectrum of dye **118** in MCH (Figure 36) was taken as reference for the pure merocyanine-like conformation **118-MC**, since dichloromethane solutions display a shoulder at longer wavelengths. As the chosen wavelength (753 nm) is far away from the absorption maximum in dichloromethane and MCH we can assume a small error from this approximation. Thus, the fraction of cyanine conformation α_{Cy} was calculated for every solvent mixture using equation (14), which has been proposed by Moore and Ray for the study of foldamers:[134]

$$\alpha_{Cy} = \frac{\varepsilon(\lambda)_{MC} - \varepsilon(\lambda)}{\varepsilon(\lambda)_{MC} - \varepsilon(\lambda)_{Cy}} \qquad (14)$$

Where $\varepsilon(\lambda)$ is the extinction coefficient at a particular wavelength for an intermediate solvent composition, $\varepsilon(\lambda)_{MC}$ and $\varepsilon(\lambda)_{Cy}$ are the extinction coefficients for the pure merocyanine and cyanine conformations, respectively, at the particular wavelength. Moreover, the values of the equilibrium constant and the free Gibbs energy for the equilibrium at each solvent composition can be derived from equations (15) and (16):

$$K_{eq} = \frac{c_{MC}}{c_{Cy}} = \frac{1 - \alpha_{Cy}}{\alpha_{Cy}} \qquad (15)$$

$$\Delta G° = -RTlnK_{eq} \qquad (16)$$

where c_{MC} and c_{Cy} represent the concentration of the merocyanine and cyanine species, respectively. In Table 9 the calculated α_{Cy}, K_{eq} and $\Delta G°$ are listed. The free energy change between both states was found to depend linearly on the solvent composition for solvent mixtures between 20 % and 100 % MeOH. The fitted data are depicted in Figure 41.

Table 9. Thermodynamic data α_{Cy}, K_{eq} and $\Delta G°$ for the solvent-dependent equilibrium between the merocyanine (MC) and cyanine (Cy) species of dye **118** in CH_2Cl_2/MeOH mixtures from the extinction values of the absorption band of the cyanine species at 753 nm.

vol % MeOH in CH_2Cl_2	α_{Cy}	K_{eq}	$\Delta G°$ (kJ mol^{-1})
0	0.04	24.90	-7.97
20	0.27	2.64	-2.40
40	0.39	1.58	-1.14
60	0.52	0.91	0.22
80	0.64	0.57	1.40
100	0.75	0.33	2.75

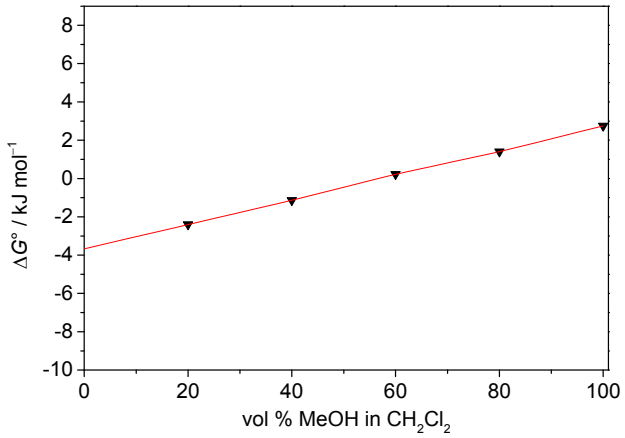

Figure 41. Plot of the $\Delta G°$ values for the equilibrium between the merocyanine **118-MC** and cyanine **118-Cy** species derived from the spectral development at the respective maximum of the cyanine band (753 nm). The solid line represents the fitting curve from linear regression analysis.

For a solvent mixture with 57 % MeOH and 43 % dichloromethane the free Gibbs energy is zero, that is, both species are isoenergetic. For higher dichloromethane contents the **118-MC** isomer is energetically more favored ($\Delta G^0 < 0$) whilst for higher MeOH contents (as well as MeOH/water mixtures) the **118-Cy** isomer is energetically favored. The result in the lower polarity environment is in accordance with the theoretical calculations on the optimized geometries in the gas phase of merocyanine **118-MC** and cyanine **118-Cy** conformations (Figure 38), which revealed a 10 kJ mol^{-1} lower energy for the **118-MC** conformation.

In summary, a new bifurcated π-scaffold has been synthesized which exhibits a conformational switching between a merocyanine-like **118-MC** donor-π-acceptor and a cyanine-like **118-Cy** zwitterionic $(D\text{-}\pi\text{-}D)^{+}\ A^{-}$ structure upon increasing solvent polarity. This conformational switching is accompanied by a shift of the absorption band by more than 160 nm from the visible (~585 nm) to the near infrared region (~750 nm) when changing the solvent from dichloromethane to methanol. Both conformations **118-MC** and **118-Cy** have been characterized by means of UV-Vis and fluorescence spectroscopy. Additionally, the structure of **118-MC** has been confirmed by single crystal analysis. The equilibrium between both conformations can be controlled by variation of the solvent polarity, as illustrated for CH_2Cl_2/MeOH mixtures. In MCH solutions of dye **118** exclusively the merocyanine conformation **118-MC** was present, while in methanol/water mixtures with 40 % water dye **118** featured almost exclusively the cyanine conformation **118-Cy**. Further studies on the spectroscopic features of this and related molecules as well as those towards interconversion of the two conformations by external stimuli are planned.

Chapter 4

Summary & Conclusion

The application of organic compounds as semiconductors has gained increasing interest in the last years. Organic materials can be prepared rather inexpensively, thus offering the possibility of price reduction in comparison with silicon-based solar cells. Previous work by the groups of Meerholz and Würthner demonstrated the suitability of merocyanine dyes for organic solar cell applications.[4] The aim of this thesis was to explore new merocyanine derivatives with optical and electrochemical properties adapted to photovoltaic applications as well as sufficient thermal stability to be vacuum-processed, since this technique provides a better control of the active layer morphology and consequently higher solar cell performance.[34] Merocyanine dyes based on various indanedione and thiazole derivatives as acceptor moieties combined with different donor groups varying from indolenine to naphthostyryl or quinoline derivatives were synthesized. The optical and electrochemical properties of the obtained compounds were studied by means of UV-Vis spectroscopy and cyclic voltammetry and their suitability for solar cell application was evaluated. The semiconducting properties of the dyes were as well studied in transistor devices and selected molecules were tested in vacuum-processed solar cell devices in collaboration with the Meerholz group in Cologne.

In **Chapter 2** the basic physical concepts needed for understanding the processes involved in energy generation from light have been described. Moreover, a literature overview on D-π-A based organic solar cells has been presented. Donor-acceptor dyes and in particular merocyanine dyes have demonstrated to be useful chromophores for photovoltaic applications. Their straight-forward synthesis allows combining an uncountable number of different electron-rich and electron-poor moieties, thus generating a huge library of compounds whose optical properties can be easily tuned. Indeed, dyes absorbing from the UV region up to the near infrared region have been synthesized in simple one or two step procedures. Furthermore, merocyanine dyes display very high extinction coefficients, thus featuring high absorption of light even in very thin films with low dye content. The dipole moments which characterize this kind of push-pull chromophores have been for years the

reason not to use them as organic semiconductors, arguing that they should act as traps for charge carriers.[16] However, previous studies by the groups of Meerholz and Würthner[4a] have demonstrated that these dyes tend to self-assemble in dimer units with nearly no overall dipole moment, reducing the dipolar disorder in amorphous and in particular in crystalline materials. Their suitability as semiconductors has as well been recently demonstrated through application in transistor devices, where hole mobilities up to 0.67 $cm^2 V^{-1} s^{-1}$ could be achieved.[42b] Another advantage of merocyanine dyes is their relatively small size, which allows for both solution and vacuum-processing. While solution-processing has demonstrated to be an inexpensive and useful tool to test the suitability of merocyanine dyes as donor materials for organic solar cells, vacuum-processing allows for a better control of the blend morphology and higher performances.[4b] Finally, at the end of **Chapter 2** a short introduction about the exciton theory developed by Kasha can be found.

In **Chapter 3** the results achieved within this thesis have been presented and discussed. First of all, the syntheses of all the studied compounds are described in section 3.1. Usually the synthetic path followed was the Knoevenagel condensation between a C-H active (hetero-)aromatic building block and an aldehyde or imine derivative. This straightforward procedure delivers the polymethine dyes in moderate to high yields and allows the combination of multiple donor and acceptor moieties. The donor and acceptor units used in this work are depicted in Chart 14.

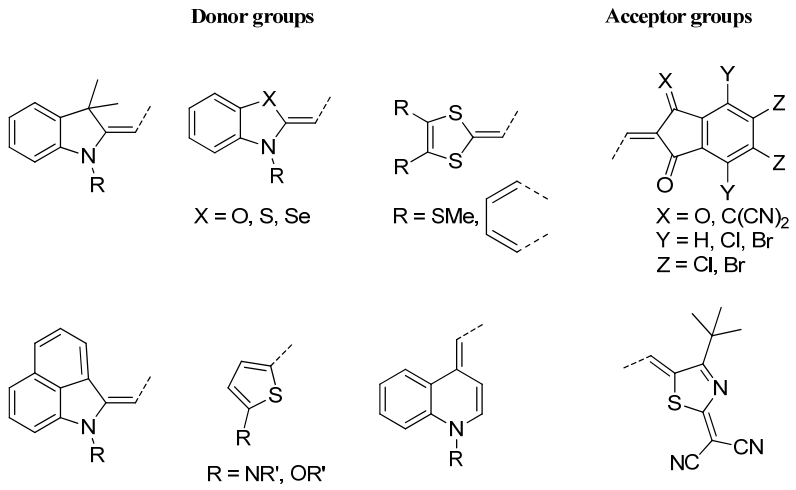

Chart 22. Chemical structure of donor and acceptor units used as building blocks for the synthesis of merocyanine dyes.

In Section 3.2 a series of structurally related D-A merocyanine dyes bearing an indanedione or malononitrile-indanedione acceptor moiety linked to different donor units such as indolenine, benzoselenazole or thiophene derivatives has been presented. On the molecular level most of the studied chromophores display similar absorption properties in the 550 - 600 nm range. Exceptions are on the one hand, the naphthostyryl and quinoline derivatives, which show absorption maxima at around 650 nm due to the high electron-donating character of the donor units and on the other hand 1,3-indanedione derivatives, which display blue-shifted absorption about ~500 nm due to the shorter conjugation path provided by this acceptor unit. With regard to the application of the dyes as donor materials for organic solar cells, electrochemical measurements revealed favorable HOMO levels for obtaining V_{OC} values about 1.0 eV and LUMO levels which should provide enough driving force for the exciton dissociation at the donor/acceptor interface of BHJ solar cells.

On the supramolecular level single crystal measurements revealed three different packing motifs for the studied molecules depending on dipole orientation and contact to the neighboring dyes. Thus, dyes belonging to group (I) showed isolated antiparallel dimers with no π-contact to the neighboring molecules, while dyes in group (II) formed one-dimensional π-stacks of antiparallel dimeric units. Finally, dyes classified in group (III) arranged in staircase-like slipped parallel π-stacks within a herringbone structure. The latter packing arrangement was found to be most favorable for charge transport in OTFT devices. Indeed, for the benzoselenazole derivative **97** (Figure 42) the highest hole mobilities of this series could be measured (μ_p = 0.08 $cm^2\ V^{-1}\ s^{-1}$).

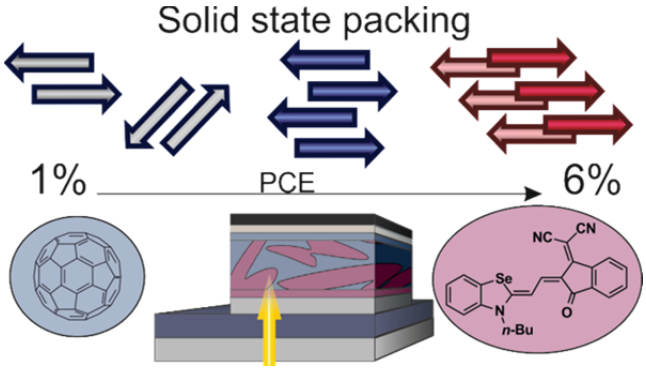

Figure 42. Illustration of the different packing motifs displayed by the studied merocyanines and the corresponding solar cell performance.

Solar cell devices were prepared taking C_{60} as acceptor material (Figure 42). While most of the dyes displayed decent power-conversion efficiencies higher than 3 %, selenium containing dye **97** benefited from its high charge carrier mobility and favorable packing motif, thus reaching a *PCE* of 5.2 % in simple device architectures. The latter could be even optimized by addition of neat donor and acceptor layers above and below the active layer, which raised the *PCE* to a record value of 6.2 %. The superiority of devices based on dye **97** has been attributed to the slipped π-stacking packing motif (group III), the *J*-type coupling with very high absorption displayed in the blend with C_{60}, together with the higher polarizability of selenium and the high charge carrier mobility found in OTFT devices.

Continuing with the search of suitable absorbers for organic solar cells, section 3.3 deals with the optimization of the energy levels of the donor materials with respect to fullerene acceptors. Indeed, while an energy offset between the LUMO levels of donor and acceptor materials of 0.3 eV should be provided to ensure an efficient exciton dissociation at the donor/acceptor interface, higher offsets lead to energy losses. 1,3-indanedione derivatives display strong absorption in the 500 nm region, which makes them interesting for application as complementary absorbers in tandem solar cells in combination with long-wavelength absorbing dyes such as ZnPc.[35] However, usually their LUMO levels are much higher than those of C_{60}. In this regard, functionalizing the acceptor unit with electron-withdrawing groups such as halogen atoms[48, 125] can be a useful strategy to lower the energy levels without much altering the optical properties. In section 3.3 new chlorinated and brominated chromophores have been characterized. The effect of the halogen atoms was found to be more pronounced on the lowering of the LUMO than on the HOMO orbitals. Furthermore, the energy levels of indanedione derivatives were more sensible to halogenation than the ones of malononitrile derivatives. Thus, the energy offset of the merocyanines with respect to C_{60} was reduced from ~1 eV to ~0.85 eV for dichlorinated, or ~0.75 eV for tetrachlorinated dyes in the case of 1,3-indanedione derivatives, while malononitrile-indanedione derivatives displayed even smaller offsets of ~0.5 eV after chlorination. These results together with the decent hole mobilities of $\mu_p \approx 10^{-2}$ cm^2 V^{-1} s^{-1} found in OTFT devices make the studied dyes promising donor materials for application in tandem solar cell devices.

Chance has always been an essential part of scientific discoveries. The role of the scientist is to be able to identify interesting phenomena, understand and use them. In this regard the isolation of several side-products from reactions aiming at compounds presented in section 3.3 was the starting point for the study of chromophores presented in sections 3.4 and 3.5. Indeed, the π-extended halogenated side-products could be identified and their origin was elucidated. Thus, a new synthetic path involving an extended indanedione acceptor moiety was established and π-extended merocyanine dyes bearing solubilizing alkyl chains within the polymethine bridge or bifurcated AD_2 scaffolds were envisaged. In section 3.4 the optical properties of the side-products as well as the merocyanine dyes bearing solubilizing chains have been described. Most of the chromophores displayed sharp absorption bands in the $550 - 650$ nm range with extinction coefficients varying from ~85 to $\sim 200 \cdot 10^3$ M^{-1} cm^{-1}, depending on the presence of halogens in the conjugated scaffold. All halogenated compounds featured higher extinction coefficients, probably due to the larger dipole moment of the molecules provided by the halogen atoms. These strong absorbers could be interesting candidates for application in transparent organic solar cells with absorption in the near infrared region. Thanks to the solubilizing chains, the dyes can be easily solution-processed.

Moreover, the bifurcated AD_2 scaffold described in section 3.5 was obtained by reaction of a π-extended indanedione acceptor unit with two aldehyde donor units. This molecule revealed a high sensibility to solvent polarity. Indeed, a conformational switch between a merocyanine-like **118-MC** donor-π-acceptor and a cyanine-like **118-Cy** zwitterionic $(D\text{-}\pi\text{-}D)^+ A^-$ structure upon increasing solvent polarity was observed in UV-Vis studies (Figure 43). This conformational switching was characterized by a shift of the main absorption band from the visible (ca. 585 nm) to the near infrared (ca. 750 nm) region when varying from medium polarity solvents such as dichloromethane to highly polar ones such as methanol. This change of more than 160 nm cannot be attributed to conventional solvatochromism effects,[20, 133] since the shift is not gradual but a bimodal absorption can be observed, with one maximum at ca. 585 nm and another one at ca. 750 nm. This is most clear in ethanol solutions, where both bands are almost equally intense.

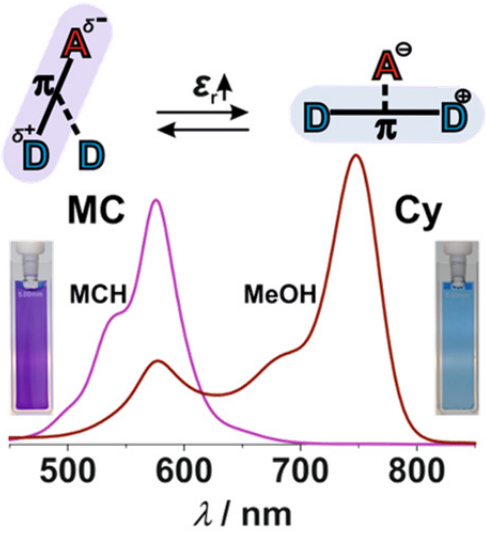

Figure 43. Solvent polarity directed conformational switching between a merocyanine-like and a cyanine-like structure.

Both conformations have been characterized by UV-Vis and fluorescence spectroscopy. The fact that two different emission and excitation spectra were found for the short and long-wavelength absorption bands is indicative of the presence of two distinct species. Additionally, the merocyanine-like conformation could be confirmed by single crystal analysis, where a flat D-A scaffold was found between the acceptor unit and one of the donor units, while the second donor unit was distorted from planarity. The equilibrium between both conformations can be directed by variation of the solvent polarity. In unpolar solvents such as MCH exclusively the merocyanine conformation was present, as indicated by the absorption spectrum, which was almost identical to the D-A reference dye. Moreover, in dichloromethane the merocyanine conformation still predominated, but the absorption was broader and a shoulder at longer wavelengths was already observed. In CH_2Cl_2/MeOH mixtures with increasing methanol content a rapid increase of the intensity of the band at ~750 nm together with a decrease of the band at ~585 nm was observed. Finally, methanol/water mixtures with 40 % water provided the cyanine conformation almost exclusively.

In summary, the present thesis comprises the synthesis of new functional merocyanine dyes, the study of their electro-optical properties as well as solid state packing and their application as p-type semiconductor materials in transistor and solar cell devices. The absorption properties of the obtained compounds could be modified by variation of the donor unit, the introduction of electron-withdrawing substituents in the acceptor unit or

elongation of the polymethine chain. For a particular dye, the absorption band could be shifted by more than 160 nm by increasing the solvent polarity due to a conformational switch between a merocyanine-like and a cyanine-like structure. Single crystal analyses revealed that the studied dyes tend to pack either in an antiparallel fashion forming dimers with no overall dipole moment or in a staircase-like pattern where the dipole moments point to the same direction and are only balanced by another staircase oriented in the opposite direction (stair dimer). With respect to application as semiconductor materials, the latter packing arrangement resulted most favorable for charge carrier mobility. We concluded that this packing motif is preserved in the solar cell devices, where the selenium-containing dye afforded the highest performance of this series for an optimized planar-mixed heterojunction solar cell (6.2 %).

Chapter 5

Zusammenfassung & Schlussfolgerung

Die Anwendung organischer Substanzen als Halbleiter in organischen Solarzellen hat in den letzten Jahren großes Interesse geweckt. Da sich organische Materialien kostengünstiger herstellen lassen, ermöglichen sie eine Kostensenkung im Vergleich zu siliziumbasierten Systemen. Frühere Arbeiten von Meerholz und Würthner bewiesen die Eignung von Merocyaninfarbstoffen als Donormaterialien in organische Solarzellen.[4] Ziel meiner Arbeit war die Entwicklung neuer Merocyaninfarbstoffe mit für die Anwendung in der organischen Photovoltaik adaptierten optischen und elektrochemischen Eigenschaften. Dazu sollten die hergestellten Farbstoffe genügend thermische Stabilität aufweisen, da die Vakuumprozessierung eine bessere Kontrolle der Morphologie der aktiven Schicht in der Solarzelle und damit höhere Leistungen ermöglicht als Lösungsprozessierung.[34] Merocyaninfarbstoffe wurden basierend auf Indandion- und Thiazolakzeptoreinheiten, in Kombination mit verschiedenen Donoreinheiten wie z. B. Indolenin, Naphthostyryl oder Chinolindonoreinheiten synthetisiert. Anschließend wurden die optischen und elektrochemischen Eigenschaften der Substanzen mittels UV-Vis Spektroskopie und Cyclovoltammetrie untersucht, um die Eignung der Moleküle für die Anwendung in Solarzellen zu bestimmen. Zusätzlich wurden die Ladungstransporteigenschaften einiger Substanzen in organischen Dünnschichttransistoren untersucht. Ausgewählte Farbstoffe wurden anschließend als Donormaterialien in vakuumprozessierten Solarzellen verwendet. Die organischen Solarzellen wurden im Arbeitskreis von Prof. Dr. Klaus Meerholz (Universität Köln) angefertigt und charakterisiert.

In Kapitel 2 wurden zunächst die physikalischen Grundlagen der Energieerzeugung aus Sonnenlicht, der Zellarchitektur sowie der Charakterisierung organischer Solarzellen präsentiert. Dazu wurde eine umfassende Literaturübersicht zum Thema Donor-Akzeptor (D-A) basierte organische Solarzellen vorgestellt. D-A Farbstoffe und insbesondere Merocyaninfarbstoffe haben sich als geeignete Chromophore für die organische Photovoltaik erwiesen. Dank ihrer einfachen Synthese können zahlreiche elektronenarme und elektronenreiche Einheiten kombiniert werden. Dies führt zu einer großen Bibliothek

von Substanzen, deren optische Eigenschaften sich nahezu beliebig einstellen lassen. In der Tat konnten Farbstoffe, die vom UV-Bereich bis zum Nahinfrarot absorbierten, in ein oder zwei synthetischen Stufen hergestellt werden. Merocyaninfarbstoffe zeigen sehr hohe Extinktionskoeffizienten, was eine hohe Lichtabsorption auch in sehr dünnen Schichten mit geringer Farbstoffmenge ermöglicht. Die Grundzustandsdipolmomente dieser Substanzklasse waren jahrelang der Grund sie als Halbleiter nicht anzuwenden, da sie als Ladungsträgerfallen galten.[16] Studien von Meerholz und Würthner zeigten jedoch, dass Merocyaninfarbstoffe zentrosymmetrische Dimereinheiten mit minimalen Gesamtdipolmomenten bilden.[4a] Dadurch wird die dipolgenerierte Unordnung in amorphen und vor allem in kristallinen Schichten stark reduziert. Die Eignung von Merocyaninfarbstoffen als Halbleiter wurde erst vor kurzem erfolgreich demonstriert, indem Transistorbauteile mit Ladungsträgermobilitäten bis zu 0.67 $cm^2 V^{-1} s^{-1}$ vorgestellt wurden.[42b] Die niedrigmolekularen Farbstoffe haben zusätzlich den Vorteil, dass sie sowohl aus Lösung als auch mittels vakuumbasierter Techniken prozessiert werden können. Die Prozessierung aus Lösung hat sich als eine günstige und schnelle Methode erwiesen, die zur schnellen Einschätzung größerer Sammlungen von Farbstoffe geeignet ist, wobei die Vakuumprozessierung eine bessere Kontrolle der Morphologie der Solarzellen ermöglicht, wodurch höhere Effizienzen erreicht werden können.[4b] Am Ende des Kapitels wurden die Grundlagen der von Kasha entwickelten Exzitonentheorie erläutert.

Im Kapitel 3 wurden die erzielten Ergebnisse dieser Arbeit vorgestellt und diskutiert. Kapitel 3.1 umfasst die Synthese der in dieser Arbeit studierten Merocyaninfarbstoffe. Diese werden üblicherweise durch Knoevenagel Kondensation zwischen einem C-H aktivierten (hetero-)aromatischen Baustein und einem Aldehyd- oder Iminderivat hergestellt. Diese Prozedur liefert Polymethinfarbstoffe in hohen Ausbeuten und ermöglicht die Kombination verschiedener Donor- und Akzeptoreinheiten. Die in dieser Arbeit eingesetzten Donor- und Akzeptoreinheiten sind in Tafel 22 abgebildet.

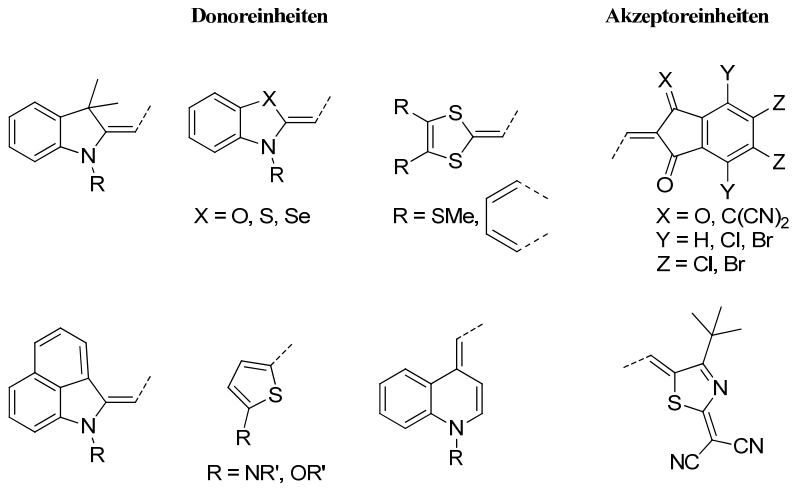

Tafel 22. Chemische Strukturen der verwendeten Donor- und Akzeptoreinheiten.

In Kapitel 3.2 wird eine Serie strukturähnlicher Verbindungen mit Indandion- und Malononitril-Indandion-Akzeptoreinheiten, welche zu verschiedenen Donoreinheiten verbunden sind, diskutiert. Die Donoreinheiten variieren von Indolenin oder Benzoselenazol bis zu Thiophenderivaten. Die Absorption der Farbstoffe deckt den Bereich zwischen 550 – 600 nm ab. Ausnahmen sind einerseits die Naphthostyryl und Chinolinderivate, die aufgrund des stärkeren Donorcharakters eine bathochrom verschobene Absorption zeigen. Andererseits absorbieren Derivate des 1,3-Indandion aufgrund des kürzeren konjugierten Systems bei 500 nm. Dazu zeigen die Moleküle günstige Energieniveaus für die Anwendung in organischen Solarzellen in Kombination mit dem Akzeptormaterial C_{60}. Die berechneten HOMO-Niveaus würden zu V_{OC}-Werten von ca. 1.0 eV führen. Andererseits würden die berechneten LUMO-Niveaus eine effiziente Aufspaltung des Exzitons an der Donor/Akzeptor Grenzfläche der Solarzelle ermöglichen.

Die Einkristallröntgenstrukturanalyse zeigte drei grundsätzlich verschiedene Packungstypen in Bezug auf die Orientierung der Dipolmomente und den Kontakt zwischen benachbarten Molekülen. Einerseits wurden zentrosymmetrische Dimere als Packungseinheit gefunden, welche isoliert vorlagen (Gruppe I) bzw. eindimensionale Stapel bildeten (Gruppe II). Andererseits bildeten Substanzen der Gruppe (III) treppenartige Stapel mit parallel orientierten Dipolmomenten. Dieses für den Ladungstransport besonders günstige Packungsmotiv zeigte Lochträgermobilitäten von $\mu_p = 0.08\ cm^2\ V^{-1}\ s^{-1}$ für Farbstoff **97**.

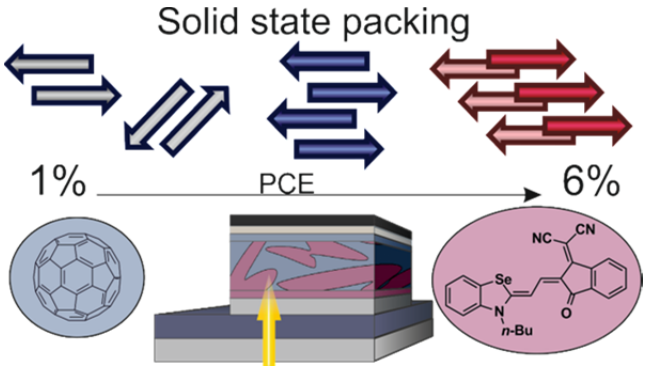

Abbildung 42. Verschiedene Packungsmuster der untersuchten Merocyaninfarbstoffe und deren Wirkungsgrad in Solarzellen.

Zusätzlich wurden Solarzellen gebaut, wobei die aktive Schicht aus einer Mischung von einem Merocyaninfarbstoff und C_{60} bestand (Abbildung 42). Die Mehrheit der Zellen wiesen hierbei Effizienzen größer als 3 % auf. Das selenbasierte Derivat **97** zeigte in einfachen Bauteilarchitekturen dank seiner hohen Ladungsträgermobilität und seines hochgeordneten Packungsmotivs einen Wirkungsgrad von 5.2 %. Dieser wurde weiter optimiert, indem eine Schicht reinen Donors und Akzeptors unter und über der aktiven Schicht hinzugefügt wurde, wodurch der Wirkungsgrad der Zelle bis auf 6.2 % gesteigert werden konnte. Die gute Leistung des Selenderivats **97** ist sowohl auf sein treppenartiges Packungsmotiv, die *J*-artige Kopplung mit sehr hoher Absorption in Mischungen mit C_{60}, als auch auf die höhere Polarisierbarkeit des Selens sowie die hohe Lochträgermobilität zurückzuführen.

Auf der Suche nach weiteren geeigneten Molekülen zur Anwendung in organischen Solarzellen, befasst sich Kapitel 3.3 mit der Optimierung des Energieniveaus der Donormaterialien. Ein Energieversatz zwischen den LUMO Energieniveaus der Donor- und Akzeptormaterialien von 0.3 eV ist erwünscht, um eine effiziente Exzitonendissoziation an der Donor/Akzeptor Grenzfläche zu ermöglichen. Höhere Energieunterschiede führen jedoch zu Verlusten. 1,3-Indandionderivate zeigen starke Absorptionsbanden bei ~500 nm, wodurch sie interessante Farbstoffe zur Anwendung in Tandemsolarzellen in Kombination mit langwelligen Absorbern wie z. B. ZnPc sind.[35] Hinderlich sind die hohen Energieniveaus der Farbstoffe in Vergleich zu C_{60}. Eine Möglichkeit die Energieniveaus eines Moleküls zu senken, ohne die spektralen Eigenschaften entscheidend zu beeinflussen, ist die Funktionalisierung der Akzeptoreinheit mit Halogenatomen.[48, 125] Dieses Konzept wurde in Kapitel 3.3 angewendet, indem neue chlorierte und bromierte Chromophore charakterisiert wurden. Die Halogenatome zeigten

eine größere Wirkung auf die LUMO- als auf die HOMO-Niveaus. Die Wirkung von Chloratomen war interessanterweise für Moleküle mit Indandion-Akzeptoreinheit intensiver als für Malononitril-Indandion-Derivate. Insgesamt wurde der Abstand der LUMO-Niveaus zwischen den Farbstoffen mit Indandionderivaten als Akzeptor zu C_{60} von ~1 eV zu ~0.85 eV für dichlorierte, und ~0.75 eV für tetrachlorierte Verbindungen reduziert. Malononitril-Indandionderivate zeigten ihrerseits noch geringere Unterschiede von 0.5 eV zum LUMO-Niveau von C_{60}. Zusammen mit den ordentlichen Lochmobilitäten, die für dichlorierte Moleküle in Transistorbauteilen gemessen wurden, erscheinen die neuen halogenierten Substanzen hochinteressant für die Anwendung in Tandemsolarzellen.

Der Zufall bleibt ein entscheidender Teil vieler wissenschaftlicher Entdeckungen. Die Aufgabe des Wissenschaftlers ist es die interessanten Phänomene zu erkennen, diese zu verstehen und zu nutzen. Während der Synthese halogenierter Verbindungen (Kapitel 3.3) wurden mehrere Nebenprodukte isoliert. Diese Nebenprodukte konnten erfolgreich identifiziert werden und deren Entstehung konnte aufgeklärt werden. Hierdurch konnte eine neue synthetische Route für π-erweiterte hochlösliche Polymethinfarbstoffe (3.4) und V-förmige Gerüste (3.5) ausgehend von einer π-erweiterten Indandion-Akzeptoreinheit entwickelt werden. Im Kapitel 3.4 wurden die optischen Eigenschaften der Nebenprodukte sowie der hochlöslichen Polymethinfarbstoffe zusammengefasst. Die meisten Verbindungen zeigten scharfe Absorptionsbanden im Bereich von 550 – 650 nm. Die Extinktionskoeffizienten variierten zwischen ~85 und ~$200 \cdot 10^3$ M^{-1} cm^{-1}. Interessanterweise zeigten halogenierte Verbindungen höhere Extinktionskoeffizienten als nicht halogenierte Moleküle, was wahrscheinlich auf ihre höheren Dipolmomente zurückzuführen ist. Die untersuchten Farbstoffe zeichnen sich aufgrund der hohen Absorption im Nahinfrarotbereich als vielversprechende Kandidaten für die Anwendung als Donormaterialien für transparente Solarzellen aus. Die Moleküle können darüber hinaus dank der Alkylketten problemlos durch Lösungsprozessierung verarbeiten werden.

Das in Kapitel 3.5 beschriebene V-förmige Gerüst wurde durch Doppelkondensation einer π-erweiterten Indandion-Akzeptoreinheit und zwei Indoleninaldehydderivaten hergestellt. Diese Verbindung wies eine außergewöhnliche Empfindlichkeit gegenüber der Lösemittelpolarität auf. UV-Vis Studien deuteten auf einen Konformationswechsel zwischen einer merocyaninartigen **MC** Donor-π-Akzeptor und einer cyaninartigen **Cy**

zwitterionischen $(D\text{-}\pi\text{-}D)^{+}A^{-}$ Struktur, welcher durch Erhöhen der Lösemittelpolarität stattfindet (Abbildung 43). Dieser Konformationswechsel verdeutlicht sich durch eine Verschiebung der Absorptionsbande vom sichtbaren Bereich (~585 nm) zum Nahinfrarotbereich (~750 nm), welcher durch Variation des Lösemittels von mittelpolarem Dichlormethan zu hochpolarem Methanol zu erkennen ist. Diese erhebliche Verschiebung von mehr als 160 nm ist nicht auf konventionelle solvatochrome Effekte zurückzuführen,[20, 133] da sie nicht graduell sondern zweistufig mit einem Maximum bei ~585 nm und einem anderen bei ~750 nm erfolgt. Dies ist am deutlichsten in Ethanol, wo beide Banden fast die gleiche Intensität aufweisen.

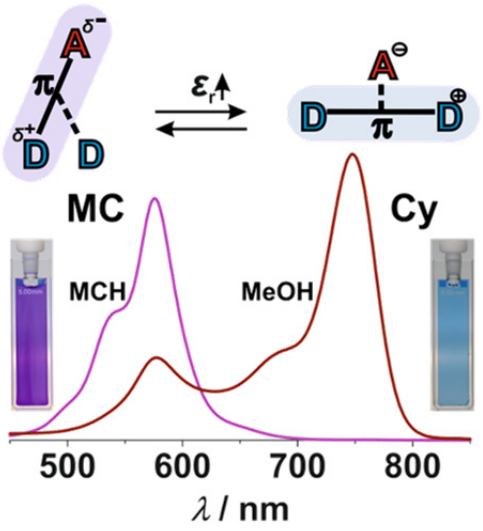

Abbildung 43. Die Lösungsmittelpolarität dirigiert einen Konformationswechsel zwischen einer merocyaninartigen und einer cyaninartigen Struktur.

Beide Konformationen konnten durch UV-Vis und Fluoreszenzspektroskopie charakterisiert werden. Die Anwesenheit zweier getrennter Spezies konnte durch der Fund verschiedener Emissions- und Anregungsspektren für die lang- und kurzwelligen Absorptionsbanden nachgewiesen werden. Zusätzlich wurde die merocyaninartige Konformation **MC** durch Einkristallröntgenstrukturanalyse bestätigt. Die Kristallstruktur zeigte ein flaches D-A Gerüst zwischen der Akzeptoreinheit und einer der Donoreinheiten, während die zweite Donoreinheit aus der Ebene verdreht erschien. Das Gleichgewicht zwischen beiden Konformationen konnte durch Variation der Lösemittelpolarität dirigiert werden. In unpolaren Lösemitteln wie z. B. MCH ist lediglich die merocyaninartige Konformation zu finden. Dies ist durch das Absorptionspektrum zu erkennen, das große Ähnlichkeiten zu der Referenzverbindung aufweist. In Dichlormethan ist die merocyaninartige Konformation noch die vorwiegende Spezies, obwohl das

Absorptionsband breiter wird. CH_2Cl_2/MeOH Mischungen, bei denen der Methanolgehalt schrittweise erhöht wurde, zeigten eine schnelle Zunahme der langwelligen Absorptionsbande und gleichzeitig eine Abnahme der kurzwelligen Absorptionsbande. In MeOH/H_2O Mischungen mit 40 % Wasser ist fast ausschließlich die cyaninartige Konformation zu finden. Weitgehende Studien dieser und verwandter Moleküle, um diesen Konformationwechsel besser zu verstehen, werden durchgeführt.

Zusammenfassend beschreibt die vorliegende Arbeit die Synthese neuer funktioneller Merocyaninfarbstoffe sowie die Studie ihrer elektro-optischen Eigenschaften, ihrer Packungsmotive im Festkörper und deren Anwendung als p-Halbleitermaterialien in Transistoren und Solarzellen. Die optischen Eigenschaften der erhaltenen Moleküle konnten durch Variation der Donoreinheiten, Einführung elektronenziehender Substituenten am Akzeptorgerüst oder durch Verlängerung der Polymethinkette modifiziert werden. Im Fall einer außergewöhnlichen Verbindung konnte die Absorption um mehr als 160 nm verschoben werden, indem die Lösemittelpolarität erhöht wurde. Diese Verschiebung entspricht einem Konformationswechsel zwischen einer merocyaninartigen zu einer cyaninartigen Struktur. Einkristallstrukturanalysen zeigten für mehrere Substanzen ein antiparalleles Packungsmuster, welches die Aufhebung des Dipolmoments auf der supramolekularen Ebene bewirkt. Die entstandenen Dimere können je nach Substituenten entweder isoliert vorliegen oder eindimensionale Stapel bilden. Andere Substanzen zeigten jedoch ein bisher unbekanntes Packungsmuster, in welchem sich die Moleküle mit parallelen Dipolmomenten in einer treppenartigen Struktur aufeinander stapeln. Das makromolekulare Dipolmoment der Treppe wird hierbei durch eine benachbarte Treppe, welche in Gegenrichtung orientiert ist, ausgeglichen. Dieses neue Packungsmotiv eignete sich sehr für guten Ladungstransport, wodurch der Wirkungsgrad einer optimierten Solarzelle des Selenderivats auf bis zu 6.2 % gesteigert werde konnte.

Chapter 6

Experimental Part

6.1 Materials and Methods

All solvents and reagents were obtained from commercial sources and used as received without further purification unless otherwise stated. Column chromatography was performed with commercial glass columns using silica gel 60M (particle size 0.04-0.063 mm) from Macherey-Nagel as stationary phase. ^{1}H NMR spectra were recorded on a Bruker Advance 400 MHz or 600 MHz spectrometer using the residual solvent peak as internal standard. All chemical shifts δ are in ppm. High-resolution mass spectra (HRMS) were recorded on an ESI MicrOTOF Focus spectrometer from Bruker Daltonics. Elemental analyses were performed on a CHN 932 analyzer (Leco Instruments GmbH, Mönchengladbach, Germany).

Origin 8.5 (OriginLab, Northampton, MA) was used as standard program to analyze, plot or fit all UV-Vis, EOA and CV data.

6.1.1 UV-Vis, EOA and CV measurements

Spectroscopic grade solvents (Uvasol) from Merck (Hohenbrunn, Germany) were used for all measurements. UV-Vis spectra of the synthesized dyes were measured on a Perkin Elmer Lambda 950, Lambda 35, or Lambda 40 UV-Vis spectrophotometer using a conventional quartz cell (light path 1 cm or 0.5 cm). Temperature was regulated by a PTP−1+1 Peltier element (Perkin Elmer). Fluorescence spectra were recorded with a PTI QM-4/2003 instrument at room temperature and analyzed with the PTI Felix32 software.

EOA measurements were carried out as follows. Dipole moments of the ground state μ_g and the dipole moment differences $\Delta\mu = \mu_e - \mu_g$ (μ_e: excited state dipole moment) of chromophores were determined by means of electro-optical absorption (EOA) spectroscopy by which the difference of absorption of a solution with ($\varepsilon^E(\varphi,\tilde{\nu})$) and

without ($\varepsilon(\tilde{\nu})$) an externally applied electric field **E** was measured with light parallely ($\varphi = 0°$) and perpendicularly ($\varphi = 90°$) polarized to the direction of **E**.[18] For uniaxial phases, induced in a solution by both an alternating and a constant electric field of about $3 \cdot 10^6$ V m^{-1}, the dichroism $\varepsilon^E(\varphi,\tilde{\nu}) - \varepsilon(\tilde{\nu})$ depends on the orientational order of the molecules due to their ground state dipole moment μ_g, the shift of the absorption band proportional to the dipole moments difference $\Delta\mu$, and on the electric field dependence of the electric transition dipole moment $\mu_{eg}(E)$. UV-Vis spectra, required for the evaluation of the integral absorption (μ^2_{eg}), were recorded with a Perkin-Elmer Lambda 950 spectrophotometer at 298 K. All measurements were carried out in anhydrous 1,4-dioxane.

Cyclic voltammetry (CV) was performed on a standard commercial electrochemical analyzer (EC epsilon; BAS Instrument, UK) in a three electrode single-compartment cell under argon. Dichloromethane (HPLC grade) was dried over calcium hydride and degassed prior to use. The supporting electrolyte tetrabutylammonium hexafluorophosphate (TBAHFP) was synthesized according to literature,[135] recrystallized from ethanol/water and dried in high vacuum. The measurements were carried out under exclusion of air and moisture at a concentration of $c \approx 10^{-4}$ M with ferrocene as internal standard for the calibration of the potential. Working electrode: Pt disc; reference electrode: Ag/AgCl; auxiliary electrode: Pt wire.

6.1.2 DFT calculations

For the calculations of the frontier molecular orbitals as well as the electrostatic surface potentials a single-point energy optimization with the Gaussian 09 software package[115a] using the B3LYP[115b-d] functional and the basis set 6-31G(d) was performed by taking the geometry of the molecules in the crystal, if the latter was provided. If no crystal was provided a geometry optimization of the molecules was performed at the same level of theory prior to calculation of the energy levels. The electrostatic surface potentials and frontier molecular orbitals were simulated from the data with the software package GaussView 5.[136] DFT calculations of the transfer integrals were done using a fragment orbital approach and a basis set orthogonalization procedure with the program ADF (Amsterdam density functional)[137] package with the basis set B3LYP and the functional TZP.

6.2 Device fabrication

6.2.1 OTFT devices

6.2.1.1 Substrates for thin films

Boron doped p-type Si(100) wafers (SiMat) were used as substrates. In the case of the untreated substrate, 100 nm SiO_2 served as dielectric layer (C_i = 34 nF cm^{-2}).

n-Tetradecylphosphonic acid (TPA) and 12,12,13,13,14,14,15,15,16,16,17,17,18,18,18-pentadecafluorooctadecylphosphonic acid (FOPA) modified substrates were prepared at the Max Planck Institut in Stuttgart in the group of Dr. Hagen Klauk. For this purpose, an 8 nm thick layer of AlO_x was deposited onto the Si/SiO_2 substrates by atomic layer deposition (ALD). The wafers were afterwards immersed in an *i*-propanol solution of TPA or FOPA to obtain highly dense monolayers with a thickness of 1.7 nm and 2.1 nm, respectively. A capacitance per unit area of C_i = 32.4 nF cm^{-2} was determined for these modified substrates. Highly reflective $Si/Al/AlO_x$/TPA substrates for spectroscopic studies were also prepared at the Max Planck Institut in Stuttgart. After thermal evaporation of a 20 nm thick aluminum layer onto silicon wafers, the substrates were briefly exposed to oxygen plasma to obtain a 3.6 nm thick AlO_x layer. The subsequent deposition of a TPA monolayer was done as described above. 15 mm thick quartz plates (Hellma Analytics) were used for additional spectroscopic studies.

6.2.1.2 Thin film and OTFT fabrication

Thin films with a nominal thickness of 30 nm were deposited onto the Si/SiO_2, TPA or FOPA modified $Si/SiO_2/AlO_x$ substrates by sublimation of the compounds under vacuum in a CreaPhys EVAP300 evaporation system. Furthermore, thin films on quartz plates were deposited by sublimation in a Boc Edwarts Auto 360 evaporation system. During the deposition on Si/SiO_2 as well as TPA and FOPA modified $Si/SiO_2/AlO_x$ substrates, the pressure was below 10^{-6} mbar. The substrate temperature was varied to improve the crystallinity of the films. The source temperature was set as needed to obtain a growth rate in the range of 0.2 - 0.8 nm min^{-1} for thin films on the Si/SiO_2 as well as TPA and FOPA modified $Si/SiO_2/AlO_x$ substrates. For thin films on quartz plates, it was set to obtain growth rates of 1.0 nm min^{-1}.

Furthermore, the fabrication of thin film transistors was carried out by thermally evaporating 30 nm gold on the active layer through a shadow mask to finally yield devices with channel lengths L of 100 µm as well as channel widths W of 200 µm. The pressure was below 10^{-6} mbar and the rate was adjusted to 1.8 - 2.4 nm min^{-1}.

6.2.1.3 OTFT characterization

Prior to characterization, all OTFTs were electrically isolated by scratching the organic film around the device with a needle of the used Micromanipulator 4060 probe station. Current voltage characteristics were recorded with an Agilent 4155C semiconductor parametric analyzer as follows. First, p-channel transfer characteristics were measured in the saturation regime at a drain-source voltage of $V_{DS} = -50$ V and a gate voltage in the range of $V_{GS} = 10$ V to −50 V. Afterwards, the corresponding output characteristics were recorded for drain-source voltages from $V_{DS} = 0$ V to −50 V at gate voltages of 0 V, −10 V, −20 V, −30 V, −40 V and −50 V. The mobility of the devices was then determined from the slope of the square root of the drain-source current I_{DS} vs. the gate voltage V_{GS} by fitting the plot in the linear regime.

6.2.2 Solar Cell fabrication and characterization

6.2.2.1 OSC fabrication

Solar cells were fabricated at the University of Cologne by the Meerholz group via thermal evaporation in a custom-made high-vacuum chamber (K.J. Lesker Co., UK) at a base pressure of 10^{-7} mbar. Commercially available indium-tin oxide (ITO) coated glass substrates were used as a transparent bottom contact. A 15 nm MoO_3 layer (99.95 %, Alfa Aesar) was applied as a hole-collecting contact on top of the ITO. The BHJ layers were fabricated by co-evaporating C_{60} (2x sublimed, CreaPhys GmbH, Dresden) and the MC dye in a 1:1 ratio at room temperature. BPhen (1x sublimed, Sensient Imaging Technologies GmbH) was utilized as an exciton blocking layer, followed by a thick 12 0nm Ag (99.9 % Alfa Aesar) top electrode. Layer thickness measurements were performed with a Veeco Dektak profilometer with a measurement accuracy of ±5 nm.

6.2.2.2 OSC characterization

The solar cell characteristics were measured at the University of Cologne by the Meerholz group using a Keithley 2425 source-measurement unit with a filtered Xe lamp, providing the AM 1.5 G solar spectrum. The intensity of the lamp was adjusted to 100 mW cm^{-2}. External quantum efficiencies (EQE) were determined using a 300 W Xenon arc lamp, a monochromator, a digital lock-in amplifier and an optical chopper (Newport Products). Absorption spectra were measured with a commercial UV-Vis spectrophotometer (PerkinElmer) in transmission geometry.

6.2.3 Thin film characterization

6.2.3.1 UV-Vis spectra of thin films

UV-Vis spectra of thin films on Si/Al/AlO_x/TPA substrates were recorded in reflection mode using an OceanOptics Maya2000 Pro spectrometer. UV-Vis spectra of thin films of dye **97** on quartz plates were recorded in transmission mode with a Perkin Elmer Lambda 950 spectrometer using an integration sphere. The normalized absorption spectra were then calculated from the obtained spectra by applying the equation $A = -\lg(T)$ and normalizing the absorption values with respect to the absorption maximum in the visible wavelength range.

6.2.3.2 AFM measurements of OTFT and OSC thin films

AFM measurements were carried out under ambient conditions in tapping mode with a Bruker AXS MultiMode™ Nanoscope IV System. The used silicon cantilevers (OMCL-AC160TS, Olympus) had a resonance frequency of ~300 kHz and a spring constant of 42 N m^{-1}).

6.2.3.3 X-ray of thin films

Powder X-ray diffraction data were collected at room temperature on a Bruker D8 Discover Diffractometer with a LynxEye-1D-Detector using Cu-$K\alpha$ radiation (unsplit $K\alpha_1$+$K\alpha_2$ doublet, mean wavelength λ = 154.19 pm). The obtained spectra were compared with the powder spectra simulated from the single crystal structure.

6.3 Synthetic procedures

Compounds (*E*)-2-(1-butyl-3,3-dimethylindolin-2-ylidene)acetaldehyde (**45**),[78-79, 82] (*E*)-2-(1,1-dimethyl-5,6-dihydro-4*H*-pyrrolo[3,2,1-*ij*]quinolin-2(1*H*)-ylidene)acetaldehyde (**49**),[81-82] 3-butyl-2-methyl-1,3-benzoxazolium iodide (**53**),[78a, 83] 3-butyl-2-methyl-1,3-benzothiazolium iodide (**54**),[78a, 83] 3-butyl-2-methyl-1,3-benzoselenazolium iodide (**55**),[78a, 83] 3,3-dichloropropen-2-al (**57**),[84] 2-(benzo[*d*][1,3]dithiol-2-ylidene)acetaldehyde (**59**),[84] sodium (*Z*)-1,2-bis(methylthio)ethene-1,2-bis(thiolate) (**61**),[86] 5-dialkylaminothiophene-2-carbaldehyde derivatives **64a-g**[88, 138] and **68a,b**,[89-90] 5-methoxythiophene-2-carbaldehyde (**70**),[91] 1-butyl-2-methylbenzo[*cd*]indol-1-ium iodide (**75**),[92] 1-butyl-4-methylquinolinium iodide (**78**),[94] 2-(3-oxo-2,3-dihydro-1*H*-inden-1-ylidene)malononitrile (**80**),[95] 4,5,6,7-tetrachloro-1*H*-indene-1,3(2*H*)-dione (**82a**),[96] 4,5,6,7-tetrabromo-1*H*-indene-1,3(2*H*)-dione (**82b**),[96] 5,6-dichloro-1*H*-indene-1,3(2*H*)-dione (**85**),[96] and 2-(4-(*tert*-butyl)thiazol-2(3*H*)-ylidene)malononitrile (**88**),[4a] were synthesized following literature procedures. All other reactants were obtained from commercial sources and used as received unless otherwise stated.

Synthesis of 2-(4,5-bis(methylthio)-1,3-dithiol-2-ylidene)acetaldehyde 62

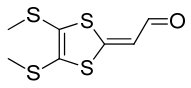

62

A 6 mL ethanol suspension of 1.5 g (7.13 mmol, 1 equiv) of 4,5-bis(methylthio)-1,3-dithiol-2-one **60** was cooled to 0 °C before 7.13 mL (14.3 mmol, 2 equiv) of freshly prepared NaOEt were dropwise added. The mixture was stirred at 0 °C for further 45 min before diethyl ether was added and was subsequently stored in the fridge for 1 h. The resulting precipitate was filtered off and washed with diethyl ether. Subsequently, the precipitate was dissolved in 10.0 mL dry THF and cooled to 0 °C. 3,3-dichloropropen-2-al **57** was dissolved in 30.0 mL dry THF and added dropwise to the reaction mixture. The latter was stirred at r.t. for 20 h before the solvent was evaporated under reduced pressure and the residue was extracted from a dichloromethane/water mixture. Compound **62** was isolated as crude product in ca. 50 % yield (0.90 g, brown oil) and was used without further purification. ^{1}H NMR (CD_2Cl_2, 400 MHz): δ 9.35 (d, J = 1.7 Hz, 1H), 6.65 (d, J = 1.7 Hz,

1H), 2.51 (s, 3H), 2.46 (s, 3H). HRMS (ESI): $[M+H]^+$: 236.95268; calcd for $[C_7H_9OS_4]^+$: 236.95307.

Synthesis of (*E*)-2-(1-butylbenzo[*cd*]indol-2(1*H*)-ylidene)acetaldehyde 76 (analogous to Ref. [93])

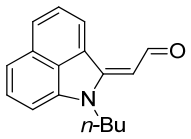

76

0.50 g (1.42 mmol, 1 equiv) salt **75** and 0.65 mL (6 equiv) DMF were dissolved in 3.0 mL acetic anhydride and refluxed for 45 min. The reaction mixture was poured into 50.0 mL diethyl ether and the resulting precipitate was filtered off and washed with diethyl ether. The obtained imine was added to a solution of 0.40 g (5.5 equiv) KOH in 20.0 mL methanol and the mixture was stirred at 70 °C for further 45 min. Water was added to the reaction mixture at r.t. and the product was extracted with dichloromethane (4 · 20.0 mL). The organic phase was dried and concentrated under reduced pressure. The aldehyde **76** was precipitated from a CH_2Cl_2/*n*-hexane mixture. Yield 0.23 g of a brown powder (0.91 mmol, 64 %). Mp = 117 – 120 °C. ^{1}H NMR (CD_2Cl_2 ,400 MHz): δ 10.39 (d, J = 7.7 Hz, 1H), 8.41 (d, J = 7.4 Hz, 1H), 7.94 (d, J = 8.1 Hz, 1H), 7.67 (dd, J = 8.1, 7.4 Hz, 1H), 7.37 - 7.50 (m, 2H), 6.85 (dd, J = 6.5, 1.2 Hz, 1H), 5.77 (d, J = 7.7 Hz, 1H), 3.89 (t, J = 7.8 Hz, 2H), 1.76 (quin, J = 8.0 Hz, 2H), 1.45 (sxt, J = 7.7 Hz, 2H), 0.97 (t, J = 7.3 Hz, 3H). HRMS (ESI): $[M+H]^+$: 252.13873; calcd for $[C_{17}H_{18}NO]^+$: 252.13829.

Synthesis of 2-(5,6-dichloro-3-oxo-2,3-dihydro-1*H*-inden-1-ylidene)malononitrile 86 (analogous to Ref. [95])

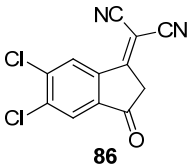

86

3.50 g (16.3 mmol, 1 equiv) 5,6-dichloro-1*H*-indene-1,3(2*H*)-dione (**85**), [96] 2.15 g (32.6 mmol, 2 equiv) malononitrile and 2.00 g (24.4 mmol, 1.5 equiv) sodium acetate were dissolved in ethanol and heated to 55 °C for 5 h. After cooling the reaction mixture, water was added and the mixture was acidified with diluted hydrochloric acid until pH = 1. The

resulting precipitate was filtered off and washed with water. Compound **86** was purified by chromatography (Acetone/*n*-hexane 20:80). Yield 2.40 g (9.12 mmol, 56 %) of a red powder. ^{1}H NMR (Acetone ,400 MHz): δ 7.93 (s, 1H), 7.16 (s, 1H). The acidic protons are not seen. MS (EI): $[M]^{+}$: 262.0; calcd for $[C_{12}H_4Cl_2N_2O]^{+}$: 261.9.

General procedure for the synthesis of precursors 111a-c

1,3-indanedione **79** or 4,5,6,7-tetrachloro-1*H*-indene-1,3(2*H*)-dione **82a** or 5,6-dichloro-1*H*-indene-1,3(2*H*)-dione (**85**) and 1.2 equiv *N*-methyl hydroxylamine were dissolved in acetone and heated to 80 °C in a pressure vessel for 20 h. The remaining acetone was evaporated under reduced pressure and the residue was purified by chromatography (CH_2Cl_2/*n*-hexane, 1:1).

Synthesis of 2-(propan-2-ylidene)-1*H*-indene-1,3(2*H*)-dione **111a**

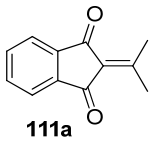

111a

Compound **111a** was obtained following the general procedure, reacting 0.50 g (3.42 mmol) of **79** and 0.34 g (4.10 mmol) *N*-methyl hydroxylamine in 10.0 mL acetone. Yield 0.30 g of a yellow powder (1.61 mmol, 47 %). Mp = 135 – 138 °C. ^{1}H NMR ($CDCl_3$, 400 MHz): δ 7.94 – 7.89 (m, 2H), 7.70 - 7.79 (m, 2H), 2.62 (s, 6H). ^{13}C NMR (CD_2Cl_2, 101 MHz): δ 191.7, 170.6, 141.5, 135.3, 127.6, 123.2, 23.8. MS (EI): $[M]^{+\cdot}$: 186.1; calcd for $[C_{12}H_5O_2]^{+\cdot}$: 186.068.

Synthesis of 4,5,6,7-tetrachloro-2-(propan-2-ylidene)-1*H*-indene-1,3(2*H*)-dione **111b**

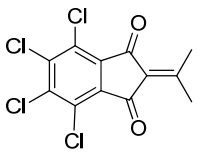

111b

Compound **111b** was obtained following the general procedure, reacting 0.50 g (1.76 mmol) of **82a** and 0.18 g (2.11 mmol) *N*-methyl hydroxylamine in 10.0 mL acetone. Yield 0.30 g of a yellow powder (0.93 mmol, 53 %). Mp = 180 – 183 °C. ^{1}H NMR ($CDCl_3$, 400 MHz): δ 2.65 (s, 6H). ^{13}C NMR (CD_2Cl_2, 101 MHz): δ 185.9, 175.7, 140.4,

135.5, 129.7, 125.8, 24.4. MS (MALDI): $[M-H]^-$: 320.986; calcd for $[C_{12}H_5Cl_4O_2]^-$: 320.90492.

Synthesis of 5,6-dichloro-2-(propan-2-ylidene)-1*H*-indene-1,3(2*H*)-dione **111c**

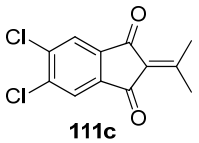

111c

Compound **111c** was obtained following the general procedure, reacting 0.10 g (0.46 mmol) of **85** and 46.0 mg (0.55 mmol) *N*-methyl hydroxylamine in 5.0 mL acetone. Yield 80.0 mg of a yellow powder (0.31 mmol, 67 %). Mp = 217 - 219 °C. ^{1}H NMR (CD_2Cl_2 ,400 MHz): δ 7.90 (s, 2H), 2.51 (s, 6H). ^{13}C NMR (CD_2Cl_2, 101 MHz): δ 188.8, 172.9, 139.7, 139.4, 126.5, 124.8, 23.6. MS (MALDI): $[M-H]^-$: 252.983; calcd for $[C_{12}H_7Cl_2O_2]^-$: 252.98286. Elemental analysis (%) calcd for $C_{12}H_8Cl_2O_2$: C, 56.50; H, 3.16; found: C, 56.03; H, 3.50.

Synthesis of acceptor material 2-(hexan-2-ylidene)-1*H*-indene-1,3(2*H*)-dione 113

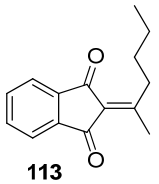

113

1,3-indanedione (1.0 g, 7 mmol), *N*-methylhydroxylamine (0.69 g, 8 mmol) and 2-hexanone (1.05 mL, 8 mmol) were heated to 125 °C in a pressure vessel for 20 h. The remaining 2-hexanone was evaporated under reduced pressure and the residue was purified by chromatography (CH_2Cl_2/*n*-hexane, 1:1). Yield 400 mg (1.75 mmol, 25 %) of a light brown viscous oil. ^{1}H NMR ($CDCl_3$, 400 MHz): δ 7.95 - 7.85 (m, 2H), 7.80 - 7.62 (m, 2H), 3.04 (t, J = 7.6 Hz, 2H), 2.61 (s, 3H), 1.56 (quin, J = 8.7 Hz, 2H), 1.46 (sxt, J = 6.9 Hz, 2H), 0.97 (t, J = 7.2 Hz, 3H). HRMS (ESI): $[M-H]^-$: 227.10672; calcd for $[C_{15}H_{15}O_2]^-$: 227.10666.

General synthetic procedure for compounds 90a,b

A 5.0 mL Ac_2O solution of one equivalent of 5-dimethylaminothiophene-2-carboxaldehyde **64a** or 5-diethylaminothiophene-2-carboxaldehyde **64b** and one equivalent of 2-(3-oxo-2,3-dihydro-1*H*-inden-1-ylidene)malononitrile **80** was heated to 90 °C for

60 min. The reaction mixture was cooled to r.t. and poured into diethyl ether. The resulting precipitate was filtered off and washed with diethyl ether, cold *i*-propanol and *n*-hexane.

Synthesis of (*Z*)-2-(2-((5-(dimethylamino)thiophen-2-yl)methylene)-3-oxo-2,3-dihydro-1*H*-inden-1-ylidene)malononitrile **90a**

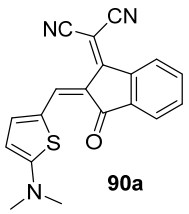

90a

For the synthesis of **90a** 1.50 g (9.66 mmol) of **64a** and 1,88 g (9.66 mmol) of **80** were reacted. Compound **90a** was recrystallized in *i*-propanol and acetic anhydride to afford 2.7 g (84 %) of a purple solid. Mp = 307 °C. ^{1}H NMR (CD_2Cl_2, 400 MHz): δ 8.59 (s, 1H), 8.50 (dd, J = 6.76 Hz, J = 1.20 Hz, 1H), 7.68 (d, J = 6.56 Hz, 1H), 7.63 - 7.55 (m, 3H), 6.35 (d, J = 5.00 Hz, 1H), 3.30 (s, 6H). HRMS (ESI): $[M]^+$: 331.07729; calcd for $[C_{19}H_{13}N_3OS]^+$: 331.07738. UV-Vis (CH_2Cl_2): λ_{max} (ε) = 572 nm (58700 M^{-1} cm^{-1}). CV: $E_{1/2,ox}$ = 542 mV vs. Fc/Fc^+, $E_{p,red}$ = - 1495 mV vs. Fc/Fc^+.

Synthesis of (*Z*)-2-(2-((5-(diethylamino)thiophen-2-yl)methylene)-3-oxo-2,3-dihydro-1*H*-inden-1-ylidene)malononitrile **90b**

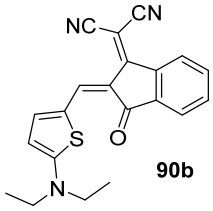

90b

For the synthesis of **90b** 1.00 g (5.45 mmol) of **64b** and 1.08 g (5.45 mmol) of **80** were reacted. Compound **90b** was recrystallized twice in *i*-propanol. Yield 1.66 g (84 %) of a purple solid. Mp = 250 °C. ^{1}H NMR (CD_2Cl_2, 400 MHz): δ 8.58 (s, 1H), 8.53 - 8.47 (m, 1H), 7.71 - 7.65 (m, 1H), 7.65 - 7.51 (m, 3H), 6.37 (d, J = 5.0 Hz, 1H), 3.62 (q, J = 7.2 Hz, 4H), 1.35 (t, J = 7.2 Hz, 6H). HRMS (ESI): $[M]^+$: 359.10814; calcd for $[C_{21}H_{17}N_3OS]^+$: 359.10923. Elemental analysis (%) calcd for $C_{21}H_{17}N_3OS$: C, 70.17; H, 4.77; N, 11.69; S, 8.92; found: C, 69.93; H, 4.72; N, 11.74; S, 8.65. UV-Vis (CH_2Cl_2): λ_{max} (ε) = 577 nm (64200 M^{-1} cm^{-1}). CV: $E_{1/2,ox}$ = 551 mV vs. Fc/Fc^+, $E_{p,red}$ = –1532 mV vs. Fc/Fc^+.

Synthesis of (*Z*)-2-(2-((5-methoxythiophen-2-yl)methylene)-3-oxo-2,3-dihydro-1*H*-inden-1-ylidene)malononitrile 91

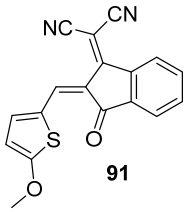

91

5-methoxythiophene-2-carboxaldehyde **70** (365 mg, 2.57 mmol) and 2-(3-oxo-2,3-dihydro-1*H*-inden-1-ylidene)malononitrile **80** (499 mg, 1 equiv) were dissolved in 5.0 mL acetic anhydride and heated to 120 °C for 4 h. After cooling, the precipitate was poured into diethyl ether, filtered off and washed with *i*-propanol and *n*-hexane. The residue was purified by chromatography (CH_2Cl_2 / Hexane 4:1) to yield in 0.465 g (57 %) of a highly insoluble orange solid. Mp = 264.84 °C. ^{1}H NMR (DMSO-d_6, 400 MHz): δ 8.65 (s, 1H), 8.50 (d, J = 7.9 Hz, 1H), 7.77 - 7.99 (m, 4H), 6.84 (d, J = 4.6 Hz, 1H), 4.16 (s, 3H). HRMS (ESI): $[M]^+$: 319.05370; calcd for $[C_{18}H_{11}N_2O_2S]^+$: 319.05357. UV-Vis (CH_2Cl_2): λ_{max} (ε) = 506 nm (41100 M^{-1} cm^{-1}). CV: $E_{p,ox}$ = 1146 mV vs. Fc/Fc^+, $E_{p,red}$ = − 1309 mV vs. Fc/Fc^+.

General synthetic procedure for compounds 92a,b

One equivalent of thiophene-2-carboxaldehyde **89a** or 5-bromothiophene-2-carboxaldehyde **89b** and one equivalent of 2-(3-oxo-2,3-dihydro-1*H*-inden-1-ylidene)malononitrile **80** were dissolved in 6.0 mL acetic anhydride and heated to 90 °C for 3 h. The reaction mixture was extracted with trichloromethane, dried and concentrated under reduced pressure.

Synthesis of (*Z*)-2-(3-oxo-2-(thiophen-2-ylmethylene)-2,3-dihydro-1*H*-inden-1-ylidene)malononitrile **92a**

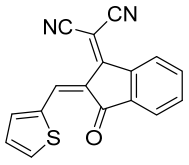

92a

For the synthesis of **92a** 500 mg (4.46 mmol) of **89a** and 866 mg (1 equiv) of **80** were reacted. Compound **92a** was purified by chromatography (CH_2Cl_2/*n*-hexane 80:20) and

precipitated from a CH_2Cl_2/*n*-hexane mixture to yield in 370 mg (29 %) of an orange powder. Mp = 228 – 230 °C. ^{1}H NMR (CD_2Cl_2, 400 MHz): δ 8.94 - 8.88 (m, 1H), 8.70 (dt, J = 7.8, 0.9 Hz, 1H), 8.00 (dt, J = 5.1, 1.2 Hz, 1H), 7.97 - 7.91 (m, 2H), 7.82 (td, J = 7.5, 1.5 Hz, 1H), 7.78 (td, J = 7.5, 1.2 Hz, 1H), 7.29 (dd, J = 5.1, 3.9 Hz, 1H). HRMS (ESI): $[M+H]^+$: 289.04310; calcd for $[C_{17}H_9BrN_2OS]^+$: 289.04301. Elemental analysis (%) calcd for $C_{17}H_8N_2OS$: C, 70.82; H, 2.80; N, 9.72; S, 11.12; found: C, 71.18; H, 2.79; N, 9.78; S, 11.04. UV-Vis (CH_2Cl_2): λ_{max} (ε) = 437 nm (20100 M^{-1} cm^{-1}).

Synthesis of (*Z*)-2-(2-((5-bromothiophen-2-yl)methylene)-3-oxo-2,3-dihydro-1*H*-inden-1-ylidene)malononitrile **92b**

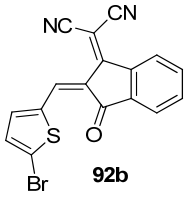

92b

For the synthesis of **92b** 500 mg (2.62 mmol) of **89b** and 510 mg (1 equiv) of **80** were reacted. Compound **92b** was purified by chromatography (CH_2Cl_2) and precipitated from a CH_2Cl_2/*n*-hexane mixture to yield in 300 mg (30 %) of a light orange solid. Mp = 261 – 263 °C. ^{1}H NMR (CD_2Cl_2, 400 MHz): δ 8.78 (d, J = 0.6 Hz, 1H), 8.71 (dt, J = 7.8, 0.9 Hz, 1H), 7.96 (ddd, J = 7.0, 1.9, 0.9 Hz, 1H), 7.84 (td, J = 7.5, 1.6 Hz, 1H), 7.80 (td, J = 7.3, 1.2 Hz, 1H), 7.61 (dd, J = 4.1, 0.6 Hz, 1H), 7.30 (d, J = 4.2 Hz, 1H). HRMS (ESI): $[M+H]^+$: 366.95338; calcd for $[C_{17}H_8BrN_2OS]^+$: 366.95352. Elemental analysis (%) calcd for $C_{17}H_7BrN_2OS$: C, 55.60; H, 1.92; N, 7.63; S, 8.73; found: C, 55.87; H, 1.91; N, 7.66; S, 8.60. UV-Vis (CH_2Cl_2): λ_{max} (ε) = 447 nm (27500 M^{-1} cm^{-1}).

Synthesis of 2-[2-(benzo[*d*][1,3]dithiol-2-ylidene)-ethylidene]-1*H*-indene-1,3(2*H*)-dione 93

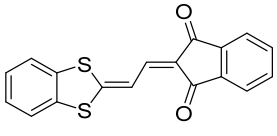

93

A 3.0 mL Ac_2O solution of 2-(benzo[*d*][1,3]dithiol-2-ylidene)acetaldehyde **59** (0.20 g, 1.03 mmol) and 1,3-indanedione **79** (0.15 g, 1.03 mmol) was heated to 90 °C for 1 h. The reaction mixture was poured into diethyl ether and the resulting precipitate was filtered off

and washed with diethyl ether, cold *i*-propanol and *n*-hexane before being recrystallized from *i*-propanol and purified by chromatography (CH_2Cl_2). Yield 100 mg (0.31 mmol, 30 %) of a red solid. Mp = 343 °C. ^{1}H NMR (CD_2Cl_2, 400 MHz): δ 7.95 (d, J = 12.8 Hz, 1H), 7.89 - 7.80 (m, 2H), 7.77 - 7.67 (m, 2H), 7.60 (d, J = 12.8 Hz, 1H), 7.56 - 7.45 (m, 2H), 7.36 - 7.26 (m, 2H). HRMS (ESI): $[M+Na]^+$: 345.00168; calcd for $[C_{18}H_{10}O_2S_2Na]^+$: 345.00144. Elemental analysis (%) calcd for $C_{18}H_{10}O_2S_2$: C, 67.06; H, 3.13; S, 19.89; found: C, 67.61; H, 3.06; S, 20.23. UV-Vis (CH_2Cl_2): λ_{max} (ε): 517 nm (62200 M^{-1} cm^{-1}). CV: $E_{p,ox}$ = 791 mV vs. Fc/Fc^+, $E_{p,red}$ = −1511 mV vs. Fc/Fc^+.

Synthesis of (*Z*)-2-(2-(2-(benzo[*d*][1,3]dithiol-2-ylidene)ethylidene)-3-oxo-2,3-dihydro-1*H*-inden-1-ylidene)malononitrile 94

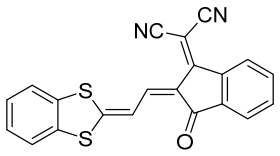

94

A 1.0 mL Ac_2O solution of 2-(benzo[*d*][1,3]dithiol-2-ylidene)acetaldehyde **59** (0.25 g, 1.3 mmol) and 2-(3-oxo-2,3-dihydro-1*H*-inden-1-ylidene)malononitrile **80** (0.25 g, 1.3 mmol, 1 equiv) was heated to 90 °C for 60 min. The reaction mixture was cooled to r.t. and poured into diethyl ether. The resulting precipitate was filtered off and washed with diethyl ether, cold *i*-propanol and *n*-hexane, before being recrystallized from *i*-propanol. Yield 0.36 g (75 %) of a violet solid. Mp = 292 – 293 °C. ^{1}H NMR ($CDCl_3$, 400 MHz): δ 8.64 (d, J = 6.6 Hz, 1H), 8.58 (d, J = 12.5 Hz, 1H), 8.39 (d, J = 12.5 Hz, 1H), 7.83 (d, J = 6.6 Hz, 1H), 7.74 - 7.66 (m, 2H), 7.63 - 7.54 (m, 2H), 7.41 - 7.34 (m, 2H). HRMS (ESI): $[M]^+$: 371.03045; calcd for $[C_{21}H_{11}N_2OS_2]^+$: 371.03073. UV-Vis (CH_2Cl_2): λ_{max} (ε) = 595 nm (61900 M^{-1} cm^{-1}). CV: $E_{p,ox}$ = 841 mV vs. Fc/Fc^+, $E_{p,red}$ = −1186 mV vs. Fc/Fc^+.

Synthesis of 2-((*Z*)-2-((*Z*)-2-(3-butylbenzo[*d*]oxazol-2(3*H*)-ylidene)ethylidene)-3-oxo-2,3-dihydro-1*H*-inden-1-ylidene)malononitrile 95

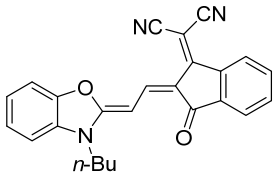

95

A 1.0 mL Ac_2O solution of 3-butyl-2-methyl-1,3-benzoxazolium iodide **53** (1.64 g, 51.8 mmol) and *N,N'*-diphenylformamidine (1.03 g, 1 equiv) was heated to 140 °C for 1 h before KOAc (0.56 g, 1.1 equiv) and 2-(3-oxo-2,3-dihydro-1*H*-inden-1-ylidene)malononitrile **80** (1.01 g, 1 equiv) were added. The reaction mixture was stirred to 120 °C for 2 h and, once cooled, poured into diethyl ether. The resulting precipitate was filtered off and washed with diethyl ether and *n*-hexane before being purified by column chromatography (CH_2Cl_2) and precipitated by addition of *n*-hexane. Yield 1.16 g (57 %) of a pink-red solid. Mp = 269 °C. ^{1}H NMR (CD_2Cl_2, 400 MHz): δ 9.06 (d, J = 13.4 Hz, 1H), 8.56 - 8.42 (m, 1H), 7.71 - 7.50 (m, 5H), 7.50 - 7.34 (m, 2H), 7.31 (d, J = 7.3 Hz, 1H), 4.15 (t, J = 7.3 Hz, 2H), 2.01 - 1.80 (m, 2H), 1.51 - 1.40 (m, 2H), 1.02 (t, J = 7.4 Hz, 3H). HRMS (ESI): $[M+H]^+$: 394.15512 calcd for $[C_{25}H_{20}N_3O_2]^+$: 394.15500. Elemental analysis (%) calcd for $C_{25}H_{19}N_3O_2$: C, 76.32; H, 4.87; N, 10.68; found: C, 76.14; H, 4.67; N, 10.74. UV-Vis (CH_2Cl_2): λ_{max} (ε) = 539 nm (46100 M^{-1} cm^{-1}). CV: $E_{1/2,ox}$ = 681 mV vs. Fc/Fc^+, $E_{p,red}$ = –1608 mV vs. Fc/Fc^+.

Synthesis of 2-((*Z*)-2-((*Z*)-2-(3-butylbenzo[*d*]thiazol-2(3*H*)-ylidene)ethylidene)-3-oxo-2,3-dihydro-1*H*-inden-1-ylidene)malononitrile 96

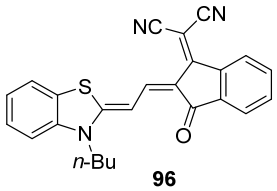

96

A 1.0 mL Ac_2O solution of 3-butyl-2-methyl-1,3-benzothiazolium iodide **54** (101 mg, 0.304 mmol) and *N,N'*-diphenylformamidine (59.1 mg, 1 equiv) was heated to 140 °C for 1 h, before KOAc (30.0 mg, 1.1 equiv) and 2-(3-oxo-2,3-dihydro-1*H*-inden-1-ylidene)malononitrile **80** (60.0 mg, 1 equiv) were added. The reaction mixture was stirred at 120 °C for 2 h before solvent removal. The residual solid was purified by column chromatography (CH_2Cl_2). Yield 46.1 mg (37 %) of a violet solid. Mp = 310 °C. ^{1}H NMR ($CDCl_3$, 400 MHz): δ 8.71 (d, J = 13.24 Hz, 1H), 8.51 (dd, J = 5.72, 1.68 Hz, 1H), 8.04 (d, J = 13.24 Hz, 1H), 7.68 (d, J = 8.48 Hz, 2H), 7.59 - 7.48 (m, 3H), 7.38 (d, J = 7.72 Hz,

1H), 7.34 (d, J = 7.64 Hz, 1H), 4.29 (t, J = 4.29 Hz, 2H), 1.92 (quint, J = 6.14 Hz, 2H), 1.58 (2H + water signal), 1.05 (t, J = 7.36 Hz, 3H). HRMS (ESI): $[M+H]^+$: 410.13111, calcd for $[C_{25}H_{20}N_3OS]^+$: 410.13271. Elemental analysis (%) calcd for $C_{25}H_{19}N_3OS$: C, 73.32; H, 4.68; N, 10.26; S, 7.83; found: C, 73.45; H, 4.60; N, 10.32; S, 7.90. UV–Vis (CH_2Cl_2): λ_{max} (ε) = 579 nm (52400 M^{-1} cm^{-1}). CV**:** $E_{p,ox}$ = 610 mV vs. Fc/Fc^+, $E_{p,red}$ = – 1582 mV vs. Fc/Fc^+.

Synthesis of 2-((*Z*)-2-((*Z*)-2-(3-butylbenzo[*d*][1,3]selenazol-2(3*H*)-ylidene)ethylidene)-3-oxo-2,3-dihydro-1*H*-inden-1-ylidene)malononitrile 97

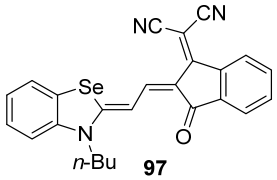

97

A 1.0 mL Ac_2O solution of 3-butyl-2-methyl-1,3-benzoselenazolium iodide **55** (100 mg, 0.263 mol) and *N,N'*-diphenylformamidine (52.0 mg, 1 equiv) was heated to 140 °C for 1.5 h before KOAc (30.0 mg, 1.1 equiv) and 2-(3-oxo-2,3-dihydro-1*H*-inden-1-ylidene)malononitrile **80** (51.0 mg, 1 equiv) were added. The reaction mixture was stirred at 120 °C for 3 h and poured into diethyl ether. The resulting precipitate was filtered off and washed with ether, before being filtered over Silica gel (CH_2Cl_2) and precipitated in *n*-hexane. Yield 30.0 mg (25 %) of a purple solid. Mp = 305 – 307 °C. ^{1}H NMR ($CDCl_3$, 400 MHz): δ 8.54 (d, J = 7.36 Hz, 1H), 8.53 (d, J = 13.76 Hz, 1H), 8.14 (d, J = 12.84 Hz, 1H), 7.71 (d, J = 6.96 Hz, 2H), 7.60 - 7.48 (m, 3H), 7.34 (d, J = 7.88 Hz, 2H), 4.30 (t, J = 7.70 Hz, 2H), 1.92 (quint, J = 8.20 Hz, 2H), 1.55 (2H + water signal), 1.07 (t, J = 7.34 Hz, 3H). HRMS (ESI): $[M]^{\bullet+}$: 457.06908, calcd for $[C_{25}H_{19}N_3OSe]^{\bullet+}$: 457.06893. Elemental analysis (%) calcd for $C_{25}H_{19}N_3OSe$: C, 65.79; H, 4.20; N, 9.21; found: C, 65.87; H, 3.97; N, 9.22. UV-Vis (CH_2Cl_2): λ_{max} (ε) = 584 nm (60200 M^{-1} cm^{-1}). CV: $E_{p,ox}$ = 626 mV vs. Fc/Fc^+, $E_{p,red}$ = −1566 mV vs. Fc/Fc^+.

Synthesis of 2-((*Z*)-2-((*E*)-2-(1-butylbenzo[*cd*]indol-2(1*H*)-ylidene)ethylidene)-3-oxo-2,3-dihydro-1*H*-inden-1-ylidene)malononitrile 99

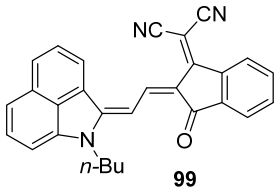

99

To 1-butyl-2-methylbenzo[*cd*]indol-1-ium iodide **75** (1.50 g, 4.27 mmol) were added 20.0 mL KOH (1 M) and the mixture was stirred at r.t. for 30 min and another 30 min after addition of 10.0 mL dichloromethane. The reaction mixture was extracted with dichloromethane (50 mL), dried and concentrated under reduced pressure. The residue was then dissolved in dry ethanol under Argon. 2-(3-oxo-2,3-dihydro-1*H*-inden-1-ylidene)malononitrile **80** (0.83 g, 1 equiv) and triethylorthoformate (1.1 mL, 1.5 equiv) were added under inert atmosphere and the mixture was refluxed for 20 h. The reaction mixture was poured into *n*-hexane and the precipitate was filtered off and purified by chromatography (CH_2Cl_2). After precipitation from a CH_2Cl_2/*n*-hexane mixture 0.20 g (11 %) of a violet solid were obtained. Mp = 286 °C. ^{1}H NMR (CD_2Cl_2, 400 MHz): δ 9.21 (d, J = 13.5 Hz, 1H), 8.82 (d, J = 7.9 Hz, 1H), 8.57 (d, J = 6.1 Hz, 1H), 8.43 (d, J = 13.6 Hz, 1H), 8.08 (d, J = 8.1 Hz, 1H), 7.83 (t, J = 7.5 Hz, 1H), 7.74 (d, J = 7.0 Hz, 1H), 7.70 - 7.47 (m, 4H), 7.19 (d, J = 7.1 Hz, 1H), 4.23 (t, J = 7.4 Hz, 2H), 1.94 (quin, J = 7.4 Hz, 2H), 1.56 (d, J = 7.5 Hz, 2H), 1.03 (t, J = 7.4 Hz, 3H). HRMS (ESI): $[M+H]^+$: 428.17555; calcd for $[C_{29}H_{22}N_3O]^+$: 428.17574. UV-Vis (CH_2Cl_2): λ_{max} (ε) = 675.75 nm (91200 M^{-1} cm^{-1}). CV: $E_{p,ox}$ = 615 mV vs. Fc/Fc^+, $E_{1/2,red}$ = −1186 mV vs. Fc/Fc^+.

Synthesis of 2-((*Z*)-2-((*E*)-2-(1-butylquinolin-4(1*H*)-ylidene)ethylidene)-3-oxo-2,3-dihydro-1*H*-inden-1-ylidene)malononitrile 101

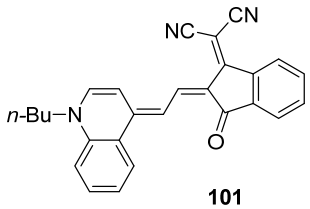

101

To *N*-butyl-4-methylquinolin-1-ium iodide **78** (1.71 g, 5.20 mmol) were added 50 mL KOH (1 M) and the mixture was stirred at r.t. for 1.5 h. The aqueous mixture, which turned from yellow to pink, was extracted with dichloromethane (50 mL), dried and concentrated under reduced pressure. The residue was then dissolved in dry ethanol. 2-(3-oxo-2,3-dihydro-1*H*-inden-1-ylidene)malononitrile **80** (1.02 g, 1 equiv) and triethylorthoformate

(1.36 mL, 1.5 equiv) were added under inert atmosphere and the mixture was refluxed for 20 h. The reaction mixture was poured into diethyl ether and the precipitate was filtered off and washed with diethyl ether, *i*-propanol and *n*-hexane, to yield 0.83 g (39 %) of a sparkling blue solid. Mp = 241 - 243°C. ^{1}H NMR ($CDCl_3$, 400 MHz): δ 8.97 (d, J = 13.84 Hz, 1H), 8.66 (d, J = 13.60 Hz, 1H), 8.56 (d, J = 8.56 Hz, 1H), 8.46 (d, J = 8.20 Hz, 1H), 7.80 (t, J = 7.82 Hz, 1H), 7.68 (d, J = 6.92 Hz, 1H), 7.66 - 7.64 (m, 1H), 7.60 (d, J = 8.08 Hz, 1H), 7.60 - 7.55 (m, 1H), 7.41 - 7.49 (m, 2H), 7.46 (J = 7.16 Hz, 1H), 4.30 (t, J = 7.32 Hz, 2H), 1.91 (quint, J = 7.45 Hz, 2H), 1.45 (sext, J = 7.56 Hz , 2H), 1.01 (t, J = 7.34 Hz, 3H). HRMS (ESI): $[M]^+$: 403.16751; calcd for $[C_{27}H_{21}N_3O]^+$: 403.16846. UV-Vis (CH_2Cl_2): λ_{max} (ε) = 656 nm (113300 $M^{-1}cm^{-1}$). CV: $E_{1/2,ox}$ = 388 mV vs. Fc/Fc^+, $E_{p,red}$ = – 1486 mV vs. Fc/Fc^+.

General synthetic procedure for compounds 102a-c and side-products

One equivalent of (*E*)-2-(1-butyl-3,3-dimethylindolin-2-ylidene)acetaldehyde **45** and one equivalent of 5,6-dichloro-1*H*-indene-1,3(2*H*)-dione **85** or 4,5,6,7-tetrachloro-1*H*-indene-1,3(2*H*)-dione **82a** or 4,5,6,7-tetrabromo-1*H*-indene-1,3(2*H*)-dione **82b**, contaminated with the respective π-extended acceptor units, were dissolved in acetic anhydride and heated to 90 °C for 60 min. The reaction mixture was poured in *n*-hexane and the resulting precipitate was purified by chromatography (CH_2Cl_2) and precipitated from a CH_2Cl_2/*n*-hexane mixture.

Synthesis of (*E*)-2-(2-(1-butyl-3,3-dimethylindolin-2-ylidene)ethylidene)-5,6-dichloro-1*H*-indene-1,3(2*H*)-dione **102a**

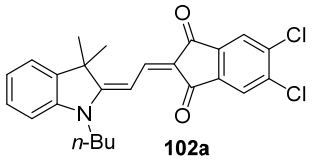

102a

Compound **102a** was synthesized following the general synthesis by reaction of **45** (0.60 g, 2.47 mmol) and **85** (0.53 g, 2.47 mmol, 1 equiv). Yield 0.63 g (58 %) of an orange crystalline solid. Mp = 222 °C. ^{1}H NMR (CD_2Cl_2, 400 MHz): δ 8.08 (d, J = 14.3 Hz, 1H), 7.79 (d, J = 0.3 Hz, 1H), 7.76 (d, J = 0.3 Hz, 1H), 7.49 (d, J = 14.3 Hz, 1H), 7.41 - 7.31 (m, 2H), 7.20 (td, J = 7.4, 1.0 Hz, 1H), 7.06 (d, J = 7.7 Hz, 1H), 3.99 (t, J = 7.5 Hz, 2H), 1.83 (quin, J = 7.7 Hz, 2H), 1.71 (s, 6H), 1.51 (sxt, J = 8.1 Hz, 2H), 1.03 (t, J = 7.4 Hz,

3H). HRMS (ESI): $[M]^+$: 439.11019; calcd for $[C_{25}H_{23}Cl_2NO_2]^+$: 439.11004. Elemental analysis (%) calcd for $C_{25}H_{23}Cl_2NO_2$: C, 68.18; H, 5.26; N, 3.18; found: C, 68.16; H, 5.49; N, 2.98. UV-Vis (CH_2Cl_2): λ_{max} (ε) = 508 nm (125800 M^{-1} cm^{-1}). CV: $E_{p,ox}$ = 669 mV vs. Fc/Fc^+, $E_{1/2,red}$ = −1790 mV vs. Fc/Fc^+.

Synthesis of (*E*)-2-(2-(1-butyl-3,3-dimethylindolin-2-ylidene)ethylidene)-4,5,6,7-tetrachloro-1*H*-indene-1,3(2*H*)-dione **102b** and side-product 2-((3*E*,5*E*)-5-(1-butyl-3,3-dimethylindolin-2-ylidene)pent-3-en-2-ylidene)-4,5,6,7-tetrachloro-1*H*-indene-1,3(2*H*)-dione **102b-2**

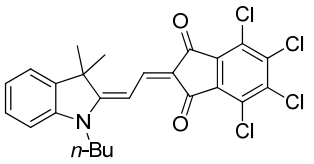

102b

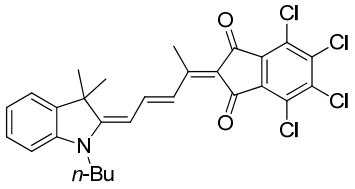

102b-2

Compound **102b** was synthesized following the general synthesis from **45** (0.25 g, 1.03 mmol) and **82a** (0.29 g, 1.03 mmol, 1 equiv). Yield 0.18 g (35 %) of an orange-red crystalline solid. Mp = 312 °C. ^{1}H NMR (CD_2Cl_2, 400 MHz): δ 8.11 (d, J = 14.4 Hz, 1H), 7.52 (d, J = 14.4 Hz, 1H), 7.38 (m, 2H), 7.23 (t, J = 7.5 Hz, 1H), 7.10 (d, J = 7.7 Hz, 1H), 4.03 (t, J = 7.4 Hz, 2H), 1.85 (quin, J = 7.5 Hz, 2H), 1.72 (s, 6H), 1.51 (sxt, J = 7.3 Hz, 2H), 1.02 (t, J = 7.4 Hz, 3H). HRMS (ESI): $[M]^+$: 507.03202; calcd for $[C_{25}H_{21}Cl_4NO_2]^+$: 507.03209. Elemental analysis (%) calcd for $C_{25}H_{21}Cl_4NO_2$: C, 58.96; H, 4.16; N, 2.75; Cl, 27.85; found: C, 58.89; H, 4.05; N, 2.84. UV-Vis (CH_2Cl_2): λ_{max} (ε) = 512 nm (117500 M^{-1} cm^{-1}). CV: $E_{p,ox}$ = 721 mV vs. Fc/Fc^+, $E_{1/2,red}$ = −1726 mV vs. Fc/Fc^+.

Side-product **102b-2**: 0.12 g (21 %) of a blue crystalline solid. Mp = 243 ºC. ^{1}H NMR (CD_2Cl_2, 400 MHz): δ 8.28 (d, J = 13.7 Hz, 1H), 8.20 (t, J = 12.8 Hz, 1H), 7.36 - 7.27 (m, 2H), 7.12 (td, J = 7.5, 0.9 Hz, 1H), 6.95 (d, J = 7.7 Hz, 1H), 6.06 (d, J = 12.4 Hz, 1H), 3.84 (t, J = 7.5 Hz, 2H), 2.73 (s, 3H), 1.83 - 1.70 (m, 2H), 1.66 (s, 6H), 1.59 - 1.39 (m, 2H), 1.00 (t, J = 7.3 Hz, 3H). HRMS (ESI): $[M+Na]^+$: 570.05267; calcd for $[C_{28}H_{25}Cl_4NNaO_2]^+$: 570.05316. Elemental analysis (%) calcd for $C_{28}H_{25}Cl_4NO_2$: C, 61.22; H, 4.59; N, 2.55; found: C, 61.04; H, 4.61; N, 2.67. UV-Vis (CH_2Cl_2): λ_{max} (ε) = 612 nm (187900 M^{-1} cm^{-1}).

Synthesis of (*E*)-4,5,6,7-tetrabromo-2-(2-(1-butyl-3,3-dimethylindolin-2-ylidene)ethylidene)-1*H*-indene-1,3(2*H*)-dione **102c** and side-product 4,5,6,7-tetrabromo-2-((3*E*,5*E*)-5-(1-butyl-3,3-dimethylindolin-2-ylidene)pent-3-en-2-ylidene)-1*H*-indene-1,3(2*H*)-dione **102c-2**

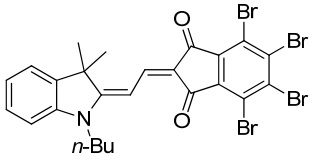

102c

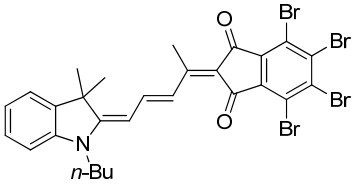

102c-2

Compound **102c** was synthesized following the general synthesis from **45** (0.25 g, 1.03 mmol) and **82b** (0.47 g, 1.03 mmol, 1 equiv). Yield 0.31 g (44 %) of an orange-red crystalline solid. Mp = 289 °C. ^{1}H NMR (CD_2Cl_2, 400 MHz): δ 8.13 (d, J = 14.4 Hz, 1H), 7.51 (d, J = 14.4 Hz, 1H), 7.45 - 7.32 (m, 2H), 7.23 (t, J = 7.5 Hz, 1H), 7.10 (d, J = 7.8 Hz, 1H), 4.04 (t, J = 7.4 Hz, 2H), 1.85 (quin, J = 7.5 Hz, 2H), 1.72 (s, 6H), 1.51 - 1.40 (m, 2H), 1.02 (t, J = 7.4 Hz, 3H). HRMS (ESI): $[M]^+$: 682.83032; calcd for $[C_{25}H_{21}Br_4NO_2]^+$: 682.83003. Elemental analysis (%) calcd for $C_{25}H_{21}Cl_4NO_2$: C, 43.70; H, 3.08; N, 2.04; found: C, 43.97; H, 2.92; N, 2.17. UV-Vis (CH_2Cl_2): λ_{max} (ε) = 515 nm (121700 M^{-1} cm^{-1}). CV: $E_{p,ox}$ = 720 mV vs. Fc/Fc^+, $E_{p,red}$ = −1781 mV vs. Fc/Fc^+.

Side-product **102c-2**: 0.07 g (9 %) of a blue crystalline solid. Mp = 240 ºC. ^{1}H NMR (CD_2Cl_2, 400 MHz): δ 8.30 (d, J = 14.4 Hz, 1H), 8.22 (d, J = 12.2 Hz, 1H), 7.40 - 7.27 (m, 2H), 7.12 (t, J = 8.2 Hz, 1H), 6.96 (d, J = 8.7 Hz, 1H), 6.07 (d, J = 12.6 Hz, 1H), 3.84 (t, J = 7.6 Hz, 2H), 2.73 (s, 3H), 1.75 (quin, J = 8.3 Hz, 2H), 1.66 (s, 6H), 1.48 (sxt, J = 7.4 Hz, 2H), 1.00 (t, J = 7.3 Hz, 3H). HRMS (ESI): $[M]^+$: 722.86130; calcd for $[C_{28}H_{25}Br_4NO_2]^+$: 722.86133. Elemental analysis (%) calcd for $^1/_2CH_2Cl_2 \cdot C_{28}H_{25}Br_4NO_2$: C, 44.48; H, 3.41; N, 1.82; found: C, 44.33; H, 3.39; N, 2.13. UV-Vis (CH_2Cl_2): λ_{max} (ε) = 616 nm (175700 M^{-1} cm^{-1}).

General synthetic procedure for compounds 103a-c

One equivalent of (*E*)-2-(1,1-dimethyl-5,6-dihydro-1*H*-pyrrolo[3,2,1-*ij*] quinolin-2(4*H*)-ylidene)acetaldehyde **49** and one equivalent of 5,6-dichloro-1*H*-indene-1,3(2*H*)-dione **85** or 4,5,6,7-tetrachloro-1*H*-indene-1,3(2*H*)-dione **82a** or 4,5,6,7-tetrabromo-1*H*-indene-1,3(2*H*)-dione **82b**, contaminated with the respective π-extended acceptor units, were

dissolved in acetic anhydride and heated to 90 °C for 60 min. The reaction mixture was poured in *n*-hexane and the resulting precipitate was purified by chromatography (CH_2Cl_2) and precipitated from a CH_2Cl_2/*n*-hexane mixture.

Synthesis of (*E*)-5,6-dichloro-2-(2-(1,1-dimethyl-5,6-dihydro-1*H*-pyrrolo[3,2,1-*ij*]quinolin-2(4*H*)-ylidene)ethylidene)-1*H*-indene-1,3(2*H*)-dione **103a**

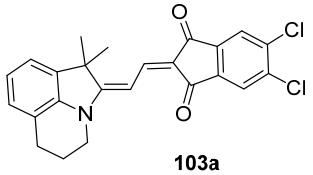

103a

Compound **103a** was synthesized following the general synthesis from **49** (0.50 g, 2.20 mmol) and **85** (0.47 g, 2.20 mmol, 1 equiv). Yield 0.49 g (53 %) of an orange crystalline solid. Mp = 313 °C. ^{1}H NMR (CD_2Cl_2, 400 MHz): δ 8.04 (d, J = 14.4 Hz, 1H), 7.77 (d, J = 0.3 Hz, 1H), 7.74 (d, J = 0.3 Hz, 1H), 7.35 (d, J = 14.4 Hz, 1H), 7.22 - 7.14 (m, 1H), 7.14 - 7.05 (m, 2H), 3.96 (br. s., 2H), 2.86 (t, J = 6.1 Hz, 2H), 2.21 (quin, J = 6.0 Hz, 2H), 1.71 (s, 6H). HRMS (ESI): $[M]^+$: 423.07881; calcd for $[C_{24}H_{19}Cl_2NO_2]^+$: 423.07874. Elemental analysis (%) calcd for $C_{24}H_{19}Cl_2NO_2$: C, 67.94; H, 4.51; N, 3.30; found: C, 67.77; H, 4.52; N, 3.20. UV-Vis (CH_2Cl_2): λ_{max} (ε) = 512 nm (120300 M^{-1} cm^{-1}). CV: $E_{p,ox}$ = 599 mV vs. Fc/Fc^+, $E_{1/2,red}$ = −1812 mV vs. Fc/Fc^+.

Synthesis of (*E*)-4,5,6,7-tetrachloro-2-(2-(1,1-dimethyl-5,6-dihydro-1*H*-pyrrolo[3,2,1-*ij*]quinolin-2(4*H*)-ylidene)ethylidene)-1*H*-indene-1,3(2*H*)-dione **103b** and side-product 4,5,6,7-tetrachloro-2-((3*E*,5*E*)-5-(1,1-dimethyl-5,6-dihydro-1*H*-pyrrolo[3,2,1-*ij*]quinolin-2(4*H*)-ylidene)pent-3-en-2-ylidene)-1*H*-indene-1,3(2*H*)-dione **103b-2**

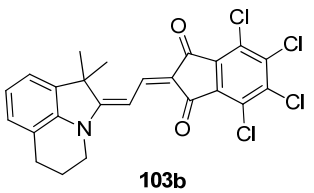

103b

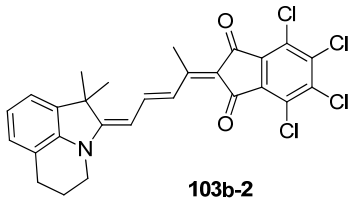

103b-2

Compound **103b** was synthesized following the general procedure from **49** (0.50 g, 2.20 mmol) and **82a** (0.63 g, 2.20 mmol, 1 equiv). Yield 0.30 g (28 %) of a pink-orange crystalline solid. Mp = decomp. at T > 350 °C. ^{1}H NMR (CD_2Cl_2, 400 MHz): δ 8.06 (d, J = 14.6 Hz, 1H), 7.43 (d, J = 14.6 Hz, 1H), 7.21 (t, J = 4.3 Hz, 1H), 7.13 (d, J = 5.0 Hz,

2H), 2.88 (t, J = 5.6 Hz, 2H), 2.22 (quin, J = 6.1 Hz, 2H), 1.72 (s, 6H). HRMS (ESI): $[M]^+$: 491.00052; calcd for $[C_{24}H_{17}Cl_4NO_2]^+$: 491.00079. Elemental analysis (%) calcd for $C_{24}H_{17}Cl_4NO_2$: C, 58.45; H, 3.47; N, 2.84; Cl, 28.75; found: C, 58.61; H, 3.50; N, 2.99. UV-Vis (CH_2Cl_2): λ_{max} (ε) = 517 nm (111700 M^{-1} cm^{-1}). CV data: $E_{p,ox}$ = 654 mV vs. Fc/Fc^+, $E_{p,red}$ = −1810 mV vs. Fc/Fc^+.

Side-product **103b-2**: 0.56 g (48 %) of a blue crystalline solid. Mp = 261 °C. ^{1}H NMR (CD_2Cl_2, 400 MHz): δ 8.27 (d, J = 13.8 Hz, 1H), 8.17 (t, J = 12.7 Hz, 1H), 7.14 (d, J = 7.3 Hz, 1H), 7.11 - 6.95 (m, 2H), 6.02 (d, J = 12.0 Hz, 1H), 3.80 (br. s., 2H), 2.83 (t, J = 6.1 Hz, 2H), 2.71 (s, 3H), 2.18 (quin, J = 5.3 Hz, 2H), 1.67 (s, 6H). HRMS (ESI): $[M]^+$: 531.03203; calcd for $[C_{27}H_{21}Cl_4NO_2]^+$: 531.03209. Elemental analysis (%) calcd for $C_{27}H_{21}Cl_4NO_2$: C, 60.81; H, 3.97; N, 2.63; found: C, 60.82; H, 3.87; N, 2.82. UV-Vis (CH_2Cl_2): λ_{max} (ε) = 619 nm (191400 M^{-1} cm^{-1}). CV: $E_{p,ox}$ = 284 mV vs. Fc/Fc^+, $E_{1/2,red}$ = −1546 mV vs. Fc/Fc^+.

Synthesis of (*E*)-4,5,6,7-tetrabromo-2-(2-(1,1-dimethyl-5,6-dihydro-1*H*-pyrrolo[3,2,1-*ij*]quinolin-2(4*H*)-ylidene)ethylidene)-1*H*-indene-1,3(2*H*)-dione **103c** and side-product 4,5,6,7-tetrabromo-2-((3*E*,5*E*)-5-(1,1-dimethyl-5,6-dihydro-1*H*-pyrrolo[3,2,1-*ij*]quinolin-2(4*H*)-ylidene)pent-3-en-2-ylidene)-1*H*-indene-1,3(2*H*)-dione **103c-2**

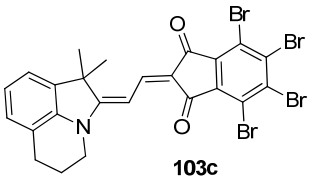

103c

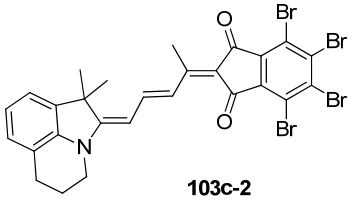

103c-2

Compound **103c** was synthesized following the general procedure from **49** (0.50 g, 2.20 mmol) and **82b** (1.01 g, 2.20 mmol, 1 equiv). Yield 0.68 g (46 %) of a pink-orange crystalline solid. Mp = decomp. at T > 325 °C. ^{1}H NMR (CD_2Cl_2, 400 MHz): δ 8.07 (d, J = 14.6 Hz, 1H), 7.42 (d, J = 14.6 Hz, 1H), 7.21 (t, J = 4.2 Hz, 1H), 7.13 (d, J = 5.0 Hz, 2H), 4.01 (br. s., 2H), 2.88 (t, J = 6.0 Hz, 2H), 2.21 (quin, J = 6.1 Hz, 2H), 1.72 (s, 6H). HRMS (ESI): $[M]^+$: 666.79830; calcd for $[C_{24}H_{17}Br_4NO_2]^+$: 666.79873. Elemental analysis (%) calcd for $C_{24}H_{17}Cl_4NO_2$: C, 42.96; H, 2.55; N, 2.09; found: C, 43.17; H, 2.48; N, 2.24. UV-Vis (CH_2Cl_2): λ_{max} (ε) = 520 nm (111800 M^{-1} cm^{-1}). CV: $E_{p,ox}$ = 662 mV vs. Fc/Fc^+, $E_{p,red}$ = −1841 mV vs. Fc/Fc^+.

Side-product **103c-2**: 0.35 g (22 %) of a blue crystalline solid. Mp = 262 ºC. ^{1}H NMR (CD_2Cl_2, 400 MHz): δ 8.28 (d, J = 13.9 Hz, 1H), 8.17 (t, J = 13.3 Hz, 1H), 7.14 (d, J = 7.3 Hz, 1H), 7.07 (d, J = 6.4 Hz, 1H), 7.02 (t, J = 7.2 Hz, 1H), 6.02 (d, J = 13.1 Hz, 1H), 3.80 (br. s., 2H), 2.83 (t, J = 6.1 Hz, 2H), 2.71 (s, 3H), 2.18 (quin, J = 6.1 Hz, 2H), 1.64 (br. s., 6H). HRMS (ESI): $[M]^+$: 706.82882; calcd for $[C_{27}H_{21}Br_4NO_2]^+$: 706.83003. Elemental analysis (%) calcd for $C_{27}H_{21}Br_4NO_2$: C, 45.61; H, 2.98; N, 1.97; found: C, 45.86; H, 2.83; N, 2.07. UV-Vis (CH_2Cl_2): λ_{max} (ε) = 623 nm (178600 M^{-1} cm^{-1}).

General synthetic procedure for 104a-c

One equivalent of 3-butyl-2-methyl-1,3-benzoxazolium iodide **53** and one equivalent of *N,N*-diphenylformamidine were stirred at 140 °C for 1.5 h in 5.0 mL acetic anhydride. After cooling the mixture, one equivalent of 5,6-dichloro-1*H*-indene-1,3(2*H*)-dione **85** or 4,5,6,7-tetrachloro-1*H*-indene-1,3(2*H*)-dione **82a** or 4,5,6,7-tetrabromo-1*H*-indene-1,3(2*H*)-dione **82b** and triethylamine (large excess) were added and the reaction mixture was stirred at 120 °C for 2 h. The obtained product was purified by chromatography or precipitated from the reaction mixture.

Synthesis of (*Z*)-2-(2-(3-butylbenzo[*d*]oxazol-2(3*H*)-ylidene)ethylidene)-5,6-dichloro-1*H*-indene-1,3(2*H*)-dione **104a**

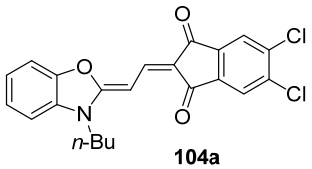

104a

Compound **104a** was synthesized following the general procedure reacting **53** (0.50 g, 1.60 mmol) with 0.31 g *N,N*-diphenylformamidine in the first step, followed by addition of 0.34 g of acceptor **85**. The residue was purified by chromatography (CH_2Cl_2/MeOH 99.5:0.5) and recrystallized from a CH_2Cl_2/*n*-hexane mixture to afford 0.30 g (45 %) of a yellow solid. Mp = 286 °C. ^{1}H NMR (CD_2Cl_2, 400 MHz): δ 8.18 (d, J = 13.8 Hz, 1H), 7.73 (d, J = 0.4 Hz, 1H), 7.75 (d, J = 0.4 Hz, 1H), 7.50 (d, J = 7.7 Hz, 1H), 7.40 (td, J = 7.7, 1.2 Hz, 1H), 7.34 (td, J = 7.7, 1.6 Hz, 1H), 7.26 (d, J = 7.8 Hz, 1H), 7.05 (d, J = 13.7 Hz, 1H), 4.09 (t, J = 7.4 Hz, 2H), 1.89 (quin, J = 7.6 Hz, 2H), 1.49 (sxt, J = 7.5 Hz, 2H), 1.02 (t, J = 7.4 Hz, 3H). HRMS (ESI): $[M]^+$: 413.05772; calcd for $[C_{22}H_{17}Cl_2NO_3]^+$: 413.05800. Elemental analysis (%) calcd for $C_{22}H_{17}Cl_2NO_3$: C, 63.78; H, 4.14; N, 3.38; found: C,

63.42; H, 4.29; N, 3.47. UV-Vis (CH_2Cl_2): λ_{max} (ε) = 482 nm (139400 M^{-1} cm^{-1}). CV data: $E_{p,ox}$ = 656 mV vs. Fc/Fc^+, $E_{p,red}$ = −1920 mV vs. Fc/Fc^+.

Synthesis of (*Z*)-2-(2-(3-butylbenzo[*d*]oxazol-2(3*H*)-ylidene)ethylidene)-4,5,6,7-tetrachloro-1*H*-indene-1,3(2*H*)-dione **104b**

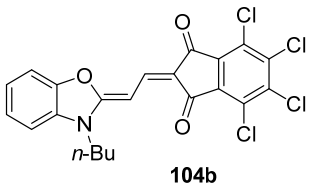

104b

Compound **104b** was synthesized following the general procedure using **53** (0.50 g, 1.60 mmol), *N,N*-diphenylformamidine (0.31 g, 1 equiv) and **82a** (0.45 g, 1 equiv). Addition of diethyl ether to the reaction mixture caused precipitation of the product, which was subsequently filtered off and washed with cold *i*-propanol and *n*-hexane. The residue was recrystallized in *i*-propanol to afford 0.47 g (62 %) of a yellow solid. Mp = 337 °C. ^1H NMR (CD_2Cl_2, 400 MHz): δ 8.18 (d, J = 13.8 Hz, 1H), 7.54 (d, J = 6.6 Hz, 1H), 7.48 - 7.33 (m, 2H), 7.29 (d, J = 7.7 Hz, 1H), 7.14 (d, J = 13.8 Hz, 1H), 4.11 (t, J = 7.3 Hz, 2H), 1.90 (quin, J = 7.1 Hz, 2H), 1.48 (sxt, J = 7.5 Hz, 2H), 1.01 (t, J = 7.3 Hz, 3H). HRMS (ESI): $[M+H]^+$: 481.98754; calcd for $[C_{22}H_{16}Cl_4NO_3]^+$: 481.98843. Elemental analysis (%) calcd for $C_{22}H_{15}Cl_4NO_3$: C, 54.69; H, 3.13; N, 2.90; found: C, 54.74; H, 3.12; N, 3.00. UV-Vis (CH_2Cl_2): λ_{max} (ε) = 486 nm (120150 M^{-1} cm^{-1}). CV: $E_{p,ox}$ = 718 mV vs. Fc/Fc^+, $E_{p,red}$ = −1822 mV vs. Fc/Fc^+.

Synthesis of (*Z*)-2-(2-(3-butylbenzo[*d*]oxazol-2(3*H*)-ylidene)ethylidene)-4,5,6,7-tetrabromo-1*H*-indene-1,3(2*H*)-dione **104c**

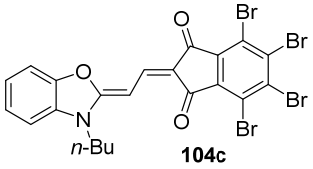

104c

Compound **104c** was synthesized following the general procedure reacting **53** (0.50 g, 1.60 mmol), *N,N*-diphenylformamidine (0.31 g, 1 equiv) and **82b** (0.73 g, 1 equiv). Addition of diethyl ether to the reaction mixture caused precipitation of the product, which was filtered off and washed with cold *i*-propanol and *n*-hexane. The residue was

recrystallized in a CH_2Cl_2/*n*-hexane/ethyl acetate/ 2:1:2 mixture to afford 0.56 g (54 %) of a yellow solid. Mp = 343 °C. ^{1}H NMR (CD_2Cl_2, 400 MHz): δ 8.18 (d, J = 13.9 Hz, 1H), 7.53 (d, J = 7.7 Hz, 1H), 7.38 (dtd, J = 16.7, 7.5, 1.7 Hz, 2H), 7.28 (d, J = 6.9 Hz, 1H), 7.14 (d, J = 13.9 Hz, 1H), 4.12 (t, J = 7.3 Hz, 2H), 1.90 (quin, J = 7.5 Hz, 2H), 1.48 (sxt, J = 7.6 Hz, 2H), 1.01 (t, J = 7.3 Hz, 3H). HRMS (ESI): $[M+H]^+$: 657.78566; calcd for $[C_{22}H_{16}Br_4NO_3]^+$: 657.78582. Elemental analysis (%) calcd for $C_{22}H_{15}Cl_4NO_3$: C, 40.24; H, 2.33; N, 2.22; found: C, 39.98; H, 2.24; N, 2.12. UV-Vis (CH_2Cl_2): λ_{max} (ε) = 489 nm (123200 M^{-1} cm^{-1}). CV: $E_{p,ox}$ = 716 mV vs. Fc/Fc^+, $E_{p,red}$ = −1794 mV vs. Fc/Fc^+.

General synthetic procedure for compounds 105a-c

One equivalent of 3-butyl-2-methyl-1,3-benzothiazolium iodide **54** and one equivalent of *N,N*-diphenylformamidine were stirred at 140 °C for 40 min - 1.5 h in 5.0 mL acetic anhydride. After cooling the mixture, one equivalent of 5,6-dichloro-1*H*-indene-1,3(2*H*)-dione **85** or 4,5,6,7-tetrachloro-1*H*-indene-1,3(2*H*)-dione **82a** or 4,5,6,7-tetrabromo-1*H*-indene-1,3(2*H*)-dione **82b** and triethylamine (large excess) were added and the reaction mixture was stirred at 120 °C for 2 - 3 h. Diethyl ether was added at r.t. and the resulting precipitate was filtered off and washed with cold *i*-propanol and *n*-hexane. The residue was purified by chromatography.

Synthesis of (*Z*)-2-(2-(3-butylbenzo[*d*]thiazol-2(3*H*)-ylidene)ethylidene)-5,6-dichloro-1*H*-indene-1,3(2*H*)-dione **105a**

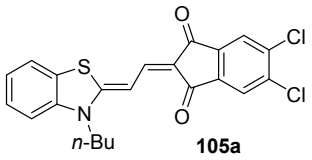

105a

Compound **105a** was synthesized following the general procedure. **54** (0.50 g, 1.50 mmol) and *N,N*-diphenylformamidine (0.29 g, 1 equiv) were reacted for 1 h before **85** (0.32 g, 1 equiv) was added and the mixture was reacted for further 3 h. Compound **105a** was purified by chromatography (CH_2Cl_2/MeOH 99.5:0.5) and precipitated from a CH_2Cl_2/*n*-hexane mixture to afford 0.30 g (46 %) of a red solid. Mp = 300 °C. ^{1}H NMR (CD_2Cl_2, 400 MHz): δ 7.81 (d, J = 13.6 Hz, 1 H), 7.74 (s, 1H), 7.71 (s, 1H), 7.68 (d, J = 8.0 Hz, 1H), 7.58 (d, J = 13.6 Hz, 1H), 7.49 (t, J = 8.4 Hz, 1H), 7.35 (dd, J = 7.7, 4.9 Hz, 2H), 4.24 (t, J = 7.5 Hz, 2H), 1.88 (quin, J = 7.7 Hz, 2H), 1.54 (sxt, J = 7.7 Hz, 2H), 1.05 (t, J = 7.4 Hz,

3H). HRMS (ESI): $[M]^+$: 429.03476; calcd for $[C_{22}H_{17}Cl_2NO_2S]^+$: 429.03516. Elemental analysis (%) calcd for $C_{22}H_{17}Cl_2NO_2S$: C, 61.40; H, 3.98; N, 3.25; found: C, 61.56; H, 3.96; N, 3.13. UV-Vis (CH_2Cl_2): λ_{max} (ε) = 519 nm (154200 M^{-1} cm^{-1}). CV data: $E_{p,ox}$ = 586 mV vs. Fc/Fc^+, $E_{p,red}$ = −1797 mV vs. Fc/Fc^+.

Synthesis of (*Z*)-2-(2-(3-butylbenzo[*d*]thiazol-2(3*H*)-ylidene)ethylidene)-4,5,6,7-tetrachloro-1*H*-indene-1,3(2*H*)-dione **105b**

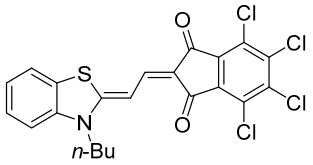

105b

Compound **105b** was synthesized following the general procedure. **54** (0.50 g, 1.50 mmol) and *N,N*-diphenylformamidine (0.40 g, 1 equiv) were reacted for 1.5 h prior addition of **82a** (0.43 g, 1 equiv) and 3 h afterwards. Compound **105b** was purified by chromatography (CH_2Cl_2) and precipitated from a CH_2Cl_2/*n*-hexane mixture to afford 0.39 g (52 %) of a pink-orange solid. Mp = 295 °C. ^1H NMR (CD_2Cl_2, 400 MHz): δ 7.81 (d, J = 13.8 Hz, 1H), 7.69 (d, J = 7.7 Hz, 1H), 7.62 (d, J = 13.7 Hz, 1H), 7.50 (ddd, J = 8.6, 7.1, 1.1 Hz, 1H), 7.35 (t, J = 7.9 Hz, 2H), 4.27 (t, J = 7.8 Hz, 2H), 1.89 (quin, J = 7.5 Hz, 2H), 1.53 (sxt, J = 8.0 Hz, 2H), 1.03 (t, J = 7.4 Hz, 3H). HRMS (ESI): $[M]^+$: 496.95697; calcd for $[C_{22}H_{15}Cl_4NO_2S]^+$: 496.95721. Elemental analysis (%) calcd for $C_{22}H_{15}Cl_4NO_2S$: C, 52.93; H, 3.03; N, 2.81; S, 6.42; found: C, 53.31; H, 3.06; N, 2.99; S, 6.37. UV-Vis (CH_2Cl_2): λ_{max} (ε) = 523 nm (141100 M^{-1} cm^{-1}). CV: $E_{p,ox}$ = 662 mV vs. Fc/Fc^+, $E_{p,red}$ = −1730 mV vs. Fc/Fc^+.

Synthesis of (*Z*)-2-(2-(3-butylbenzo[*d*]thiazol-2(3*H*)-ylidene)ethylidene)-4,5,6,7-tetrabromo-1*H*-indene-1,3(2*H*)-dione **105c**

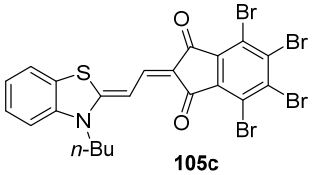

105c

Compound **105c** was synthesized following the general procedure. **54** (0.50 g, 1.50 mmol) and *N,N*-diphenylformamidine (0.30 g, 1 equiv) were reacted for 40 min before **82b**

(0.70 g, 1 equiv) was added and the mixture was reacted for further 2 h. Compound **105c** was purified by chromatography (CH_2Cl_2) and precipitated from a CH_2Cl_2/*n*-hexane mixture to afford 0.18 g (17 %) of a pink-orange solid. Mp = 304 °C. ^{1}H NMR (CD_2Cl_2, 400 MHz): δ 7.84 (d, J = 13.8 Hz, 1H), 7.70 (d, J = 7.3 Hz, 1H), 7.62 (d, J = 13.8 Hz, 1H), 7.51 (t, J = 8.6 Hz, 1H), 7.37 (t, J = 7.9 Hz, 2H), 4.28 (t, J = 7.6 Hz, 2H), 1.90 (quin, J = 7.7 Hz, 2H), 1.59 - 1.46 (m, 1H), 1.03 (t, J = 7.3 Hz, 3H). HRMS (ESI): $[M]^+$: 672.75533; calcd for $[C_{22}H_{15}Br_4NO_2S]^+$: 672.75515. Elemental analysis (%) calcd for $C_{22}H_{15}Br_4NO_2S$: C, 39.03; H, 2.23; N, 2.07; S, 4.74; found: C, 39.11; H, 2.18; N, 2.19; S, 4.68. UV-Vis (CH_2Cl_2): λ_{max} (ε) = 526 nm (144800 M^{-1} cm^{-1}). CV: $E_{p,ox}$ = 644 mV vs. Fc/Fc^+, $E_{p,red}$ = −1758 mV vs. Fc/Fc^+.

General procedure for the synthesis of 106 and 107

One equivalent of (*E*)-2-(1-butyl-3,3-dimethylindolin-2-ylidene)acetaldehyde **45** or (*E*)-2-(1,1-dimethyl-5,6-dihydro-1*H*-pyrrolo[3,2,1-*ij*]quinolin-2(4*H*)-ylidene)acetaldehyde **49** and one equivalent of 2-(5,6-dichloro-3-oxo-2,3-dihydro-1*H*-inden-1-ylidene)malononitrile **86** were dissolved in acetic anhydride and heated to 90 °C for 60 min. Diethyl ether was added at r.t. and the resulting precipitate was filtered off and washed with diethyl ether, cold *i*-propanol and *n*-hexane. The residue was purified by chromatography (CH_2Cl_2) and precipitated from a CH_2Cl_2/*n*-hexane mixture.

Synthesis of 2-((*Z*)-2-((*E*)-2-(1-butyl-3,3-dimethylindolin-2-ylidene)ethylidene)-5,6-dichloro-3-oxo-2,3-dihydro-1*H*-inden-1-ylidene)malononitrile **106**

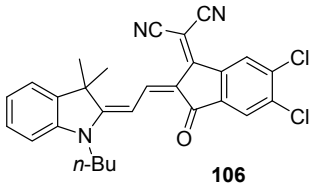

106

Compound **106** was synthesized following the general procedure reacting **45** (0.50 g, 2.10 mmol) and **86** (0.54 g, 2.10 mmol, 1 equiv). Yield 0.24 g (24 %) of a violet solid. Mp = 255 °C. ^{1}H NMR (CD_2Cl_2, 400 MHz): δ 9.01 (d, J = 13.9 Hz, 1H), 8.60 (s, 1H), 8.06 (d, J = 13.9 Hz, 1H), 7.72 (s, 1H), 7.40 (td, J = 7.3, 1.1 Hz, 2H), 7.28 (ddd, J = 7.7, 6.9, 1.0 Hz, 1H), 7.16 (dd, J = 7.6, 1.7 Hz, 1H), 4.08 (t, J = 7.5 Hz, 2H), 1.78 (s, 6H), 1.87 (quin, J = 8.2 Hz, 2H), 1.52 (sxt, J = 7.6 Hz, 2H), 1.03 (t, J = 7.4 Hz, 3H). HRMS (ESI):

$[M]^+$: 487.12093; calcd for $[C_{28}H_{23}Cl_2N_3O]^+$: 487.12127. Elemental analysis (%) calcd for $C_{28}H_{23}Cl_2N_3O$: C, 68.86; H, 4.75, N, 8.60; found: C, 68.83; H, 4.70; N, 8.48. UV-Vis (CH_2Cl_2): λ_{max} (ε) = 578 nm (59700 M^{-1} cm^{-1}). CV data: $E_{1/2,ox}$ = 745 mV vs. Fc/Fc^+, $E_{1/2,red}$ = −1411 mV vs. Fc/Fc^+.

Synthesis of 2-((*Z*)-5,6-dichloro-2-((*E*)-2-(1,1-dimethyl-5,6-dihydro-1*H*-pyrrolo[3,2,1-*ij*]quinolin-2(4*H*)-ylidene)ethylidene)-3-oxo-2,3-dihydro-1*H*-inden-1-ylidene)malononitrile **107**

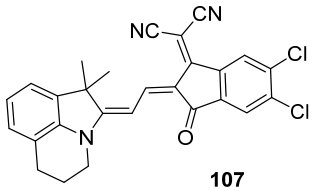

107

Compound **107** was synthesized following the general procedure reacting compounds **49** (0.50 g, 2.20 mmol) and **86** (0.56 g, 2.20 mmol, 1 equiv). Yield 0.35 g (33 %) of a violet solid. Mp = 320 °C. ^{1}H NMR (CD_2Cl_2, 400 MHz): δ 8.95 (d, J = 14.1 Hz, 1H), 8.59 (d, J = 0.3 Hz, 1H), 7.91 (d, J = 14.1 Hz, 1H), 7.70 (d, J = 0.3 Hz, 1H), 7.32 - 7.04 (m, 3H), 4.08 (t, J = 6.3 Hz, 2H), 2.90 (t, J = 6.1 Hz, 2H), 2.24 (quin, J = 6.2 Hz, 2H), 1.77 (s, 6H). HRMS (ESI): $[M]^+$: 471.08984; calcd for $[C_{27}H_{19}Cl_2N_3O]^+$: 471.08997. Elemental analysis (%) calcd for $C_{27}H_{19}Cl_2N_3O$: C, 68.65; H, 4.05; N, 8.90; found: C, 68.37; H, 4.00; N, 8.77. UV-Vis (CH_2Cl_2): λ_{max} (ε) = 579 nm (54600 M^{-1} cm^{-1}). CV data: $E_{1/2,ox}$ = 693 mV vs. Fc/Fc^+, $E_{1/2,red}$ = −1433 mV vs. Fc/Fc^+.

General procedure for the synthesis of 108 - 110

One equivalent of 3-butyl-2-methyl-1,3-benzoxazolium iodide **53** or 3-butyl-2-methyl-1,3-benzothiazolium iodide **54** or 3-butyl-2-methyl-1,3-benzoselenazolium iodide **55** and one equivalent of *N,N*-diphenylformamidine were stirred at 140 °C for 1 h in 10.0 mL acetic anhydride. After cooling the mixture, one equivalent of 2-(5,6-dichloro-3-oxo-2,3-dihydro-1*H*-inden-1-ylidene)malononitrile **86** and triethylamine (large excess) were added and the reaction mixture was stirred at 120 °C for 2 - 3 h. Diethyl ether was added at r.t. and the resulting precipitate was filtered off and washed with cold *i*-propanol and *n*-hexane. The residue was purified by chromatography (CH_2Cl_2) and precipitated from a CH_2Cl_2/*n*-hexane mixture.

Synthesis of 2-((*Z*)-2-((*Z*)-2-(3-butylbenzo[*d*]oxazol-2(3*H*)-ylidene)ethylidene)-5,6-dichloro-3-oxo-2,3-dihydro-1*H*-inden-1-ylidene)malononitrile **108**

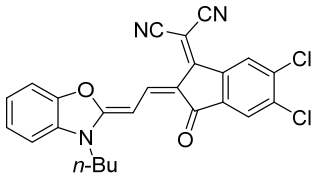

108

Compound **108** was synthesized following the general procedure from **53** (0.50 g, 1.60 mmol), *N,N*-diphenylformamidine (0.30 g, 1 equiv) and **86** (0.42 g, 1 equiv). Yield 0.07 g (9 %) of a pink solid. Mp = 315 °C. ^{1}H NMR (CD_2Cl_2, 400 MHz): δ 9.05 (d, J = 13.5 Hz, 1H), 8.57 (s, 1H), 7.66 (br. s, 1H), 7.62 (d, J = 7.9 Hz, 1H), 7.69 (s, 1H), 7.45 (quint, J = 7.5, 1.5 Hz, 2H), 7.36 (d, J = 7.1 Hz, 1H), 4.18 (t, J = 7.3 Hz, 2H), 1.92 (quin, J = 7.6 Hz, 2H), 1.49 (sxt, J = 7.9 Hz, 2H), 1.02 (t, J = 7.4Hz, 3H). HRMS (ESI): $[M]^+$: 461.06961; calcd for $[C_{25}H_{17}Cl_2N_3O_2]^+$: 461.06923. UV-Vis ($CH_2Cl_2$): λ_{max} (ε) = 543 nm (44450 M^{-1} cm^{-1}). CV data: $E_{p,ox}$ = 741 mV vs. Fc/Fc^+, $E_{1/2,red}$ = −1475 mV vs. Fc/Fc^+.

Synthesis of 2-((*Z*)-2-((*Z*)-2-(3-butylbenzo[*d*]thiazol-2(3*H*)-ylidene)ethylidene)-5,6-dichloro-3-oxo-2,3-dihydro-1*H*-inden-1-ylidene)malononitrile **109**

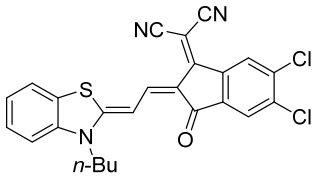

109

Compound **109** was synthesized following the general procedure from **54** (0.50 g, 1.50 mmol), *N,N*-diphenylformamidine (0.29 g, 1 equiv) and **86** (0.39 g, 1 equiv). Yield 0.03 g (4 %) of a violet solid. Mp = 343 - 344°C. ^{1}H NMR (CD_2Cl_2, 400 MHz): δ 8.70 (d, J = 13.5 Hz, 1H), 8.54 (s, 1H), 8.06 (d, J = 13.5 Hz, 1H), 7.77 (d, J = 8.1 Hz, 1H), 7.67 (s, 1H), 7.57 (ddd, J = 8.4, 7.5, 1.1 Hz, 1H), 7.50 - 7.34 (m, 2H), 4.34 (t, J = 7.9 Hz, 2H), 1.91 (quin, J = 7.7 Hz, 2H), 1.53 (sxt, J = 7.6 Hz, 2H), 1.03 (t, J = 7.4 Hz, 3H). HRMS (ESI): $[M]^+$: 477.04675; calcd for $[C_{25}H_{17}Cl_2N_3OS]^+$: 477.04639. UV-Vis ($CH_2Cl_2$): λ_{max} (ε) = 575 nm (53100 M^{-1} cm^{-1}). CV data: $E_{p,ox}$ = 693 mV vs. Fc/Fc^+, $E_{1/2,red}$ = −1416 mV vs. Fc/Fc^+.

Synthesis of 2-((*Z*)-2-((*Z*)-2-(3-butylbenzo[*d*][1,3]selenazol-2(3*H*)-ylidene)ethylidene)-5,6-dichloro-3-oxo-2,3-dihydro-1*H*-inden-1-ylidene)malononitrile **110**

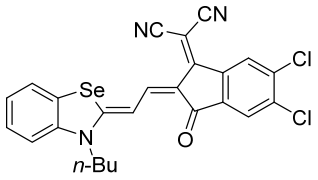

110

Compound **110** was synthesized following the general procedure from **55** (0.75 mg, 0.20 mol), *N,N*-diphenylformamidine (0,39 g, 1 equiv) and **86** (0.52 g, 1 equiv). Yield 83 mg (8 %) of a purple solid. Mp = 356 °C. ^{1}H NMR (CD_2Cl_2, 400 MHz): δ 8.71 (d, J = 13.4 Hz, 1H), 8.56 (s, 1H), 8.07 (d, J = 13.5 Hz, 1H), 7.78 (d, J = 8.6 Hz, 1H), 7.68 (s, 1H), 7.57 (d, J = 8.3 Hz, 1H), 7.46 (t, J = 7.6 Hz, 2H), 4.35 (t, J = 7.3 Hz, 2H), 1.92 (quin, J = 9.1 Hz, 2H),), 1.57 (2H + water signal), 1.04 (t, J = 7.4 Hz, 3H). HRMS (ESI): $[M+H]^+$: 525.99785; calcd for $[C_{25}H_{18}Cl_2N_3SeO]^+$: 525.99834. Elemental analysis (%) calcd for $C_{25}H_{17}Cl_2N_3SeO$: C, 57.16; H, 3.26; N, 7.99; found: C, 57.07; H, 3.25; N, 7.86. UV-Vis (CH_2Cl_2): λ_{max} (ε) = 581 nm (42500 M^{-1} cm^{-1}). CV: $E_{p,ox}$ = 660 mV vs. Fc/Fc^+, $E_{1/2,red}$ = −1480 mV vs. Fc/Fc^+.

General procedure for the synthesis of 112a,b

One equivalent of (*E*)-2-(1-butyl-3,3-dimethylindolin-2-ylidene)acetaldehyde **45** and one equivalent of 2-(propan-2-ylidene)-1*H*-indene-1,3(2*H*)-dione **111a** or 4,5,6,7-tetrachloro-2-(propan-2-ylidene)-1*H*-indene-1,3(2*H*)-dione **111b** where dissolved in acetic anhydride and heated to 90 °C for 60 min. Diethyl ether was added at r.t. and the resulting precipitate was filtered off and washed with diethyl ether, cold *i*-propanol and *n*-hexane.

Synthesis of 2-((*E*)-5-((*E*)-1-butyl-3,3-dimethylindolin-2-ylidene)pent-3-en-2-ylidene)-1*H*-indene-1,3(2*H*)-dione **112a**

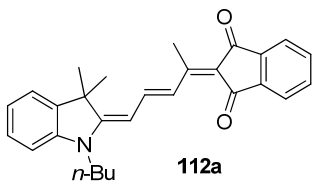

112a

Compound **112a** was synthesized following the general procedure, reacting 0.13 g (0.54 mmol) of **45** and 0.10 g (0.54 mmol) of **111a**. Yield 95.0 mg (0.23 mmol, 43 %) of a

blue powder. ^{1}H NMR (CD_2Cl_2, 400 MHz): δ 8.24 (d, J = 14.2 Hz, 1H), 8.05 (dd, J = 14.2, 12.5 Hz, 1H), 7.68 - 7.78 (m, 2H), 7.57 - 7.67 (m, 2H), 7.22 - 7.29 (m, 2H), 7.03 (td, J = 7.4, 0.9 Hz, 1H), 6.85 (d, J = 8.2 Hz, 1H), 5.94 (d, J = 12.6 Hz, 1H), 3.78 (t, J =7.6 Hz, 2H), 2.74 (s, 3H), 1.72 (quin, J = 7.3 Hz, 2H), 1.46 (sxt, J = 7.8 Hz, 2H), 0.99 (t, J = 7.4 Hz, 3H). MS (MALDI): $[M]^+$: 411.160; calcd for $[C_{28}H_{25}Cl_4NO_2]^+$: 411.219.

Synthesis of 2-((*E*)-5-((*E*)-1-butyl-3,3-dimethylindolin-2-ylidene)pent-3-en-2-ylidene)-4,5,6,7-tetrachloro-1*H*-indene-1,3(2*H*)-dione **112b**

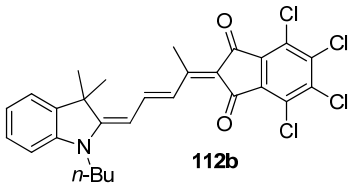

112b

Compound **112b** was synthesized following the general procedure, reacting 75.0 mg (0.31 mmol) of **45** and 0.10 g (0.31 mmol) of **111b**. Yield 95.0 mg (0.17 mmol, 56 %) of a blue powder. For characterization see **102b-2**.

2-((1*E*,2*E*)-1-(1-butyl-3,3-dimethylindolin-2-ylidene)oct-2-en-4-ylidene)-1*H*-indene-1,3(2*H*)-dione 114

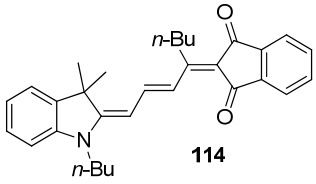

114

A 5.0 mL Ac_2O solution of (*E*)-2-(1-butyl-3,3-dimethylindolin-2-ylidene)acetaldehyde **45** (426 mg, 1.8 mmol), 2-(hexan-2-ylidene)-1*H*-indene-1,3(2*H*)-dione (400 mg, 1.8 mmol) **113** and potassium acetate (200 mg, 2.1 mmol) was stirred at r.t. for 1 h before diethyl ether was added. The potassium acetate was filtered off and the filtrate was concentrated under reduced pressure before being twice purified by chromatography (CH_2Cl_2/*n*-hexane, 4:6). Yield 427 mg (0.94 mmol, 52 %) of a blue-violet powder. Mp = 110 °C. ^{1}H NMR (CD_2Cl_2, 400 MHz): δ 8.19 (d, J = 14.4 Hz, 1H), 8.05 (dd, J = 14.3, 12.5 Hz, 1H), 7.77 - 7.67 (m, 2H), 7.67 - 7.57 (m, 2H), 7.31 - 7.19 (m, 2H), 7.03 (td, J = 7.4, 0.9 Hz, 1H), 6.85 (d, J = 7.4 Hz, 1H), 5.94 (d, J = 12.5 Hz, 1H), 3.78 (t, J = 7.7 Hz, 2H), 3.28 (t, J = 7.6 Hz, 2H), 1.73 (quin, J = 7.8 Hz, 2H), 1.64 (s, 6H), 1.63 - 1.53 (m, 4H), 1.46 (sxt, J = 7.5 Hz, 2H), 1.02 (t, J = 6.9 Hz, 3H), 1.00 (t, J = 7.7 Hz, 3H). HRMS (ESI): $[M]^+$:

453.26655; calcd for $[C_{31}H_{35}NO_2]^+$: 453.26623. Elemental analysis (%) calcd for $C_{31}H_{35}NO_2$: C, 82.08; H, 7.78; N, 3.09; found: C, 82.46; H, 8.05; N, 3.12. UV-Vis (CH_2Cl_2): λ_{max} (ε) = 584 nm (113300 M^{-1} cm^{-1}).

(*E*)-2-(1-(5-(dibutylamino)thiophen-2-yl)hept-1-en-3-ylidene)-1*H*-indene-1,3(2*H*)-dione 115

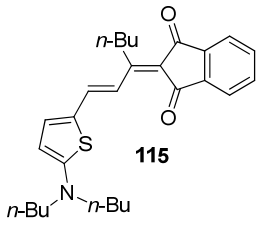

115

A 3.0 mL Ac_2O solution of 5-(dibutylamino)thiophene-2-carbaldehyde **64e** (524 mg, 2.19 mmol), and 2-(hexan-2-ylidene)-1*H*-indene-1,3(2*H*)-dione **113** (500 mg, 2.19 mmol) was heated to 90 °C for 1 h before the solvent was concentrated under reduced pressure and the residue purified twice by chromatography (CH_2Cl_2). Yield 380 mg (0.85 mmol, 39 %) of a blue powder. Mp = 80 – 82 °C. ^{1}H NMR (CD_2Cl_2, 400 MHz): δ 8.36 (d, J = 15.0 Hz, 1H), 7.77 - 7.66 (m, 2H), 7.62 (dt, J = 8.6, 3.2 Hz, 3H), 7.17 (d, J = 4.4 Hz, 1H), 5.95 (d, J = 4.4 Hz, 1H), 3.39 (t, J = 7.7 Hz, 4H), 3.22 (t, J = 7.7 Hz, 2H), 1.68 (quin, J = 7.9 Hz, 4H), 1.60 - 1.46 (m, 4H), 1.39 (sxt, J = 7.2 Hz, 4H), 0.98 (t, J = 6.8 Hz, 9H). HRMS (ESI): $[M]^+$: 449.23842; calcd for $[C_{28}H_{35}NO_2S]^+$: 449.23830. Elemental analysis (%) calcd for $C_{28}H_{35}NO_2S$: C, 74.79; H, 7.85; N, 3.12; found: C, 74.99; H, 8.08; N, 3.05. UV-Vis (CH_2Cl_2): λ_{max} (ε) = 611 nm (85300 M^{-1} cm^{-1}).

2-((1*E*,2*E*)-1-(1-butylbenzo[*cd*]indol-2(1*H*)-ylidene)oct-2-en-4-ylidene)-1*H*-indene-1,3(2*H*)-dione 116

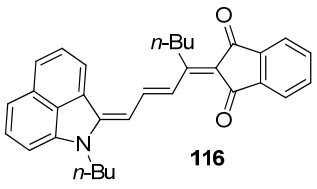

116

A 3.0 mL Ac_2O solution of (*E*)-2-(1-butylbenzo[*cd*]indol-2(1*H*)-ylidene)acetaldehyde **76** (150 mg, 0.59 mmol), 2-(hexan-2-ylidene)-1*H*-indene-1,3(2*H*)-dione (136 mg, 0.59 mmol) **113** and potassium acetate (60 mg, 0.59 mmol) was stirred at r.t. for 4.25 h before the solvent was evaporated under reduced pressure. The residue was purified by

chromatography (CH_2Cl_2). Yield 150 mg (0.32 mmol, 55 %) of a blue powder. Mp = 204 – 206 °C. ^{1}H NMR (CD_2Cl_2, 400 MHz): δ 8.46 (m, 2H), 8.03 (d, J = 7.3 Hz, 1H), 7.84 (d, J = 8.1 Hz, 1H), 7.81 - 7.72 (m, 2H), 7.72 - 7.61 (m, 3H), 7.44 (dd, J = 8.3, 7.3 Hz, 1H), 7.35 (d, J = 8.2 Hz, 1H), 6.79 (d, J = 7.1 Hz, 1H), 6.40 (d, J = 10.9 Hz, 1H), 3.97 (t, J = 7.4 Hz, 2H), 3.39 (t, J = 7.3 Hz, 2H), 1.80 (quin, J = 7.7 Hz, 2H), 1.75 - 1.56 (m, 4H), 1.49 (sxt, J = 7.7 Hz, 2H), 1.06 (t, J = 6.9 Hz, 3H), 1.00 (t, J = 7.6 Hz, 3H). HRMS (ESI): $[M]^+$: 461.23518; calcd for $[C_{32}H_{31}NO_2]^+$: 461.234493. Elemental analysis (%) calcd for $H_2O{\cdot}C_{32}H_{31}NO_2$: C, 80.14; H, 6.94; N, 2.92; found: C, 80.11; H, 7.31; N, 2.52. UV-Vis (CH_2Cl_2): λ_{max} (ε) = 635 nm (61200 M^{-1} cm^{-1}).

2-((1*Z*,2*E*)-1-(3-butylbenzo[*d*]thiazol-2(3*H*)-ylidene)oct-2-en-4-ylidene)-1*H*-indene-1,3(2*H*)-dione 117

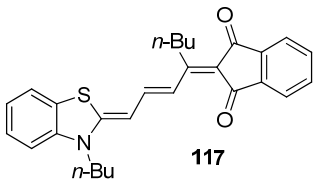

117

A 5.0 mL Ac_2O suspension of 3-butyl-2-methylbenzo[*d*]thiazol-3-ium iodide **54** (300 mg, 0.90 mmol), and DPFA (177 mg, 0.90 mmol) was heated at 140 °C for 1 h before it was cooled to r.t. and poured into diethyl ether. To a 4.0 mL Ac_2O solution of the filtrated pink precipitate were added 2-(hexan-2-ylidene)-1*H*-indene-1,3(2*H*)-dione **113** (205 mg, 0.90 mmol) and potassium acetate (140 mg, 1.35 mmol) and the mixture was stirred at r.t. for 1.5 h. After addition of diethyl ether the potassium acetate was filtered off, and the filtrate was concentrated under reduced pressure before being purified by chromatography (CH_2Cl_2). Yield 50 mg (0.11 mmol, 13 %) of a blue-violet powder. Mp = 126 – 129 °C. ^{1}H NMR (CD_2Cl_2, 400 MHz): δ 8.22 (d, J = 14.0 Hz, 1H), 7.74 - 7.65 (m, 3H), 7.60 – 7.58 (m, 2H), 7.51 (dd, J = 7.8, 0.8 Hz, 1H), 7.36 (ddd, J = 8.3, 7.3, 1.2 Hz, 1H), 7.16 (td, J = 7.6, 1.0 Hz, 1H), 7.10 (d, J = 8.3 Hz, 1H), 6.06 (d, J = 12.0 Hz, 1H), 3.98 (t, J = 7.9 Hz, 2H), 3.25 (t, J = 7.2 Hz, 2H), 1.78 (quin, J = 8.0 Hz, 2H), 1.64 - 1.46 (m, 6H + water signal), 1.02 (t, J = 7.0 Hz, 3H), 1.02 (t, J = 7.4 Hz, 3H). HRMS (ESI): $[M]^+$: 443.19118; calcd for $[C_{28}H_{29}NO_2S]^+$: 443.19135. UV-Vis (CH_2Cl_2): λ_{max} (ε) = 606 nm (109250 M^{-1} cm^{-1}).

Synthesis of 2-((2*E*,5*E*)-1,7-bis((*E*)-1-butyl-3,3-dimethylindolin-2-ylidene)hepta-2,5-dien-4-ylidene)-5,6-dichloro-1*H*-indene-1,3(2*H*)-dione 118

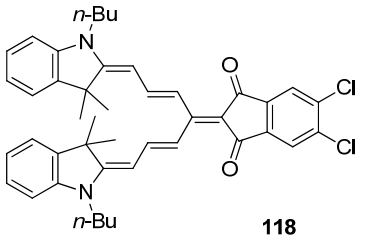

118

2.5 equivalents of (*E*)-2-(1-butyl-3,3-dimethylindolin-2-ylidene)acetaldehyde **45** (0.41 g, 1.68 mmol), one equivalent of 5,6-dichloro-2-(propan-2-ylidene)-1*H*-indene-1,3(2*H*)-dione **111c** (0.17 g, 0.66 mmol) and KOAc (4.2 equiv) were dissolved in acetic anhydride and heated to 140 °C for 120 min. The reaction mixture was concentrated under reduced pressure and the residue was purified by chromatography (CH_2Cl_2/*n*-Hexane 1:1). Yield 130 mg (0.18 mmol, 28 %) of a blue powder. Mp = 223 - 226 °C. ^{1}H NMR (CD_2Cl_2, 400 MHz): δ 7.68 (s, 2H), 7.67 (dd, J = 13.8, 12.3 Hz, 2H), 7.58 (d, J = 13.7 Hz, 2H), 7.22 (td, J = 7.7, 1.2 Hz, 2H), 7.16 (d, J = 7.3 Hz, 2H), 6.95 (td, J = 7.4, 0.8 Hz, 2H), 6.81 (d, J = 7.9 Hz, 2H), 5.96 (d, J = 12.0 Hz, 2H), 3.78 (t, J = 7.6 Hz, 4H), 1.75 (quin, J = 8.0 Hz, 4H), 1.50 (s, 12H), 1.50 - 1.40 (m, 4H), 1.03 (t, J = 7.3 Hz, 6H). ^{1}H NMR (MeOD, 400 MHz): δ 7.84 (t, J = 13.4 Hz, 2H), 7.61 (s, 2H), 7.27 - 7.33 (m, 4H), 7.01 - 7.11 (m, 6H), 6.11 (d, J = 13.2 Hz, 2H), 3.96 (t, J = 7.4 Hz, 4H), 1.78 (quin, J = 7.5 Hz, 4H), 1.45 - 1.54 (m, 16H), 1.02 (t, J = 7.4 Hz, 6H). HRMS (ESI): $[M+H]^+$: 705.30139; calcd for $[C_{44}H_{47}Cl_2N_2O_2]^+$: 705.30091. Elemental analysis (%) calcd for $C_{44}H_{46}Cl_2N_2O_2$: C, 74.88; H, 6.57; N, 3.97; found: C, 74.49; H, 6.65; N, 3.66. UV-Vis (CH_2Cl_2): λ_{max} (ε) = 585 nm (97600 M^{-1} cm^{-1}). CV: $E_{p,ox}$ = 94 mV vs. Fc/Fc^+, $E_{1/2,red}$ = −1482 mV vs. Fc/Fc^+.

Synthesis of 2-((*E*)-4-((*E*)-1-butyl-3,3-dimethylindolin-2-ylidene)but-2-en-1-ylidene)-5,6-dichloro-1*H*-indene-1,3(2*H*)-dione 120

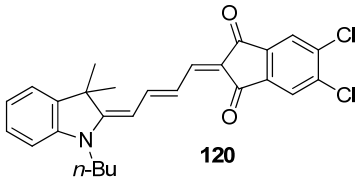

120

80 mg (0.23 mmol, 1.3 equiv) 1-butyl-2,3,3-trimethyl-3*H*-indol-1-ium iodide **43**, 50 mg (0.17 mmol, 1 equiv) (*E*)-5,6-dichloro-2-(3-methoxyallylidene)-1*H*-indene-1,3(2*H*)-dione **114** and 20 mg (0.23 mmol, 1.3 equiv) NaOAc were dissolved in a methanol/trichloromethane mixture 1:1 and stirred at 75 °C for 30 min in a microwave reactor. The reaction mixture was concentrated under reduced pressure and the residue was

purified by chromatography (CH_2Cl_2). Yield 60 mg (0.13 mmol, 73 %) of a blue crystalline solid. Mp = 208 - 212 °C. ^{1}H NMR (CD_2Cl_2, 400 MHz): δ 7.88 (t, J = 11.9 Hz, 1H), 7.79 (dd, J = 1.9, 0.3 Hz, 2H), 7.52 - 7.66 (m, 2H), 7.27 - 7.37 (m, 2H), 7.14 (td, J = 7.5, 0.9 Hz, 1H), 6.97 (d, J = 8.5 Hz, 1H), 6.04 (d, J = 13.3 Hz, 1H), 3.84 (t, J = 7.6 Hz, 2H), 1.75 (quin, J = 7.6 Hz, 2H), 1.65 (s, 6H), 1.46 (sxt, J = 7.3 Hz, 2H), 1.00 (t, J = 7.4 Hz, 3H). HRMS (ESI): $[M]^+$: 465.12594; calcd for $[C_{27}H_{25}Cl_2NO_2]^+$: 465.12569. Elemental analysis (%) calcd for $^2/_5$ $CH_2Cl_2 \cdot C_{27}H_{25}Cl_2NO_2$: C, 65.77; H, 5.20; N, 2.80; found: C, 65.68; H, 5.22; N, 2.97. UV-vis (CH_2Cl_2): λ_{max} (ε) = 602 nm (174600 M^{-1} cm^{-1}).

General synthetic procedure for dyes 121a-g

One equivalent of 5-dialkylaminothiophene-2-carboxaldehyde **64a-g** or **68a,b** and one equivalent of 2-(4-(*tert*-butyl)thiazol-2(5*H*)-ylidene)malononitrile **88** where dissolved in 2.0 – 5.0 mL acetic anhydride and heated to 90 °C for 1 h. The resulting precipitate was filtered off and washed with diethyl ether, *i*-propanol and *n*-hexane.

Synthesis of (*Z*)-2-(4-(*tert*-butyl)-5-((5-(dimethylamino)thiophen-2-yl)methylene)thiazol-2(5*H*)-ylidene)malononitrile **121a**

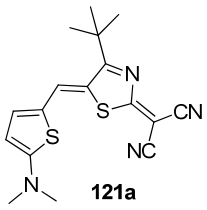

121a

Compound **121a** was obtained following the general procedure from **64a** (0.500 g, 3.22 mmol) and 2-(4-(*tert*-butyl)thiazol-2(5*H*)-ylidene)malononitrile **88** (0.661 g, 1 equiv). Yield 0.88 g (80 %) of highly insoluble green sparkling solid. Mp = 341 °C. ^{1}H NMR (DMSO, 400 MHz): δ 8.45 (s, 1H), 8.17 (d, J = 5.32 Hz, 1H), 6.92 (d, J = 5.20 Hz, 1H), 3.41 (s, 6H), 1.46 (s, 9H). HRMS (ESI): $[M]^+$: 342.09696; calcd for $[C_{17}H_{18}N_4S_2]^+$: 342.09729. UV-Vis (CH_2Cl_2): λ_{max} (ε) = 646 nm (122700 M^{-1} cm^{-1}). CV: $E_{1/2,ox}$ = 360 mV vs. Fc/Fc^+, $E_{p,red}$ = −1340 mV vs. Fc/Fc^+.

Synthesis of (*Z*)-2-[4-(*tert*-butyl)-5-(5-(diethylamino)thiophen-2-yl)methylene)thiazol-2(5*H*)-ylidene]malononitrile **121b**

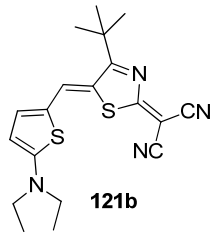

121b

Compound **121b** was obtained following the general procedure from **64b** (90 mg, 0.48 mmol) and **88** (100 mg, 0.48 mmol). Compound **121b** was purified by chromatography (CH_2Cl_2) and precipitated from *n*-hexane/CH_2Cl_2. Yield 120 mg (0.32 mmol, 66 %) of a blue crystalline solid. Mp = 258 – 263 °C. ^{1}H NMR (CD_2Cl_2, 400 MHz): δ 8.07 (s, 1H), 7.51 (d, J = 4.9 Hz, 1H), 6.30 (d, J = 4.9 Hz, 1H), 3.59 (q, J = 7.2 Hz, 4H), 1.47 - 1.56 (s, 9H + water signal), 1.34 (t, J = 7.2 Hz, 6H). HRMS (ESI): $[M]^+$: 370.12792; calcd for $[C_{19}H_{22}N_4S_2]^+$: 370.12804. Elemental analysis (%) calcd for $C_{19}H_{22}N_4S_2$: C, 61.59; H, 5.98; N, 15.12; S, 17.31; found: C, 61.85; H, 6.11; N, 14.79; S, 17.02. UV-Vis (CH_2Cl_2): λ_{max} (ε) = 649 nm (125800 M^{-1} cm^{-1}).

Synthesis of (*Z*)-2-[4-(*tert*-butyl)-5-((5-(piperidin-1-yl)thiophen-2-yl)methylene)thiazol-2(5*H*)-ylidene]malononitrile **121c**

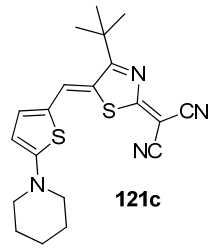

121c

Compound **121c** was obtained following the general procedure from **64c** (200 mg, 1.02 mmol) and **88** (210 mg, 1.02 mmol). Compound **121c** was purified by chromatography (CH_2Cl_2) and precipitated from *n*-hexane/CH_2Cl_2. Yield 240 mg (0.62 mmol, 61 %) of a blue powder. Mp = 294 – 295 °C. ^{1}H NMR (CD_2Cl_2, 400 MHz): δ 8.06 (s, 1H), 7.50 (d, J = 4.9 Hz, 1H), 6.37 (d, J = 4.9 Hz, 1H), 3.59 (t, J = 5.5 Hz, 4H), 1.60 - 1.89 (m, 6H), 1.51 (s, 9H + water signal). HRMS (ESI): $[M]^+$: 382.12825; calcd for $[C_{20}H_{22}N_4S_2]$: 382.12804. Elemental analysis (%) calcd for $C_{20}H_{22}N_4S_2$: C, 62.79; H, 5.80; N, 14.65; S, 16.76; found: C, 62.35; H, 5.99; N, 14.36; S, 16.39. UV-Vis (CH_2Cl_2): λ_{max} (ε) = 651 nm (131900 M^{-1} cm^{-1}).

Synthesis of (*Z*)-2-[4-(*tert*-butyl)-5-(5-(dipropylamino)thiophen-2-yl)methylene)thiazol-2(5*H*)-ylidene]malononitrile **121d**

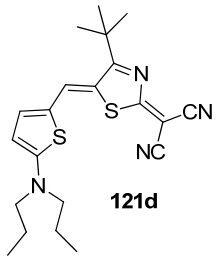

121d

Compound **121d** was obtained following the general procedure from **64d** (100 mg, 0.48 mmol) and **88** (100 mg, 0.48 mmol). Yield 115 mg (0.28 mmol, 60 %) of a blue powder. Mp = 294 - 295 °C. ^{1}H NMR (CD_2Cl_2, 400 MHz): δ 8.06 (s, 1H), 7.50 (d, J = 5.0 Hz, 1H), 6.30 (d, J = 4.9 Hz, 1H), 3.49 (t, J = 8.1 Hz, 4H), 1.77 (sxt, J = 7.7 Hz, 4H), 1.52 (s, 9H), 1.00 (t, J = 7.4 Hz, 6H). HRMS (ESI): $[M]^+$: 398.15943; calcd for $[C_{21}H_{26}N_4S_2]^+$: 398.15934. UV-Vis (CH_2Cl_2): λ_{max} (ε) = 651 nm (126300 M^{-1} cm^{-1}).

Synthesis of (*Z*)-2-[4-(*tert*-butyl)-5-(5-(dihexylamino)thiophen-2-yl)methylene)thiazol-2(5*H*)-ylidene]malononitrile **121e**

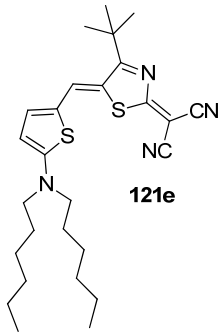

121e

Compound **121e** was obtained following the general procedure from **64f** (600 mg, 2.03 mmol) and **88** (420 mg, 2.03 mmol). Compound **121f** was purified by chromatography (CH_2Cl_2) and precipitated from *n*-hexane/CH_2Cl_2. Yield 570 mg (1.17 mmol, 58 %) of a green powder. Mp = 165 – 166 °C. ^{1}H NMR (CD_2Cl_2, 400 MHz): δ 8.05 (s, 1H), 7.48 (d, J = 4.8 Hz, 1H), 6.28 (d, J = 4.9 Hz, 1H), 3.50 (t, J = 7.9 Hz, 4H), 1.60 - 1.81 (m, 4H), 1.51 (s, 9H + water signal), 1.27 - 1.44 (m, 12H), 0.90 (t, J = 6.9 Hz, 6H). HRMS (ESI): $[M]^+$: 482.25317; calcd for $[C_{27}H_{38}N_4S_2]$: 482.25324. Elemental analysis (%) calcd for $C_{27}H_{38}N_4S_2$: C, 67.18; H, 7.93; N, 11.61; S, 13.28; found: C, 67.25; H, 8.18; N, 11.54; S, 12.86. UV-Vis (CH_2Cl_2): λ_{max} (ε) = 652 nm (147400 M^{-1} cm^{-1}).

Synthesis of (*Z*)-2-[4-(*tert*-butyl)-5-(5-(butyl(ethyl)amino)thiophen-2-yl)methylene) thiazol-2(5*H*)-ylidene]malononitrile **121f**

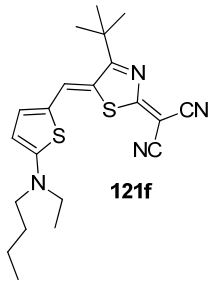

121f

Compound **121f** was obtained following the general procedure from **64g** (103 mg, 0.48 mmol) and **88** (100 mg, 0.48 mmol. Compound **121f** was precipitated from *n*-hexane/CH_2Cl_2. Yield 80 mg (0.20 mmol, 41 %) of a blue powder. Mp = 248 – 251 °C. ^{1}H NMR (CD_2Cl_2, 400 MHz): δ 8.10 (s, 1H), 7.54 (d, J = 4.9 Hz, 1H), 6.34 (d, J = 4.9 Hz, 1H), 3.63 (q, J = 7.3 Hz, 2H), 3.55 (t, J = 7.7 Hz, 2H), 1.66 - 1.85 (m, 2H), 1.56 (s, 9H + water signal), 1.46 (sxt, J = 7.6 Hz, 2H), 1.37 (t, J = 7.2 Hz, 3H), 1.03 (t, J = 7.5 Hz, 3H). HRMS (ESI): $[M]^+$: 398.15906; calcd for $[C_{21}H_{26}N_4S_2]^+$: 398.15934. Elemental analysis (%) calcd for $^1/_8Ac_2O{\cdot}C_{21}H_{26}N_4S_2$: C, 62.78; H, 6.55; N, 13.62; S, 15.59; found: C, 62.61; H, 6.56; N, 13.60; S, 15.65. UV-Vis (CH_2Cl_2): λ_{max} (ε) = 650 nm (130800 M^{-1} cm^{-1}).

Synthesis of (*Z*)-2-[4-(*tert*-butyl)-5-((5-(pyrrolidin-1-yl)thiophen-2-yl)methylene)thiazol-2(5*H*)-ylidene]malononitrile **121g**

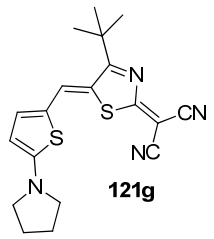

121g

Compound **121g** was obtained following the general procedure from **68a** (181 mg, 1.00 mmol) and **88** (205 mg, 1.00 mmol). Compound **121g** was purified by chromatography (CH_2Cl_2/MeOH 99.5:0.5). Yield 159 mg (0.43 mmol, 43 %) of a blue powder. Mp = 307 - 309 °C (Decomp). ^{1}H NMR ($CDCl_3$, 400 MHz) δ 8.07 (s, 1H), 7.51 (d, J = 4.8 Hz, 1H), 6.25 (d, J = 4.8 Hz, 1H), 3.63–3.56 (m, 4H), 2.21 - 2.15 (m, 4H), 1.52 (s, 9H). HRMS (ESI): calcd for $C_{19}H_{20}N_4S_2$ $[M]^+$: 368.11239, found: 368.11262. UV-Vis (CH_2Cl_2): λ_{max} (ε) = 651 nm (124100 M^{-1} cm^{-1}). CV data: $E_{1/2}^{ox}$ = 338 mV vs Fc/Fc^+, E_p^{red} = –1386 mV vs Fc/Fc^+.

Synthesis of (*Z*)-2-(4-(*tert*-butyl)-5-((5-(di-p-tolylamino)thiophen-2-yl)methylene)thiazol-2(5*H*)-ylidene)malononitrile **121h**

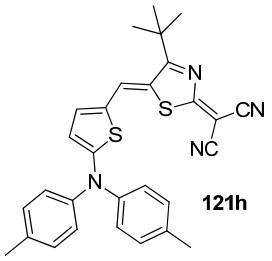

121h

Compound **121h** was obtained following the general procedure from **68b** (1.00 g, 3.25 mmol) and **88** (734 mg, 3.58 mmol). Compound **121h** was purified by chromatography (CH_2Cl_2). Yield 275 mg (0.56 mmol, 17 %) of a green powder. Mp = 324 – 325 °C. ^{1}H NMR (CD_2Cl_2, 400 MHz): δ 8.03 (s, 1H), 7.42 (dd, J = 4.6, 0.5 Hz, 1H), 7.12 - 7.30 (m, 8H), 6.41 (d, J = 4.6 Hz, 1H), 2.38 (s, 6H), 1.51 (s, 9H). HRMS (ESI): $[M]^+$: 494.15943; calcd for $[C_{29}H_{26}N_4S_2]$: 494.15934. Elemental analysis (%) calcd for $C_{29}H_{26}N_4S_2$: C, 70.41; H, 5.30; N, 11.32; S, 12.96; found: C, 70.14; H, 5.34; N, 11.24; S, 12.72. UV-Vis (CH_2Cl_2): λ_{max} (ε): 664 nm (77000 M^{-1} cm^{-1}).

Synthesis of (*Z*)-2-[5-(2-(benzo[*d*][1,3]dithiol-2-ylidene)-ethylidene)-4-(*tert*-butyl)-thiazol-2(5*H*)-ylidene]-malononitrile 123

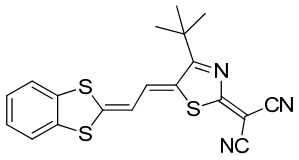

123

A 10.0 mL Ac_2O solution of 2-(benzo[*d*][1,3]dithiol-2-ylidene)-acetaldehyde **59** (0.50 g, 2.5 mmol, 1.7 equiv) and 2-(4-(*tert*-butyl)thiazol-2(5*H*)-ylidene)-malononitrile **88** (0.32 g, 1.5 mmol) was heated to 90 °C for 1 h. Diethyl ether was added and the resulting precipitate was filtered off and washed with diethyl ether, cold *i*-propanol and *n*-hexane before being precipitated from a CH_2Cl_2/*n*-hexane mixture. Yield 224 mg (0.59 mmol, 38 %) of a blue solid. Mp = 290 °C. ^{1}H NMR (CD_2Cl_2, 400 MHz): δ 7.69 (d, J = 12.1 Hz, 1H), 7.57 - 7.46 (m, 2H), 7.39 - 7.29 (m, 2H), 6.39 (d, J = 12.1 Hz, 1H), 1.53 (s, 9H). HRMS (ESI): $[M+H]^+$: 382.04958; calcd for $[C_{19}H_{16}N_3S_3]$: 382.05009. Elemental analysis (%) calcd for $C_{19}H_{15}N_3S_3$: C, 59.81; H, 3.96; N, 11.01; S, 25.21; found: C, 59.63; H, 3.82; N, 10.84; S, 25.28. UV-Vis (CH_2Cl_2): λ_{max} (ε): 609 nm (57000 M^{-1} cm^{-1}). CV: $E_{1/2,ox}$ = 578 mV vs. Fc/Fc^+, $E_{p,red}$ = −1081 mV vs. Fc/Fc^+.

Synthesis of (*Z*)-2-(5-(2-(4,5-bis(methylthio)-1,3-dithiol-2-ylidene)ethylidene)-4-(*tert*-butyl)thiazol-2(5*H*)-ylidene)malononitrile 124

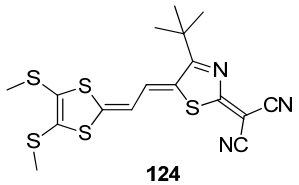

124

An 3.0 mL Ac_2O solution of 2-(4,5-bis(methylthio)-1,3-dithiol-2-ylidene)acetaldehyde **62** (100 mg, 0.423 mmol) and 2-(4-(*tert*-butyl)thiazol-2(5*H*)-ylidene)malononitrile **88** (90 mg, 0.423 mmol) was heated to 90 °C for 1 h. After solvent removal the product was purified by column chromatography (CH_2Cl_2). Yield 20 mg (11 %) of an amorphous blue powder. Mp = 216 – 220 °C. ^{1}H NMR (CD_2Cl_2, 400 MHz): δ 7.52 (d, J = 12.0 Hz, 1H), 6.28 (d, J = 12.3 Hz, 1H), 2.51 (s, 3H), 2.50 (s, 3H), 1.51 (s, 9H). HRMS (ESI): $[M]^{\bullet+}$: 423.00193; calcd for $[C_{17}H_{17}N_3S_5]^{\bullet+}$: 423.00205. UV-Vis ($CH_2Cl_2$): λ_{max} (ε) = 630 nm (29800 M^{-1} cm^{-1}). CV: $E_{1/2,ox}$ = 527 mV vs Fc/Fc^+, $E_{p,red}$ = – 1056 mV vs Fc/Fc^+.

Synthesis of (*Z*)-2-(4-(*tert*-butyl)-5-((5-methoxythiophen-2-yl)methylene)thiazol-2(5*H*)-ylidene)malononitrile 125

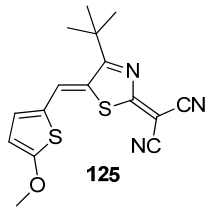

125

5-methoxythiophene-2-carboxaldehyde **70** (1.20 g, 8.44 mmol) and 2-(4-(*tert*-butyl)thiazol-2(5*H*)-ylidene)malononitrile **88** (1.71 g, 1 equiv) where dissolved in 2.0 mL acetic anhydride and heated to 120 °C for 20 h. The reaction turned from yellow to dark pink. The resulting precipitate was filtered off and washed with diethyl ether, *i*-propanol and *n*-hexane. The residue was purified by chromatography (CH_2Cl_2/MeOH 95:5) to yield in 0.84 g (30 %) of a violet powder. Mp = 260 – 261 °C. ^{1}H NMR (DMSO, 400 MHz): δ 7.97 (d, J = 0.60 Hz, 1H), 7.35 (d, J = 4.36 Hz, 1H), 6.45 (d, J = 4.36 Hz, 1H), 4.09 (s, 3H), 1.51 (s, 9H). HRMS (ESI): $[M]^+$: 330.07306; calcd for $[C_{16}H_{16}N_3OS_2]^+$: 330.07293. UV-Vis (CH_2Cl_2): λ_{max} (ε) = 538 nm (39200 M^{-1} cm^{-1}). CV: $E_{1/2,ox}$ = 830 mV vs. Fc/Fc^+, $E_{p,red}$ = – 1150 mV vs. Fc/Fc^+.

Synthesis of (*Z*)-2-(4-(*tert*-butyl)-5-((5-(methylthio)thiophen-2-yl)methylene)thiazol-2(5*H*)-ylidene)malononitrile 126

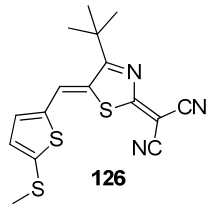

126

An 8.0 mL Ac_2O solution of 5-(methylthio)thiophene-2-carbaldehyde **122** (1.00 g, 6.32 mmol) and 2-(4-(*tert*-butyl)thiazol-2(5*H*)-ylidene)malononitrile **88** (1,30 g, 6.32 mmol) was heated to 90 °C for 20 h. After solvent removal the product was purified by column chromatography (CH_2Cl_2). Yield 700 mg (32 %) of blue needles. Mp = 269 – 271 °C. ^{1}H NMR (CD_2Cl_2, 400 MHz): δ 8.05 (d, J = 0.6 Hz, 1H), 7.47 (dd J = 4.1 Hz, J = 0.6 Hz, 1H), 7.07 (d, J = 4.1 Hz, 1H), 2.71 (s, 3H), 1.56 (s, 9H). HRMS (ESI): $[M]^{\bullet+}$: 346.05041; calcd for $[C_{16}H_{15}N_3S_3]^{\bullet+}$: 345.5054. UV-Vis ($CH_2Cl_2$): λ_{max} (ε) = 544 nm (35100 M^{-1} cm^{-1}). CV: $E_{p,ox}$ = 921 mV vs Fc/Fc^+, $E_{p,red}$ = – 1062 mV vs Fc/Fc^+.

Synthesis of 2-((*Z*)-4-(*tert*-butyl)-5-((*Z*)-2-(3-butylbenzo[*d*]thiazol-2(3*H*)-ylidene)ethylidene)thiazol-2(5*H*)-ylidene)malononitrile 127

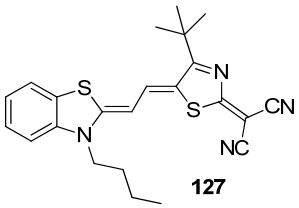

127

3-butyl-2-methyl-1,3-benzothiazolium iodide **54** (0.20 g, 0.60 mmol) and *N*,*N*-diphenylformamidine (0.12 g, 1 equiv) were stirred at 120 °C for 2 h in 5.0 mL acetic anhydride. After cooling the reaction mixture, triethylamine (0.2 mL, 2.5 equiv) and 2-(4-(*tert*-butyl)thiazol-2(5*H*)-ylidene)malononitrile **88** (0.12 g, 1 equiv) were added and the reaction mixture was stirred at 90 °C for 20 h. Diethyl ether was added to the cooled reaction mixture until a precipitate appeared. The precipitate was filtered off and washed with diethyl ether, *i*-propanol and *n*-hexane and the residue was purified by chromatography (CH_2Cl_2) to afford 46 mg (18 %) of a blue solid. Mp = 329 °C. ^{1}H NMR (CD_2Cl_2, 400 MHz): δ 8.09 (d, J = 13.0 Hz, 1H), 7.70 (d, J = 7.8 Hz, 1H), 7.63 - 7.47 (m, 1H), 7.47 - 7.29 (m, 2H), 5.84 (d, J = 13.0 Hz, 1H), 4.19 (t, J = 7.7 Hz, 2H), 1.84 (quin, J = 7.8 Hz, 2H), 1.52 (s, 9H + water signal), 1.51 - 1.43 (m, 2H), 1.02 (t, J = 7.3 Hz, 3H).

HRMS (ESI): $[M+H]^+$: 421.15151; calcd for $[C_{23}H_{25}N_4S_2]^+$: 421.15165. Elemental analysis (%) calcd for $C_{23}H_{24}N_4S_2$: C, 65.68; H, 5.75; N, 13.32; S, 15.25; found: C, 65.61; H, 5.98; N, 13.37; S, 15.24. UV-Vis (CH_2Cl_2): λ_{max} (ε) = 631 nm (124700 M^{-1} cm^{-1}). CV: $E_{p,ox}$ = 403 mV vs. Fc/Fc^+, $E_{p,red}$ = – 1493 mV vs. Fc/Fc^+.

Synthesis of 2-((*Z*)-4-(*tert*-butyl)-5-((*Z*)-2-(3-butylbenzo[*d*][1,3]selenazol-2(3*H*)-ylidene)ethylidene)thiazol-2(5*H*)-ylidene)malononitrile 128

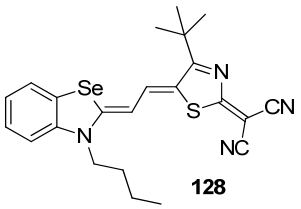

128

3-butyl-2-methyl-1,3-benzoselenazolium iodide **55** (0.11 g, 0.29 mmol) and *N*,*N*-diphenylformamidine (0.057 g, 1 equiv) were stirred at 120 °C for 2 h in 5.0 mL acetic anhydride. After cooling the mixture, triethylamine (0.1 mL, 2.0 equiv) and 2-(4-(*tert*-butyl)thiazol-2(5*H*)-ylidene)malononitrile **88** (0.11 g, 2 equiv) were added and the reaction mixture was stirred at 90 °C for 3 h. The mixture was then poured into diethyl ether, filtered off and washed with diethyl ether. The residue was purified by chromatography (CH_2Cl_2) to yield in 8.6 mg (6 %) of a blue solid. Mp = 334 °C. ^{1}H NMR (DMSO-d_6, 400 MHz): δ 8.10 - 8.18 (m, 2H), 7.89 (d, J = 8.2 Hz, 1H), 7.64 (t, J = 8.7 Hz, 1H), 7.48 (t, J = 8.1 Hz, 1H), 6.55 (d, J = 13.6 Hz, 1H), 4.57 (t, J = 7.5 Hz, 2H), 1.72 (quin, J = 7.5 Hz, 2H), 1.46 (s, 9H), 1.39 (sxt, J = 7.7 Hz, 2H), 0.92 (t, J = 7.4 Hz, 3H). HRMS (ESI): $[M]^{\bullet+}$: 469.09625; calcd for $[C_{23}H_{25}N_4SSe]^{\bullet+}$: 469.09602. Elemental analysis (%) calcd for $C_{23}H_{24}N_4SSe$: C, 59.09; H, 5.17; N, 11.98; S, 6.86; found: C, 59.40; H, 5.19; N, 11.79; S, 6.51. UV-vis (CH_2Cl_2): λ_{max} (ε) = 638 nm (144400 M^{-1} cm^{-1}). CV: $E_{1/2,ox}$ = 363 mV vs. Fc/Fc^+, $E_{p,red}$ = −1474 mV vs. Fc/Fc^+.

6.4 Single crystal structure data

The single crystal X-ray data were collected with a Bruker X8APEX-II_KAPPA diffractometer with APEX CCD area detector and graphite monochromated $Mo_{K\alpha}$ radiation or a Bruker D8Quest Kappa Diffractometer using $Cu_{K\alpha}$ radiation from an Incoatec IμS microsource with Montel multi layered mirror, a Photon100 CMOS detector and Apex2* software at 100 K. The structures were solved using direct methods, refined with SHELX software package[139] and expanded using Fourier techniques. All non-hydrogen atoms were refined anisotropically. Hydrogen atoms were assigned idealized positions and were included in structure factors calculations. The crystal structures of dyes **129** and **130** have been reported elsewhere.[42a]

Crystal data of dye **90a**: $C_{19}H_{13}N_3OS$, M_r = 331.38, dark green block-shaped crystal, 0.288×0.105×0.063, monoclinic space group $P2_1/c$, a = 9.1178(13) Å, b = 23.329(3) Å, c = 7.3158(11) Å, α = 90.00°, β = 92.835(5)°, γ = 90.00°, V = 1554.3(4) Å^3, Z = 4, ρ_{calcd} = 1.416 g·cm^{-3}, μ = 1.933 mm^{-1}, F(000) = 688, T = 108(2) K, R_1 = 0.0323, wR^2 = 0.0830, 50126 independent reflections [2θ≤136.78°] and 219 parameters.

Crystal data of dye **90b** (CCDC:1406539): $C_{21}H_{17}N_3OS$, M_r = 359.43, dark green block-shaped crystal, 0.500×0.044×0.037, monoclinic space group $P2_1/n$, a = 4.9606(2) Å, b = 13.7482(5) Å, c = 26.0232(10) Å, α = 90.00°, β = 93.2860(16)°, γ = 90.00°, V = 1771.85(12) Å^3, Z = 4, ρ_{calcd} = 1.347 g·cm^{-3}, μ = 1.737 mm^{-1}, F(000) = 752, T = 100(2) K, R_1 = 0.0401, wR^2 = 0.0849, 3450 independent reflections [2θ≤144.36°] and 237 parameters.

Crystal data of dye **95** (CCDC:1406535): $C_{25}H_{19}N_3O_2$, M_r = 393.43, red block-shaped crystal, 0.207×0.243×0.302, monoclinic space group C2/c, a = 16.4756(18) Å, b = 18.589(2) Å, c = 13.4659(15) Å, α = 90.00°, β = 99.8950(10)°, γ = 90.00°, V = 4062.7(8) Å^3, Z = 8, ρ_{calcd} = 1.286 g·cm^{-3}, μ = 0.083 mm^{-1}, F(000) = 1648, T = 168(2) K, R_1 = 0.0410, wR^2 = 0.0975, 4000 independent reflections [2θ≤52.04°] and 272 parameters.

Crystal data of dye **96** (CCDC:1406539): $C_{25}H_{19}N_3OS$, M_r = 409.49, dark red prism-shaped crystal, 0.404×0.098×0.045, monoclinic space group $P2_1/c$, a = 18.0569(8) Å, b = 4.7287(2) Å, c = 24.2655(11) Å, α = 90.00°, β = 97.157(2)°, γ = 90.00°, V = 2055.78(16) Å^3, Z = 4, ρ_{calcd} = 1.323 g·cm^{-3}, μ = 1.567 mm^{-1}, F(000) = 856, T = 200(2) K,

R_1 = 0.0372, wR^2 = 0.0900, 4152 independent reflections [2θ≤148.88°] and 272 parameters.

Crystal data of dye **97** (CCDC:1406537): $C_{25}H_{19}N_3OSe$, M_r = 456.39, dark red needle-shaped crystal, 0.439×0.126×0.100, monoclinic space group $P2_1/c$, a = 18.1452(8) Å, b = 4.7127(2) Å, c = 24.4115(11) Å, α = 90.00°, β = 96.5210(10)°, γ = 90.00°, V = 2073.99(16) Å^3, Z = 4, ρ_{calcd} = 1.462 g·cm^{-3}, μ = 2.620 mm^{-1}, F(000) = 928, T = 200(2) K, R_1 = 0.0234, wR^2 = 0.0634, 34791 independent reflections [2θ≤149.12°] and 273 parameters.

Crystal data of dye **118** (CCDC1436889): $C_{44}H_{46}Cl_2N_2O_2$, M_r = 705.73, blue needle-shaped crystal, 0.155 x 0.133 x 0.063, triclininc space group $\mathbf{P\bar{1}}$, a = 10.0740(3) Å, b = 11.8025(3) Å, c = 17.7776(5) Å, α = 74.2230(10)°, β = 84.4990(10)°, γ = 86.4350(10)°, V = 2023.29(10) Å^3, Z = 2, ρ_{calcd} = 1.158 g cm^{-3}, μ = 1.722 mm^{-1}, F(000) = 748, T = 100(2) K, R_1 = 0.0442, wR^2 = 0.1374, 42735 independent reflections [2 θ ≤ 149.414°] and 459 parameters.

References

[1] a) P. Würfel, *Physics of Solar Cells: From Basic Principles to Advanced Concepts*, WILEY-VCH Verlag GmbH & Co. KGaA, Weinheim, **2009**; b) P. D. Frischmann, K. Mahata, F. Würthner, *Chem. Soc. Rev.* **2013**, *42*, 1847; c) N. S. Lewis, *Science* **2007**, *315*, 798.

[2] NREL, National Renewable Energy Laboratory (NREL), http://www.nrel.gov/.

[3] a) J. Zhou, Y. Zuo, X. Wan, G. Long, Q. Zhang, W. Ni, Y. Liu, Z. Li, G. He, C. Li, B. Kan, M. Li, Y. Chen, *J. Am. Chem. Soc.* **2013**, *135*, 8484; b) J. Zhou, X. Wan, Y. Liu, Y. Zuo, Z. Li, G. He, G. Long, W. Ni, C. Li, X. Su, Y. Chen, *J. Am. Chem. Soc.* **2012**, *134*, 16345; c) Y. Liu, C. C. Chen, Z. Hong, J. Gao, Y. M. Yang, H. Zhou, L. Dou, G. Li, Y. Yang, *Sci. Rep.* **2013**, *3*, 3356; d) T. S. van der Poll, J. A. Love, T.-Q. Nguyen, G. C. Bazan, *Adv. Mater.* **2012**, *24*, 3646; e) Y. H. Chao, J. F. Jheng, J. S. Wu, K. Y. Wu, H. H. Peng, M. C. Tsai, C. L. Wang, Y. N. Hsiao, C. L. Wang, C. Y. Lin, C. S. Hsu, *Adv. Mater.* **2014**, *26*, 5205; f) Z. C. He, C. M. Zhong, S. J. Su, M. Xu, H. B. Wu, Y. Cao, *Nat. Photonics* **2012**, *6*, 591; g) A. K. Kyaw, D. H. Wang, D. Wynands, J. Zhang, T.-Q. Nguyen, G. C. Bazan, A. J. Heeger, *Nano Lett.* **2013**, *13*, 3796.

[4] a) H. Bürckstümmer, E. V. Tulyakova, M. Deppisch, M. R. Lenze, N. M. Kronenberg, M. Gsänger, M. Stolte, K. Meerholz, F. Würthner, *Angew. Chem., Int. Ed.* **2011**, *50*, 11628; b) V. Steinmann, N. M. Kronenberg, M. R. Lenze, S. M. Graf, D. Hertel, K. Meerholz, H. Bürckstümmer, E. V. Tulyakova, F. Würthner, *Adv. Energy Mater.* **2011**, *1*, 888.

[5] C. W. Tang, *Appl. Phys. Lett.* **1986**, *48*, 183.

[6] a) A. Moliton, J. M. Nunzi, *Polym. Int.* **2006**, *55*, 583; b) B. Kippelen, J.-L. Brédas, *Energy Environ. Sci.* **2009**, *2*, 251.

[7] a) J. J. M. Halls, C. A. Walsh, N. C. Greenham, E. A. Marseglia, R. H. Friend, S. C. Moratti, A. B. Holmes, *Nature* **1995**, *376*, 498; b) G. Yu, J. Gao, J. C. Hummelen, F. Wudl, A. J. Heeger, *Science* **1995**, *270*, 1789.

[8] M. Knupfer, *Appl. Phys. A: Mater. Sci. Process.* **2003**, *77*, 623.

[9] V. Coropceanu, J. Cornil, D. A. da Silva Filho, Y. Olivier, R. Silbey, J.-L. Brédas, *Chem. Rev.* **2007**, *107*, 926.

[10] a) S. Khodabakhsh, B. M. Sanderson, J. Nelson, T. S. Jones, *Adv. Funct. Mater.* **2006**, *16*, 95; b) S. Winkler, J. Frisch, P. Amsalem, S. Krause, M. Timpel, M. Stolte, F. Würthner, N. Koch, *J. Phys. Chem. C* **2014**, *118*, 11731.

[11] J.-L. Brédas, J. E. Norton, J. Cornil, V. Coropceanu, *Acc. Chem. Res.* **2009**, *42*, 1691.

[12] a) G. A. Chamberlain, *Solar Cells* **1983**, *8*, 47; b) D. Wöhrle, D. Meissner, *Adv. Mater.* **1991**, *3*, 129.

[13] S. Gunes, H. Neugebauer, N. S. Sariciftci, *Chem. Rev.* **2007**, *107*, 1324.

[14] a) Y. He, G. Zhao, B. Peng, Y. Li, *Adv. Funct. Mater.* **2010**, *20*, 3383; b) G. Zhao, Y. He, Y. Li, *Adv. Mater.* **2010**, *22*, 4355; c) F. G. Brunetti, X. Gong, M. Tong, A.

J. Heeger, F. Wudl, *Angew. Chem.* **2010**, *122*, 542; d) P. Sullivan, A. Duraud, l. Hancox, N. Beaumont, G. Mirri, J. H. R. Tucker, R. A. Hatton, M. Shipman, T. S. Jones, *Adv. Energy Mater.* **2011**, *1*, 352; e) G. D. Sharma, P. Suresh, J. A. Mikroyannidis, M. M. Stylianakis, *J. Mater. Chem.* **2010**, *20*, 561.

[15] a) A. Mishra, P. Bäuerle, *Angew. Chem., Int. Ed.* **2012**, *51*, 2020; b) Y. Lin, Y. Li, X. Zhan, *Chem. Soc. Rev.* **2012**, *41*, 4245; c) Y. W. Li, Q. Guo, Z. F. Li, J. N. Pei, W. J. Tian, *Energy Environ. Sci.* **2010**, *3*, 1427.

[16] A. Dieckmann, H. Bässler, P. M. Borsenberger, *J. Chem. Phys.* **1993**, *99*, 8136.

[17] F. Würthner, S. Yao, T. Debaerdemaeker, R. Wortmann, *J. Am. Chem. Soc.* **2002**, *124*, 9431.

[18] F. Würthner, S. Yao, J. Schilling, R. Wortmann, M. Redi-Abshiro, E. Mecher, F. Gallego-Gomez, K. Meerholz, *J. Am. Chem. Soc.* **2001**, *123*, 2810.

[19] F. Würthner, R. Wortmann, K. Meerholz, *ChemPhysChem* **2002**, *3*, 17.

[20] F. Würthner, G. Archetti, R. Schmidt, H.-G. Kuball, *Angew. Chem., Int. Ed.* **2008**, *47*, 4529.

[21] a) F. Würthner, C. Thalacker, R. Matschiner, K. Lukaszuk, R. Wortmann, *Chem. Commun.* **1998**, 1739; b) S. R. Marder, J. W. Perry, *Science* **1994**, *263*, 1706.

[22] H. Bässler, *Phys. Stat. Sol.* **1993**, *175*, 15.

[23] D. L. Morel, A. K. Ghosh, T. Feng, E. L. Stogryn, P. E. Purwin, R. F. Shaw, C. Fishman, *Appl. Phys. Lett.* **1978**, *32*, 495.

[24] a) A. K. Ghosh, T. Feng, *J. Appl. Phys.* **1978**, *49*, 5982; b) G. A. Chamberlain, P. J. Cooney, S. Dennison, *Nature* **1981**, *289*, 45; c) G. A. Chamberlain, R. E. Malpas, *Faraday Discuss. Chem. Soc.* **1980**, *70*, 299; d) T. Moriizumi, K. Kudo, *Appl. Phys. Lett.* **1981**, *38*, 85; e) T. Skotheim, J. M. Yang, J. Otvos, M. P. Klein, *J. Chem. Phys.* **1982**, *77*, 6151.

[25] K. Kudo, M. Yamashina, T. Moriizumi, *Jpn. J. Appl. Phys.* **1984**, *23*, 130.

[26] V. Z. Shirinian, A. A. Shimkin, *Top. Heterocycl. Chem.* **2008**, *14*, 75.

[27] N. M. Kronenberg, M. Deppisch, F. Würthner, H. W. Lademann, K. Deing, K. Meerholz, *Chem. Commun.* **2008**, 6489.

[28] N. M. Kronenberg, H. Bürckstümmer, M. Deppisch, F. Würthner, K. Meerholz, *J. Photon. Energy* **2011**, *1*, 011101.

[29] H. Bürckstümmer, N. M. Kronenberg, M. Gsänger, M. Stolte, K. Meerholz, F. Würthner, *J. Mater. Chem.* **2010**, *20*, 240.

[30] H. Bürckstümmer, N. M. Kronenberg, K. Meerholz, F. Würthner, *Org. Lett.* **2010**, *12*, 3666.

[31] A. Zitzler-Kunkel, M. R. Lenze, N. M. Kronenberg, A.-M. Krause, M. Stolte, K. Meerholz, F. Würthner, *Chem. Mater.* **2014**, *26*, 4856.

[32] M. Kasha, H. R. Rawls, M. A. El-Bayoumi, *Pure Appl. Chem.* **1965**, *11*, 371.

[33] A. Zitzler-Kunkel, M. R. Lenze, K. Meerholz, F. Würthner, *Chem. Sci.* **2013**, *4*, 2071.

[34] N. M. Kronenberg, V. Steinmann, H. Bürckstümmer, J. Hwang, D. Hertel, F. Würthner, K. Meerholz, *Adv. Mater.* **2010**, *22*, 4193.

[35] V. Steinmann, T. E. Umbach, M. Schadel, J. Krumrain, M. R. Lenze, H. Bürckstümmer, F. Würthner, K. Meerholz, *Org. Electron.* **2013**, *14*, 2029.

[36] V. Steinmann, N. M. Kronenberg, M. R. Lenze, S. M. Graf, D. Hertel, H. Bürckstümmer, F. Würthner, K. Meerholz, *Appl. Phys. Lett.* **2011**, *99*, 193306.

[37] S. W. Chiu, L. Y. Lin, H. W. Lin, Y. H. Chen, Z. Y. Huang, Y. T. Lin, F. Lin, Y. H. Liu, K.-T. Wong, *Chem. Commun.* **2012**, *48*, 1857.

[38] A. Ojala, H. Bürckstümmer, M. Stolte, R. Sens, H. Reichelt, P. Erk, J. Hwang, D. Hertel, K. Meerholz, F. Würthner, *Adv. Mater.* **2011**, *23*, 5398.

[39] M. M. Safont-Sempere, G. Fernández, F. Würthner, *Chem. Rev.* **2011**, *111*, 5784.

[40] A. Ojala, H. Bürckstümmer, J. Hwang, K. Graf, B. von Vacano, K. Meerholz, P. Erk, F. Würthner, *J. Mater. Chem.* **2012**, *22*, 4473.

[41] A. Ojala, A. Petersen, A. Fuchs, R. Lovrincic, C. Pölking, J. Trollmann, J. Hwang, C. Lennartz, H. Reichelt, H. W. Höffken, A. Pucci, P. Erk, T. Kirchartz, F. Würthner, *Adv. Funct. Mater.* **2012**, *22*, 86.

[42] a) A. Liess, L. Huang, A. Arjona-Esteban, A. Lv, M. Gsänger, V. Stepanenko, M. Stolte, F. Würthner, *Adv. Funct. Mater.* **2015**, *25*, 44; b) A. Lv, M. Stolte, F. Würthner, *Angew. Chem., Int. Ed.* **2015**, *54*, 10512.

[43] J. Roncali, *Acc. Chem. Res.* **2009**, *42*, 1719.

[44] P. F. Xia, X. J. Feng, J. Lu, S.-W. Tsang, R. Movileanu, Y. Tao, M. S. Wong, *Adv. Mater.* **2008**, *20*, 4810.

[45] W. F. Zhang, G. M. Ng, H. L. Tam, M. S. Wong, F. R. Zhu, *J. Polym. Sci., Part A: Polym. Chem.* **2011**, *49*, 1865.

[46] E. Ripaud, T. Rousseau, P. Leriche, J. Roncali, *Adv. Energy Mater.* **2011**, *1*, 540.

[47] A. Mishra, M. K. R. Fischer, P. Bäuerle, *Angew. Chem., Int. Ed.* **2009**, *48*, 2474.

[48] Q. Liu, K. Jiang, B. Guan, Z. Tang, J. Pei, Y. Song, *Chem. Commun.* **2011**, *47*, 740.

[49] J. K. Lee, J. Kim, H. Choi, K. Lim, K. Song, J. Ko, *Tetrahedron* **2014**, *70*, 6235.

[50] H. M. Ko, H. Choi, S. Paek, K. Kim, K. Song, J. K. Lee, J. Ko, *J. Mater. Chem.* **2011**, *21*, 7248.

[51] J. Kim, H. M. Ko, N. Cho, S. Paek, J. K. Lee, J. Ko, *RSC Adv.* **2012**, *2*, 2692.

[52] S. R. Bobe, A. Gupta, A. Rananaware, A. Bilic, S. V. Bhosale, S. V. Bhosale, *RSC Adv.* **2015**, *5*, 4411.

[53] L. Y. Lin, Y. H. Chen, Z. Y. Huang, H. W. Lin, S. H. Chou, F. Lin, C. W. Chen, Y. H. Liu, K.-T. Wong, *J. Am. Chem. Soc.* **2011**, *133*, 15822.

[54] H. W. Lin, L. Y. Lin, Y. H. Chen, C. W. Chen, Y. T. Lin, S. W. Chiu, K.-T. Wong, *Chem. Commun.* **2011**, *47*, 7872.

[55] Y. H. Chen, L. Y. Lin, C. W. Lu, F. Lin, Z. Y. Huang, H. W. Lin, P. H. Wang, Y. H. Liu, K.-T. Wong, J. Wen, D. J. Miller, S. B. Darling, *J. Am. Chem. Soc.* **2012**, *134*, 13616.

[56] Y. Zou, J. Holst, Y. Zhang, R. J. Holmes, *J. Mater. Chem. A* **2014**, *2*, 12397.

[57] H.-W. Lin, J.-H. Chang, W.-C. Huang, Y.-T. Lin, L.-Y. Lin, F. Lin, K.-T. Wong, H.-F. Wang, R.-M. Ho, H.-F. Meng, *J. Mater. Chem. A* **2014**, *2*, 3709.

[58] V. Jeux, D. Demeter, P. Leriche, J. Roncali, *RSC Adv.* **2013**, *3*, 5811.

[59] A. Leliège, C.-H. L. Regent, M. Allain, P. Blanchard, J. Roncali, *Chem. Commun.* **2012**, *48*, 8907.

[60] J. W. Choi, C.-H. Kim, J. Pison, A. Oyedele, D. Tondelier, A. Leliège, E. Kirchner, P. Blanchard, J. Roncali, B. Geffroy, *RSC Adv.* **2014**, *4*, 5236.

[61] Z. Wang, X.-F. Wang, D. Yokoyama, H. Sasabe, J. Kido, Z. Liu, W. Tian, O. Kitao, T. Ikeuchi, S.-I. Sasaki, *J. Phys. Chem. C* **2014**, *118*, 14785.

[62] N. F. Montcada, L. Cabau, C. V. Kumar, W. Cambarau, E. Palomares, *Org. Electron.* **2015**, *20*, 15.

[63] M. Cheng, X. Yang, C. Chen, Q. Tan, L. Sun, *J. Mater. Chem. A* **2014**, *2*, 10465.

[64] H. Gao, Y. Li, L. Wang, C. Ji, Y. Wang, W. Tian, X. Yang, L. Yin, *Chem. Commun.* **2014**, *50*, 10251.

[65] H.-I. Lu, C.-W. Lu, Y.-C. Lee, H.-W. Lin, L.-Y. Lin, F. Lin, J.-H. Chang, C.-I. Wu, K.-T. Wong, *Chem. Mater.* **2014**, *26*, 4361.

[66] D. Yang, Q. Yang, L. Yang, Q. Luo, Y. Huang, Z. Lu, S. Zhao, *Chem. Commun.* **2013**, *49*, 10465.

[67] D. Yang, Q. Yang, L. Yang, Q. Luo, Y. Chen, Y. Zhu, Y. Huang, Z. Lu, S. Zhao, *Chem. Commun.* **2014**, *50*, 9346.

[68] D. Yang, Y. Zhu, Y. Jiao, L. Yang, Q. Yang, Q. Luo, X. Pu, Y. Huang, S. Zhao, Z. Lu, *RSC Adv.* **2015**, *5*, 20724.

[69] Y. Chen, Y. Zhu, D. Yang, Q. Luo, L. Yang, Y. Huang, S. Zhao, Z. Lu, *Chem. Commun.* **2015**.

[70] U. Mayerhöffer, K. Deing, K. Gruß, H. Braunschweig, K. Meerholz, F. Würthner, *Angew. Chem., Int. Ed.* **2009**, *48*, 8776.

[71] M. Gsänger, E. Kirchner, M. Stolte, C. Burschka, V. Stepanenko, J. Pflaum, F. Würthner, *J. Am. Chem. Soc.* **2014**, *136*, 2351.

[72] a) E. E. Jelley, *Nature* **1936**, *138*, 1009; b) G. Scheibe, *Angew. Chem.* **1937**, *50*, 212; c) E. E. Jelley, *Nature* **1937**, *139*, 631.

[73] H. von Berlepsch, C. Böttcher, L. Dähne, *J. Phys. Chem. B* **2000**, *104*, 8792.

[74] a) S. Ganapathy, S. Sengupta, P. K. Wawrzyniak, V. Huber, F. Buda, U. Baumeister, F. Würthner, H. J. M. de Groot, *PNAS* **2009**, *106*, 11472; b) W. J. Harrison, D. L. Mateer, G. J. T. Tiddy, *J. Phys. Chem.* **1996**, *100*, 2310; c) N. Fukutake, T. Kobayashi, *Chem. Phys. Lett.* **2002**, *356*, 368; d) G. J. T. Tiddy, D. L. Mateer, A. P. Ormerod, W. J. Harrison, D. J. Edwards, *Langmuir* **1995**, *11*, 390.

[75] a) T. Forster, *Naturwissenschaften* **1946**, *33*, 166; b) G. Scheibe, F. Haimerl, W. Hoppe, *Tetrahedron Lett.* **1970**, *11*, 3067; c) H. Bücher, H. Kuhn, *Chem. Phys. Lett.* **1970**, *6*, 183.

[76] a) E. G. McRae, M. Kasha, *J. Chem. Phys.* **1958**, *28*, 721; b) M. Kasha, *Radiat. Res.* **1963**, *20*, 55.

[77] a) A. S. Davydov, *J. Exptl. Theoret. Phys. (U.S.S.R.)* **1948**, *18*, 210; b) A. S. Davydov, *Theory of Molecular Excitons*, Plenum Press, New York, **1971**.

[78] a) A. Pardal, S. Ramos, P. Santos, L. Reis, P. Almeida, *Molecules* **2002**, *7*, 320; b) B. T. Makowski, B. Valle, K. D. Singer, C. Weder, *J. Mater. Chem.* **2012**, *22*, 2848.

[79] M. Hirano, K. Osakada, H. Nohira, A. Miyashita, *J. Org. Chem.* **2002**, *67*, 533.

[80] J. Wang, W.-F. Cao, J.-H. Su, H. Tian, Y.-H. Huang, Z.-R. Sun, *Dyes Pigm.* **2003**, *57*, 171.

[81] a) T. Zimmermann, *J. Heterocycl. Chem.* **2000**, *37*, 1571; b) T. Zimmermann, O. Brede, *J. Heterocycl. Chem.* **2004**, *41*, 103.

[82] J. Wang, W.-F. Cao, J.-H. Su, H. Tian, Y.-H. Huang, Z.-R. Sun, *Dyes Pigm.* **2003**, *57*, 171.

[83] K. M. Shafeekh, M. K. A. Rahim, M. C. Basheer, C. H. Suresh, S. Das, *Dyes Pigm.* **2013**, *96*, 714.

[84] G. Märkl, N. Aschenbrenner, A. Baur, C. Rastorfer, P. Kreitmeier, *Helv. Chim. Acta* **2003**, *86*, 2589.

[85] M. Levas, E. Levas, *Bull. Soc. Chim. Fr.* **1959**, 1800.

[86] P. J. Skabara, R. Berridge, K. Prescott, L. M. Goldenberg, E. Orti, R. Viruela, R. Pou-Amerigo, A. S. Batsanov, J. A. K. Howard, S. J. Coles, M. B. Hursthouse, *J. Mater. Chem.* **2000**, *10*, 2448.

[87] D. Prim, G. Kirsch, J. F. Nicoud, *Synlett* **1998**, *1998*, 383.

[88] F. Würthner, S. Yao, J. Schilling, R. Wortmann, M. Redi-Abshiro, E. Mecher, F. Gallego-Gomez, K. Meerholz, *J. Am. Chem. Soc.* **2001**, *123*, 2810.

[89] Z. Lu, R. J. Twieg, *Tetrahedron* **2005**, *61*, 903.

[90] M. Watanabe, T. Yamamoto, M. Nishiyama, *Chem. Commun.* **2000**, 133.

[91] R. M. F. Batista, S. P. G. Costa, M. Belsley, C. Lodeiro, M. M. M. Raposo, *Tetrahedron* **2008**, *64*, 9230.

[92] a) T. G. Deligeorgiev, N. I. Gadjev, K. H. Drexhage, *Dyes Pigm.* **1991**, *15*, 215; b) F. A. Mikhailenko, N. P. Vasilenko, A. D. Kachkovskii, Y. I. Rozhinskii, *Zh. Org. Khim.* **1982**, *18*, 435; c) Y. I. Rozhinskii, M. A. Mostoslavskii, *Zh. Org. Khim.* **1972**, *8*, 2177.

[93] a) I. G. Davydenko, A. D. Kachkovsky, M. L. Dekhtyar, Y. L. Slominskii, A. I. Tolmachev, *J. Phys. Org. Chem.* **2010**, *23*, 96; b) F. Würthner, *Synthesis* **1999**, *1999*, 2103.

[94] P. Quagliotto, N. Barbero, C. Barolo, E. Artuso, C. Compari, E. Fisicaro, G. Viscardi, *J. Colloid Interface Sci.* **2009**, *340*, 269.

[95] Y. Cui, H. Ren, J. Yu, Z. Wang, G. Qian, *Dyes Pigm.* **2009**, *81*, 53.

[96] D. R. Buckle, H. Smith, Deutsche Patentanmeldung (Beecham Group Ltd., Brentford, Middlesex, UK) P 2 261 568.5 (25.01.**1972**), 2-Nitroindan-1,3-dion-

Verbindungen, Verfahren zu ihrer Herstellung und diese Verbindungen enthaltende Arzneipräparate.

[97] J. Lasri, G. Gajewski, M. F. C. Guedes da Silva, M. L. Kuznetsov, R. R. Fernandes, A. J. L. Pombeiro, *Tetrahedron* **2012**, *68*, 7019.

[98] F. J. Kunz, O. E. Polansky, *Monatsh. Chem.* **1969**, *100*, 95.

[99] A. V. Kulinich, N. A. Derevyanko, E. K. Mikitenko, A. A. Ishchenko, *J. Phys. Org. Chem.* **2011**, *24*, 732.

[100] C. J. MacNevin, D. Gremyachinskiy, C.-W. Hsu, L. Li, M. Rougie, T. T. Davis, K. M. Hahn, *Bioconjugate Chem.* **2013**, *24*, 215.

[101] F. Würthner, K. Meerholz, *Chemistry* **2010**, *16*, 9366.

[102] a) N. Cho, J. Kim, K. Song, J. K. Lee, J. Ko, *Tetrahedron* **2012**, *68*, 4029; b) H.-W. Lin, S.-W. Chiu, L.-Y. Lin, Z.-Y. Hung, Y.-H. Chen, F. Lin, K.-T. Wong, *Adv. Mater.* **2012**, *24*, 2269; c) A. Leliège, J. Grolleau, M. Allain, P. Blanchard, D. Demeter, T. Rousseau, J. Roncali, *Chem. Eur. J.* **2013**, *19*, 9948.

[103] a) S. Krause, M. Stolte, F. Würthner, N. Koch, *J. Phys. Chem. C* **2013**, *117*, 19031; b) C. Ritzel, E. Schmälzlin, C. R. Bräuchle, K. Meerholz, A. Rössler, C. Ernst, J. Wichern, P. Boldt, Proc. SPIE 3796, Organic Nonlinear Optical Materials, **1999**, pp. 202.

[104] M. M. Chehimi, M. Delamar, *J. Electron Spectrosc. Relat. Phenom.* **1989**, *49*, 231.

[105] A. Cerniani, R. Passerini, *J. Chem. Soc.* **1954**, 2261.

[106] a) P. Zacharias, M. C. Gather, M. Rojahn, O. Nuyken, K. Meerholz, *Angew. Chem., Int. Ed.* **2007**, *46*, 4388; b) C. M. Cardona, W. Li, A. E. Kaifer, D. Stockdale, G. C. Bazan, *Adv. Mater.* **2011**, *23*, 2367.

[107] L. J. A. Koster, V. D. Mihailetchi, P. W. M. Blom, *Appl. Phys. Lett.* **2006**, *88*, 093511.

[108] L. Onsager, *J. Am. Chem. Soc.* **1936**, *58*, 1486.

[109] F. Würthner, R. Wortmann, R. Matschiner, K. Lukaszuk, K. Meerholz, Y. DeNardin, R. Bittner, C. Bräuchle, R. Sens, *Angew. Chem., Int. Ed. Engl.* **1997**, *36*, 2765.

[110] C. F. Macrae, P. R. Edgington, P. McCabe, E. Pidcock, G. P. Shields, R. Taylor, M. Towler, J. van de Streek, *J. Appl. Crystallogr.* **2006**, *39*, 453.

[111] a) B. P. Rand, D. P. Burk, S. R. Forrest, *Phys. Rev. B* **2007**, *75*, 115327; b) M. C. Scharber, D Mühlbacher, M Koppe, P Denk, C Waldauf, A J. Heeger, C. J. Brabec, *Adv. Mater.* **2006**, *18*, 789.

[112] H. van Eersel, R. A. J. Janssen, M. Kemerink, *Adv. Funct. Mater.* **2012**, *22*, 2700.

[113] N. M. Kronenberg, H. Bürckstümmer, M. Deppisch, F. Würthner, K. Meerholz, *J. Photon. Energy* **2011**, *1*, 011101.

[114] a) R. Fitzner, E. Mena-Osteritz, A. Mishra, G. Schulz, E. Reinold, M. Weil, C. Korner, H. Ziehlke, C. Elschner, K. Leo, M. Riede, M. Pfeiffer, C. Uhrich, P. Bauerle, *J. Am. Chem. Soc.* **2012**, *134*, 11064; b) K. Paudel, B. Johnson, M. Thieme, M. M. Haley, M. M. Payne, J. E. Anthony, O. Ostroverkhova, *Appl. Phys. Lett.* **2014**, *105*, 043301.

[115] a) M. J. Frisch, G. W. Trucks, H. B. Schlegel, G. E. Scuseria, M. A. Robb, J. R. Cheeseman, G. Scalmani, V. Barone, B. Mennucci, G. A. Petersson, H. Nakatsuji, M. Caricato, X. Li, H. P. Hratchian, A. F. Izmaylov, J. Bloino, G. Zheng, J. L. Sonnenberg, M. Hada, M. Ehara, K. Toyota, R. Fukuda, J. Hasegawa, M. Ishida, T. Nakajima, Y. Honda, O. Kitao, H. Nakai, T. Vreven, J. A. Montgomery Jr., J. E. Peralta, F. Ogliaro, M. J. Bearpark, J. Heyd, E. N. Brothers, K. N. Kudin, V. N. Staroverov, R. Kobayashi, J. Normand, K. Raghavachari, A. P. Rendell, J. C. Burant, S. S. Iyengar, J. Tomasi, M. Cossi, N. Rega, N. J. Millam, M. Klene, J. E. Knox, J. B. Cross, V. Bakken, C. Adamo, J. Jaramillo, R. Gomperts, R. E. Stratmann, O. Yazyev, A. J. Austin, R. Cammi, C. Pomelli, J. W. Ochterski, R. L. Martin, K. Morokuma, V. G. Zakrzewski, G. A. Voth, P. Salvador, J. J. Dannenberg, S. Dapprich, A. D. Daniels, Ö. Farkas, J. B. Foresman, J. V. Ortiz, J. Cioslowski, D. J. Fox, Gaussian 09 Revision D.01, Gaussian, Inc., Wallingford, CT, USA, **2009**; b) A. D. Becke, *Phys. Rev. A* **1988**, *38*, 3098; c) A. D. Becke, *J. Chem. Phys.* **1993**, *98*, 5648; d) C. Lee, W. Yang, R. G. Parr, *Phys. Rev. B* **1988**, *37*, 785.

[116] L. Beer, A. W. Cordes, D. J. T. Myles, R. T. Oakley, N. J. Taylor, *CrystEngComm* **2000**, *2*, 109.

[117] J.-H. Dou, Y.-Q. Zheng, T. Lei, S.-D. Zhang, Z. Wang, W.-B. Zhang, J.-Y. Wang, J. Pei, *Adv. Funct. Mater.* **2014**, *24*, 6270.

[118] a) J. L. Brédas, J. P. Calbert, D. A. da Silva Filho, J. Cornil, *PNAS* **2002**, *99*, 5804; b) D. A. da Silva Filho, E. G. Kim, J. L. Brédas, *Adv. Mater.* **2005**, *17*, 1072.

[119] C. Poelking, M. Tietze, C. Elschner, S. Olthof, D. Hertel, B. Baumeier, F. Würthner, K. Meerholz, K. Leo, D. Andrienko, *Nat. Mater.* **2015**, *14*, 434.

[120] D. Bagnis, L. Beverina, H. Huang, F. Silvestri, Y. Yao, H. Yan, G. A. Pagani, T. J. Marks, A. Facchetti, *J. Am. Chem. Soc.* **2010**, *132*, 4074.

[121] a) H. Yamagata, D. S. Maxwell, J. Fan, K. R. Kittilstved, A. L. Briseno, M. D. Barnes, F. C. Spano, *J. Phys. Chem. C* **2014**, *118*, 28842; b) J. D. A. Lin, O. V. Mikhnenko, J. Chen, Z. Masri, A. Ruseckas, A. Mikhailovsky, R. P. Raab, J. Liu, P. W. M. Blom, M. A. Loi, C. J. Garcia-Cervera, I. D. W. Samuel, T.-Q. Nguyen, *Mater. Horiz.* **2014**, *1*, 280.

[122] a) F. Würthner, T. E. Kaiser, C. R. Saha-Möller, *Angew. Chem., Int. Ed.* **2011**, *50*, 3376; b) D. Kurrle, J. Pflaum, *Appl. Phys. Lett.* **2008**, *92*, 133306; c) P. E. Hartnett, A. Timalsina, H. S. S. R. Matte, N. Zhou, X. Guo, W. Zhao, A. Facchetti, R. P. H. Chang, M. C. Hersam, M. R. Wasielewski, T. J. Marks, *J. Am. Chem. Soc.* **2014**, *136*, 16345.

[123] R. Schmidt, M. M. Ling, J. H. Oh, M. Winkler, M. Könemann, Z. Bao, F. Würthner, *Adv. Mater.* **2007**, *19*, 3692.

[124] B. A. Jones, M. J. Ahrens, M.-H. Yoon, A. Facchetti, T. J. Marks, M. R. Wasielewski, *Angew. Chem., Int. Ed.* **2004**, *43*, 6363.

[125] a) M. L. Tang, J. H. Oh, A. D. Reichardt, Z. Bao, *J. Am. Chem. Soc.* **2009**, *131*, 3733; b) Y. Takao, T. Masuoka, K. Yamamoto, T. Mizutani, F. Matsumoto, K. Moriwaki, K. Hida, T. Iwai, T. Ito, T. Mizuno, T. Ohno, *Tetrahedron Lett.* **2014**, *55*, 4564; c) A. M. Hiszpanski, J. D. Saathoff, L. Shaw, H. Wang, L. Kraya, F.

Lüttich, M. A. Brady, M. L. Chabinyc, A. Kahn, P. Clancy, Y.-L. Loo, *Chem. Mater.* **2015**, *27*, 1892.

[126] a) M. Mladenova, L. Ventelon, M. Blanchard-Desce, *Tetrahedron Lett.* **1999**, *40*, 6923; b) V. Alain, S. Rédoglia, M. Blanchard-Desce, S. Lebus, K. Lukaszuk, R. Wortmann, U. Gubler, C. Bosshard, P. Günter, *Chem. Phys.* **1999**, *245*, 51.

[127] a) H. John, C. Briehn, J. Schmidt, S. Hünig, J. Heinze, *Angew. Chem., Int. Ed.* **2007**, *46*, 449; b) C. Song, T. M. Swager, *Org. Lett.* **2008**, *10*, 3575; c) R. M. Meudtner, S. Hecht, *Angew. Chem., Int. Ed.* **2008**, *47*, 4926; d) M. Wolffs, N. Delsuc, D. Veldman, N. V. Anh, R. M. Williams, S. C. J. Meskers, R. A. J. Janssen, I. Huc, A. P. H. J. Schenning, *J. Am. Chem. Soc.* **2009**, *131*, 4819; e) K. Miwa, Y. Furusho, E. Yashima, *Nat. Chem.* **2010**, *2*, 444; f) F. Schlosser, M. Moos, C. Lambert, F. Würthner, *Adv. Mater.* **2013**, *25*, 410; g) I. Pochorovski, F. Diederich, *Acc. Chem. Res.* **2014**, *47*, 2096.

[128] S. Saito, J.-Y. Shin, J. M. Lim, K. S. Kim, D. Kim, A. Osuka, *Angew. Chem.* **2008**, *120*, 9803.

[129] M. J. Marsella, R. J. Reid, S. Estassi, L.-S. Wang, *J. Am. Chem. Soc.* **2002**, *124*, 12507.

[130] a) C. Yuan, S. Saito, C. Camacho, S. Irle, I. Hisaki, S. Yamaguchi, *J. Am. Chem. Soc.* **2013**, *135*, 8842; b) C. Yuan, S. Saito, C. Camacho, T. Kowalczyk, S. Irle, S. Yamaguchi, *Chem. Eur. J.* **2014**, *20*, 2193.

[131] S. Dähne, *Chimia* **1991**, *45*, 288.

[132] S. Pascal, A. Haefele, C. Monnereau, A. Charaf-Eddin, D. Jacquemin, B. Le Guennic, C. Andraud, O. Maury, *J. Phys. Chem. A* **2014**, *118*, 4038.

[133] a) C. Reichardt, *Chem. Rev.* **1994**, *94*, 2319; b) F. Effenberger, F. Würthner, *Angew. Chem., Int. Ed. Eng.* **1993**, *32*, 719.

[134] J. Moore, C. Ray, *Adv. Polym. Sci.* **2005**, *177*, 91.

[135] A. J. Fry, in *Laboratory Techniques in Electroanalytical Chemistry* (Eds.: P. T. Kessing, W. R. Heineman), Marcel Dekker Ltd, New York, **1996**, p. p.481.

[136] R. Dennington, T. Keith, J. Millam, GaussView, Version 5, Semichem Inc., Shawnee Mission, KS, **2009**.

[137] ADF, 2013.01; Scientific Computing and Modelling NV, Amsterdam, **2013**.

[138] a) D. Prim, G. Kirsch, J.-F. Nicoud, *Synlett* **1998**, 383−384; b) H. Hartmann, S. Scheithauer, *J. Prakt. Chem.* **1969**, *311*, 827.

[139] G. Sheldrick, *Acta Crystallogr., Sect. A: Found. Adv.* **2008**, *64*, 112.

Acknowledgements

This work was realized at the Institute of Organic Chemistry of the Julius-Maximilians-Universität Würzburg.

I would like to thank the following persons who have helped me during the realization of this thesis:

First of all I want to express my gratitude to my "Doktorvater" Prof. Dr. Frank Würthner for giving me the opportunity of joining his research group and entrusting me this interesting topic at the interface of chemistry, physics and material science. Thanks for the excellent working conditions provided, as well as the constant scientific support and fruitful discussions which have contributed to my personal and professional development.

I kindly thank Prof. Dr. Klaus Meerholz and his research group in Cologne for the successful collaboration during the last four years. I am particularly grateful to Julian Krumrain for the fabrication of organic solar cells.

I sincerely thank Dr. Matthias Stolte for being always available and in good mood for enriching discussions on organic electronics. Thanks as well for the EOA measurements, the moral and scientific support during the last four years and the revision of this thesis.

I thank Andreas Liess, Astrid Kudzus, Dr. Lizhen Huang, and Dr. Aifeng Lv for the fabrication of transistor devices and Dr. Vladimir Stepanenko for AFM measurements. Moreover, I thank Dr. David Schmidt, Ana-Maria Krause, Dr. Christian Burschka and Dr. Marcel Gsänger for single crystal analyses, and again Dr. David Schmidt and Ana-Maria Krause for thin-film XRD measurements and DSC measurements, respectively. Eva Kirchner and Valentin Kunz are kindly thanked for temperature-dependent NMR measurements.

For the synthetic support and cordial working atmosphere I am obliged to Christian Simon, Petra Seufert-Baumbach and Joachim Bialas. I further thank Thorsten Günder for his disposition and continuous interest in merocyanine dye research during his Bachelor thesis.

Dr. Michael Büchner, Fritz Dadrich, Antje Hautzinger and Juliane Adelmann are kindly thanked for the MS measurements. Likewise I thank Dr. Matthias Grüne, Elfriede Ruckdeschel and Patricia Altenberger for NMR measurements, as well as Liselotte

Michels and Sabine Timmroth for elemental analyses. Bernd Brunner is also thanked for the help with computer problems.

I want to specially thank the people who helped with the correction of this thesis: Dr. Matthias Stolte, Dr. Sabin-Lucian Suraru, Tobias Bach, Andreas Liess and Valentin Kunz.

I want to express my gratitude to all members of the Würthner group as well as the Beuerle and Fernandez groups for providing always a nice atmosphere at work and outside work. Particularly I thank Sabin for the uncountable scientific and personal discussions, as well as being always there; Valentin, for the cooking evenings; Jana, for the Mädelsabende; Andreas L. for the fruitful collaboration and being always in a good mood and Ayan for the Bollywood evenings. Sabin, Jana, Andreas, Valentin, Marcus, Ayan, Reinhard, Annike, Eva, Steffanie, Christina, Benjamin, Charlotte, thank you for the Barbecue evenings.

Agradezco a mis padres el apoyo moral durante los últimos diez años. A mis amigas Nuria, Carla y Elena, que a pesar de la distancia no hayamos perdido el contacto. A Tobias, que ha experimentado conmigo los altos y bajos propios del doctorado y ha sabido apoyarme en todo momento. Por último quiero dedicar este trabajo a mi madre, sin cuya fé en mí y apoyo incondicional a lo largo de los años no habría llegado hasta donde estoy.